

Analysis of Rotation Experiments in TFTR

A THESIS

Presented to

The Academic Faculty

by

Gabriella Pautasso

**In Partial Fulfillment
of the Requirements for the Degree
Doctor of Philosophy
in Nuclear Engineering**

Georgia Institute of Technology

December 1991

Analysis of Rotation Experiments in TFTR

APPROVED:

W.M. Stacey

A.V. Larson

J. Mandrekas

S.D. Scott

C.E. Thomas

Date approved by Chairman: 12/18/91

A Giorgio. Grazie per avermi perdonata.

A Edith, ringraziandoti per la preziosa amicizia ed il buon esempio.

** * * FOREWORD * * **

From: *Leben des Galileo* by Bertolt BRECHT

THE PHILOSOPHER Your Highness, my esteemed colleague and I are supported by no less an authority than the divine Aristotle.

GALILEO Gentlemen, belief in the authority of Aristotle is one thing, observable facts are another. ... I'm used to seeing the gentlemen of all faculties close their eyes to all facts and act as if nothing had happened. I show them my calculations, and they smile ... But truth is the child of time, not of authority. Our ignorance is infinite, let's whittle away just one cubic millimeter. ...

THE PHILOSOPHER Mr. Galilei, the truth can lead to all sort of things!

ANDREA Then why did you recant? ...

GALILEO They showed me the instruments. ... (Pause)

ANDREA (loud) In science only one thing counts: contribution to knowledge.

GALILEO And that I have supplied. Welcome to the gutter ...

THE SECOND BOY (to Andrea) You say you're a scholar. Then tell me: can people fly through the air? ...

ANDREA ... No one can fly through the air on a stick. Unless it has some sort of machine attached to it. Such machines don't exist yet. Maybe they never will because man is too heavy. But of course, we don't know ... We have hardly begun.

ACKNOWLEDGEMENTS

I would like to begin my list of acknowledgements with the members of my thesis committee. Special thanks go to: Dr. Steve Scott, at PPPL, who taught me the rudiments of plasma parameters analysis and provided unselfish guidance and insights through the course of the thesis; Prof. W.M. Stacey, my advisor, for making this dissertation possible – his patience and persistence will hardly be forgotten; Prof. Tommy Thomas for his continuous support and careful advice; Prof. Alan Larson for reading both my qualifying report and this thesis so carefully; John (Dr. J. Mandrekas) for always having in his file-cabinet the right paper able to answer my question, and for spending many hours discussing plasma physics.

I am indebted to the Princeton Plasma Physics Laboratory, which hosted me there for six months, and to several researchers of the TFTR team (Drs. K. Hill, M. Bitter, H. Hsuan, A. Ramsey and S. Cowley, among others) for all the technical information and help they provided. I also wish to express my appreciation to the whole TFTR team, who was responsible for producing the data that were used in this thesis.

Thanks to Peter (P. Halvorson) who rescued me over and over again when my “anachronism” was an obstacle to a fruitful collaboration with computers and software. Then last, but not least, I am grateful to Claudine (Ms. C. Vogel) for her friendship and unlimited encouragement at much needed times.

This work was supported by the US Department of Energy under the Grant No. DE-FG05-87ER51112 with the Georgia Tech Research Corporation.

SUMMARY

The study of momentum confinement is a valuable means of investigating the mechanisms governing confinement in tokamak plasmas.

A dedicated rotation experiment was conducted in TFTR, in September 1988, employing the recently installed CHERS diagnostic. Shots at different values of plasma current, magnetic field, injected beam power and injection direction were made, to study the parametric dependence of local fluxes of momentum and energy.

This Thesis is focused on the study of momentum confinement. Its purposes are to analyze the data of the TFTR rotation experiment, to document the results and to compare the experimental results with the predictions of neoclassical and anomalous momentum transport theories. Since the gyroviscous theory has been found previously to reproduce the experimental momentum confinement times and its parametric dependence in several devices, particular attention is devoted to the evaluation of the magnitude of the poloidal variation of densities and rotation frequencies that determine the magnitude of the gyroviscous momentum flux.

We find that: (1) Ware's cold ions theory underpredicts the observed viscosity by a few orders of magnitude; (2) each of the anomalous theories considered predicted torque flows which show magnitudes, radial profiles and parametric dependences on plasma parameters different from those of the experimental torque flow; (3) up-down poloidal asymmetries of density and rotation frequency, evaluated with a model which neglects heat flux and includes the effect of anomalous particle fluxes, are found to be much smaller than ϵ ; (4) the gyroviscous torque is at least one order of magnitude smaller than the experimental torque flow.

Contents

FOREWORD	ii
ACKNOWLEDGEMENTS	iii
SUMMARY	iv
TABLE OF CONTENTS	v
LIST OF TABLES	x
LIST OF FIGURES	xi
1 INTRODUCTION	1
2 PLASMA DIAGNOSTICS AND DATA INTERPRETATION	5
2.1 Diagnostics	5
2.1.1 Diagnostics for $v_\phi(R)$ measurements	5
2.1.2 TFTR diagnostics	8
2.2 Interpretation of experimental data	11
3 THEORIES FOR MOMENTUM TRANSPORT	18
3.1 Introduction	18
3.2 Theories of neoclassical momentum transport	18
3.2.1 The viscosity tensor	18
3.2.2 The theory of gyroviscosity	23

3.2.3	Ware's cold ions theory	26
3.2.4	Neoclassical additions to Braginskii's tensor	27
3.2.5	Rotational viscosity	29
3.3	Theories of anomalous momentum transport	30
3.3.1	Anomalous viscosity due to stochastic magnetic perturbations	30
3.3.2	Anomalous viscosity due to ITG modes	31
3.3.3	Anomalous viscosity due to trapped and untrapped particle modes	33
4	PREVIOUS ROTATION EXPERIMENTS AND COMPARISON WITH THEORIES	34
4.1	Introduction	34
4.2	Rotation data and their analysis	34
4.2.1	PLT	36
4.2.2	PDX	38
4.2.3	ISX-B	39
4.2.4	DIII	40
4.2.5	ASDEX	44
4.2.6	TFTR	47
4.2.7	JET	54
4.2.8	PBX-M	57
4.3	Summary of previous results	58
4.3.1	Parametric dependence of $v_{\phi}^{ex}(0)$, τ_{ϕ}^{ex} and $\chi_{\phi}^{ex}(r)$	58
4.3.2	Comparison of theory with experiments	61
5	A TFTR ROTATION EXPERIMENT: Exp. 44. MACHINE AND PLASMA PARAMETERS	64
6	COMPARISON OF THEORY AND EXPERIMENT	82
6.1	Gyroviscous theory	82

6.2	Ware's cold ions theory	93
6.3	Anomalous torque flows	93
6.4	Anomalous momentum diffusivities	96
7	VARIATION ON THE FLUX SURFACE OF n_j AND $\Omega_{\phi j}$: THEO-	
	RIES AND PREVIOUS EXPERIMENTS	100
7.1	Introduction	100
7.2	Theoretical estimates of \tilde{n}_j	101
7.2.1	\tilde{n}_j due to friction forces	101
7.2.2	\tilde{n}_{ji} due to perpendicular NBI	105
7.2.3	\tilde{n}_j due to asymmetric particle sources	106
7.2.4	\tilde{n}_j due to inertia forces	106
7.2.5	\tilde{n}_j due to momentum input, inertia and friction	107
7.3	Experimental measurements of \tilde{n}_j	108
7.3.1	\tilde{n}_I in ALCATOR A	108
7.3.2	\tilde{n}_I in PLT	110
7.3.3	\tilde{n}_I in PDX	110
7.3.4	\tilde{n}_I in ASDEX	113
7.3.5	\tilde{n}_I in TEXT	115
7.4	Theoretical estimates of $\tilde{\Omega}_{\phi j}$	117
7.5	Experimental measurements of $\tilde{\Omega}_{\phi j}$	118
7.6	Poloidal velocity	119
7.6.1	Theoretical estimates of the poloidal velocity	119
7.6.2	Experimental measurements of v_θ	121
7.7	Summary	125
8	POLOIDAL VARIATIONS OF DENSITY AND ROTATION FRE-	
	QUENCY IN TFTR Exp. 44	127
8.1	Introduction	127

8.2	Measurements of \tilde{n}_j and $\tilde{\Omega}_{\phi j}$ in TFTR Exp.44	128
8.2.1	Measurements of $n_e^2 Z_{eff}(R)$	128
8.2.2	Measurements of $\Omega_{\phi I}(R)$	130
8.3	Continuity equation and form of the poloidal flow	131
8.4	Radial momentum balance equation and form of the toroidal flow . .	133
8.5	Form of $\tilde{\Omega}_{\phi j}(r, \theta)$ and $\Xi_j(r)$	136
8.5.1	Poloidal variations of $\Omega_{\phi j}$	136
8.5.2	Relation to gyroviscous torque	140
8.6	Poloidal momentum balance equation	144
8.6.1	General case	144
8.6.2	Case $\vec{q}_j = 0$	146
8.7	Could anomalous forces affect \tilde{n}_j , $\tilde{\Omega}_{\phi j}$, $v_{\theta j}$?	151
8.7.1	Introduction	151
8.7.2	Fluctuation measurements and inferred fluctuation-driven radial flux	152
8.7.3	Conclusion	156
8.8	Radial velocities	157
8.9	Poloidal variations of n_j and $\Omega_{\phi j}$ (case $\vec{q}_j = 0$)	160
8.9.1	Poloidal variations of n_I	160
8.9.2	Impurities poloidal flow	161
8.9.3	Density poloidal variations and poloidal flow of main ions . . .	161
8.9.4	Discussion of the results	163
8.10	Evaluation of \tilde{n}_j , $\tilde{\Omega}_{\phi j}$ and $K_{\phi}(r)$ (case $\vec{q}_j \neq 0$)	177
8.10.1	Poloidal momentum balance equation	177
8.10.2	Finite-heat-flux viscosity model	179
8.10.3	Discussion of K_{ϕ}^{gv*} and \hat{K}_{ϕ}^{gv}	181
8.11	Comparison of results with previous work and discussion of uncertainties	182
8.11.1	Comparison of results with previous works	182

8.11.2 How believable are our estimate of \tilde{n}_j , $\tilde{\Omega}_\phi$, and Ξ_j for TFTR	
Exp.44 ?	186
9 SUMMARY, CONCLUSIONS AND FUTURE WORK	190
9.1 Summary and conclusions	190
9.2 Suggestions for future work	192
A Heat flow balance equation	193
B Friction force	194
C Neoclassical viscous forces	195
Bibliography	198

List of Tables

3.1	The viscosity tensor elements	20
4.1	Summary of rotation experiments	35
4.2	TFTR regimes	53
5.1	Summary of plasma parameters for P_b and I_p scan in Exp. 44	66
5.2	Summary of plasma parameters for B_ϕ scan in Exp. 44	67
5.3	Electrons, thermal and fast ions stored energy	79

List of Figures

2.1	Doppler shift of the TiXXI K_α line	7
2.2	Measurements of $v_\phi(R)$ by CHERS and XCS	9
2.3	Measurements of Z_{eff} by the PHA and VB diagnostics	10
4.1	Scaling of $v_\phi^{ex}(0)$ with P_b in PLT	36
4.2	Scaling of $v_\phi^{ex}(0)$ with P_b and I_p in ISX-B	41
4.3	Comparison of $v_\phi^{ex}(0)$ with $v_\phi^{gv}(0)$ in ISX-B	42
4.4	τ_E and τ_ϕ in DIII	43
4.5	Comparison of τ_ϕ^{ex} and τ_ϕ^{gv} in DIII	45
4.6	Comparison of $v_\phi^{ex}(0)$ with $v_\phi^{gv}(0)$ in TFTR	48
4.7	$v_\phi(0)$ for L-mode TFTR discharges	49
4.8	τ_ϕ versus Z_{eff} and I_p in TFTR	51
4.9	Comparison of η_i^{ex} and χ^{ni} with TFTR experimental data	52
4.10	Gyroviscous predictions of τ_ϕ in JET	56
4.11	Comparison of τ_ϕ^{exp} with τ_ϕ^{ex} from several tokamaks	61
5.1	Time history of the TFTR Exp. 44 plasma parameters	65
5.2	$v_{\phi I}$ versus input torque in Exp. 44	68
5.3	Plasma parameter profiles in Exp. 44	69
5.4	Radial profiles of torque flows in Exp. 44	72
5.5	$\tau_{\phi th}$ versus input torque in Exp. 44	73
5.6	Time histories of \bar{n}_e , \mathcal{P}_{n_e} , N_b and N_e in Exp. 44	76
5.7	Evolution of H-alpha emission profile in Exp. 44	77

5.8	Fraction of power losses versus \bar{n}_e in Exp. 44	78
5.9	τ_E versus injected power in Exp. 44	80
5.10	$\tau_{\phi th}$ versus τ_E in Exp. 44	81
6.1	Comparison of $v_\phi^{gv}(0)$ with $v_\phi^{ex}(0)$ in Exp.44	83
6.2	Comparison of τ_ϕ^{gv} with τ_ϕ^{ex} in Exp.44.	84
6.3	Scaling of τ_ϕ^{ex} with $T_i(0)$ in Exp.44	86
6.4	Scaling of τ_ϕ^{ex} with \bar{Z} in Exp.44	87
6.5	Scaling of τ_ϕ^{ex} B in Exp.44	88
6.6	Comparison of K_ϕ^{ex} with theoretical predictions in Exp.44	89
6.7	Comparison of $v_\phi^{gv}(0)$ ($\hat{Z} = Z_{eff}$ model) with $v_\phi^{ex}(0)$ in Exp.44	91
6.8	Evaluation of the parameter γ_c in Exp.44	92
6.9	Comparison of η_i^{ex} with theoretical predictions in Exp.44	94
6.10	Comparison of χ_ϕ^{ex} with theoretical predictions in Exp.44	97
6.11	Scaling of χ_ϕ^{ex} with plasma parameters in Exp.44	98
7.1	Theoretical prediction of density asymmetries in TEXT	105
7.2	Density asymmetries in Alcator A	109
7.3	Density asymmetries in PDX	112
7.4	Neoclassical predictions of \bar{n} in PDX	113
7.5	USX-ray image of the ASDEX NBI plasma	114
7.6	Density asymmetries in TEXT	116
7.7	Radial profiles of v_θ and v_ϕ in L-mode and H-mode, from JFT-2M	123
8.1	X-ray vertical image of a TFTR plasma	129
8.2	Magnitude of the main ion source	133
8.3	Magnitude of terms entering the expression of $\Omega_{\phi j}$	138
8.4	Radial profiles of the poloidal momentum balance equation terms (deuterium)	148

8.5	Radial profiles of the poloidal momentum balance equation terms, (carbon)	149
8.6	Radial profiles of $v_{\phi j}/v_{thj}$ and ν_j^*	151
8.7	Comparison between Γ_i^{ex} and the $\Gamma_i^{\tilde{E}}$ in TEXT	155
8.8	$v_{\theta I}(r)$ calculated for $\gamma_I = 0.0, 0.1$ ($q=0$)	165
8.9	$\tilde{n}_{I(c,s)}$ calculated for $\gamma_I = 0.0, 0.1$ and with $v_{\theta*}$	166
8.10	$v_{\theta i}$ calculated for $\gamma_i = 0.0, 0.5, 0.9$ and $\gamma_I = 0.1$ ($q=0$)	167
8.11	$\tilde{n}_{i(c,s)}$ calculated for $\gamma_i = 0.0, 0.5, 0.9$ and $\gamma_I = 0.1$	168
8.12	Radial profiles of the $(\Theta G/Z)_{eff}$ parameter	172
8.13	Radial profiles of K_{ϕ}^{qv} 's	173
8.14	Radial profiles of G_{qv_i} and G_{Ξ_i}	175

Chapter 1

INTRODUCTION

The issue of confinement and how it can be extrapolated from measurements in today's tokamaks to predict the performance of future ones is a fundamental one in magnetic fusion. The assumptions made regarding confinement determine the size of the device, and therefore its cost, and the accuracy of these assumptions impacts the actual performance. This is the reason why, in the last years, highest priority has been given, in the Magnetic Fusion Energy program, to the understanding of transport and confinement, encouraging selected experiments, the development of new theories and diagnostics, and an extensive comparison between theories and experimental results.

The study of momentum confinement, in neutral-beam-injection (NBI) discharges has been part of this effort.

The torque from the neutral beams causes the plasma to rotate up to velocities comparable to the sound speed. It is observed that a sheared velocity profile establishes itself in a short time (tens of milliseconds) and that an exponential-like decay of the velocity follows the beam turn-off. These are manifestations of radial transfer of angular momentum, which results from viscous forces present in the plasma and from the exchange of momentum between the plasma and the external systems, whose investigation is useful for the following reasons. Due to the large difference between proton and electron masses, momentum transport can be studied neglecting electrons and electron-ion coupling, allowing ion transport effects to be isolated. Convection of momentum is usually less important than momentum conduction and uncertainties in momentum convection, therefore, cause smaller uncertainties in the measured momentum fluxes and the inferred momentum diffusion coefficients. Rotation affects

particle and, possibly, thermal energy transport, as well as momentum transport, requiring an understanding of the origin of their interrelation, in order to identify the best confinement conditions for the future machines.

An extensive database of rotation speed measurements in tokamaks with unbalanced NBI has been accumulating in the last decade [1]–[22] and it covers a broad range of plasma dimensions, densities and temperatures. In most of the early experiments, the data did not provide a complete characterization of the plasma conditions; only the central rotation velocity was routinely determined by measuring the Doppler shift of emission lines from impurities present in the plasma center. Charge exchange recombination spectroscopy (CHERS) diagnostics, that allow a simultaneous determination of velocity and ion temperature profiles, have become operative only in the last few years. Valuable radial profiles of momentum diffusion coefficients and of the momentum fluxes can now be calculated using these measurements and compared with the local levels of transport predicted by different theories.

The analysis to date of the experimental data has not been able to suggest a simple and universal dependence of the central velocity or of the momentum confinement time on the experimental parameters. The apparently complex dependence of the momentum confinement properties on the plasma conditions has suggested an examination of the local parametric dependence of momentum fluxes, of the associated global confinement times and of rotation velocities that are predicted by theoretical models.

Several momentum transport theories have been developed to explain the observed momentum confinement times during NBI and the velocity decay following beam turn-off. Classical and perpendicular neoclassical viscous forces are orders of magnitude smaller than the slowing-down forces acting on the rotating plasma [3]. The gyroviscous neoclassical force [23], which depends on poloidal asymmetries of the rotation velocity and density, is of the proper magnitude to account for the the

momentum confinement times observed on several machines [20],[24] when these asymmetries are of order the inverse aspect ratio, $\epsilon = r/R$. Although there is some evidence suggesting order ϵ asymmetries for collisional ions, a self-consistent solution for these asymmetries was not carried out for any of the rotation experiments. Recent works by Ware [25], Hsu and Sigmar [26] and Stacey and Neeley [27], not yet compared with rotation measurements, have revisited the neoclassical theory and pointed out some possible new mechanisms of momentum transport.

Momentum diffusion coefficients have been derived for anomalous theories based, respectively, upon stochastic magnetic perturbations [28]–[30], untrapped particle modes [31],[32], and ion-temperature-gradient-driven modes [33]–[40]. Comparison of the anomalous theories with the experiments has been extensive only for the last theory, carried out mostly in the last two years, and has led to conflicting evidence on the role of these modes in determining momentum confinement.

The comparison between theories and rotation experiments has not yet led to a clear understanding of the causes of momentum transport, but an extensive quantitative test of these theories has not yet been done.

A dedicated rotation experiment, “Exp. 44”, was conducted in TFTR, in September 1988, employing the recently installed CHERS diagnostic [41]. It is particularly suited for a careful comparison with theoretical predictions. Shots at different values of plasma current, magnetic field, injected beam power and injection direction were made, to study the parametric dependence of local fluxes of momentum and energy, and the corresponding global confinement times, as well as their correlation.

This Thesis will be focused on the study of momentum confinement. Its purposes are to analyze the data of the TFTR rotation experiments (Exp. 44), to document the results and to compare the experimental results with the predictions of neoclassical and anomalous momentum transport theories, in order to evaluate the ability of the latter to reproduce the magnitude and the parametric dependences that are observed

experimentally. Since the gyroviscous theory has been found previously to reproduce the experimental momentum confinement times and its parametric dependence in several devices, particular attention will be devoted to the evaluation of the magnitude of the poloidal variation of densities and rotation frequencies that determine the magnitude of the gyroviscous momentum flux.

The Thesis is organized as follows. Chapter 2 includes a description of the physical principles used for plasma velocity measurements and of the TFTR diagnostics used in Exp. 44. The basic equations and the definition of theoretical and experimental quantities, needed for the analysis of rotation experiments, are also given in Chapter 2. In Chapter 3, the neoclassical and anomalous theories of momentum confinement are summarized, along with their assumptions, and the theoretical formulas for the momentum flux and related quantities are given. In Chapter 4, previous rotation experiments from a variety of tokamaks and their comparison with theoretical formulas are reviewed. Chapter 5 documents the experimental conditions and the plasma parameters characteristic of the TFTR experiment. In Chapter 6, the predicted momentum fluxes and diffusion coefficients are compared with the corresponding experimental quantities and the results are discussed. Due to the fundamental role of the density and velocity poloidal variations in determining the magnitude of the gyroviscous force, experimental evidence of such asymmetries and related theoretical works are reviewed in Chapter 7. This same Chapter includes a review of measurements of poloidal velocity and related theoretical works, since v_θ plays a role in determining the density and velocity asymmetry magnitude. Chapter 8 is dedicated to the calculation of the ion density and velocity poloidal variations for some typical discharges of Exp. 44. The principal conclusions are summarized in Chapter 9 and suggestions for future work are made.

Chapter 2

PLASMA DIAGNOSTICS AND DATA INTERPRETATION

2.1 Diagnostics

This Section presents a brief overview of the physical principles used for plasma velocity measurements. A description of the TFTR diagnostics used in Exp. 44, to measure the plasma parameter of interest for our analysis, follows.

2.1.1 Diagnostics for $v_\phi(R)$ measurements

The toroidal velocity of ions is evaluated by the analysis of the Doppler shift of particular radiative emission lines or by analyzing the Mirnov coils signal.

Doppler shift based diagnostics ^[42] - Measurements of the Doppler shift of spectral lines over a broad range - from the visible region to the x-ray region- have been successfully used to determine v_ϕ by means of their interrelation: $v_\phi/c = \lambda/\lambda_0 - 1$ (with λ_0 and λ the observed wavelengths of the emitter at rest and in the rotating plasma, respectively).

The line radiation of metal ions with hydrogen- and helium-like outer electron structure (Fe, Ni, W, Cr, Ti, etc.), mostly present in the plasma center, were used in the earlier diagnostics. These lines lie in the x-ray region of the spectrum and for this reason crystal x-ray spectrometers are employed. This technique allows the measurement of $v_\phi(0)$ (and of $T_i(0)$; see Fig. 2.1) during the entire course of the discharge, with a time resolution of tens of ms, and a spatial resolution of a few cms, depending on the temperature gradient and the impurity diffusion process. In a plasma with nonuniform temperature, the different ionization stages tend to distribute

themselves in overlapping concentric shells, with the lowest ionization stages occurring in the coolest regions.

Valuable profile measurements were derived by observing emission from different ion species located at different radii, but this method yields a coarse spatial resolution and it was difficult to apply systematically to a large number of discharges. Therefore the systematic studies of radial profiles of momentum fluxes and diffusion coefficients and their parametric dependence have been undertaken only recently.

Charge exchange recombination diagnostics (CHERS or CERS or CXR), now available on all the major tokamaks, record the radiation emitted when injected neutral beams (A^0) interacts with the plasma ions (I^{+n})

$$A^0 + I^{+n} = A^+ + I^{+(n-1)} + h\nu$$

Emission from intrinsic (O,C) or injected (He) impurities, whose spectral lines are normally in the visible and near UV region of the spectrum, are usually used. The spatial resolution - essentially the width, in minor radius, of the intersection between the beam of neutral particles and the CHERS sightline - ranges from 2 to 10 cm, from the center to the edge, and a 10-100 ms measurement time is required.

The velocity profile is usually measured for $R \geq R_0$ and then extrapolated to the rest of the plasma region by making use of the assumption that the flux surface rotates as a rigid body, i.e. $v_\phi(r, \theta) = \Omega_\phi(r) R(r, \theta)$.

Mirnov coil signals ^[3] - A poloidal array of magnetic pickup loops (Mirnov coils) can detect rotating MHD structures in the plasma. The velocity profile is determined by comparing the phase of oscillation between adjacent pickup loops, when the mode structure and radial location of the MHD instability are known. The rotation of the MHD instability may not be correlated with the rotation of the bulk plasma, as happens if fishbone oscillations are present. When mode oscillations can be correlated with the toroidal rotation of the bulk plasma, these measurements may be in error by as much as 15 %, while the radial position of the mode resonant surface, determined from the soft-x-ray measurements, is known to within 2 cm.

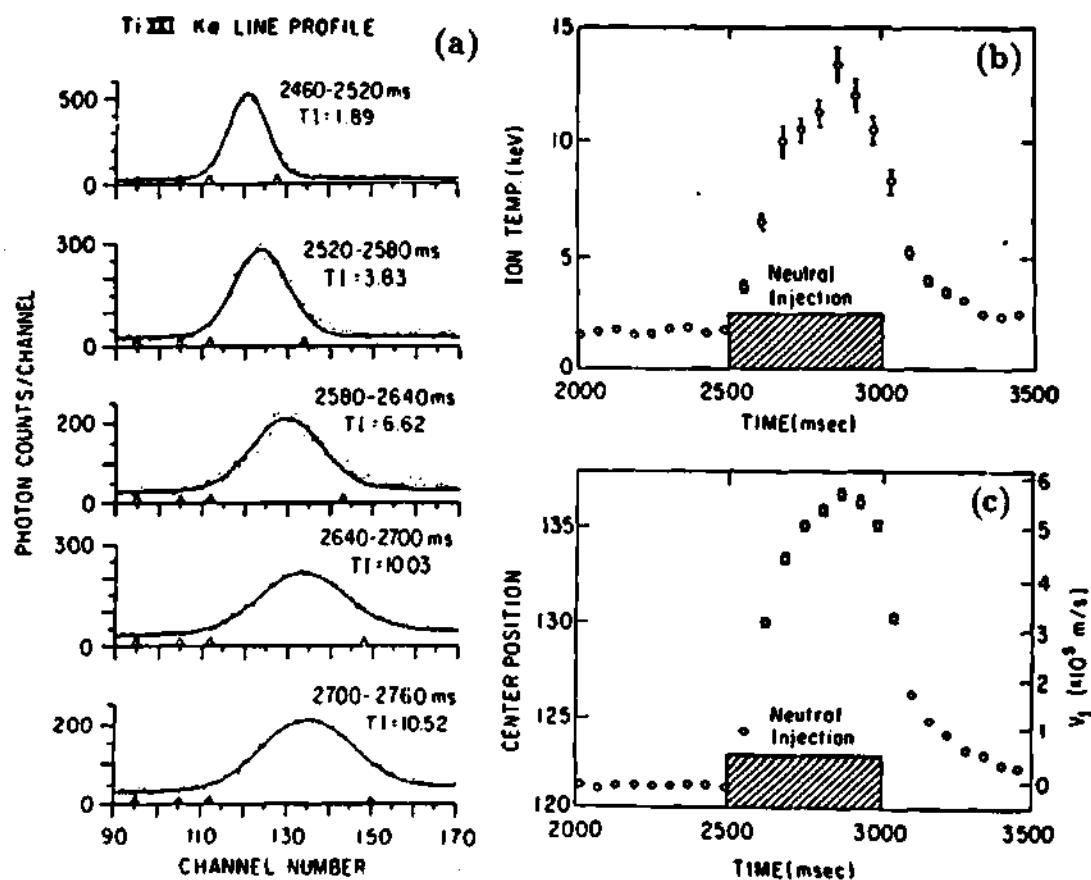


Figure 2.1: (a) Doppler shift of the TiXXI K_α line recorded by the Crystal Spectrometer on TFTR [43]. Inferred $T_i(0)$ (b) and $v_\phi(0)$ (c) time histories [43]

2.1.2 TFTR diagnostics

During the plasma discharges of Exp. 44, most of the plasma parameters of interest for our analysis were monitored by more than one diagnostic.

The electron density, n_e , and the electron temperature, T_e , were continuously measured by the Multichannel Far-Infrared Interferometer (MIRI) ^[44] and by the Electron Cyclotron Emission (ECE) ^[45] diagnostic, respectively. An Abel inversion technique was then used for the evaluation of $n_e(R, t)$. Both the MIRI $n_e(R, t)$ and the ECE $T_e(R, t)$ agree quite well (within 10 %) with the single-time-point measurements of the same profiles by the Thomson Scattering (TS) diagnostic.

The v_ϕ and T_i central values and radial profiles were obtained by the Charge Exchange Recombination Spectroscopy (CHERS) diagnostic ^[41] after 400 or 900 ms of NB injection, using a Diagnostic Neutral Beam (DNB) injector to enhance the production of charge-exchange impurity lines (C VI, 5292 Å). Time histories of central toroidal velocity, $v_\phi(0)$, and central ion temperature, $T_i(0)$, were determined from the Doppler shift of the Ni XXVII resonance line measured by a horizontal X-ray Crystal Spectrometer (XCS; $K_\alpha = 1.5879$ Å) ^[46]. The good agreement between $v_\phi(0)$ as measured by CHERS and by the XCS is shown in Fig. 2.2. Only the CHERS data will be used in the analysis outlined in following chapters.

The impurity concentration was inferred from the intensity of radiation emission measured by the Visible Bremsstrahlung (VB) ^[47] and by the Pulse Height Analysis (PHA) diagnostics. The VB radiation, at 5235 Å, is measured along a quasi-tangential chord. The PHA diagnostic uses a centrally viewing X-ray detector to perform time-dependent measurements of low- and medium-Z impurity concentration. The agreement between the Z_{eff}^{VB} and the Z_{eff}^{PHA} was good for co-injection shots, while in counter-injection shots the PHA data are 30 % higher than the VB data, as shown in Fig. 2.3. In NBI plasmas, the Z_{eff}^{VB} data are considered more accurate than the Z_{eff}^{PHA} data ^[48] and therefore will be used for the evaluation of the low Z impurity

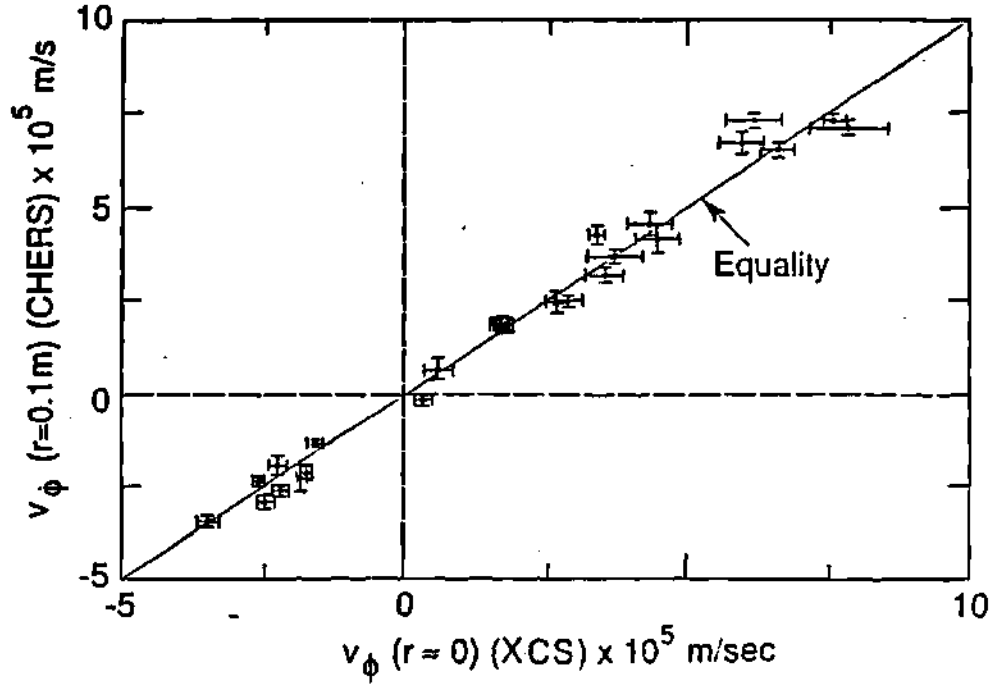


Figure 2.2: Comparison between the central toroidal velocity measured by the CHERS and the XCS diagnostics.

concentration in this analysis. The interpretation of the PHA measurements to infer the values of Z_{eff}^{PHA} requires the knowledge of recombination and excitation rates and of the impurities charge-state equilibrium, which are difficult to evaluate.

The metallic impurity content, $Z_{met} = Z_M^2 n_M / n_e$ is evaluated from the PHA measurements and it is considered a rather accurate measurement. The VB and PHA diagnostics did not measure the radial distribution of impurities and could provide only average values of Z_{eff} and Z_{met} .

The H_α Interference Filter Array (HAIFA) diagnostic, viewing the TFTR inner limiter, provides a measurement of the total H_α emission at five different poloidal angles, $0-30^\circ$ from the midplane, which allows the evaluation of the flux of deuterium from the inner wall [49].

Seven fission detectors, distributed around the TFTR torus, monitored the neu-

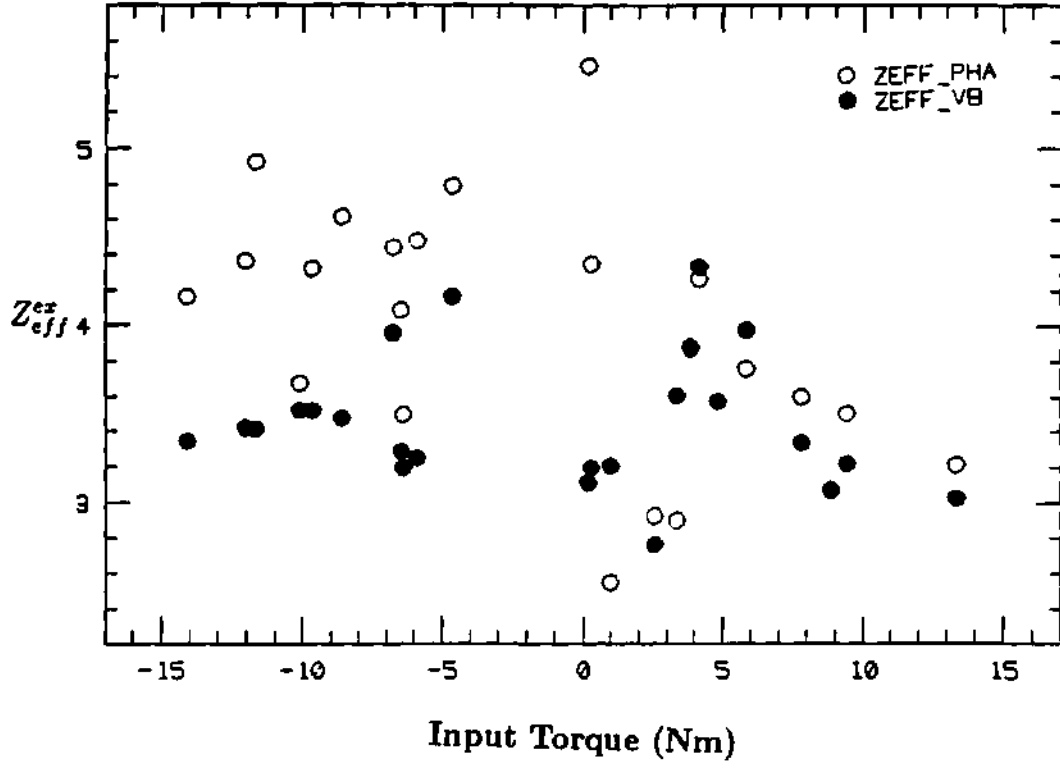


Figure 2.3: Measurements of Z_{eff} by the PHA (○) and by the VB (●) diagnostics versus input torque.

tron source strength of the plasma during each shot. [50]

The X-ray Imaging System (XIS) is composed of an array of ~ 40 detectors viewing different chords of the plasma above and below the midplane and recording the soft x-ray emission integrated along these chords [51]. The local emission is proportional to $\sum_j n_e n_j Z_j^2 \sqrt{T_e} \exp(-E_f/T_e)$, where E_f is the cut-off energy of a Be filter used to reject soft x-rays less than ~ 2 keV. The comparison between the emissions from two chords symmetric with respect to the horizontal midplane can give information about poloidal asymmetries of $n_e^2 Z_{eff}$ (assuming $T_e = \text{const}(\theta)$). The error affecting the emissivity measurements is of the order of 10 %.

2.2 Interpretation of experimental data

This Section addresses the analysis of plasma rotation experiments by introducing the basic equations, defining the notation and deriving a series of quantities conventionally used in the description of these experiments. Moreover, since the 1D, steady state, transport code SNAP [52] has been extensively used for the data analysis of Exp. 44, references are made to it, in order to illustrate the models contained in this code that pertain to momentum transport analysis.

The equations describing particle and momentum balance for species j - the $(1, m_j \vec{v}_j)$ first two moments of the Boltzmann equation - are, respectively [53]:

$$\frac{\partial n_j}{\partial t} + \nabla \cdot (n_j \vec{v}_j) = S_j \quad (2.1)$$

$$m_j \frac{\partial}{\partial t} (n_j \vec{v}_j) + \nabla \cdot (n_j m_j \vec{v}_j \vec{v}_j + \vec{\Pi}_j) + \nabla p_j + n_j e_j (\nabla \Phi + \vec{B} \times \vec{v}_j) = \vec{R}_j + \vec{\mathcal{M}}_j \quad (2.2)$$

where m_j and e_j are the mass and charge of species j , S_j represents the particle sources and sinks, \vec{v}_j is the fluid velocity, p_j is the pressure, $\vec{\Pi}_j$ is the viscosity tensor, \vec{R}_j is the collisional friction term, $\vec{\mathcal{M}}_j$ represents the external momentum sources and sinks, and Φ and \vec{B} are the electrostatic potential and the magnetic field.

In order to allow analytical treatment of the above equations, the flux surfaces are assumed circular, that is:

$$R = R_0 h, \quad B = B_0 / h, \quad h \equiv 1 + \epsilon_0 \cos \theta, \quad \epsilon_0 \equiv r / R_0 ;$$

and the plasma properties are considered independent of the toroidal coordinate. The orthogonal coordinate system, (r, θ, ϕ) , has length elements $dl_r = dr$, $dl_\theta = r d\theta$, $dl_\phi = R d\phi$, and unit vectors indicated as \hat{r} , $\hat{\theta}$, $\hat{\phi}$ and directed in the radial, poloidal and toroidal directions. This approximation is appropriate for the TFTR plasmas for which the flux surfaces are modestly shifted ($\Delta R_o/a \leq 15\%$) and slightly elongated ($k < 1.05$) circular flux surfaces.

The flux surface average of a quantity 'x' is indicated as $\langle x \rangle \equiv \int x h d\theta / (2\pi)$.

The toroidal component of Eq.(2.2) describes the balance among the forces that determine the observed toroidal plasma rotation. Multiplying Eq.(2.2) by $(R\hat{\phi})$, summing over species and flux surface averaging we obtain:

$$\sum_j m_j \langle R \frac{\partial n_j v_{\phi j}}{\partial t} \rangle + \sum_j \langle R \hat{\phi} \nabla \cdot \vec{\Pi}_j \rangle = \quad (2.3)$$

$$\langle R \mathcal{M}_\phi \rangle - \sum_j m_j \langle R \hat{\phi} \nabla \cdot (n_j \vec{v}_j \vec{v}_j) \rangle \quad (2.4)$$

Axisymmetry, charge neutrality and $\mathcal{M}_\phi \equiv \sum_j \hat{\phi} \vec{\mathcal{M}}_j$ have been used.

It is experimentally difficult to measure the difference among the toroidal rotation speeds of the different ion species, since it is comparable to the magnitude of the measurement error. Therefore, for the purpose of interpreting the experimental data, the toroidal velocity is assumed to be the same for each plasma species. Eq.(2.3) then becomes:

$$R_0 m_{av} \frac{\partial}{\partial t} (n_{eth}(r) v_\phi(r)) + \mathcal{K}_\phi(r) = \mathcal{T}_\phi(r) - m_{av} \frac{R_0}{r} \frac{\partial}{\partial r} (r v_\phi(r) \Gamma_e(r)) \quad (2.5)$$

where

- $m_{av} \equiv \sum_j m_j n_j / \sum_j n_j$ is the average ion mass. SNAP considers four ion species (H, D, C and metal impurity) and the fast ions are not included in the summation. Z_{eff} and Z_{met} are assumed to be a constant and, therefore, the impurity densities have the same radial profile as n_e .

- $n_{eth} = n_e - n_{fi}$, where n_{fi} is the fast ion density. SNAP assumes that fast ions become thermal ions when their energy falls below $3/2 T_i$.
- $\mathcal{K}_\phi \equiv \sum_j < R \hat{\phi} \nabla \cdot \vec{\Pi}_j >$ is the viscosity torque density;
- $\mathcal{T}_\phi \equiv < R \mathcal{M}_\phi >$ is the beam torque density delivered to the thermal plasma, evaluated in SNAP with a numerical solution of the Fokker Planck equation.

The fast ion distribution is calculated assuming no anomalous diffusion of the fast ions, which is consistent with the TFTR experiments [54].

- The last term in Eq.(2.5) is the convected torque density. SNAP calculates the beam electron source, \mathcal{S}_b , by evaluating the ionization rate of the beam neutrals, and the wall source, \mathcal{S}_w , making use of results from the Degas code [49] and of the edge integrated H_α emission; then it evaluates the electron flux, $\Gamma_e = n_e v_{er}$ by solving the continuity equation to obtain :

$$\Gamma_e = \frac{1}{r} \int_0^r (\mathcal{S}_b + \mathcal{S}_w - \frac{\partial n_e}{\partial t}) r' dr' \quad (2.6)$$

The temporal evolution of $n_j(R)$ and $v_{\phi j}(R)$ are measured by a variety of diagnostics reviewed in Section 2.1. SNAP computes the configuration of shifted circular flux surfaces consistent with a kinetic analysis of plasma pressure. To make contact with the experimental configuration, each flux surface ψ^* is associated with the coordinate $r^* = [R(\psi^*, 0) - R(\psi^*, \pi)]/2$. For the purpose of obtaining radial profiles of the plasma parameters:

- $\Omega_\phi \equiv v_\phi/R$ and T_i are assumed constant on a particular magnetic surface and only the data points outside the magnetic axis, $r > R_o$, are used (because the points on the inside have larger error bars);
- the $n_e(r)$ and $T_e(r)$ profiles are commonly obtained using the entire profile:
 $n_e(r') = n_e(R_l, 0) = n_e(R_r, \pi/2)$ and $r' = (R_l + R_r)/2$.

The momentum balance for the plasma enclosed by the flux surface 'r' is obtained by integrating $(Eq.(2.5) \times (2\pi)^2 Rr)$ over the interval $[0,r]$, providing the definition for the experimental conductive torque flux as a function of measured plasma parameters:

$$K_\phi^{ex}(r) = (2\pi)^2 R_0 \int_0^r \mathcal{K}_\phi(r') r' dr' \equiv T_\phi(r) - K_\phi^{cv}(r) - \dot{Y}_{\phi th}(r) \quad (2.7)$$

where:

- $T_\phi(r) = (2\pi R_0)^2 \int_0^r \mathcal{M}_\phi r' dr'$ is the total torque input in the region $[0,r]$;
- $K_\phi^{cv}(r) = (2\pi R_0)^2 m_{av} r v_\phi(r) \Gamma_e(r)$ is the convective torque flux across the flux surface 'r';
- and $Y_{\phi xx}(r) = (2\pi R_0)^2 \int_0^r m_{av} n_{exx} v_\phi r' dr'$ is the thermal ($xx = th$) or total ($xx = tot$) plasma angular momentum stored in the region $[0,r]$. Our analysis will focus only on the thermal component of the stored momentum.

Since SNAP is a steady state code and the analysis of the TFTR parameters will be limited to quasi-steady-state plasma conditions, the term $\dot{Y}_{\phi th}$, in Eq.(2.7), vanishes.

It is one objective of the theoretical investigations to identify the transport mechanism that can contribute to the torque flux and to provide analytical expressions of it, indicated as K_ϕ^{theo} , to compare with K_ϕ^{ex} .

The experimental conductive momentum confinement time, for the region $[0,r]$, is then defined as the momentum replacement rate:

$$\tau_{\phi xx}^{ex}(r) \equiv \frac{Y_{\phi xx}^{ex}(r)}{T_\phi(r) - \dot{Y}_{\phi xx}(r)} \quad (2.8)$$

With density and velocity profiles of the form:

$$x(r) = x(0)(1 - (r/a)^2)^{\alpha_x} \quad (2.9)$$

in steady state conditions, one derives:

$$\tau_{\phi xx}^{ex}(a) = \frac{m_{av} n_{exx}(0) v_\phi(0) 2(\pi a R_0)^2}{T_\phi(a) (1 + \alpha_n + \alpha_v)} \quad (2.10)$$

The appropriate definition of a corresponding theoretical momentum confinement time is then suggested by Eqs. (2.7) and (2.2), with K_ϕ^{ex} replaced by K_ϕ^{theo} :

$$\tau_{\phi xx}^{theo}(r) = \frac{Y_{\phi xx}(r)}{K_\phi^{theo}(r) + K_\phi^{cv}(r)} \quad (2.11)$$

Since it is experimentally observed that $K_\phi^{cv}(r) \ll K_\phi^{ex}(r)$, the convective torque flux is sometimes neglected in the above definition, Eq.(2.11).

In the literature, one also encounters the definition of the momentum transport time on a given flux surface, which is a measure of the rate at which momentum is transferred from that flux surface:

$$\tau_{\phi(loc)}^{ex/theo}(r) = \frac{m_{av} n_e(r) v_\phi(r) R_0}{K_\phi^{ex/theo}(r)} \quad (2.12)$$

While reviewing the rotation experiments in Chapter 4, we are going to encounter the momentum diffusivities χ_ϕ^{ex} and χ_ϕ^{eff} , evaluated from experimental data, using a balance equation of the form of Eq.(2.5). The χ_ϕ^{ex} is implicitly defined by the assumption that the viscous torque has the form:

$$K_\phi^{ex}(r) = -m_{av} \frac{R_0}{r} \frac{\partial}{\partial r} (r \chi_\phi^{ex} n_e \frac{\partial v_\phi}{\partial r}) \quad (2.13)$$

An effective diffusivity, χ_ϕ^{eff} , is defined by the following expression:

$$K_\phi^{ex}(r) + K_\phi^{cv}(r) \equiv -m_{av} \frac{R_0}{r} \frac{\partial}{\partial r} (r \chi_\phi^{eff} n_e \frac{\partial v_\phi}{\partial r}) \quad (2.14)$$

Experimental and theoretical τ_ϕ and χ_ϕ are related in the following manner:

$$\tau_\phi(r) = \frac{r^2}{\chi_\phi(r)} \left[\frac{L_v}{\tau} \frac{\int_0^r n_e(r') v_\phi(r') r' dr'}{n_e(r) v_\phi(r) \tau^2} \right] \equiv \frac{r^2}{\chi_\phi(r)} g(r) \quad (2.15)$$

where $L_x = (\frac{\partial x}{\partial r}/x)^{-1}$ is the scale length of the parameter x , and $g(r)$ is a geometric factor defined by Eq.(2.15).

While the evaluation of $\tau_\phi^{ex}(a)$ is not ambiguous, one must be careful in the formulation of the global momentum confinement time predicted by a given theory. For example, $\tau_\phi^{theo}(a)$ from Eq.(2.11), with $r=a$, can be used to express the theoretical

predictions of momentum transfer mechanisms active only at the edge, if K_ϕ^{theo} has a form similar to Eq.(2.13) that allows the integral defining K_ϕ^{theo} to be performed analytically. Clearly, this would not provide a good measure of the momentum confinement in the central region, and one must define $\tau_\phi^{theo}(a)$ in a different way. One encounters different choices in the literature. In Ref. [24], the $\tau_{\phi(loc)}^{theo}$ evaluated for average plasma parameters was assumed to represent the global momentum confinement time. In Ref. [28], it was assumed that $\tau_\phi^{theo}(a) \sim a^2/\chi_\phi$, with χ_ϕ evaluated for some average values of the plasma parameters.

Comparative studies of momentum and thermal transport are often carried out and will be discussed during the Thesis. The thermal diffusivities, χ_j^{ex} and χ_j^{eff} , are defined by the following expression for the experimental total heat flux attributed to species j [55]:

$$Q_{rj}^{ex} \equiv q_{rj}^{ex}(r) + \frac{3}{2}\Gamma_j T_j = -n_j \chi_j^{ex} \frac{\partial T_j}{\partial r} + \frac{3}{2}\Gamma_j T_j = -n_j \chi_j^{eff} \frac{\partial T_j}{\partial r} \quad (2.16)$$

The experimental total heat flux is evaluated from the solution of the following energy balance equation [56]:

$$\frac{1}{r} \frac{\partial}{\partial r} (r Q_{rj}) = W_j^{ex} \quad (2.17)$$

where W_j^{ex} represents sources and sinks of energy, in particular:

$$W_e^{ex} \equiv W_{b,e} + W_{ions,e} + W_{OH} - W_{rad} \quad (2.18)$$

$$W_{ions}^{ex} \equiv W_{b,ions} + W_{b,th} - W_{ions,e} + W_{visc} - W_{cx} \quad (2.19)$$

where the subscripts refer to: $b, e(ions)$: energy exchange from the beams to the electrons (ions), evaluated by solving the Fokker-Planck equation; $ions, e$: energy exchange between ions and electrons; OH : ohmic heating power; rad : radiated power, measured with the bolometer [57]; bth : energy carried by the thermalizing beams; $visc$: work done by the viscous forces; cx : charge exchange losses.

For a discussion on how Eq.(2.17) is derived from the $(m_j v_j^2/2)$ moment of the Boltzman equation ^[53] and therefore on the approximations contained in Eq.(2.17), we address the reader to Ref. [55].

Chapter 3

THEORIES FOR MOMENTUM TRANSPORT

3.1 Introduction

The so called ‘classical’ [58] and ‘neoclassical’ [59] theories of plasma transport refer to a description of the plasma as an ensemble of particles interacting among themselves through short-range Coulomb collisions and subject to quasistationary (with respect to their characteristic frequencies of motion) electric and magnetic field forces. The neoclassical theory departs from the classical in treating the spatial variation of B at the kinetic level. Theories that describe the plasma particles interacting mainly with fluctuating electric and magnetic fields, directly related to collective fluctuations of macroscopic parameters (n , T , v , etc.), whose driving forces and saturation mechanisms depend on the theory, are called anomalous [60].

In this Chapter, we present several theoretical expressions for the viscous forces subdivided according to the above classification. Emphasis is given to the theoretical investigation of toroidal momentum transport, which is also the major objective of this Thesis.

3.2 Theories of neoclassical momentum transport

3.2.1 The viscosity tensor

The viscosity tensor, as derived by Braginskii [58], is commonly represented as

$$\begin{aligned}\Pi_{\alpha\beta,j} &= \Pi_{\alpha\beta,j}^0 + \Pi_{\alpha\beta,j}^{1,2} + \Pi_{\alpha\beta,j}^{3,4} \\ &\equiv -(\eta_0 W_{\alpha\beta}^0)_j - (\eta_1 W_{\alpha\beta}^1 + \eta_2 W_{\alpha\beta}^2)_j + (\eta_3 W_{\alpha\beta}^3 + \eta_4 W_{\alpha\beta}^4)_j\end{aligned}\tag{3.1}$$

where the $W_{\alpha\beta,j}^m$ s are the strain tensors, and the η_{mj} s are the viscosity coefficients.

The $W_{\alpha\beta,j}^m$ s are related to variations in the flow field. For toroidal flux-surface geometry, these are given in Table 3.1 [23].

A great deal of work has been done to evaluate the η_{mj} s in the framework of the neoclassical theory.

Parallel viscosity

The classical parallel viscosity coefficient, as derived by Braginskii [58], is:

$$\eta_{0j}^{cl} = 0.96 n_j T_j / \nu_{jj} \quad (3.2)$$

where ν_{jj} is the self-collision frequency.

An expression for the neoclassical parallel viscosity coefficient, valid in any collisionality regime, was derived by Hirshman [61]:

$$\eta_{0j}^{Hir} = \frac{m_j n_j v_{thj} q R_0 \nu_j^*}{(1 + \nu_j^*)(1 + \epsilon^{1.5} \nu_j^*)} \quad (3.3)$$

where

$$\nu_j^* = \frac{\nu_j}{\epsilon_0^{1.5} \omega_{trj}} \quad \omega_{trj} \equiv \frac{v_{thj}}{qR} \quad (3.4)$$

and

$$\nu_j = \sum_k \nu_{jk} = \sum_k \sqrt{\pi} \frac{16}{3} \frac{e^4 \ln \Lambda_j n_k Z_j^2 Z_k^2}{m_j (v_{thj}^2 + v_{thk}^2)^{1.5}} \left(\frac{1}{m_j} + \frac{1}{m_k} \right) \quad (3.5)$$

q is the safety factor and v_{thj} is the thermal velocity, ν_{jk} is the collisional frequency of species j with species k . Subsequent work [62] has confirmed this expression. Note that η_{0j}^{Hir} reduces to η_{0j}^{cl} for one ion species plasma in the collisional regime.

The viscosity tensor as written in Table 3.1 is the complete viscosity tensor only when there is no heat flux, an unrealistic situation in actual fusion devices. Work has

The viscosity tensor elements, where $A_0 = 2\{-\{(\partial V_r/\partial l_r) + [(1/R)(\partial R/\partial l_r) + \{1/B_r\}(\partial B_r/\partial l_r)]V_r + f_r R\{\partial(V_r R^{-1})/\partial l_r\}\}$.			
	Parallel $\Pi_{\alpha\beta}^0 \equiv -\eta_0 W_{\alpha\beta}^0$	Perpendicular $\Pi_{\alpha\beta}^{12} \equiv -(\eta_1 W_{\alpha\beta}^1 + \eta_2 W_{\alpha\beta}^2)$	Gyroviscous $\Pi_{\alpha\beta}^{34} \equiv (\eta_3 W_{\alpha\beta}^3 + \eta_4 W_{\alpha\beta}^4)$
Π_{rr}	$\frac{1}{2}\eta_0 A_0$	$\eta_1 \left((RB_r)^{-1} \frac{\partial(RB_r V_r)}{\partial l_r} - f_r R \frac{\partial(V_r R^{-1})}{\partial l_r} \right)$	$-\eta_3 \left(h_r \frac{\partial(V_r h_r^{-1})}{\partial l_r} - f_r R \frac{\partial(V_r R^{-1})}{\partial l_r} \right)$
$\Pi_{\theta r} = \Pi_{r\theta}$	0	$-\eta_1 h_r \frac{\partial(V_r h_r^{-1})}{\partial l_r}$ $+ (\eta_2 - \eta_1) f_r R \frac{\partial(V_r R^{-1})}{\partial l_r}$	$-\eta_3 (RB_r)^{-1} \frac{\partial(RB_r V_r)}{\partial l_r}$ $-(\eta_4 - \eta_3) f_r R \frac{\partial(V_r R^{-1})}{\partial l_r}$
$\Pi_{\theta\theta} = \Pi_{\theta\theta}$	0	$-\eta_2 R \frac{\partial(V_r R^{-1})}{\partial l_r}$	$-\eta_4 R \frac{\partial(V_r R^{-1})}{\partial l_r}$
Π_{rr}	$\frac{1}{2}\eta_0 A^0$	$-\eta_1 (RB_r)^{-1} \frac{\partial(RB_r V_r)}{\partial l_r}$ $+ (\eta_1 - 2\eta_2) f_r R \frac{\partial(V_r R^{-1})}{\partial l_r}$	$\eta_3 h_r \frac{\partial(V_r h_r^{-1})}{\partial l_r}$ $+ (2\eta_4 - \eta_3) f_r R \frac{\partial(V_r R^{-1})}{\partial l_r}$
$\Pi_{r\theta} = \Pi_{\theta r}$	$-\frac{1}{2}\eta_0 f_r A^0$	$-\eta_2 R \frac{\partial(V_r R^{-1})}{\partial l_r}$	$\eta_4 R \frac{\partial(V_r R^{-1})}{\partial l_r}$
$\Pi_{\theta\theta}$	$-\eta_0 A^0$	$2\eta_2 f_r R \frac{\partial(V_r R^{-1})}{\partial l_r}$	$-2\eta_4 f_r R \frac{\partial(V_r R^{-1})}{\partial l_r}$

Table 3.1: The viscosity tensor elements [23]

been done to derive the parallel viscous stress that arises in response to a heat flux [63],[64]. For arbitrary collisionality the parallel viscous force can be written:

$$\nabla \cdot \vec{\Pi}_j^0 = \hat{b}(\hat{b} \cdot \nabla)(p_{\parallel} - p_{\perp})_j - \frac{1}{3} \nabla(p_{\parallel} - p_{\perp})_j + (p_{\parallel} - p_{\perp})_j [(\hat{b} \cdot \nabla) \hat{b} - \frac{\hat{b}}{B}(\hat{b} \cdot \nabla) B] \quad (3.6)$$

with:

$$\hat{b} \equiv \vec{b}_{\phi} + \vec{b}_{\theta} = \vec{B}/B \quad (3.7)$$

Ref.[64] gives the following expression for the anisotropic pressure term:

$$\begin{aligned} (p_{\parallel} - p_{\perp})_j &= \frac{m_j n_j}{\tau_{jj}} \frac{\langle B^2 \rangle \hat{b} \cdot \nabla B}{\langle (\hat{B} \cdot \nabla B)^2 \rangle B_{\theta}} (\zeta_{1j} v_{\theta j} - \zeta_{2j} \frac{2}{5} \frac{q_{\theta j}}{p_j}) \\ &= \frac{m_j n_j}{\tau_{jj}} \frac{2R_0}{\beta^2 h} (\zeta_{1j} v_{\theta j} - \zeta_{2j} \frac{2}{5} \frac{q_{\theta j}}{p_j}) \sin \theta \\ &\equiv (p_{\parallel} - p_{\perp})_{js} \sin \theta \end{aligned} \quad (3.8)$$

Equation (3.8) was derived assuming a plasma density constant on the flux surface.

The expressions for the viscosity coefficients, ζ_{nj} , given in Ref. [64] are:

$$\begin{aligned} \zeta_{1j} &= g[\sqrt{2} - \ln(1 + \sqrt{2})] = 0.533g \\ \zeta_{2j} &= g[4/\sqrt{2} - 5 \ln(1 + \sqrt{2})/2] = 0.625g \\ g &= \frac{1}{1 - 1.46\sqrt{\epsilon}} - 1 \end{aligned} \quad (3.9)$$

Perpendicular viscosity

$\eta_{1j}^cl = \eta_{2j}^cl/4$ and $\eta_{2j}^cl = 1.2n_j T_j \nu_{jj}/\omega_{cj}^2$ are the classical perpendicular viscosity coefficients [58], and $\omega_{cj} = e_j B/m_j$ is the gyrofrequency.

The formulation of neoclassical transport for a plasma with arbitrary rotation, without impurities, in different collisional regimes [65]–[68], and with impurities in banana regime [69], has shown that, while both particle and heat fluxes are enhanced with respect to their classical values, perpendicular viscosity remains essentially at the classical level.

Hinton and Wong [68] showed, by taking appropriate moments of the Boltzman equation, that the neoclassical part of the viscous torque flux, in a strongly rotating plasma, can be written:

$$\Pi_2 = -\frac{m}{e} < \int \frac{m}{2} R^2 v_\phi^2 C^l(\bar{f}^1) dv^3 > \quad (3.10)$$

where $\Pi_2/|\nabla\psi|$ is equivalent in our notation to $K_\phi/(2\pi R 2\pi r)$. They solved from the kinetic theory for the first-order, gyro-averaged distribution function, \bar{f}_j^1 , under the collisionality constraint $\nu_{ii}/\omega_{ti} \sim 1$. For ions in the Pfirsch-Schluter regime, they found that the neoclassical part of the viscosity is proportional to the up-down asymmetry in the magnetic field, and that the resulting momentum transport coefficient is given by the neoclassical result. In the banana regime, similarly to Refs. [65], [66], they found that the perpendicular viscosity coefficient resembles the classical result, modified by the factor q^2 , that is:

$$\eta_{2j}^{neo} = 0.1 q^2 \rho_i^2 \nu_{ii} \quad (3.11)$$

Hogan [67] found that, in the collisional regime, the neoclassical η_{2j} is enhanced by a factor of $(1 + 2.31 q^2)$ with respect to the classical expression. Ref. [66] reported a different viscosity coefficient, which scales as ν_{ii}^{-1} , which is believed [67] to be consequence of a priori ordering, which restricted the flow speed to small values.

Gyroviscosity

$\eta_3 = \eta_4/2$ and $\eta_4 = n_j T_j / \omega_{cj}$ are the classical gyroviscous coefficients [58]; $\omega_{cj} = e_j B / m_j$ is the cyclotron frequency for species j. Their magnitude is independent of the collisionality regime.

3.2.2 The theory of gyroviscosity

The lower limit to momentum transport is that described by the neoclassical theory. When Braginskii's stress tensor (see Section 3.2.1) is extended to include toroidal effects [23], the toroidal component of the viscous torque, $\langle R\hat{\phi}\nabla\cdot\vec{\Pi} \rangle$, reduces to the sum of the perpendicular viscosity contribution:

$$\langle R\hat{\phi}\nabla\cdot\vec{\Pi}_j^{1,2} \rangle = \langle \frac{1}{Rh_\theta} \frac{\partial}{\partial l_\psi} (R^3 h_\theta \eta_{2j} \frac{\partial \Omega_{\phi j}}{\partial l_\phi}) \rangle \quad (3.12)$$

and of the gyroviscosity contribution:

$$\langle R\hat{\phi}\nabla\cdot\vec{\Pi}_j^{3,4} \rangle = - \langle \frac{1}{Rh_\theta} \frac{\partial}{\partial l_\psi} (R^3 h_\theta \eta_{4j} \frac{\partial \Omega_{\phi j}}{\partial l_\theta}) \rangle \quad (3.13)$$

where h_x and l_x are the metric and length elements in a (ψ, θ, ϕ) flux surface coordinate system.

The neoclassical perpendicular viscous torque of Eq.(3.12) long has been recognized to be one-to-two orders of magnitude smaller than is necessary to account for measured momentum confinement times [2]. Stacey and Sigmar [23] noted that if the poloidal asymmetry in density or rotation velocity was order $\epsilon = r/R$, then the neoclassical gyroviscous torque of Eq.(3.13) was the correct magnitude to account for measured momentum confinement times. The experimental and theoretical evidence for $O(\epsilon)$ poloidal asymmetries was summarized in Refs. [70] and [71].

In the circular flux surface approximation, Eq.(3.13) for the gyroviscous torque becomes:

$$\langle R\hat{\phi}\nabla\cdot\vec{\Pi}_j^{3,4} \rangle \equiv \frac{1}{r} \frac{\partial}{\partial r} \langle r R \Pi_{\phi\psi j}^{3,4} \rangle = - \frac{1}{r} \frac{\partial}{\partial r} \langle \eta_{4j} R^2 \frac{\partial \Omega_{\phi j}}{\partial \theta} \rangle \quad (3.14)$$

Approximating

$$x(r, \theta) \equiv x_o(r)[1 + \tilde{x}] = x_o(r)[1 + \tilde{x}_s \sin\theta + \tilde{x}_c \cos\theta] \quad (3.15)$$

($x = n_j, v_{\phi j}$) and assuming \tilde{x} to have a weak radial dependence (i.e. setting $\partial\tilde{x}/\partial r = 0$) led [23] to the following approximation for the gyroviscous torque:

$$\langle R\hat{\phi}\nabla\cdot\vec{\Pi}_j^{3,4} \rangle \equiv - \frac{1}{r} \frac{\partial}{\partial r} \langle \eta_{4j} R^2 \frac{\partial \Omega_{\phi j}}{\partial \theta} \rangle \simeq - \frac{1}{2} \tilde{\Theta}_j \frac{r}{R} \frac{\partial}{\partial r} (\eta_{4j o} v_{\phi j o}) \quad (3.16)$$

where

$$\tilde{\Theta}_j \equiv \frac{\tilde{v}_{js}}{\epsilon} (4 + \frac{\tilde{n}_{jc}}{\epsilon}) + \frac{\tilde{n}_{js}}{\epsilon} (1 - \frac{\tilde{v}_{jc}}{\epsilon}) \quad (3.17)$$

A local momentum transport time was derived according to the definition given in Eq.(2.12) [24], treating the plasma as consisting of a single ion species with charge Z_{eff} :

$$\tau_{\phi(loc)}^{gv}(r) = \frac{2eBR^2Z_{eff}}{T_i(r)\tilde{\Theta}G} \quad (3.18)$$

with $G(r) = -r/(\eta_{4j}v_{\phi j}) \frac{\partial}{\partial r}(\eta_{4j}v_{\phi j})$. In using this expression [24] to compute a global momentum confinement time, $\tilde{\Theta}$ and G were set equal to unity and an average temperature was used. A theoretical expression for $v_{\phi}(0)$ was then obtained by equating the input central torque, $R_0M_{\phi}(0)$, to the central angular momentum loss rate, $m_i n_i v_{\phi}(0) R \tau_{\phi(loc)}^{gv}$:

$$v_{\phi}(0) = \frac{M_{\phi}(0)2eBZ_{eff}R^2}{m_i n_i(0)T_i(0)} \quad (3.19)$$

An effective gyroviscous momentum flux was later constructed by using an effective $\tilde{\Theta}$ that was independent of position:

$$\Pi_{\phi\psi_j}^{3,4}(r) \equiv \frac{K_{\phi j}^{gv}(r)}{rR^2(2\pi)^2} = -\frac{\tilde{\Theta}_j}{2rR^2} \int_0^r [r' \frac{\partial}{\partial r'}(\eta_{4j}v_{\phi j})] r' dr' \quad (3.20)$$

Subsequently, expressions for the momentum confinement time and central rotation speed which took into account radial profiles were developed [20] using the approximation of Eq.(3.16):

$$\tau_{\phi}^{gv}(a) = \frac{\sum_j \int_0^a < Rm_j n_j v_{\phi j} > r dr}{\sum_j \int_0^a < R\hat{\phi} \cdot \vec{\Pi}_j > r dr} \simeq \frac{2eBR^2\hat{Z}}{\tilde{\Theta}T_i(0)} \frac{h_{nvT}}{h_{nv}} \frac{\bar{m}_D}{m_D} \quad (3.21)$$

$$\begin{aligned} v_{\phi}^{gv}(0) &\equiv \frac{T_{\phi}(a)}{\sum_j (\int_0^a [R\hat{\phi} \cdot \nabla \cdot \vec{\Pi}_j > + \frac{\partial}{\partial t} < Rm_j n_j v_{\phi j} >] r dr) / v_{\phi j}(0)} \\ &= \frac{2eBT_{\phi}(a) h_{nvT}\hat{Z}}{V_p m_D \tilde{\Theta} n_e(0) T_i(0) (1 + f\tau_{\phi}^{gv})} \end{aligned} \quad (3.22)$$

Here, the quantities h_{xy} are radial integrals involving the profiles of the quantities 'x' and 'y', the last term in Eq.(3.21) is a mass factor that is unity in deuterium plasmas, $\tilde{\Theta}$ is an effective value for the impurity species, V_p is the plasma volume and

$$f = \frac{\dot{N}_e}{N_e} + \frac{\dot{v}_\phi}{v_\phi} \quad (3.23)$$

In order to obtain the effective gyroviscous torque for the plasma, Eq.(3.16), must be summed over ion species. Since the concentration of various ion species is usually unknown, some model is necessary to obtain an expression that can be evaluated from experimental parameters. The simplest model [24] is to assume that the plasma consists of a single effective species with charge $Z = Z_{eff}$ and $m_p n_p = \sum_j m_j n_j \simeq m_D n_e$, which leads to

$$\hat{Z} = Z_{eff} \quad (3.24)$$

in Eqs. (3.21) and (3.22). A second model [20] results from assuming that a single dominant impurity determines both Z_{eff} and the total gyroviscous torque. In this case, charge neutrality and the definition of Z_{eff} can be used together with Eq.(3.16) to obtain

$$\hat{Z} = Z(Z - 1)/(Z_{eff} - 1) \quad (3.25)$$

This last model can be extended to include a metal impurity, in which case

$$\hat{Z} = \bar{Z} \equiv Z(Z - 1)/(Z_{eff} - Z_{met} - 1) \quad (3.26)$$

Thus:

$$\hat{Z} = \begin{cases} Z_{eff} & (3.27) \end{cases}$$

$$\hat{Z} = \begin{cases} Z(Z - 1)/(Z_{eff} - 1) & (3.28) \end{cases}$$

$$\hat{Z} = \begin{cases} Z(Z - 1)/(Z_{eff} - Z_{met} - 1) & (3.29) \end{cases}$$

3.2.3 Ware's cold ions theory

Ware [25] pointed out that the magnitude of the perpendicular viscous torque of Eq.(3.12) can be enhanced by an excess of cold ions in an ion-impurity plasma. Recycling at the wall produces low energy ions with about 1 eV energy, a factor of 20-50 times less than the local T_i . The expectation for the presence of rotating cold ions in the plasma bulk relies on the different temperature dependence of the energy equilibration time, $\nu_{Ej} \propto n_h/T_h^{3/2}$, and the momentum exchange time, $\nu_{\phi j} \propto n_I Z_I^2/T_c^{3/2}$, which allows the cold ions to acquire momentum faster than internal energy (the subscripts 'c' and 'h' refer to hot' and cold' respectively.)

The starting point for the development of Ware's theory is the neoclassical expression for the radial flux of toroidal momentum for species j:

$$\Pi_{\phi\psi j} = - \int \frac{d\theta}{2\pi} \int m_j v_{\parallel} \frac{\mu B + v_{\parallel}^2}{\omega_{cj} R} \sin\theta \tilde{f}_{js} d^3v \quad (3.30)$$

where \tilde{f}_{js} is the part of the distribution function which varies as $\sin\theta$ and is odd in v_{\parallel} , given by:

$$\beta \frac{v_{\parallel}}{r} \frac{\partial \tilde{f}_{js}}{\partial \theta} = \sum_k [C_{jk}(\tilde{f}_{jc}, f_{k0}) + C_{jk}(\tilde{f}_{kc}, f_{j0})] \quad (3.31)$$

Indicating the main ion distribution function as $f_i = f_h + f_c$, where, for simplicity, f_h and f_c are assumed Maxwellians, and proceeding from the kinetic equations, Ware derived the following expression for the viscous torque:

$$K_{\phi}^{cold}(r) = -3.3 m_i n_c \nu_{ci} (\epsilon \rho_{I\theta})^2 \frac{\partial v_{\phi}}{\partial r} \mathcal{F} r (2\pi R_0)^2 \quad (3.32)$$

with:

$$\nu_{ci} = \sqrt{2\pi} \frac{4}{3} \frac{n_I e^4 Z^2 \ln \Lambda}{\sqrt{m_i} T_c^{3/2}} \quad y = \frac{m_i T_I}{m_I T_c} \quad (3.33)$$

and

$$\mathcal{F}(y) = \frac{1}{(1+y)^{3/2}} \frac{1 - Z_I (\frac{m_i}{m_I})^2 + (\frac{2}{5} + \frac{3}{5} Z_I \frac{m_i}{m_I}) y - (\frac{3}{5} + \frac{2}{5} Z_I \frac{m_i}{m_I}) \frac{m_i}{m_I} \frac{1}{y}}{1+y} \quad (3.34)$$

Eq.(3.32) can be rewritten as:

$$K_{\phi}^{cold}(r) = \mathcal{A} \frac{n_c}{n_e} y^{3/2} \mathcal{F}(y) \quad (3.35)$$

with

$$\mathcal{A} = 3.33 m_i \left(\frac{m_I}{m_i} \right)^{3/2} n_e (\nu_{cI} T_c^{3/2}) \frac{(\epsilon \rho_{I\theta})^2}{T_I^{3/2}} \left(-\frac{\partial v_{\phi}}{\partial r} \right) (2\pi R_o)^2 r \quad (3.36)$$

\mathcal{A} is a function of the plasma parameters that are known from the experimental measurements.

In the TFTR plasma, the main light impurity is carbon ($Z_{eff} = 2 - 4$) and the metal impurities are Ni, Fe, Cr, with a $Z_{met} = 0.2 - 0.8$. Assuming carbon ($Z_C = 6$, $m_C = 12 m_p$) or iron ($Z_{Fe} = 24$, $m_{Fe} = 55.8 m_p$) as the main impurity, Eq.(3.35) becomes:

$$K_{\phi}^{cold}(r) \simeq \mathcal{A} \frac{n_c}{n_e} \frac{1}{(1 + \frac{m_I T_c}{m_i T_I})^{3/2}} \equiv \mathcal{A} \gamma_c \quad (3.37)$$

The associated momentum confinement time for the plasma in the volume out to radius 'r' is:

$$\tau_{\phi}^{cold}(r) = \frac{L_{\phi}(r)}{K_{\phi}^{cold}(r) + T_{\phi}^{cv}(r)} \quad (3.38)$$

According to Ware, the presence of low energy ions leads also to a simple explanation of various particle transport features observed in several tokamaks [72]: pulsed gas puffing leading to rapid increase of central density but no increase in ion energy content, improved energy containment when recycling is reduced, no neoclassical peaking of n_I with normal conditions, large decrease in n_I with pulsed gas puffing, increase of n_I in center with pellet injection, and others.

3.2.4 Neoclassical additions to Braginskii's tensor

In a recent work [26], Hsu and Sigmar rederived the viscosity tensor for an impure, strongly rotating, collisional plasma and found additional terms to the Braginskii's result, due to large rotation. Since their derivations have been carried out for a

collisional regime that does not represent the TFTR plasma, their results are not a priori applicable for a comparison with the experimental data.

Hsu and Sigmar adopted the Larmor radius expansion of the kinetic equation in conjunction with a moment approach, the outline of which is given in Ref. [73]. Their transport problem is described by the set of moment equations 1, $m_j \bar{v}$, $m_j(\bar{v}\bar{v} - v^2/3 \bar{I})$, for each order in $\delta_{\theta j} \equiv \rho_{\theta i}/L$ (where $\rho_{\theta i}$ is the ion Larmor radius and L the radial length scale). The results were discussed for the cases $\Delta \equiv (\sqrt{2}\delta_{\theta j} Z^2 \nu_{jj}/\omega_{trj}) \sim O(\delta_{\theta j})$ and $\sim O(1)$, where $\omega_{trj} = v_{thj}/(qR)$ is the transient frequency,

The momentum flux, as derived by them, is the sum of the classical perpendicular flux and of a neoclassical term. This last term, namely

$$\Pi_{\phi\psi j} = -\frac{B}{\beta\omega_{cj}R}[\Omega_{\phi j} < \frac{R^2}{B}R_{||j} > + < \frac{3B_\phi^2 R^2 - B^2 R^2}{4B^2}\Pi_{c||j} >] \quad (3.39)$$

where

$$\Pi_{c||j} = \hat{b} \cdot \vec{\Pi}_{cj} \hat{b} \quad \vec{\Pi}_{cj} \equiv \int d\bar{v} m_j (\bar{v}\bar{v} - v^2 \bar{I}/3) C_j(f_j) \quad (3.40)$$

is a factor of $\beta^{-2} = (B/B_\theta)^2$ larger than the classical flux. It generates the following torque flow, explicitly driven by the up-down density modulation,

$$K_\phi^{H\&S}(r) = (2\pi R_0)^2 v_{\phi 0} \frac{n_{I0} T_i}{\omega_{ci}} \epsilon \tilde{n}_{Is} \mathcal{B} \quad (3.41)$$

with \mathcal{B} a function of plasma parameters and of order $\sim v_{\theta j} \sqrt{Z_I} (v_{thi}/v_{\phi i})^2 / [\beta(1 + T_i/T_e)]$ when $m_I \simeq Z_I m_i$.

The corresponding local momentum replacement time, as defined by Hsu and Sigmar, is

$$\tau_{\phi(loc)}^{H\&S}(r) \equiv \frac{m_j n_j v_{\phi j} R}{\frac{1}{r} \frac{\partial}{\partial r} (\tau R \Pi_{\phi\psi j})} \simeq (n_i q R) / (2\epsilon \delta_{\theta i} v_{thi} l_\phi n_{Is} \mathcal{B}) \sim \frac{e B_\phi R^2 \bar{Z}}{2 T_i \mathcal{B} \tilde{n}_{Is} / \epsilon} \quad (3.42)$$

where $l_\phi = \tau R / (2K_\phi) \frac{\partial}{\partial r} (K_\phi / R) \sim 1/2$.

We note that $K_\phi^{H\&S}$ and $\tau_{\phi}^{H\&S}$ are of the same parameter dependence as for the gyroviscous theory. However, the physical origin is of collisional nature.

3.2.5 Rotational viscosity

Stacey and Neeley ^[27] recently solved the neoclassical momentum transport problem for collisional ($\nu_* \gg 1$) ions in a strongly rotating ($v_\phi \sim v_{th}$) tokamak plasma. They expanded the first-order distribution function $f_1 = \bar{f}_1 + \tilde{f}_1$ into a gyroangle-averaged (\bar{f}_1) and a gyroangle-dependent (\tilde{f}_1) component and solved the resulting kinetic equations. Then they evaluated the lowest order momentum fluxes:

$$\vec{\Pi}_j(f_1^j) \equiv m_j \int (\bar{v}\bar{v} - \frac{1}{3}v^2\vec{I})f_1^j d^3v \equiv \vec{\Pi}(\bar{f}_1^j) + \vec{\Pi}(\tilde{f}_1^j) \quad (3.43)$$

They recovered the previous gyroviscous results of Section 3.2.1 from \bar{f}_1 and obtained a new “rotational” viscosity of collisional origin from \tilde{f}_1 . The “rotational” viscous torque was found to have the form:

$$\langle R\hat{\phi} \nabla \cdot \vec{\Pi}_j^{rot} \rangle \simeq -\frac{1}{2}\bar{\Theta}_j^{rot} \frac{r}{R} \frac{\partial}{\partial r} (\eta_{4jo} v_{\phi jo}) \quad (3.44)$$

where $\bar{\Theta}_j^{rot}$ is a complicated function of poloidal asymmetries in density, velocity and flux surface geometry which is order unity when these asymmetries are order ϵ . Thus, it follows that the form of the gyroviscous results, Eqs. (3.20) - (3.22), also obtain for the “rotational” viscosity, even though the former is of a non-collisional origin and the latter is of a collisional origin.

3.3 Theories of anomalous momentum transport

3.3.1 Anomalous viscosity due to stochastic magnetic perturbations

Morozov and Pogutze [30],[28] proposed an anomalous viscosity mechanism based on small-scale turbulence. They derived a self-consistent set of equations (continuity, generalized vortex, generalized Ohm's law and heat transport equations) for the description of nonlinear low-frequency electromagnetic oscillations in plasmas and the associated transport processes. These equations were obtained for a non-collisional, cylindrical plasma; included nonuniformity of current, pressure and rotation; and were used to evaluate the different fluxes across surfaces moving with the plasma to determine the transport coefficients. The viscosity coefficient was found to be related to the electron thermal diffusivity as (for $\frac{m_e}{m_i \beta_e} < 1$):

$$\chi_\phi^{smp} \simeq \chi_e^{smp} \frac{m_i \beta_e}{m_e} = C_1 \frac{c^2 v_e}{\omega_{pe}^2 q R} \epsilon^\gamma \frac{m_i \beta_e}{m_e} \propto \frac{A_i \epsilon^\gamma T_e^{1.5}}{q R_o B^2} \quad (3.45)$$

where C_1 is a constant of $O(1)$, $\gamma = 1 - 2$, $\epsilon = r/R_o$, $\beta_e = \frac{n_e T_e}{B^2/(2\mu_o)}$, $A_i = m_i/m_p$, and $m_{i,p,e}$ are the ion, proton and electron masses. We can construct the torque flow from Eq.(2.13) to compare with the experiments:

$$K_\phi^{smp}(r) = (2\pi R)^2 r m_D n_e(r) \chi_\phi^{smp} \frac{\partial}{\partial r} v_\phi(r) \quad (3.46)$$

It is worth noting that Kadomtsev and Pogutse [29] addressed the problem of calculating the anomalous electron transport from stochastic magnetic perturbations and derived an expression for χ_e^{smp} . The parametric dependence of χ_ϕ^{smp} is common to other theories, such as the collisional trapped electron modes and microtearing modes, and it is also close to the one inferred from the Merezhkin scaling law, and to the empirical formula proposed by Ohkawa, as reviewed in Ref. [60].

Morozov et al. [31] have recently pointed out that, in spite of the relatively good description of τ_E and τ_ϕ that, they found, was provided by their theory, the oscillation spectra seen experimentally have a maximum at $k_\perp \rho_i \sim 1$. and, according to the theory, should not contribute to the transport.

3.3.2 Anomalous viscosity due to ITG modes

The ion-temperature-gradient (ITG) driven modes are electrostatic drift waves driven unstable by an ion-pressure gradient. Their presence requires a threshold condition $\eta_i \equiv \frac{dn(T_i)}{dn(n_i)} > \eta_i^{cr} \sim 1 - 2$, and implies $\chi_i = \chi_\phi$ increasing with η_i .

The evaluation of the momentum flux due to electrostatic drift waves, that is: [34]

$$m_j n_j \chi_{\phi j} \frac{\partial v_\phi}{\partial r} = -m_j n_j \langle \tilde{v}_{rj} \tilde{v}_\phi \rangle = m_j n_j \sum_{k'} \langle k_y' \tilde{\Phi}_{k'} \tilde{v}_{||-k'} \rangle \quad (3.47)$$

(k' is the wavelenght number, $\langle \rangle$ indicates time average, \tilde{x} is the fluctuating component of x) requires the determination of the oscillation spectra and saturation levels of the fluctuations. There exist different approaches for modelling plasma systems to evaluate the plasma parameter fluctuations, and for this reason the ITG modes theory is still in evolution.

The extension to a subsonic rotating plasma [34] of the earlier nonlinear theory [35], developed for sheared slab geometry and focused on the lowest radial eigenstate of the system, leads to the the following expression for the turbulent momentum diffusivity:

$$\chi_\phi^{\eta_{iss}} = \chi_i^{\eta_{iss}} = 1.3 \frac{\rho_s^2 c_s}{L_s} \left[\frac{1 + \eta_i}{r} + \left(\frac{L_n}{2c_s} \frac{dv_\phi}{dr} \right)^2 \right] \quad (3.48)$$

The meanings of the new symbols are: $\tau = T_e/T_i$, $L_s = \frac{q^2}{\epsilon} \frac{dq}{dr}^{-1}$, $L_n = n_e \frac{dn_e}{dr}^{-1}$, $c_s = \sqrt{\frac{T_e}{m_i}}$ and $\rho_s = c_s \frac{eB}{m_i}$.

A slightly different expression for χ_i , less dependent on η_i , has also been derived for toroidal geometry [36]:

$$\chi_i^{\eta_{tor}} \simeq \omega_{*e} \rho_s^2 \frac{L_s(1 + \eta_i)}{R\tau} \propto \frac{(1 + \eta_i)}{L_n/L_s} \sqrt{A_i} \frac{\sqrt{T_e T_i}}{RB^2} \quad (3.49)$$

The role of higher radial eigenstates in sonic ITG driven turbulence was explored in Ref. [36], and it was concluded that χ_i is enhanced beyond estimates based on the lowest eigenstate alone.

The above formulas for the ion momentum and thermal diffusivities were derived assuming: one-fluid description of the ions; fully developed turbulence, that is $\eta_i \gg$

η_i^{cr} ; and $L_n, \eta_i \ll \infty$, which excludes the flat density profiles characteristic of H mode shots. The first assumption makes a simulation of the TFTR results questionable since the fast ion population is a large fraction of the total one. It is not clear, either, if L_n or rather L_{nth} , the density scale length of the thermal ions, should be used in the formula. In any case, the magnitude of $\chi_\phi^{\eta_i^{ss}}$ exceeds the experimental values of the diffusivity by 1 – 2 orders of magnitude and the proper scale length choice is not the issue.

The argument that a large diffusion coefficient should flatten the temperature and velocity profiles, and hence reduce transport, has motivated recent works by Romanelli [38] and Hahm [39] focused on the derivation of an expression for η_i^{cr} as a function of the plasma parameters. Romanelli's expression for η_i^{cr} is [38]:

$$\eta_i^{Rom} = (1. + 1./\tau)2L_n/R_o \quad (3.50)$$

and Hahm and Tang derived [39]:

$$\eta_i^{H\&T} = 2\frac{\tau - b_s}{\tau + b_s} + 1.88\frac{L_{ni}}{L_s}(1 + \frac{1}{\tau}), \quad b_s = k_\theta^2 \rho_s^2 \quad (3.51)$$

(k_θ being the poloidal wavelength)

Near threshold, the use of Horton's expression for χ_i , based on toroidal quasilinear theory,

$$\chi_i^{\eta_i^H} = \sqrt{\eta_i - \eta_i^{cr}} \frac{\rho_s^2 c_s L_s}{L_n R_o} \propto \sqrt{\eta_i - \eta_i^{cr}} \frac{L_s}{L_n} \sqrt{A_i} \frac{T_e^{1.5}}{R_o B^2} \quad \eta_i \geq \eta_i^{cr} \quad (3.52)$$

was recommended in Ref. [74]. The torque flow, in the form given by Eq.(3.46), will be computed using $\chi_\phi^{\eta_i} \sim \chi_i^{\eta_i^H}$ and Romanelli's expression for η_i^{cr} for the purpose of the comparison with TFTR Exp. 44 data discussed in Chapter 6.

In a recent article, Mattor and Diamond [40] derived an expression for $\chi_i^{\eta_i}$ valid in the range $0.95 \leq \eta_i \leq 0.95 + (1 + 1/\tau)L_n/L_s \equiv \eta_i^{M\&D}$:

$$\chi_i^{M\&D} = N_{th} \frac{(1 + 1/\tau)^2}{2\sqrt{\pi}} \left(\frac{L_T}{L_s}\right)^2 \frac{\rho_i^2 v_{thi}}{L_s} \quad (3.53)$$

(with N_{th} a threshold function dependent on η_i).

3.3.3 Anomalous viscosity due to trapped and untrapped particle modes

Osipenko et al. [32] have studied ion transport due to interaction of ions with the electrostatic part of the drift oscillations in collisionless, rotating tokamak plasmas, using a Hamiltonian formalism. The total momentum flux is defined by:

$$m_i n_j v_{ri}^{up} v_{||} - m_i n_i \chi_{\phi i}^{up} \frac{\partial v_{||}}{\partial r} \quad (3.54)$$

$$= - \sum_{\vec{l}, \omega} \int d\vec{J} d\vec{\theta} \frac{D_o}{2m_i^2 (2\pi)^2 r R} \vec{l} \cdot \frac{\partial f_{i0}}{\partial \vec{J}} \vec{l} \cdot \frac{\partial B_i r^2}{\partial \vec{J}} \delta(B_i r^2 - [\int B_i r^2 f_i d^3 v])$$

where \vec{J} and $\vec{\theta}$ are the action-angle variables, \vec{l} is the vector of integers corresponding to the Fourier harmonics in the angular space θ , and D_o is a diffusion coefficient describing the evolution of the lower order distribution function f_{i0} . The spectrum used is a model spectrum which agrees with experimental observation: a gaussian spectrum with $\delta\omega \sim \sqrt{2T_e/m_i}/L_n$.

They found that the contribution of trapped ions to diffusion and heat conduction is $\sqrt{\epsilon}$ times lower than that of passing particles, although the main contribution to electron transport comes from the trapped electrons. The viscosity coefficient due to untrapped particles (up), as derived by them, is

$$\chi_{\phi}^{up} = .083 \frac{\rho_s}{L_n} \frac{T_e}{eB} \frac{T_e}{T_i} \propto \sqrt{A_i} \frac{T_e^{2.5}}{T_i} \frac{1}{L_n B^2} \quad (3.55)$$

and the corresponding trapped particle coefficient is ρ_s/a times lower. The corresponding torque flow is of the form given by Eq.(3.46).

Chapter 4

PREVIOUS ROTATION EXPERIMENTS AND COMPARISON WITH THEORIES

4.1 Introduction

Measurements of toroidal rotation in Ohmically Heated (OH) or NBI plasmas, with and without pellet injection and Radio Frequency (RF) heating, have been routinely performed in the last decade on most of the existing tokamaks. While a very extensive collection of rotation data is available, a relatively limited number of theories, in comparison with the variety of thermal transport theories, have been formulated in the attempt of explaining the experimental observations, and only a rather modest effort of comparison between theory and the data has been made.

In this Chapter, we present a review of the major toroidal rotation experiments performed in tokamaks and of the transport analysis and attempted theoretical interpretation of the measurements, when available. The few measurements of poloidal rotation rotation velocity available and related theoretical analysis, are discussed in another Chapter (Section 7.6).

4.2 Rotation data and their analysis

A review of rotation experiments carried out on several tokamaks and of the related analysis, when available, is presented in this Section. Table 4.1 summarizes the range of plasma parameters covered by the reviewed experiments.

machine	Ref.	a (cm)	R (cm)	B (T)	I_p (MA)	E_h (keV)	P_h (MW)	$n_e \cdot 10^{19}$ (m ⁻³)	T_e/N_e 10 ⁻¹⁹ (Nm)	$T_e(0)$ (keV)	$T_i(0)$ (keV)	$v_{th}(0) \cdot 10^{-6}$ (m/s)	τ_E (ms)	τ_p (ms)	Z_{eff}	$\chi_e(0, a)$ (m ² /s)	NOTE
PLT	[1]	40	130	2.5	0.3-0.45	40	≤ 1.0	1.5-4	~ 0.25	1-2	1.3-3	0.2-2	~ 100	10-30	2.5	1-5	$H^+, D^+ \rightarrow H^+, D^+$
PDX	[2]	43	143	0.8-2.2	0.2-0.5	50	3.5-5	2-5	~ 0.1	~ 1	~ 1.8	0.5-2		100-180	2-4	1, 7	
ISX-B	[3]	25	93	1.4	0.16	32	0.2-2	4-5	0.7	~ 1	0.4-1.3	0.6-1.2		10-15	2.5	3.2, 2.4	
DIH	[4]	40	143	1.5-2.5	0.3-0.9	70	2.5-6	4-8	~ 0.15	2.5-3.7	2-3.5	0.5-2.5	25-40 40-60	15-30 40-60	~ 2	2-4	limiter divertor
ASDEX	[9] [70]	40	154	1.7-2.4	0.32-0.42	40	0.3-2.2	2.5-9		0.75-1.45	1-2	0.5-3 2	25-150 150	50-100 150		0.2, 0.8	$H^+, D^+ \rightarrow H^+, D^+$ H^+
TFTR	[11] [12] [14]	82 58-84 71, 80 79	258 245-29 ~ 240 245	4.7 2.8-5.1 2.6-5 2.9, 3.8, 4.8	2.2 0.45-2.2 0.6-1.4 1.1, 1.8	80 100 65-80	1.5-5.6 ≤ 6.3 ≤ 18 4.4-15	4.6 0.8-9 1-5 1-2.8			2.5-4.8 2-12 5-30 4-6.5	0.5-1.6 0.5-6 5-6 ≤ 23	20-30 100 100 80-170	~ 100 2-10 3-15	2-3 (?) 2-6		$D^+ \rightarrow D^+$ center jaws inner bumper Hot ion mode
JET	[20]	110	300	2.2-3.5	~ 3	65-80	4-15	2.5-8.2	~ 0.05		9-13 2-8	0.6-3.6 0.6-2.7	300-600 400-1000	100-200 200-500	3-4 2-3		L mode H mode
PBX-M	[22]	30	165	1.1-1.3	0.3-0.55 0.33 0.33	40-45 2.7 2.2	3.8-6.5 2.7 2.2	 3.6 (0) 4.3 (0)		1.5-2.5 1.8 1.4	1.5-5.5 3.2 1.7	1-3.9 1.9 0.7	50 50 50	~ 50 45 50	1.5-2 1.7 1.5-2.1		ind. = 17-21 % NBI \perp NBI
ALCATOR	[65]	10	54	≤ 10	0.1-0.3	/	/	~ 10		~ 0.1	≤ 0.1		5-20		~ 1.5		OH

Table 4.1: Summary of rotation experiments plasma parameters

4.2.1 PLT

The earliest measurements of toroidal rotation were made on the Princeton Large Torus (PLT). Two-data-points reconstruction of the toroidal plasma rotation profile in PLT [1] was made possible by the measurements of the Doppler shift of the 2665 Å emission line of FeXX, radiating at the plasma center, and of the 2271 Å line of CV, present near the plasma edge, for a variety of plasma and NBI conditions.

In absence of NBI, a central velocity of $1.5 \cdot 10^4$ m/s in the counter direction, that is in the direction opposite to the plasma current, was observed.

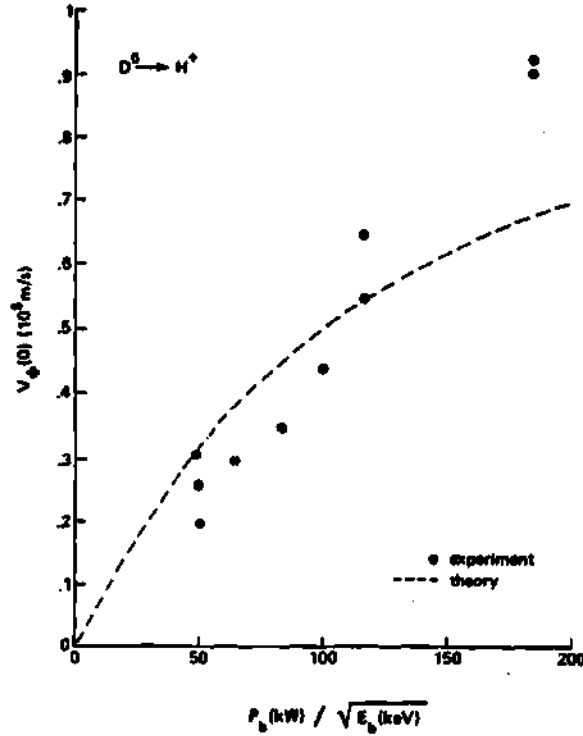


Figure 4.1: Scaling of $v_{\phi}^{ex}(0)$ with P_b in PLT and comparison with $v_{\phi}^{gv}(0)$, Eq.(3.19) [24].

During NBI, the steady state central rotation velocity scaled linearly with P_b (beam power), as shown in Fig. 4.1, and decreased with \bar{n}_e (line average density), but less rapidly than $1/\bar{n}_e$, suggesting an increase of τ_{ϕ} with density. When normalized

to injected power, the magnitude of the net induced rotation velocities for a co- and counter- discharges were identical. When co- and counter-beams were injected simultaneously, the induced rotation speed appeared to be equal to the difference in rotation speeds that would have been induced by the beams separately.

Velocities attained for $D^0 \rightarrow H^+$ were higher than those for $H^0 \rightarrow D^+$, at equal P_b and \bar{n}_e , but only by about 20 %, rather less than expected from the plasma mass ratio, implying a larger τ_ϕ for the D plasma.

The change of peak-to-peak field ripple on axis from 0.5% to 2.5 % did not produce a discernible influence on rotation, indicating that ripple-viscosity [75] was not a dominant momentum transport mechanism.

Modeling of $v_\phi(0)$ with Eq.(2.13) gave momentum diffusivities dependent on n_e . In a higher density case ($\bar{n}_e = 2.8 \cdot 10^{19} m^{-3}$) the spatial and time evolution of v_ϕ^{ex} was well described by $\chi_\phi(r) = 4.5 \cdot 10^{21}/n_e(r) m^{-1}s^{-1}$. In the lower density case, ($\bar{n}_e = 1.8 \cdot 10^{19} m^{-3}$) it was necessary to use a χ_ϕ decreasing from $6 m^2/s$ at the center to $3 m^2/s$ at the edge.

An earlier version of the gyroviscous formula for $v_\phi(0)$, Eq.(3.19), predicted the magnitude and several features of the experimental results quite well [24]: magnitude of $v_\phi(0)$ independent of direction of injection, decrease of $v_\phi(0)$ with increasing n_e and higher values of $v_\phi(0)$ for $D^0 \rightarrow H^+$ than for $H^0 \rightarrow D^+$, due to differences in $T_i(0)$. A comparison of experimental and theoretical (Eq.(3.19)) values of $v_\phi(0)$ shows good agreement except at higher P_b , where the theoretical results begins to show a saturation of $v_\phi(0)$ versus P_b , that is not observed in the experimental data (see Fig. 4.1).

4.2.2 PDX

Toroidal and poloidal rotation were measured in the Princeton Divertor Experiment, PDX, in OH and NBI discharges, in both circular and diverted configurations, [3] with three diagnostics: 1) the Fast Rotating Mirror measuring the Doppler shift of intrinsic or laser ablated impurity lines in the range 2000-6000 Å ; 2) Bragg x-ray crystal spectrometer measuring the Doppler shift of the 2.61 Å K_α resonant line of TiXXI, concentrated at the plasma center, and of the 3834 Å of TiXVII, at $r \sim 25$ cm; 3) a poloidal array of Mirnov coils which detect rotating MHD structures in the plasma.

The poloidal velocity measurements are reviewed in Section 7.6.

During the OH phase the central toroidal rotation was found to be $\sim 10^3 - 10^4$ m/s and in the direction opposite to the current.

For the range of parameters listed in Table 4.1, $v_\phi(0)$ appeared to scale linearly with P_b/\bar{n}_e , independently of I_p (plasma current), and to saturate at higher P_b , when plotted as a function of P_b only (since \bar{n}_e increases with P_b). The momentum confinement time during NBI was not studied, but the previous observations about $v_\phi(0)$ would suggest a τ_ϕ^{ex} independent of T_ϕ/\bar{n}_e .

It was also concluded that the momentum confinement was better for D than for H discharges, and better for diverted than for limiter discharges.

The 1/e decay time of $v_\phi(0)$ and $v_\phi(r = 25 \text{ cm})$, after termination of NBI, was found to be ~ 90 ms and ~ 170 ms, respectively, independent of \bar{n}_e and I_p .

The velocity profile was constructed using measurements by all three diagnostics for a few shots and the momentum diffusivity was calculated by simulating momentum transport with Eqs. (2.5) and (2.13). χ_ϕ^{ex} was found to increase with plasma radius from $\sim 1 \text{ m}^2/\text{s}$, at the center, to $\sim 7 \text{ m}^2/\text{s}$ at the edge.

This value of the momentum diffusivity, inferred for a discharge with main ions in the plateau regime, was compared with an expression for the perpendicular neoclassi-

cal viscosity constructed by assuming that χ_ϕ scales in the same way as the heat conduction in the transition from the fluid to the collisionless regime: $\chi_\phi(r) \propto \rho_i^2 q^2 \nu_i \epsilon^{-3/2}$. (This is not correct; see Chapter 3). The discrepancy between χ_ϕ^{neo} and χ_ϕ^{ex} varied from 100 (center) to 10-50 (edge), implying that the neoclassical perpendicular viscosity theory was inadequate in explaining the observations.

The damping time due to magnetic field ripple was calculated to be several seconds and could not influence the observed rotation decay.

The $v_\phi^{ex}(0)$ and τ_ϕ^{ex} data were compared with the prediction of the gyroviscous theory, in the form given by Eqs. (3.18) and (3.19) and found to be in good agreement [24].

4.2.3 ISX-B

Plasma rotation in the Impurity Study Experiment version B, ISX-B, was studied by Isler et al. [4]. One of the purposes of the rotation study was to determine the dependence of τ_E on v_ϕ , since it was found that $\tau_E \propto P_b^{-2/3}$. The neoclassical theory predicts a dependence of χ_i on v_ϕ , but thermal analyses indicated that the controlling factor in establishing the discussed dependence was the electron channel. Moreover, momentum confinement 'per se' was an incentive for the experiment since the standard neoclassical perpendicular viscosity could not explain the low v_ϕ^{ex} data, while the ion thermal conductivity and the particle fluxes, at least qualitatively, exhibited neoclassical behaviour.

A new beamline was installed to allow discharges with different values of $(P_{co} - P_{ctr})/(P_{co} + P_{ctr})$ and a spectrometer system measuring Doppler shift from recycling impurities was employed.

In the co-injection discharges, $v_\phi(0)$ did not increase proportionally to P_b (at fixed \bar{n}_e , I_p and B_ϕ), but saturated at low P_b , making it unlikely for the toroidal rotation to be the driving mechanism for the $\tau_E - P_b$ dependence; $v_\phi(0)$ was also found to be

independent of \bar{n}_e and I_p . This is shown in Fig. 4.2.

τ_ϕ was evaluated for one shot during and after NBI and found to be considerably larger during the decay after NBI termination than during the flattop, an effect which is consistent with the acceleration effect of a negative \dot{Y}_ϕ during the decay - see Eq.(2.11). A momentum diffusivity decreasing with minor radius ($3.2\text{-}2.4\text{ m}^2/\text{s}$) was obtained when Eq.(2.13) was used to model the velocity profiles during NBI reconstructed from analysis of emission lines of C and O ions located at different radii.

Counter-injection shots in ISX-B always disrupted after 30-80 ms of injection because of impurity accumulation, and a detailed study of $v_\phi(0)$ and τ_ϕ was not possible; but it appeared that, before the disruption, $v_\phi(0)$ did not differ significantly in magnitude from the central velocity in co-injection discharges with similar P_b .

Partially balancing co-injection with counter-injection was found to reduce v_ϕ more than expected on the basis of the net co-injected power, indicating that τ_ϕ depends on the total injected power.

An earlier version of the gyroviscous expressions for τ_ϕ and $v_\phi(0)$ (Eqs (3.18) and (3.19)) could reproduce the magnitude and the observed parametric dependence of the experimental data taken during NBI [24]. The saturation of $v_\phi(0)$ with P_b was seen to be accounted for quite well by the corresponding increase in $T_i(0)$ (see Fig. 4.3), and $v_\phi(0)$ was predicted to be only weakly dependent on n_e and I_p . The temperature dependence of Eq.(3.19) also accounted for the partially balanced injection results cited in the previous paragraph.

4.2.4 DIII

Plasma rotation was measured in Doublet III, DIII, for a variety of I_p , P_b , \bar{n}_e , limiter and divertor discharges [5]-[7] with a six-chord CERS system, measuring the Doppler

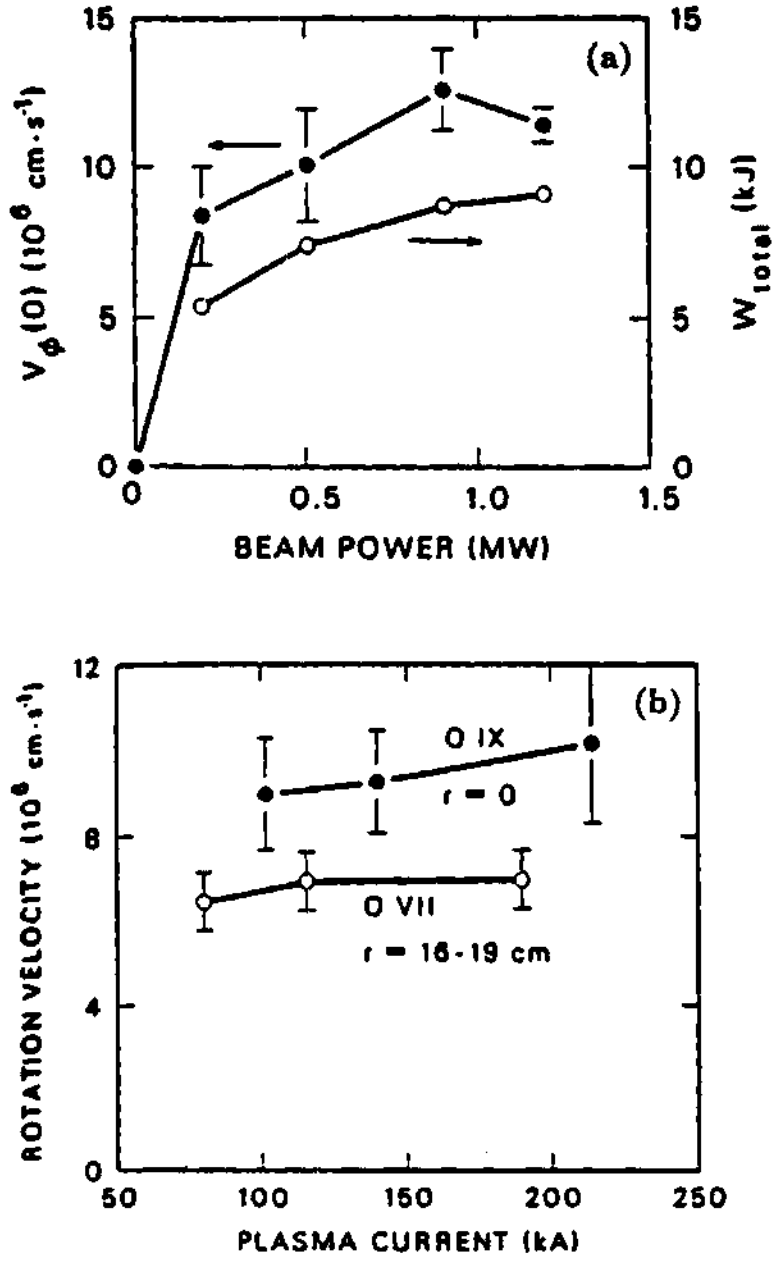


Figure 4.2: (a) Scaling of $v_\phi^{cz}(0)$ and stored energy with P_b in ISX-B. (b) Scaling of $v_\phi(0)$ and $v_\phi(\sim 16 \text{ cm})$ with I_p on ISX-B [4].

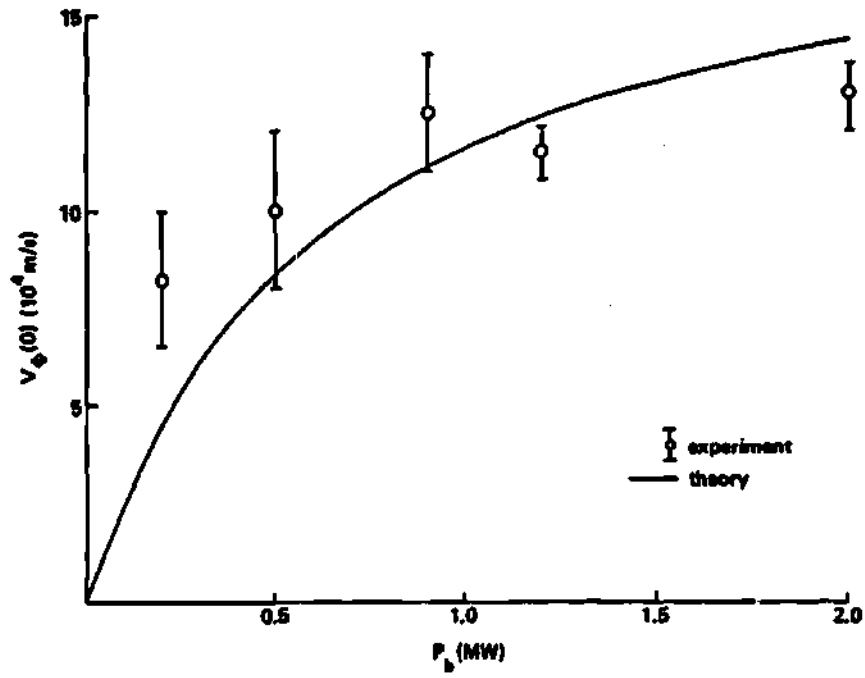


Figure 4.3: Comparison of $v_\phi^{ex}(0)$ from ISX-B with $v_\phi^{gv}(0)$, Eq.(3.19) [24].

shift of the HeII 468.568 nm line, and a single-chord spectrometer measuring the 297.57 nm line from OVIII [5],[6]. It was verified that the toroidal rotation frequency is constant over the flux surface and that all the ions (O and He) share the same toroidal velocity, within the experimental error of the measurements (from the published figures one would infer error bars smaller than 10 %).

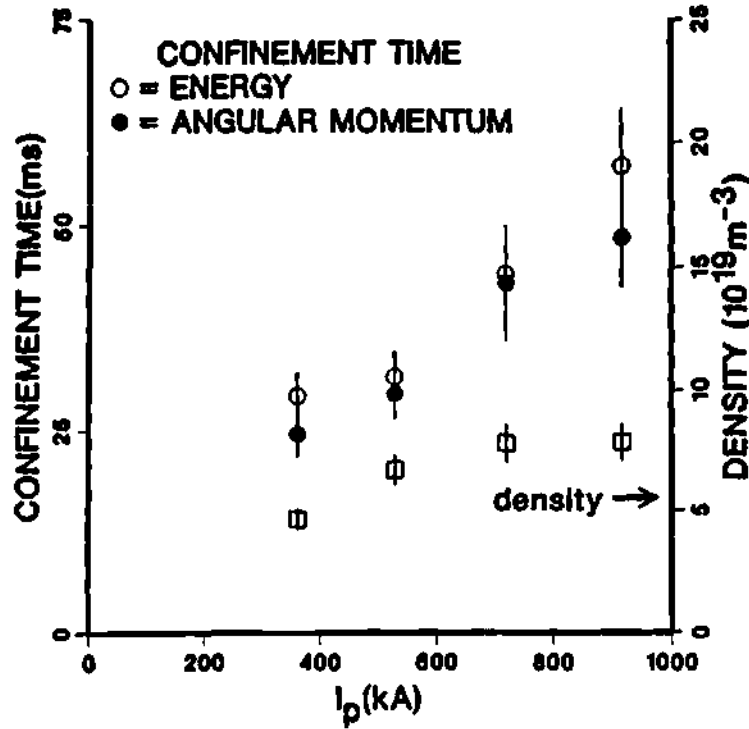


Figure 4.4: Energy and angular momentum confinement times versus plasma current for a set of divertor discharges in DIII [5]

In divertor discharges, $v_\phi(0)$ was found to increase approximately linearly with the torque (at fixed \bar{n}_e , I_p and B), independently of beam species, and the profile was found to be more peaked at higher injected torque. In limiter discharges ($D^0 \rightarrow D^+$ only), $v_\phi(0)$ showed saturation with increasing torque, but \bar{n}_e was not kept constant.

The momentum confinement time was shown to decrease with P_b in both limiter and divertor shots, to be equal to τ_E in the divertor discharges and 30 % less than τ_E in the limiter discharges. The decrease was stronger in the limiter cases and was

attributed to the peaking of $v_\phi(r)$ with P_b in diverted plasmas. At equal P_b , τ_ϕ was considerably lower in the limiter configuration ($\tau_\phi^{lim} \sim 2/5 \tau_\phi^{div}$). At fixed P_b and \bar{n}_e , τ_ϕ (and τ_E) increased linearly with I_p (see Fig. 4.4). Since $v_\phi(0)$ had a weak dependence on I_p , the linear increase of τ_ϕ with plasma current was due to the broadening of the n_e and v_ϕ profile with increasing I_p , that were used in constructing the experimental τ_ϕ .

Divertor discharges that never exhibit sawtooth oscillations in the soft x-ray signal had poorer momentum and energy confinement times. This is probably due to the growth of a magnetic island that almost prevented plasma rotation [5].

An earlier version of the gyroviscous theory without profile effects, Eq.(3.18), predicted τ_ϕ of the same magnitude as the measured τ_ϕ , as shown in Fig. 4.5. However apparent disagreement between plasma parameter dependences predicted by the gyroviscous theory and observed in the experiment were reported for DIII [5]. The dependence of the experimental τ_ϕ on current was due to a broadening of the profile, while the earlier theory does not include profile effects. We evaluated the approximate magnitude of these profile effects, using the published data, and found that, still, the omission of profile effects in the theory could not completely explain the difference between experiments and theory observed in the scaling of τ_ϕ with I_p .

4.2.5 ASDEX

Rotation in the Axisymmetric Divertor Experiment, ASDEX, plasma, under different NBI conditions, was determined with a five-chord CERS from the Doppler shift of the 343.4 nm line of CV and the 297 nm line of OVII. A number of features in the momentum confinement properties were reported in Refs. [8], [9], while a more complete analysis of the same L-mode discharges can be found in Ref. [10].

The observed toroidal velocities for co-NBI are well described by an offset-linear

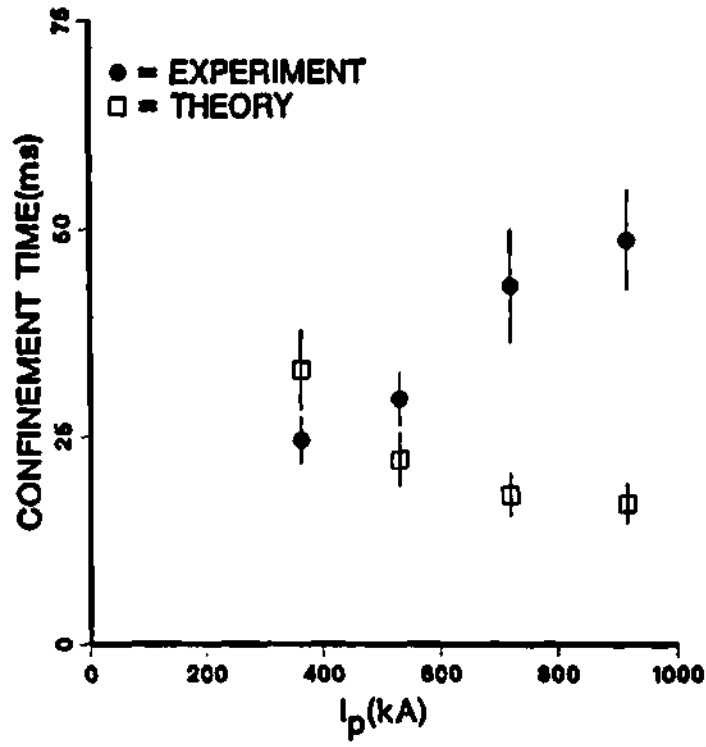


Figure 4.5: Comparison of τ_{ϕ}^{ex} (EXPERIMENT) and $\tau_{\phi(loc)}^{gv}$ (THEORY) from Eq.(3.18) in DIII [5]

scaling of $v_\phi(0)$ with P_b/\bar{n}_e , without any clear dependence on current and magnetic field. The extrapolation of the data points for $P_b \rightarrow 0$ and the measurements of velocity decay after beam turn off indicate that τ_ϕ decreased with increasing P_b .

The values of $v_\phi(0)$ in a counter-NBI discharge reached nearly twice the value obtained in co-injection under almost identical conditions. Simultaneous increase of \bar{n}_e , τ_p , τ_E and τ_ϕ are observed in counter-NBI accompanied by a peaking of the density profile. Throughout all the experiment puffing of CD_4 (originally used to reduce the thermal load of the divertor and prolong the discharge) and pellet injection were used to control the density profile.

The analysis of a series of counter-NBI discharges showed the importance of the density peaking factor, $\mathcal{P}_n = n_e(0)/[n_e]$ in determining the momentum confinement. An expression of the form:

$$v_\phi(0) \propto (const + \mathcal{P}_n)P_b/[n_e]$$

was found to fit the velocity measurements of the velocity in counter-NBI, while the momentum confinement time was fitted by an offset linear function of P_b .

Comparison between the velocity scaling for co- and counter-NBI, assuming equal plasma parameters, showed that there is some improvement in the counter- confinement which cannot be attributed to \mathcal{P}_n .

The improvement of confinement with the peaking factor suggested ^[8] that the stabilization of η_i modes could be the cause of it. According to Ref. [8], during counter-NBI, χ_ϕ^{ex} showed a reduction over the whole plasma cross-section and local analysis of momentum and thermal ion transport showed that χ_ϕ and χ_i were in good agreement with $\chi_i^{\eta_i}$. A simulation of momentum transport, reported in Ref. [10], instead, showed that the change of the torque deposition profile with \mathcal{P}_n can account for about two-thirds of the measured variation of τ_ϕ with the peaking factor.

4.2.6 TFTR

Since the Tokamak Fusion Test Reactor, TFTR, became operative in 1984, considerable effort has been devoted by experimenters to measure plasma velocities, to construct databases of rotation speeds and to analyze these data, in order to understand momentum confinement [11]–[16].

Prior to 1987, the rotation velocity data (and the T_i data, as well) were obtained from measurements of the Doppler shift of the TiXXI K_α resonance line by a Bragg bent crystal spectrometer of high spectral resolution and were limited to the plasma center [46].

The CERS diagnostic began providing sensible measurements of velocity and ion temperature profiles in the summer of 1987 [41].

Results from an early beam power scan experiment were reported in Ref. [12]. The series of shots were run in deuterium plasma varying P_b in range 1.2–5.6 MW. The other plasma parameters are listed in Table 4.1. The central rotation velocity, measured from Doppler shift of the TiXXI K_α line, varied as $v_\phi(0) = 3.0 \cdot 10^4 + 2.34 \cdot 10^4 P_b$ m/s, with P_b in MW [20].

The measured central rotation frequency from this P_b scan was compared with the theoretical prediction of an earlier version of the gyroviscous theory, Eq.(3.19), and found in good agreement, as shown in Fig. 4.6 [20]. There was similar good agreement between experimental (reported in Ref. [76]) and theoretical τ_ϕ .

A comprehensive outline of rotation measurements and their analysis prior to 1987, was given in Ref. [76]. The database of ~ 400 shots taken, in part, in 1985, during operation on the outer moveable limiter (only co-NBI), and, in part, in 1986, during discharges run off the inner bumper limiter (co-, counter- and balance NBI) spans a wide range of plasma parameters. These are summarized in Table 4.1.

The following observations were reported. It was found that the limiter configuration did not significantly affect momentum transport. The central velocity increased in an offset-linear fashion, independent of I_p , with T_ϕ/\bar{n}_e , in spite of the increase of n_e

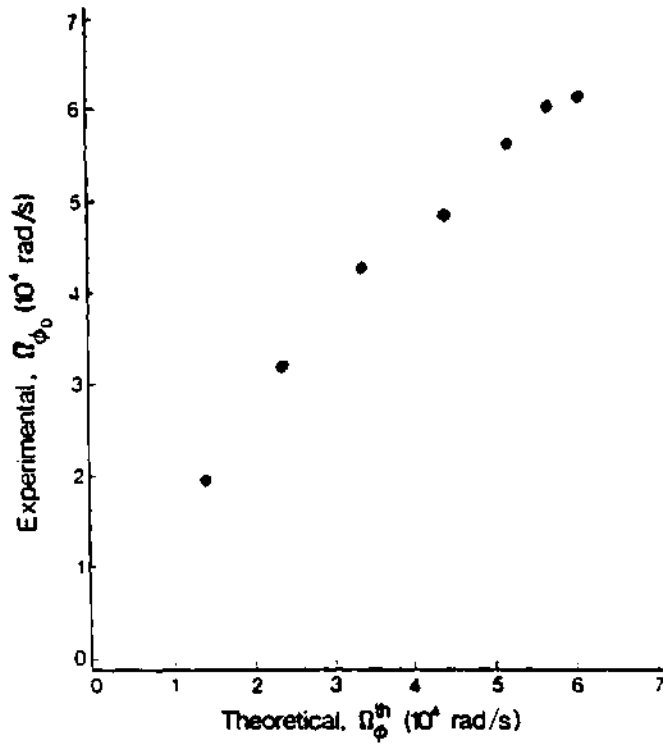


Figure 4.6: Comparison of $v_\phi^{ex}(0)$ with $v_\phi^{gn}(0)$, Eq.(3.19) in TFTR [20].

with I_p . This indicated a nonlinear dependence of $v_\phi(0)$ on T_ϕ/\bar{n}_e , at small values of torque input per particle, and the absence of saturation of the central velocity, up to $T_\phi/\bar{n}_e < 1.1 \cdot 10^{-18} \text{ Nm}^4$ (see Fig.(4.7)). At the same value of T_ϕ/\bar{n}_e , $v_\phi(0)$ was $\sim 20\%$ lower in counter-injection than in co-injection (similarly to $T_i(0)$, found to be lower in counter- than in co-, at comparable P_b/\bar{n}_e). The central velocity was also found to be less in the pre-compression configuration ($R=3$ and $a=0.85$ m) with respect to $R=2.55$ and $a=0.82$ m.

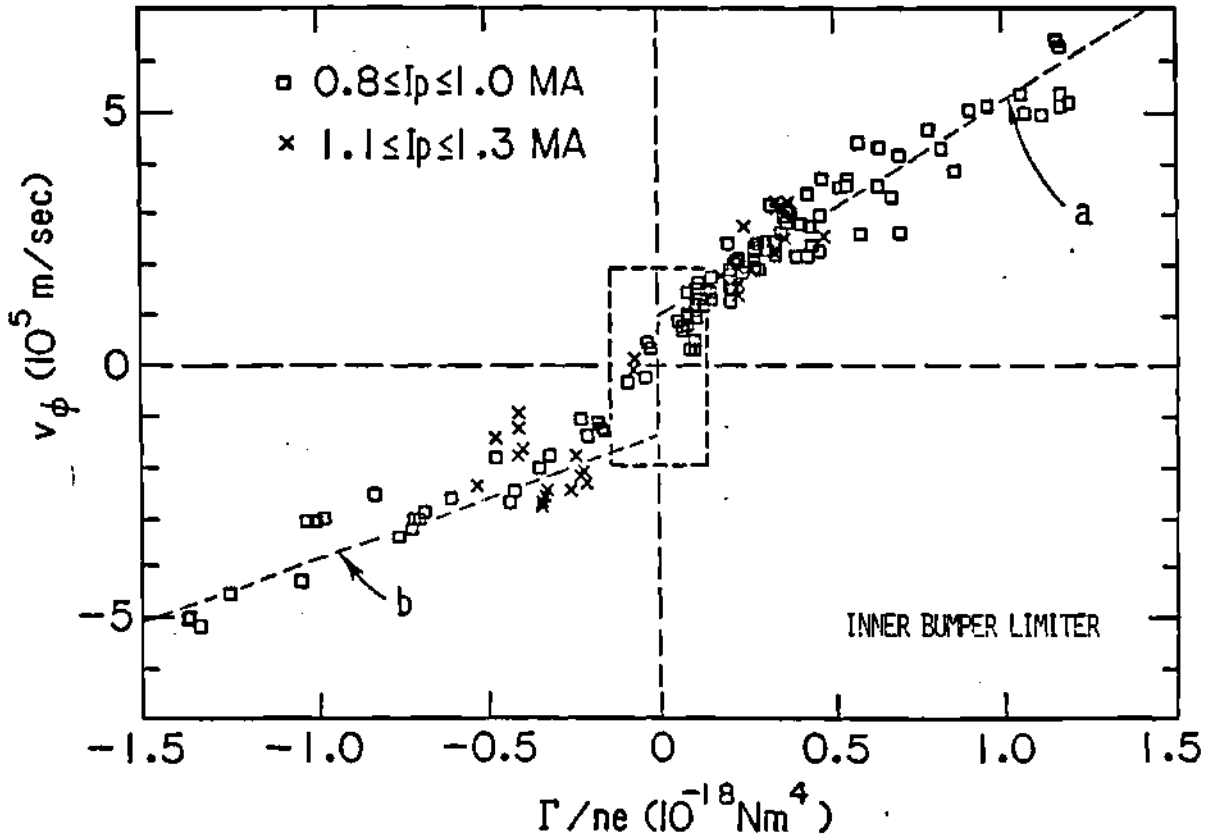


Figure 4.7: $v_\phi(0)$ L-mode discharges in TFTR versus input torque per particle [76].

The momentum confinement time, computed towards the end of NBI, assuming a parabolic velocity profile, showed modest deterioration with P_b and $T_i(0)$ in counter-

injection, little or no variation in co-injection and no clear dependence on Z_{eff} and B. It seemed to improve with I_p in the movable limiter discharges; a series of shots at small minor radius, large R and low I_p showed the lowest confinement time but it was not clarified if this indicated a dependence on R or rather I_p .

The post-injection (e-folding) velocity decay time was found to decrease with $v_\phi(0)$, measured at the end of NBI, and to be substantially longer (twice) than the steady state τ_ϕ , as previously observed on ISX-B and PDX.

Momentum confinement times constructed from early TFTR data were generally within a factor of 2-3 of the prediction of the gyroviscous theory [76],[20], Eq.(3.18). When the data were plotted against the variables T_i , B, Z_{eff} and R, no scaling was evident [11] (see Fig. 4.8). Subsequent analysis have shown that these data are not adequate to determine a B or R dependence, due to the small range of variation of B and R, compared to the errors affecting the data. Z_{eff} measurements were unavailable for several shots, and the T_i and v_ϕ profiles are completely unknown.

An interesting modulated edge heating experiment [76] was performed by pulsed injection of the beams through the plasma edge. Since $v_\phi(0)$ increased to 2/3 of its value obtained during central heating, it was ruled out that ripple or other edge damping mechanisms governed rotation in TFTR. A momentum transport simulation, using a diffusive transport model with $\chi_\phi = 0.3$ m/sec, could reproduce the observed central velocity time history. The χ_ϕ required to reproduce the central velocity, in a similar, modulated, central heating shot, was half the magnitude of the edge injection one.

A rotation experiment, consisting of a series of discharges at different values of I_p , B, R, P_b and direction of injection was conducted in TFTR in September 1988 [14],[16]. The discharges were of the kind later indicated as hot-ion-mode [15], with characteristics between the L-mode and the Supershot ones (see Table 4.2). Since

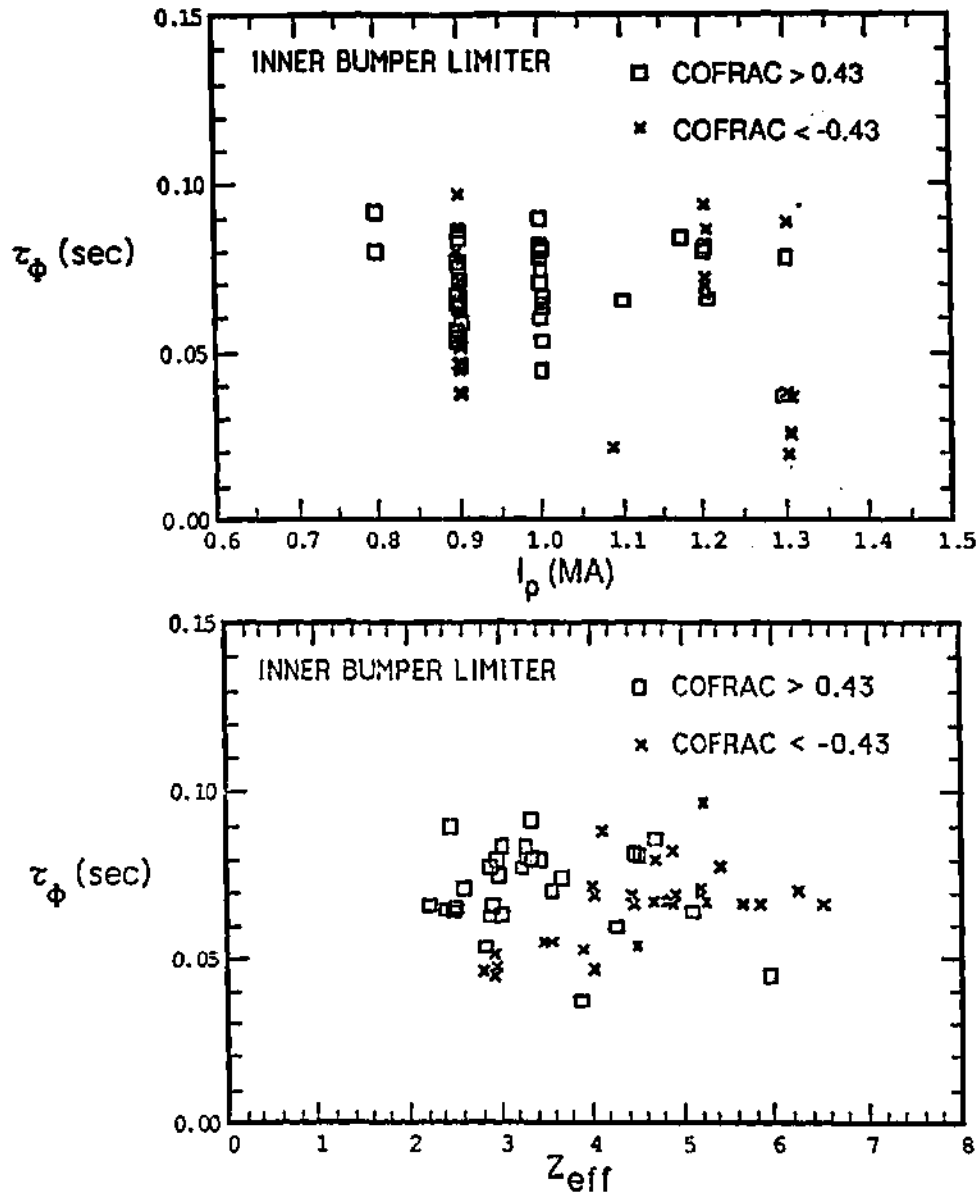


Figure 4.8: L-mode discharges did not show a clear variation of τ_ϕ^{ex} on plasma current or Z_{eff} [76]

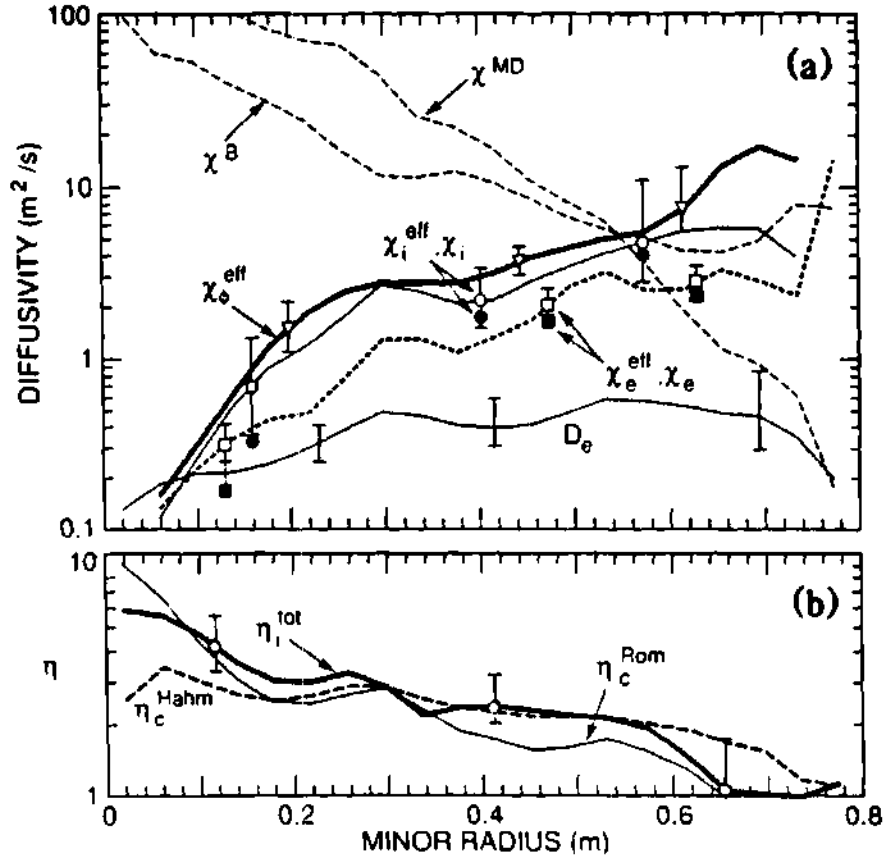


Figure 4.9: (a) Experimentally determined particle diffusivity and effective momentum and thermal diffusivities. Also shown are the theoretical χ_ϕ^{MD} [34] (labeled MD) and η_i^{tot} [36] (labeled B). (b) Comparison of measured η_i^{tot} with the theoretical estimates η_i^{Rom} [38] and $\eta_i^{H\&T}$ [39] (labeled Hahm)

	<i>L mode</i>	<i>Hot-Ion mode</i>	<i>Supershot</i>
recycling (H_α)	high	low	low
injection	any	co-counter	balanced
\mathcal{P}_n	< 1.7	1.7-2	2-3
τ_E (s)	< 0.09	0.1-0.13	> 0.13
τ_E/τ_E^I	≤ 1.3	≤ 2	≤ 3
$n_{fast}(0)/n_e(0)$	lower	0.1-0.4	higher
$T_i(0)$ keV	2-10	10-20	20-30

Table 4.2: Characterization of TFTR confinement regimes [15]

velocity, density and temperature profiles were measured, this experiment was particularly suitable for the study of correlation between local transport coefficients of momentum and thermal diffusivities. The interest in such correlation is dictated by previous experimental observations of $\chi_i \sim \chi_\phi \ll \chi_i^{neo}$ on TFTR [14] and DIII [6], and by the hypothesis that the ITG modes or other electrostatic turbulence mechanisms can dictate the confinement properties.

The analysis, reported in Ref. [16], shows:

- a strong correlation among the transport coefficients ($\chi_\phi/\chi_i = 0.7 - 2$, $\chi_\phi/\chi_e = 1.2 - 3.1$);
- a strong radial dependence and an increase of χ_ϕ and χ_i from the center to the edge by up to a factor of 100;
- a weak dependence on global parameters that precludes the precise determination of their scaling (ex.: $\chi_\phi \sim P_b^{0.23} I_p^{-0.59} B^{0.16} r/a^{1.22}$).

The theoretical estimates of η_i^{Rom} , Eq.(3.50), and $\eta_i^{H\&T}$, Eq.(3.51), are found to be within a factor of 2 of the measured η_i^{ex} (see Fig. 4.9). The theoretical $\chi_\phi^{\eta_{ss}}$, Eq.(3.48), and $\chi_i^{tor} \equiv \chi_\phi^{\eta_i}$, Eq.(3.49), have been compared with the experimental diffusivities

and shown to overestimate/underestimate them by two orders of magnitude at the center/edge [16].

Subsequently, a similar analysis was conducted for a series of L-mode shots. The local χ s were found to be qualitatively similar to the hot-ion-mode diffusivities, but quantitatively higher (factor of 2 for χ_ϕ) and improving with I_p . η_i^{ex} was found to exceed η_i^{Rom} and hot-ion- η_i by a factor up to 8, suggesting that, in L-mode discharges, transport is not governed by marginal stability (the transport does not increase in order to cause η_i^{ex} to approach η_i^{cr}).

4.2.7 JET

A large number of rotation measurements have been taken during NBI discharges in the Joint European Torus, JET, for a variety of plasma conditions: H^0 and D^0 in D^+ plasmas, inner and outer limiter, X point, L and H modes, with and without RF-heating, and with different degrees of elongation ($k=1-1.8$). A partial description of these measurements is given in Refs. [17] – [19]; a more complete description of a subset of the JET database, through September 1988, can be found in Ref. [20].

Rotation velocities have been measured in JET with several methods: [17] 1) central velocities were determined from the Doppler shift of a Ni XXVII resonance line observed by an x-ray crystal spectrometer; 2) a multi-chordal (8 lines) visible charge exchange diagnostic measures the Doppler shifted light from excited CVII and OIX ions providing velocity and ion temperature profiles; 3) occasionally, an XUV spectrometer detected the emission lines of lower ionization states of Ni and C ions, providing velocity profiles and differences in v_ϕ during OH and Ion Cyclotron Radio Frequency (ICRF) heating; 4) the MHD coils, measuring \tilde{B} , could provide rotation data when the MHD activity was significant ($\tilde{B}_\theta/B_\theta \leq 10^{-4}$).

The x-ray and XUV diagnostics showed that the plasma rotation frequency was

$\leq 10^4$ rad/s during OH and in the direction counter to the plasma current; ICRF had the effect of increasing the central rotation in the counter-direction [18].

With NBI, the central rotation velocity tended to saturate with increasing $P_b/[n_e]$ and to increase slightly with I_p for both counter- and co-injection. ($[n_e]$ indicates the average volume density) Roughly twice the value of $P_b/[n_e]$ was needed in L-mode to produce a $v_\phi(0)$ comparable to the $v_\phi(0)$ attained in H-mode. [20]. H mode shots, characterized by a reduced H_α signal, by a flat $n_e(r)$ and somewhat flatter $v_\phi(r)$ (and increased τ_E), systematically show a momentum confinement higher than the L mode shots (see Table 4.1).

Ref. [19] reported that $v_\phi(0)$ was found to be strongly correlated with $T_i(0)$; the relation: $\Omega_{\phi i}(0) \sim 6.2 \times T_i(0) \text{ krad}/(s \text{ keV})$ could fit a large set of NBI data, with moderate MHD activity, independently of the other plasma parameters.

MHD activity was found to affect the momentum transport considerably [21]: at the appearance of a locked mode the rotation stops on a 100 ms timescale; when high MHD activity was present there was evidence, from the MHD and XUV diagnostics, of flattening of the velocity profile.

Also ICRF, when tuned to the H minority, caused a sharp drop of up to a factor of two in the rotation velocity. This was explained [17] by the cumulative effect of the increase in number of beam ions scattered into trapped orbits, of density rise during RF-heating and the induced counter-velocity that seems inherent with ICRF in JET.

The result of a momentum transport analysis for a H mode shot, affected by sawteeth, was reported in Ref. [18]. The experimentally inferred momentum diffusivity was found to decrease with minor radius from $\chi_\phi(0) \sim 0.4 - 0.6 \text{ m}^2/s$ (at sawtooth peak/crash) to $\chi_\phi(a) \sim 0.1 \text{ m}^2/s$. An extensive comparison between χ_ϕ^{eff} and χ_i^{eff} yielded the following result:

$$\chi_\phi^{eff} = (Z_I + 1 - Z_{eff})/Z_I(1 \pm 0.3) \chi_i^{eff} \text{ (with } Z=4 \text{ or } 6, \text{ for Be or C),}$$

that is similar to the TFTR finding [16]: $\chi_\phi^{eff} \sim \chi_i^{eff}$.

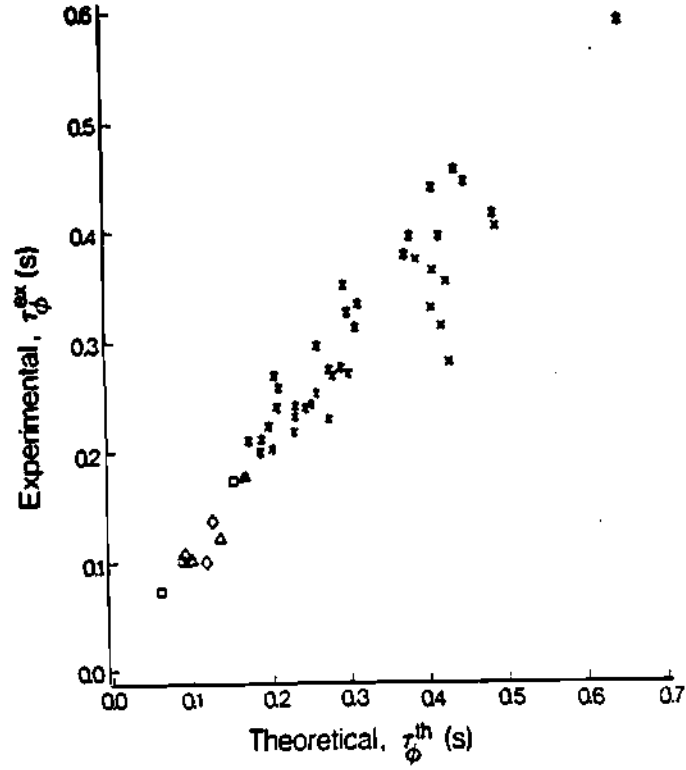


Figure 4.10: Comparison of experimental and theoretical momentum confinement time in JET. Legend: (*) H-mode, NBI only; (x) H-mode like, NBI+ICRF; (Δ) L-mode, NBI only; (\diamond) L-mode, NBI+ICRF; (\square) L-mode "jolly good" [20]

The momentum confinement time inferred from experiment and the prediction of the gyroviscous theory, with profile effects included, (Eq. 3.21), were in rather good agreement (See Fig. 4.10) [20]. Distinctly lower τ_ϕ were found for L-mode discharges than for H-mode discharges. These differences were explainable via Eq.(3.21), with $\hat{Z} = Z_{eff}$ (Eq.(3.25)), in terms of differences in Z_{eff} , temperature and profile shape. The scaling of $v_\phi(0)$ and τ_ϕ with Z_{eff} and T_i predicted by Eq.(3.22) and Eq.(3.21) was found in the data when the correlation between Z_{eff} and T_i was taken into account.

Comparison of more recent JET measurements with the gyroviscous theory was stated [19] to show an order of magnitude underprediction of $\Omega_\phi(0)$. However, the authors incorrectly modified Eq.(3.22) and overestimated the viscous force by an order of magnitude. It can be inferred from their results that Eq.(3.22) predicts the correct order of magnitude for $\Omega_\phi(0)$.

A set of momentum diffusivities [19] were compared with the η_i theory prediction, in the form of Eq.(3.48), at an unspecified radial location. The discharges with a flat density profile had a χ_ϕ^{ex} much lower than the η_i -predictions, while the shots with more peaked $n_e(r)$ showed a better agreement.

4.2.8 PBX-M

A multispatial and multispectral (CVII, OIX) CERS diagnostic is available on PBX-M for the measurements of $v_\phi(r)$ and $T_i(r)$.

PBX-M has two nearly perpendicular NB injectors and two more tangential NB injectors that allow the study of toroidal rotation with different torque values and constant injected power (and vice versa).

A series of experimental results were presented in Ref. [22] for H mode shots and plasma parameters listed in Table 4.1. Independently of the NB injectors configuration, $v_\phi(0)$ was found to be $\propto T_\phi$ and to be more peaked with increasing T_ϕ ; $v_\phi(0)$ was insensitive to \bar{n}_e , suggesting $\tau_\phi \propto \bar{n}_e$.

The comparison between one parallel and one perpendicular NBI shots, with similar injected power, and similar in the OH phase, showed $v_\phi(0)$ and $T_i(0)$ considerably higher in the parallel injection case, and a momentum confinement time similar in the two cases (note that, roughly, $T_i(0)$ (keV) $\sim P_{abs}/\bar{n}_e$ (MW)). The local momentum transport analysis of the two shots showed $\chi_\phi^{ex} \sim \chi_i^{neo}$ increasing with minor radius, and a factor of two larger in the perpendicular injection case, with respect to the parallel injection case. The χ_i and χ_e radial profiles showed radial dependence (constant or decreasing with r) and magnitude (up to a factor of 10 larger) different from those of χ_ϕ .

4.3 Summary of previous results

4.3.1 Parametric dependence of $v_\phi^{ex}(0)$, τ_ϕ^{ex} and $\chi_\phi^{ex}(r)$

The question of how $v_\phi^{ex}(0)$ scales with the main machine parameters has been investigated since the earliest rotation experiments. The computation of $\tau_\phi^{ex}(a)$ has been carried out extensively only in recent experiments (DIII, ASDEX, JET and TFTR), since it requires information on the radial profiles of n_e and v_ϕ .

A consistent picture has not yet emerged about the dependence of v_ϕ and τ_ϕ on P_b and n_e .

The central rotation velocity was found:

- to be $\propto T_\phi/\bar{n}_e$ in PDX, and $\propto T_\phi$ ($\bar{n}_e = const$) in PLT, DIII(divertor) and PBX-M ($\bar{n}_e = const$) ;
- to be $\propto (T_\phi/\bar{n}_e + const)$ in TFTR and ASDEX;
- to saturate with increasing $T_\phi/[n_e]$ in JET and with increasing T_ϕ in ISX-B (with $\bar{n}_e = const$) and DIII(limiter) (and \bar{n}_e dependent on P_b).

This translates into conflicting evidence about the dependence of τ_ϕ on T_ϕ ($\propto P_b$ for same beam species) and n_e , since τ_ϕ and v_ϕ are related in the following way (from

Eq.(2.10), for fixed geometric parameters):

$$v_\phi(0) \propto \frac{T_\phi}{[n_e]} \frac{\tau_\phi^{ex}}{m_{eff}} \left(\frac{1 + \alpha_n + \alpha_v}{1 + \alpha_n} \right) \quad (4.1)$$

Assuming velocity and density profiles weakly varying through the experiment, the global momentum confinement time appears:

- to increase with \bar{n}_e in PLT, ISX-B and PBX-M, and
- to be independent of T_ϕ/\bar{n}_e in PDX.

$\tau_\phi^{ex}(a)$, computed from measured profiles, was found:

- to decrease with T_ϕ in limiter and divertor DIII discharges (even if for different reasons);
- to depend essentially on \mathcal{P}_n in ASDEX;
- to deteriorate, modestly, with P_b in the TFTR counter-NBI.

The I_p dependence of $v_\phi(0)$ (and τ_ϕ in the most recent experiments) was also checked and found to be absent in most of the machines, with the exception of DIII, where a τ_ϕ^{ex} showed a linear increase with increasing I_p , but this was attributed to v_ϕ profile broadening with I_p .

An improvement in momentum confinement from H plasmas to D plasmas was observed in PLT and PDX, which is in agreement with the trend observed in several tokamaks of confinement properties improving with main ion mass.

Any B dependence of $v_\phi(0)$ was found to be absent or unclear (TFTR).

There are substantial differences among the different machines on how the momentum confinement in co- and counter-NBI compares:

- some magnitude of rotation velocity was obtained in PLT for same magnitude of T_ϕ/\bar{n}_e with co- counter-NBI;

- a substantial improvement of momentum confinement, due to a simultaneous increase of n_e and v_ϕ , was observed in the ASDEX counter-NBI, relative to co-NBI;
- $v_\phi(0)$ was found lower in the TFTR counter-NBI than in the co-NBI at the same magnitude of T_ϕ/\bar{n}_e .

The trend towards larger momentum confinement time in larger machines is clear from Table 4.1. In Ref. [77], the τ_ϕ^{ex} s from a collection of discharges from several tokamaks were shown to be aligned about the straight line given by: $\tau_\phi(s) \sim a^2/3(m^2)$ or, alternatively, $\tau_\phi(s) \sim aR^2/15(m^{-3})$.

Ref. [77] and Table 4.1 point out that there is a general tendency to observe $\tau_E \propto \tau_\phi$, but no general scaling laws of τ_ϕ as function of a few plasma parameters (of the kind derived for τ_E [78]) is suggested by the previous discussion. In particular, the favorable dependence of τ_E on I_p is not observed for τ_ϕ^{ex} (with the exception of DIII). On the other hand, a systematic attempt to fit a theoretical formula to or derive an empirical formula for the scaling of τ_ϕ and v_ϕ with the plasma parameters, has never been undertaken.

Momentum confinement is degraded by RF heating (JET). It clearly improves in divertor discharges, with respect to limiter discharges, in DIII, JET and PDX. Momentum confinement is also higher in H-mode plasmas, with respect to L-mode, in JET and ASDEX.

An extensive study of χ_ϕ^{ex} in TFTR discharges has shown a weak dependence of the momentum diffusivity on the controllable plasma parameters P_b , I_p and B.

4.3.2 Comparison of theory with experiments

The complicated dependence of momentum confinement properties on plasma conditions suggests to look for parametric dependence of v_ϕ , τ_ϕ or K_ϕ inferred from theoretical models. An extensive, quantitative test of all the theories reviewed in Chapter 3 has not been done.

Previous comparisons of theory and experiments have been most extensive for the gyroviscous theory. Measured and predicted magnitudes for τ_ϕ and/or v_ϕ were found to be in reasonable agreement in ISX-B, PLT, DIII, JET and TFTR, as discussed previously. Observed parametric dependences could be accounted for in ISX-B, PLT, JET and some of the TFTR data. Disagreement between plasma parameter dependences predicted by the gyroviscous theory and observed in the experiments were reported in DIII and other TFTR data.

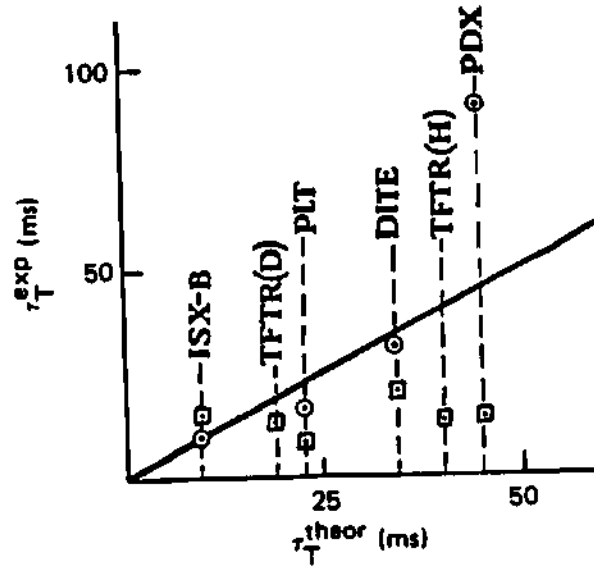


Figure 4.11: Comparison of τ_ϕ^{mp} with τ_ϕ^{ex} from several tokamaks [28].

A comparison of the predictions of the 'smp' theory with momentum confinement

times in several tokamaks (ISX-B, TFTR, PLT, DITE and PBX), and shown in Fig. 4.11 was reported in Ref.[28]. The magnitude of the predicted τ_ϕ was found to agree with the measurements, but the limited number of discharges considered (one for each machine) and the lack of profiles information does not allow any conclusions about the parametric dependence and the local value of the 'smp' momentum flux.

Measurements on TEXT revealed density fluctuations propagating in the ion diamagnetic drift direction that suggest the presence of ITG modes [33].

In TFTR [16] the η_i^{ex} is close to the theoretical predictions of the threshold value, but a recent perturbation study in supershots [15] has produced results in disagreement with the hypothesis of transport controlled by ITG marginal stability. According to the theory, the steady state η_i^{ex} should have a value close to the threshold η_i^{cr} , above which the ITG mode becomes unstable, increasing the heat transport and acting as a feedback on $T_i(r)$ and therefore on η_i^{ex} . During a discharge, the equilibrium η_i was changed by raising L_n with pellet injection and gas puffing. It was observed that T_i and ∇T_i did not change, that is η_i^{ex} did not adjust to maintain itself at the level of η_i^{cr} , as postulated by the theory. By contrast, T_e changed rapidly, showing a decrease in L_{Te} as ∇n_e decreased and reversed its sign. These observations lead to the conclusion that the ion thermal transport in TFTR supershots is not controlled by ITG turbulence. [15].

When an ITG transport model was included in the simulation of TFTR ohmic experiments [79], it succeeded in predicting the degradation of the energy confinement at high density accompanied by $\eta_i \geq 1.5$. Radial profiles of momentum diffusivities predicted by the ITG modes theory have been compared with experimental data [16] and found to be in strong disagreement.

We are not aware of comparison of rotation experiments data with the prediction of trapped/untrapped electron modes or other drift waves models. $\tilde{E} \times \tilde{B}$ turbulence affects both momentum and energy transport and give rise to $\chi_i \sim \chi_e \sim \chi_\phi$ [80].

Investigation of energy transport, based on drift waves models, can give information on a mechanism that affects momentum transport as well. There exist several simulations of energy confinements based on drift waves models. Dominguez and Waltz [81] incorporated diffusion coefficients due to trapped and circulating electron modes in a transport model, which included η_i and low- m tearing modes as well, to simulate experimental heat transport data from several tokamaks (DIII, ISX-B, Alcator A and C, and JET). They found that the dissipative trapped electron modes can explain the low density neo-Alcator scaling of τ_E , that ITG modes are likely to be responsible for the energy saturation at higher densities, and that collisional drift modes, accompanied by low- m tearing modes (Venetian blinds), accounts for the favorable I_p dependence of τ_E .

Ware's cold ions theory has been claimed [72] to explain rotation measurements and a number of particle transport features in several tokamaks. No comparison between the theoretical torque flux, Eq.(3.32), and the experimental one has been published.

Chapter 5

A TFTR ROTATION EXPERIMENT: Exp. 44. MACHINE AND PLASMA PARAMETERS

The experiment Exp. 44 was carried out in TFTR in September 1988. The principal objective of Exp. 44 was to obtain measurements of the v_ϕ and T_i profiles, using the recently installed CHERS diagnostic, for a variety of machine and plasma parameters in low-recycling discharges.

The experiment consisted of a series of co-, counter- and balanced NBI shots at different plasma currents ($I_p = 1.1$ and $I_p = 1.7, 1.8$ MA), with a total injected beam power, P_b , ranging from 4 to 14.5 MW. The injection of deuterium neutral beams into a well conditioned deuterium target plasma lasted 0.5 or 1 seconds. Other plasma parameters, which remained fixed, were:

minor radius, $a = 0.79$ m;

major radius, $R = 2.45$ m;

maximum beam energy, $E_b \simeq 100$ keV;

beam tangency radii ranging from 1.74 to 2.99 m;

beam species mix by neutral current fraction, 45:28:26 (1 : 1/2 : 1/3), and

magnetic field, $B_t = 4.75$ T.

Also a magnetic field scan was performed at $B_t = 2.9, 3.8$ and 4.8 T, at $I_p = 1.0$ MA, using 7 MW of co-beam or 12 MW of counter-beam power. The experimental conditions, at the time of the diagnostic neutral beam (DNB) injection, at which time the plasma parameters had reached quasi steady state values, are summarized in Tables 5.1 and 5.2. The parameter listed in these Tables, and not yet defined, are: \bar{n} is the line average density; $\mathcal{P}_x \equiv x(0)/[x]$ is the peakedness factor for the plasma

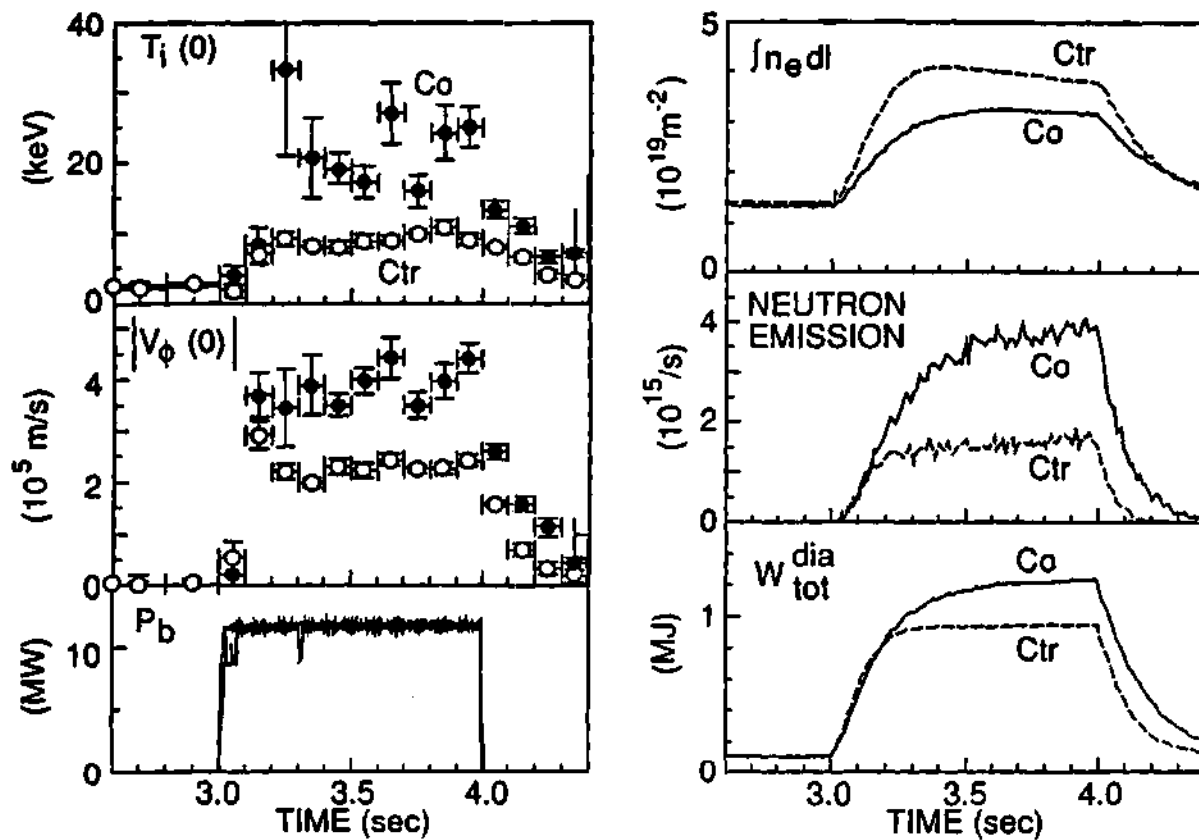


Figure 5.1: Time histories of several plasma parameters ($T_i(0)$ and $v_\phi(0)$ as measured by the XCS, P_b , $\int n_e dl$, neutron emission and total stored energy, W_{tot} , diamagnetic) for Shot 37309, co-injection, and Shot 37313, counter-injection, both with $P_b = 11.6$ MW, $I_p = 1.1$ MA, $B = 4.75$ Tesla.

I_p		P_b	\bar{n}_e	\mathcal{P}_{n_e}	$\frac{n_{Ti}(0)}{n_e(0)}$	$v_\phi(0)$	\mathcal{P}_{v_ϕ}	$T_i(0)$	\mathcal{P}_{T_i}	$T_e(0)$	\mathcal{P}_{T_e}	Z_{eff}^{VB}	Z_{eff}^{met}	$\frac{Y_{\phi Ti}}{Y_{\phi tot}}$	$\frac{W_{Ti}}{W_{tot}}$
1.1	co	4.4	1.4	2.0	0.32	3.0	4.0	11.5	3.6	4.8	3.2	3.9	0.63	0.70	0.59
		7.3	1.6	1.9	0.35	3.9	3.9	14.3	3.8	5.5	3.3	4.0	0.58	0.71	0.65
		11.6	2.0	1.9	0.20	5.5	6.6	21.7	4.8	6.5	3.3	3.1	0.61	0.77	0.59
1.1	ctr	7.3	2.2	1.8	0.25	-2.3	3.5	8.0	4.8	6.3	3.4	4.0	0.30	0.62	0.50
		12.0	2.4	1.9	0.27	-3.6	5.2	10.1	2.9	5.3	3.0	3.5	0.35	0.69	0.53
		15.0	2.5	1.8	0.34	-3.7	4.3	11.6	3.1	5.2	2.9	3.4	0.42	0.70	0.58
1.8	co	4.6	2.0	1.7	0.20	2.4	3.8	9.6	3.0	4.6	2.6	3.6	0.38	0.68	0.41
		9.2	2.5	1.9	0.15	4.2	5.2	16.1	3.7	5.7	3.0	3.2	0.47	0.59	0.40
		13.6	2.8	1.9	0.14	5.0	4.4	19.1	3.7	5.9	2.9	3.0	0.43	0.57	0.41
1.7	ctr	5.1	2.2	1.9	0.18	-1.7	3.2	7.4	2.9	5.0	2.7	4.2	0.29	0.56	0.41
		10.1	3.0	1.9	0.15	-2.9	3.9	9.9	2.7	4.6	2.4	3.5	0.28	0.51	0.37
		15.1	3.4	1.7	0.20	-2.4	3.0	8.1	2.2	4.8	2.5	3.3	0.20	0.56	0.40
1.1	bal	14.1	2.3	2.0	0.37	/	/	20.8	2.8	4.5	2.8	3.1	0.88	/	0.63

Table 5.1: Summary of plasma parameters for the P_b , I_p , co- and counter-injection scans in Exp. 44. Units: I_p (MA), \bar{n}_e ($10^{19} m^{-3}$), v_ϕ ($10^5 m/s$), T_i and T_e (KeV).

B_t		P_b	\bar{n}_e	\mathcal{P}_{n_e}	$\frac{n_{Li}(0)}{n_e(0)}$	$v_\phi(0)$	\mathcal{P}_{v_ϕ}	$T_i(0)$	\mathcal{P}_{T_i}	$T_e(0)$	\mathcal{P}_{T_e}	Z_{eff}^{VB}	Z_{eff}^{met}	$\frac{Y_{\phi Li}}{Y_{\phi tot}}$	$\frac{W_{Li}}{W_{tot}}$
2.9	co	6.8	1.1	2.5	0.21	7.1	5.3	19.6	6.4	4.6	3.1	3.2	0.45	0.74	0.71
	cnt	12.7	2.2	1.8	0.39	-2.4	4.0	7.3	3.4	3.7	2.5	3.2	0.26	0.74	0.62
3.8	co	6.6	1.2	1.9	0.21	6.1	4.9	21.9	5.9	4.9	3.3	2.8	0.47	0.74	0.65
	ctr	12.4	2.1	1.9	0.28	-4.2	5.1	11.9	3.7	4.0	2.7	3.3	0.40	0.67	0.56
4.8	co	6.7	1.3	1.9	0.33	5.5	5.2	12.8	4.2	4.7	3.1	3.6	0.47	0.72	0.66
	ctr	12.4	2.2	1.9	0.32	-3.8	4.8	10.7	3.5	4.0	2.9	3.3	0.39	0.69	0.57

Table 5.2: Summary of plasma parameters for the B_ϕ scan at $I_p = 1\text{ MA}$ in Exp. 44.
Units: I_p (MA), \bar{n}_e (10^{19} m^{-3}), v_ϕ (10^5 m/s), T_i and T_e (KeV).

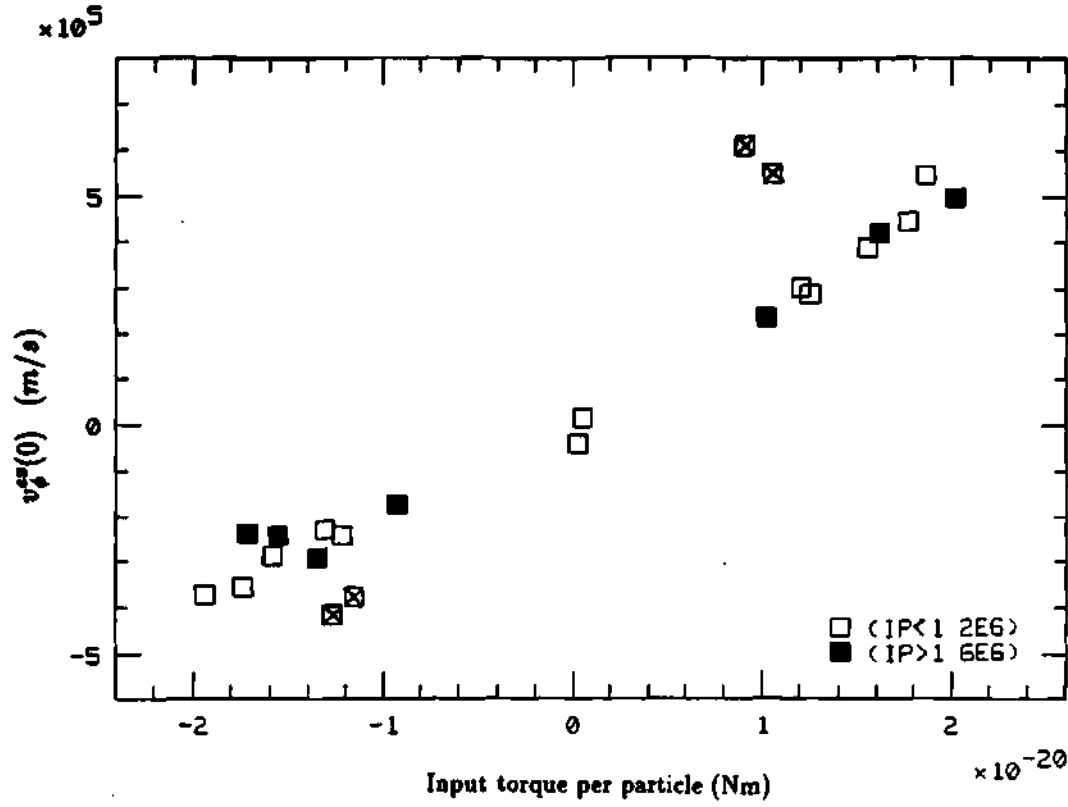


Figure 5.2: Central rotation velocity, $v_{\phi}^{ex}(0)$, as measured by CHERS, versus input torque per particle (\square $I_p = 1 - 1.1$ MA; \blacksquare : $I_p = 1.7 - 1.8$ MA; \times : $B < 4$ Tesla)

parameter x , where $[x]$ is the volume average of $x(r)$; $Z_{met} = n_M Z_M^2 / n_e$, where "M" denotes a metallic impurity; $L_{\phi fi} / L_{\phi tot}$ and W_{fi} / W_{tot} are the fraction of angular momentum and energy, respectively, stored in the fast ions.

Time traces of several of the measured parameters are shown in Fig. 5.1 for a co- and a counter-injected discharge. The co-injected discharge had a lower density and higher ion temperature, stored energy and neutron emission rate than the counter-injected discharge, for the same NB power. The rotation speed was greater for co- than counter-injection.

This set of uni-directional discharges, designated as Hot-Ion-Mode discharges, showed characteristics between the L-mode and the Supershot discharges, that is:

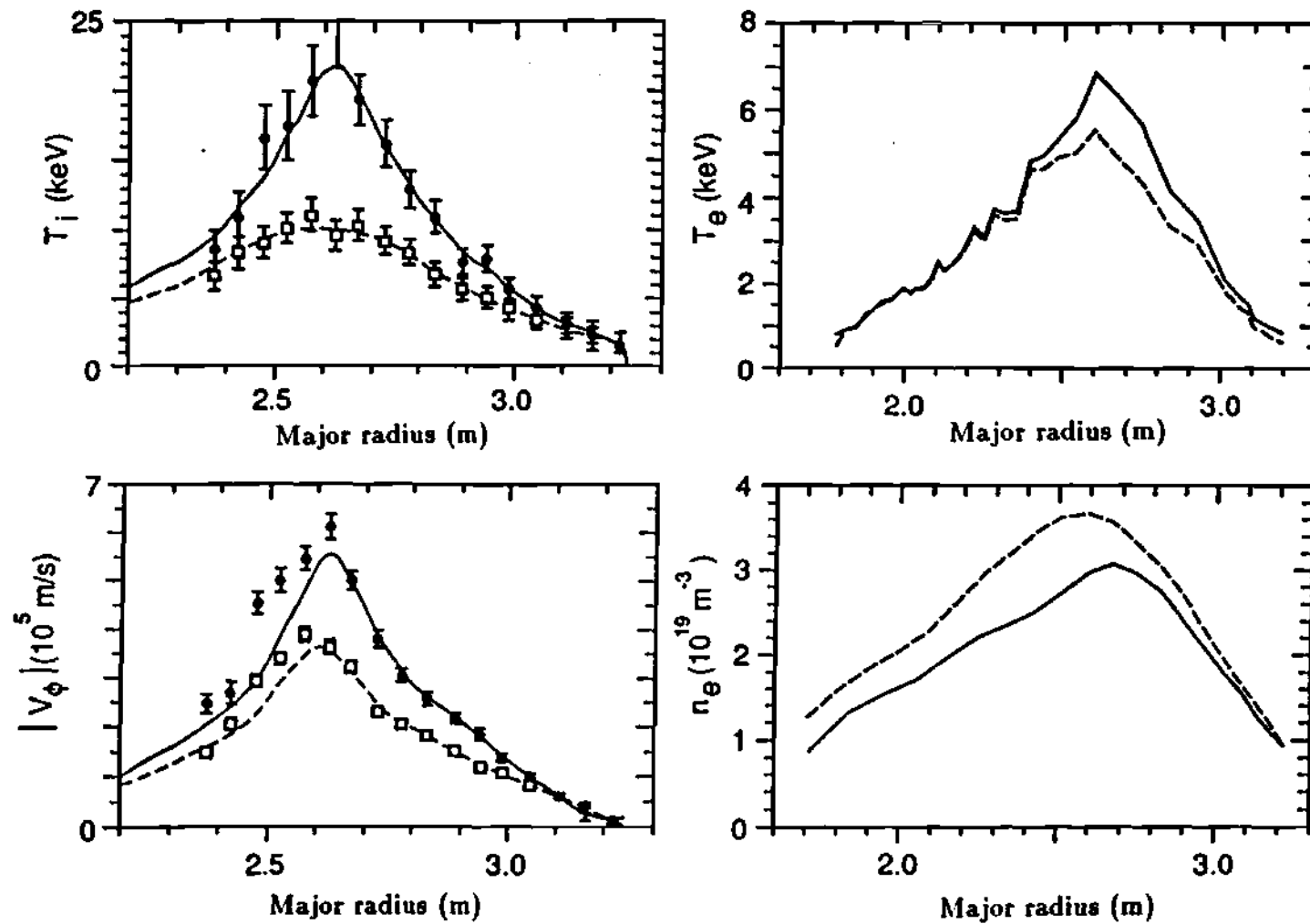


Figure 5.3: Measured plasma parameters profiles at $P_B = 11.6$ MW for Shot 37309, co-injection (—) and Shot 37313, counter-injection (- - -).

low recycling, low ohmic target density (typically $1.2 - 1.5 \cdot 10^{19} m^{-3}$), density peakedness $\mathcal{P}_{n_e} = 1.7 - 2$, τ_E up to twice the L-mode value, a large fast ion population ($n_{fi}(0)/n_e(0) = 0.1 - 0.4$) and a relatively high ion temperature ($T_i(0) = 10 - 20 keV$). Higher \mathcal{P}_{n_e} is usually accompanied by higher τ_E .

The rotation data taken in this experiment are characterized by the plot of central rotation velocities shown in Fig. 5.2. Central rotation velocities up to 5.7×10^5 m/s were obtained in the co-injection, low current shots. For the same value of injected torque per particle, the central velocity is 10-20 % lower in counter-injection shots. There does not appear to be a plasma current dependence of the rotation velocity. Most of the $v_\phi(0)$ data points show a linear dependence on $T_\phi(a)/\bar{n}_e$, with the exception of the low-B shots, which also exhibit the lowest densities, strongly beam dominated, and a very peaked velocity profile.

The peakedness of the velocity profile, $\mathcal{P}_{v_\phi} = 3 - 6.5$, increases with I_p and is less for counter- than co-injection. Characteristic velocity profiles are shown in Fig. 5.3. The lines in the v_ϕ and T_i plots are not a fit of the experimental data but represent a mapping of the data for $R > R_0$ onto flux surfaces performed by SNAP. Comparison of the data points for $R < R_0$ with the mapping thus provides an indication of any in-out asymmetry in the data. The T_i data seem to be quite uniform (with respect to in-out asymmetry) over the flux surface, as would be expected from consideration of the rapid heat conduction along field lines. The v_ϕ data, on the other hand, exhibit an in-out asymmetry larger than the experimental error. The symmetry found in the $T_i(r)$ data would suggest that the asymmetry in the v_ϕ data is real, not an artifact of the mapping procedure, but we cannot exclude that some systematic error, not reflected in the error bars, can affect the rotation measurements.

Typical torque flow terms are shown in Fig. 5.4 for Shot 37309-123, with 11.6 MW of co-injected power, $I_p = 1.1 MA$ and $B = 4.75 Tesla$. The convected torque flow, T_ϕ^{cv} , is approximately 1-10% of the conducted flow, K_ϕ^{ex} , over most of the plasma

region, and the total cx losses amount to only a few percent.

The accuracy of the calculated source of torque can be checked with a couple of methods. Since the calculated neutron emission depends on whether the beams are deposited (most of the neutrons are from beam-beam and beam-target interaction), one can compare the calculated and measured neutron rates. Since the fusion cross-section is heavily weighted to high energy, good agreement with measured neutrons provides some confidence that the initial deposition profile is correct, but less about whether the fast ions are well-confined radially. A second check can be done by comparing the total stored energy as calculated by SNAP from density and temperature measurements and calculated fast ions, with the same quantity measured by a diamagnetic loop.

The difference between calculated and measured neutrons was, on average, +20% for counter-injection and -17% for co-injection shots. The uncertainty affecting the neutron measurements is estimated to be $\sim 12\%$. The origin of this disagreement, which suggests a systematic error is affecting the measurement procedure or the calculation, has not been clarified yet.

Some discrepancy is also found between the stored energy inferred from magnetic measurements and the one resulting from the SNAP kinetic calculations. The diamagnetic stored energy from magnetic measurements agrees with the calculated value to within $\pm 10\%$.

If the discrepancies between the measured and calculated neutron production rate and stored energy are due to systematic errors in the modeling, this could also affect the torque deposition calculation. The credibility of the SNAP deposition profile is suggested by the good agreement with TRANSP [82] calculations, which employ a more sophisticated deposition and thermalization profile model (particle-following Monte Carlo code).

The thermal momentum confinement times, constructed from Eq.(2.12) and plotted in Fig. 5.5, show a modest degradation with P_b , a significant increase with I_p and

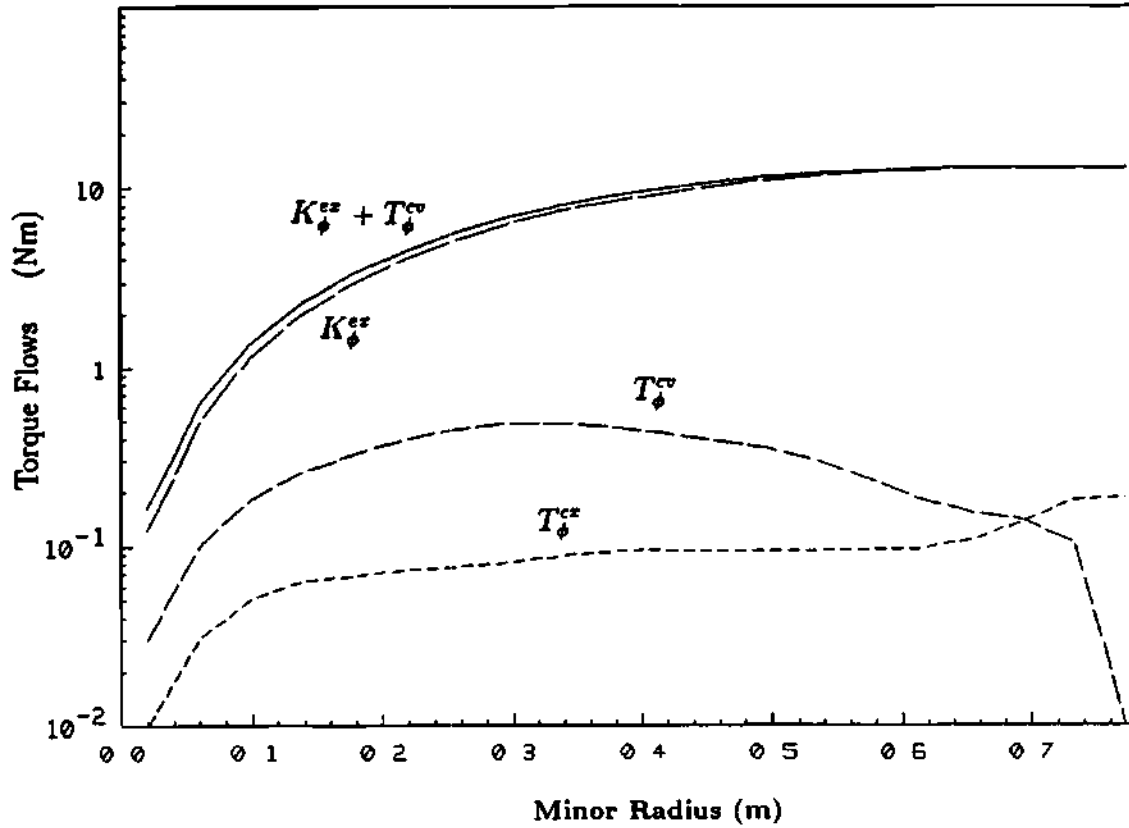


Figure 5.4: Radial profiles of the convective, T_{ϕ}^{cv} , and of the conductive, K_{ϕ}^{ex} , torque flows and of the torque flow lost by charge exchange, T_{ϕ}^{ex} , constructed from experimental data by the SNAP code. (Shot 37309)

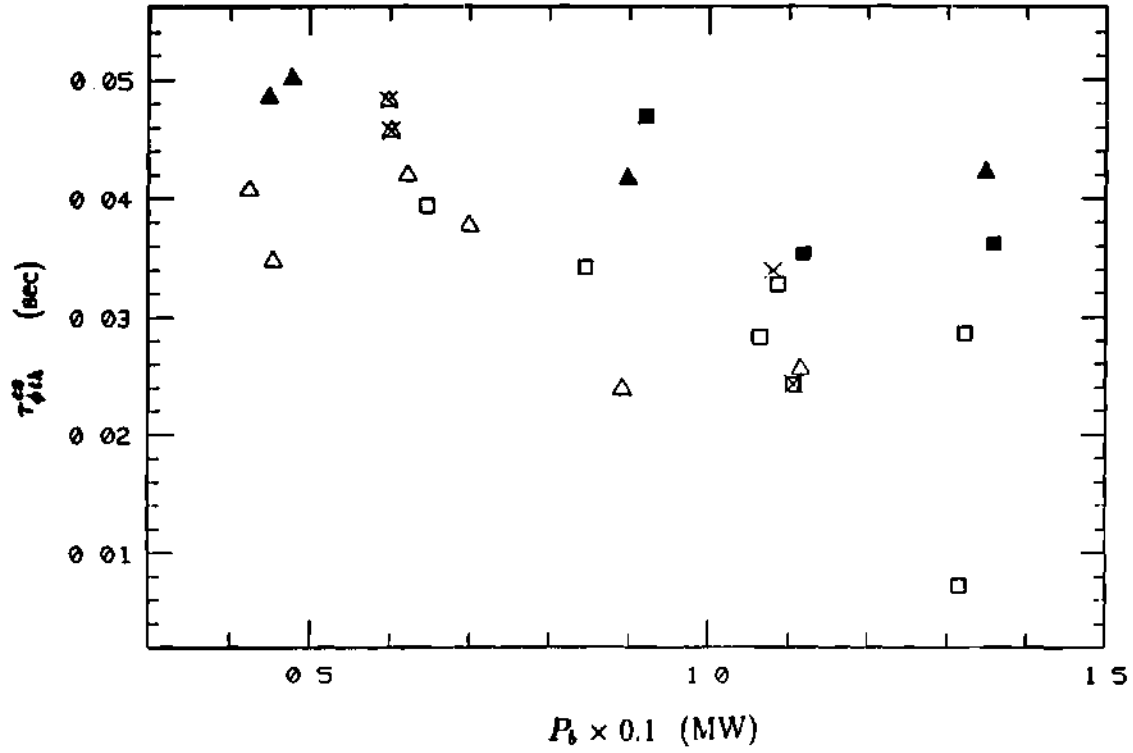


Figure 5.5: Experimental thermal momentum confinement time, $\tau_{\phi th}^{cx}$, versus input power.

(Δ : co-injection shots at $I_p = 1.1\text{--}1.3 \text{ MA}$; \blacktriangle : co-injection shots at $I_p = 1.7\text{--}1.8 \text{ MA}$; \square : counter-injection shots at $I_p = 1.1\text{--}1.3 \text{ MA}$; \blacksquare : counter-injection shots at $I_p = 1.7\text{--}1.8 \text{ MA}$; \times : $B < 4 \text{ Tesla}$).

no clear dependence on the direction of injection. As shown in Table 5.2, the peakedness of the velocity profile increases with I_p , which may be (?) related to the increase of $\tau_{\phi th}^{ex}$ with I_p . The total momentum confinement time is $\tau_{\phi tot}^{ex} \sim 3\tau_{\phi th}^{ex}$ (which means that 2/3 of the plasma momentum is carried by the fast ions), and for $\tau_{\phi tot}^{ex}$ the I_p dependence disappears because of the decrease of n_{fi} with increasing I_p .

Central ion temperatures up to 25 keV were reached in low current, balanced and co-injection shots. For the same value of injected power, $T_i(0)$ decreases with I_p and is less for counter-injection than for co-injection, consistent with the increase in \bar{n}_e with I_p and with higher \bar{n}_e for counter- than for co-injection. The ion temperature peakedness, $\mathcal{P}_{T_i} = 2.2 - 4.8$, increases with I_p and P_b and is less for counter- than co-injection, similarly to \mathcal{P}_{v_e} .

Typically the electron density increases during the beam heating, reaching an equilibrium value in ~ 300 ms. \bar{n}_e increases with P_b , I_p and from co- to counter-injection. The \bar{n}_e is $\sim 35\%$ higher in the high current shots; $\mathcal{P}_{n_e(0)}$ does not show a clear P_b or I_p dependence. Typical n_e profiles are shown in Fig. 5.3 for co- and counter-injection shots.

For the same I_p and P_b , the co- and counter-injection shots have remarkably different density-rise histories and the final \bar{n}_e is 10-30 % higher in the counter- shots. A larger density in the proximity of the inner bumper limiter is also a characteristic of the counter- density profiles. Fig. 5.6 illustrates the rate of rise of N_e , the total electron density, compared to the integrated beam electron source, N_b , for 14 MW co- and counter- shots. During the first 200 ms, $\partial N_e / \partial t$ is approximately equal to the rate of beam electron input, $\partial N_b / \partial t$, for the co-injected shots, but it is 1.5-2.5 times higher in the counter-injected shots, suggesting an enhancement of the electron influx from the wall. There is a substantial difference in the magnitude and poloidal profile of the H_α signal (see Fig. 5.7) between co- and counter-injection, suggesting a substantial influence of the direction of injection on the edge conditions.

Charge exchange, first-orbit and shine-thru losses were calculated to determine their contribution to the difference in \dot{N}_e between co- and counter-injection. The fraction of power loss, indicative of the fraction of particle loss, is plotted versus \bar{n}_e in Fig. 5.8, for different tangency radii, corresponding to the inner and outer beam sources lines of sight, and different direction of injection (co: $R_T > 0$; counter: $R_T < 0$).

The first orbit losses are higher in counter-injected shots, while charge exchange and shine-thru losses are almost independent of direction of injection. But since the final \bar{n}_e in counter-shots is 10-30 % higher than it is in co-shots, at fixed P_b , the calculated total losses differ only by a few percent between co- and counter-injection and cannot account for the different electron density time histories observed in the experiments.

The VB diagnostic was used to determine the density of the light impurities, principally carbon. The metal content, evaluated from the PHA measurements, was small in all discharges (metal contribution to $Z_{eff}, Z_{met} \sim 0.3$), except for the low current co-injection shots, where $Z_{met} = 0.6-0.8$. No information was available on the radial distribution of the impurities; therefore Z_{eff} and Z_{met} are assumed constant in our analysis. The PHA value of Z_{eff} is larger by about 10-30 % for counter- than co-injected shots, which together with the data given in Fig. 5.1, suggests that the higher \bar{n}_e and lower $T_i(0)$ for counter- than co-injection could be associated with larger impurity accumulation. However, VB values of Z_{eff} , which are considered more accurate than the PHA values, do not support this explanation.

The partition of the stored energy among the different plasma components is summarized in Table 5.3. $W_j \equiv 3/2 n_j T_j + m_j n_j v_{\phi j}^2 / 2$ is the energy associated with plasma species j and calculated from kinetic measurements. The total energy confinement time, $\tau_E = \sum_j W_j / (P_b + P_{OH})$, is plotted in Fig. 5.9 for all the shots. The magnitude of τ_E is in the range $1.5 - 2 \tau_{Gold84}$, with $\tau_{Gold84} = 0.044 P_{(b+OH)}^{0.5} I_p R^{1.75} a^{-0.37}$, [83], for

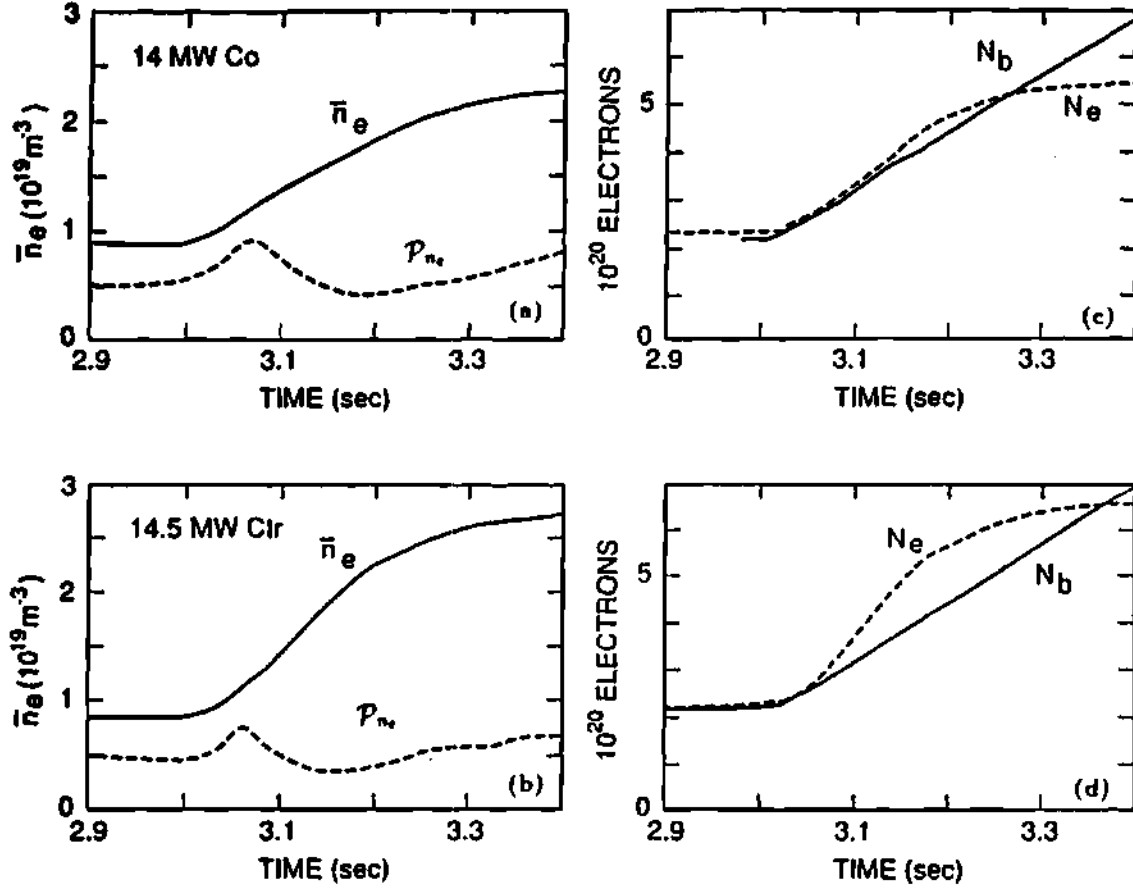


Figure 5.6: (a) Time histories of the line averaged density, \bar{n}_e , (—) and of the density peakedness, P_{ne} , (- - -) during co-injection of 14 MW (Shot 37356); (b) as (a) but during counter-injection of 14.5 MW (Shot 37358); (c) time histories of time integrated number of beam particles injected, N_b ($\times 10^{-20}$), (—) and of the integrated electron density, N_e ($\times 10^{-20}$), (- - -), for Shot 37356; (d) as (c) but for Shot 37358.

(Shots at $I_p = 1.1 MA$, $B = 4.75 Tesla$).

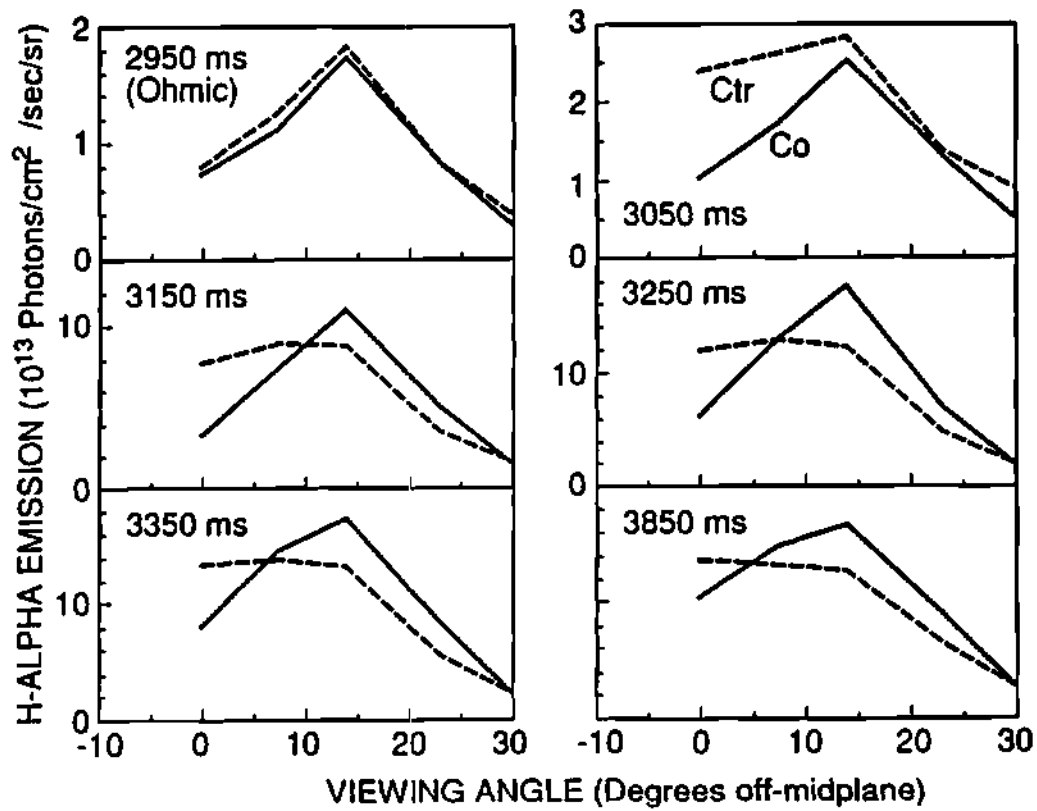


Figure 5.7: Evolution of the H-alpha emission profile during co- (—) and counter-injection (- - -), indicating a modification of the edge transport.

(Shots 37309 and 37313)

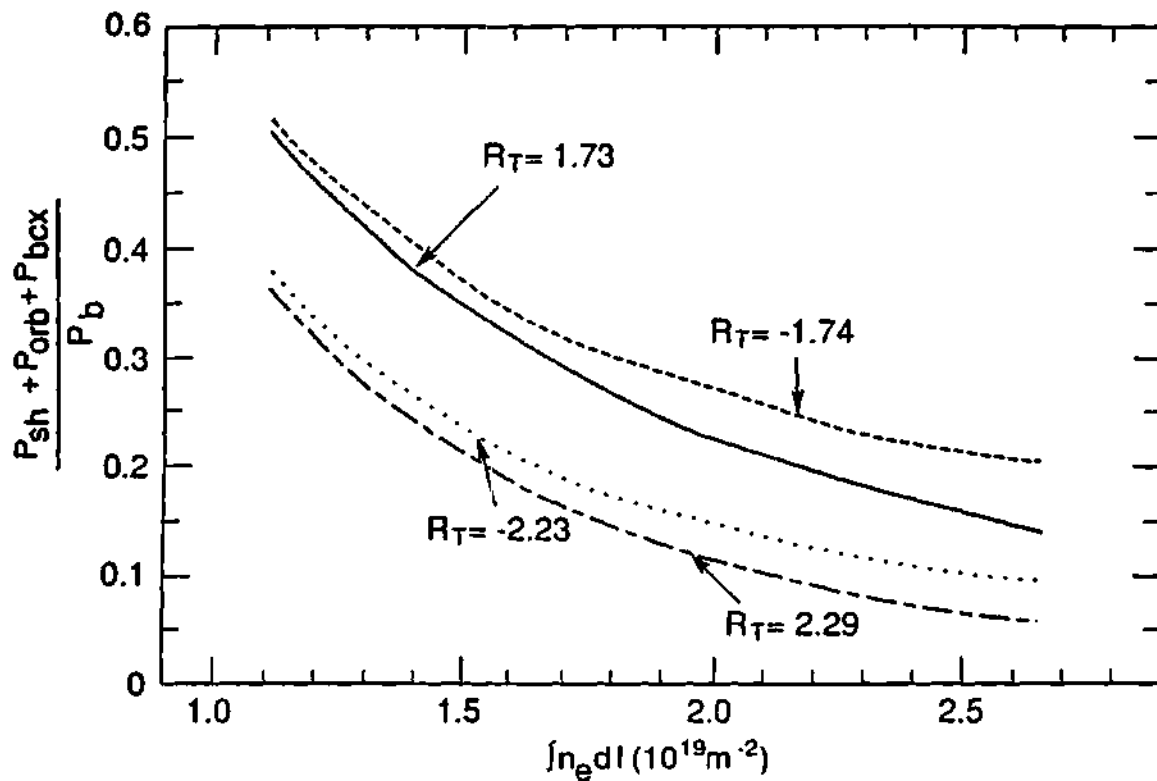


Figure 5.8: Fraction of power losses due to shine-thru (sh), first-orbit losses (orb) and beam charge-exchange (bcx) versus \bar{n}_e , for the most perpendicular ($|R_T| \sim 1.73$ m) and the most tangential ($|R_T| \sim 2.25$ m) beam sources. $R_T < 0$ indicates counter-injection.

the higher current shots, and $1 - 1.7 \tau_{Gold84}$ for the lower current ones. The thermal energy confinement time, τ_{Eth} is $\sim \tau_{Gold84} \pm 15\%$ and it shows a correlation with $\tau_{\phi th}$ (see Fig. 5.10). No correlation is observed between τ_E and $\tau_{\phi tot}$.

(A)	$I_p = 1.0 \times 10^6$		$I_p = 1.1 \times 10^6$		$I_p \geq 1.7 \times 10^6$	
(ms)	co	counter	co	counter	co	counter
W_e/P_b	19 - 25	~ 22	20 - 25	40 - 30	60 - 30	65 - 35
W_{ith}/P_b	~ 20	15 - 20	15 - 26	30 - 20	52 - 44	40 - 34
W_{fi}/P_b	~ 90	~ 58	92 - 80	70 - 60	78 - 55	72 - 50

Table 5.3: Kinetic energy stored in the electrons, 'e', thermal ions, 'i th', and fast ions, 'fi', normalized with respect to the input power (ms). When a range of values is given they correspond to : lower $P_b \rightarrow$ higher P_b for $I_p \geq 1.1 MA$; lower $B_t \rightarrow$ higher B_t for $I_p = 1 MA$.

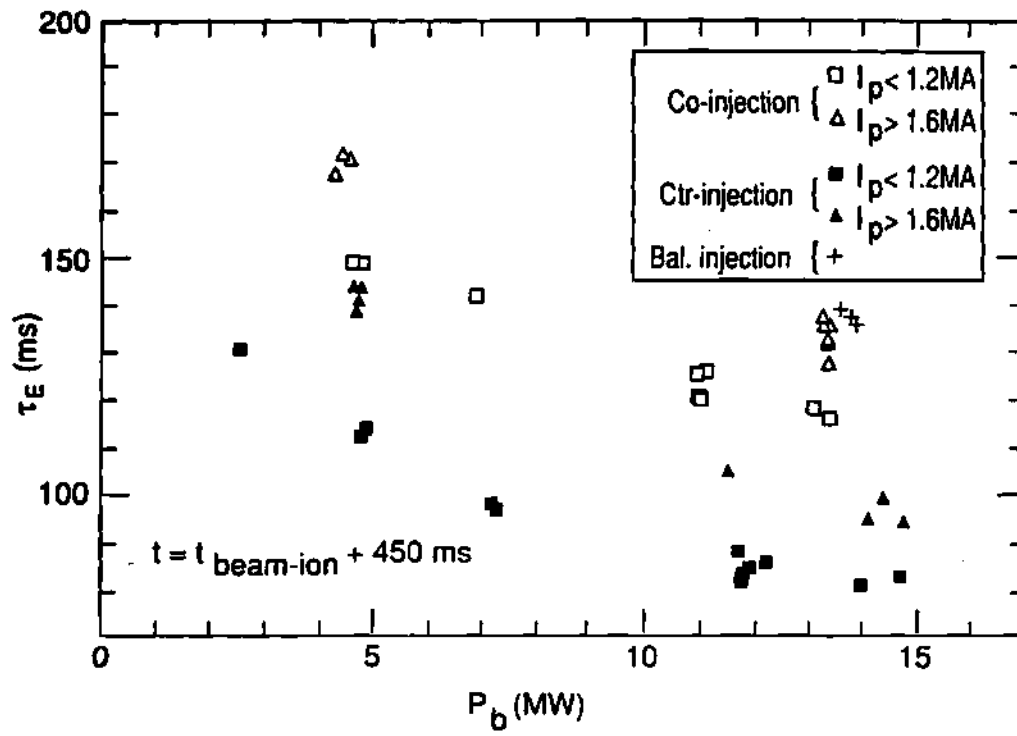


Figure 5.9: Energy confinement time, τ_E , versus injected power, P_b .

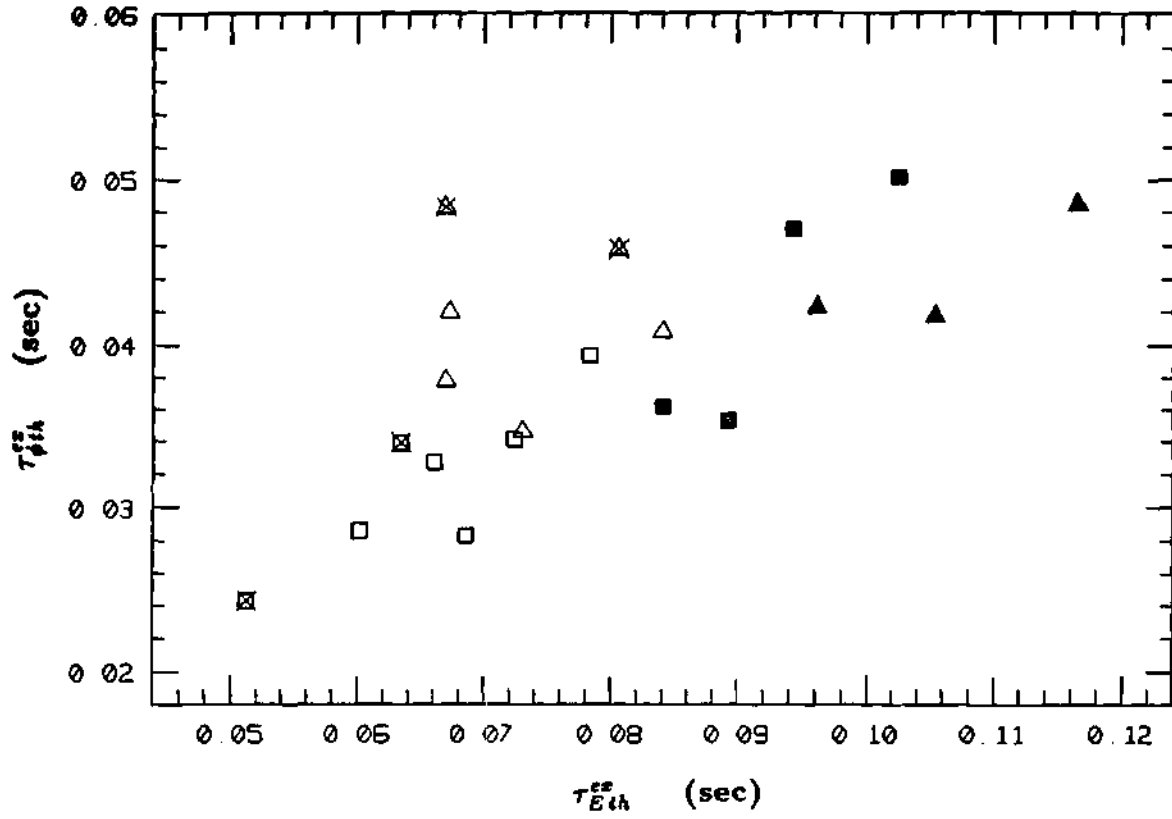


Figure 5.10: Experimental thermal momentum confinement time, $\tau_{\phi th}^{ex}$, versus energy confinement time, $\tau_{E th}^{ex}$. (Δ : co-injection shots at $I_p = 1.1-1.7$ MA; \blacktriangle : co-injection shots at $I_p = 1.7-1.8$ MA; \square : counter-injection shots at $I_p = 1.1-1.7$ MA; \blacksquare : counter-injection shots at $I_p = 1.7-1.8$ MA; \times : $B < 4$ Tesla).

Chapter 6

COMPARISON OF THEORY AND EXPERIMENT

This Chapter contains the comparison between the theoretical predictions of momentum confinement properties (momentum flow, momentum confinement time, momentum diffusivity and toroidal velocity) with the corresponding experimental quantities measured in Exp.44.

6.1 Gyroviscous theory

The gyroviscous theory embodied in Eqs. (3.20) - (3.22) was applied to the analysis of Exp.44, making use of experimental data to evaluate the parameters entering these formulas. Two different models for summing over ion species to obtain an effective plasma gyroviscous torque are examined, corresponding to the expressions for \hat{Z} , given by Eqs. (3.26) and (3.24).

Case $\hat{Z} = \bar{Z} \equiv Z(Z-1)/(Z_{eff}-Z_{met}-1)$, Eq.(3.26) - A comparison of theoretical (Eq.(3.22)) and experimental central rotation velocities for all the shots in Exp.44 is given in Fig. 6.1, and a similar comparison of theoretical (Eq.(3.21)) and experimental momentum confinement times is given in Fig. 6.2. The agreement is reasonably good, although there is a general tendency to overpredict τ_ϕ for the counter-injection shots and to underpredict it for the co-injected shots. The VB values of Z_{eff} , which were similar for co- and counter-injection, were used to evaluate τ_ϕ^{gv} . If the PHA values of Z_{eff} , which were larger for counter- than co-injection were used, the predicted values of τ_ϕ^{gv} for counter-injection would be reduced relative to the τ_ϕ^{gv} for co-injection, improving the agreement with experiment. A value $\tilde{\Theta}=1.5$ was found to provide a good fit of the gyroviscous formulas to the data, which implies the assumption of $O(\epsilon)$

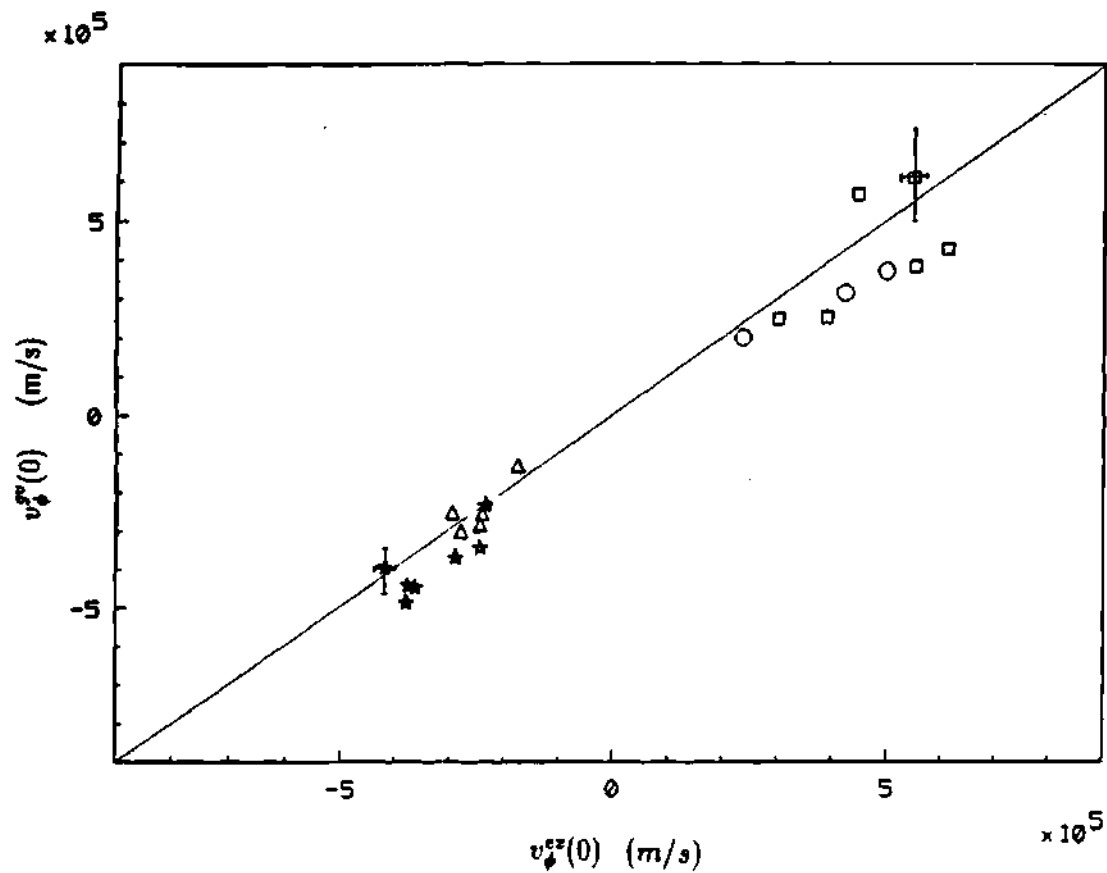


Figure 6.1: Comparison of the toroidal central velocity predicted by the gyroviscous theory ($v_{\phi}^{gv}(0)$) with the experimental measurements ($v_{\phi}^{ex}(0)$). (\square : co-injection shots at $I_p = 1-1.1$ MA; \circ : co-injection shots at $I_p = 1.7-1.8$ MA; \triangle : counter-injection shots at $I_p = 1-1.1$ MA; \star : counter-injection shots at $I_p = 1.7-1.8$ MA).

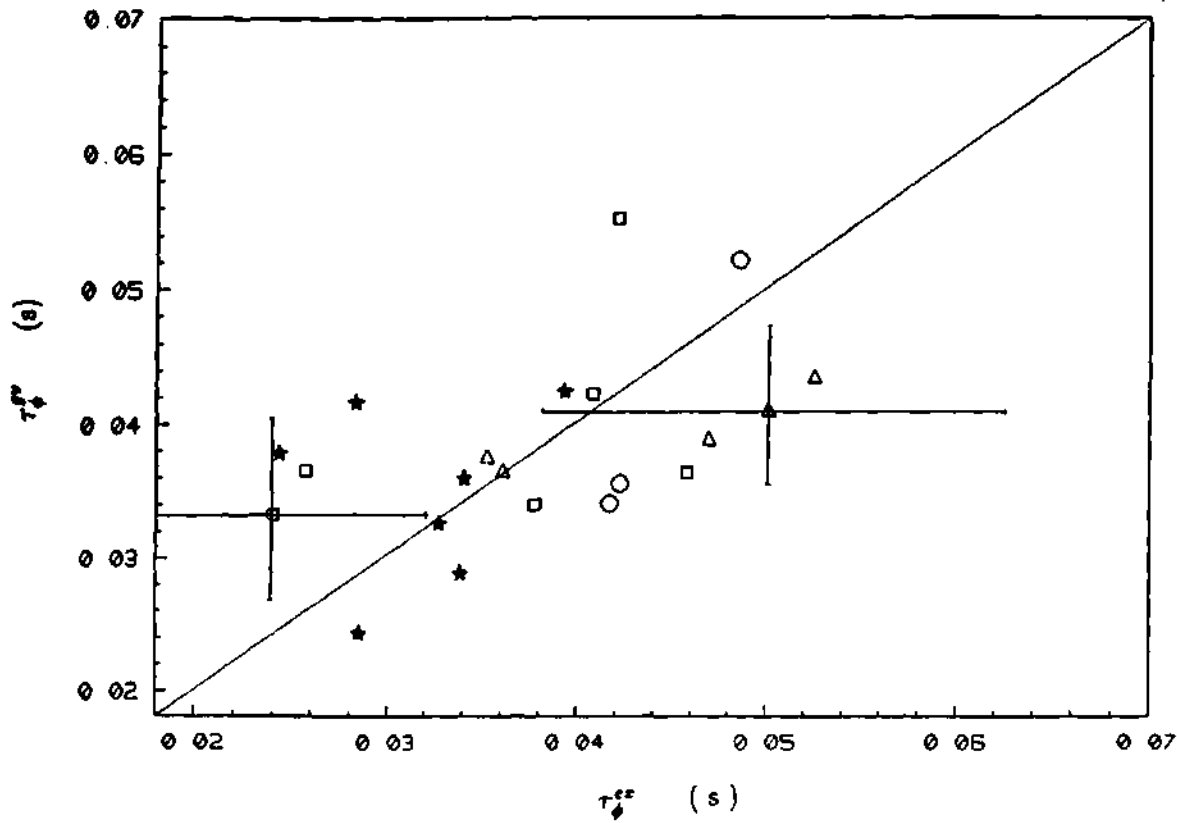


Figure 6.2: Comparison of the experimental, τ_{ϕ}^{ex} , and the gyroviscous, τ_{ϕ}^{gv} , momentum confinement times. (\square : co-injection shots at $I_p = 1.1-1.7$ MA; \circ : co-injection shots at $I_p = 1.7-1.8$ MA; \triangle : counter-injection shots at $I_p = 1.1-1.7$ MA; \star : counter-injection shots at $I_p = 1.7-1.8$ MA).

poloidal asymmetries for the impurities, if all of the gyroviscous damping is provided by the impurities. The possibility of $O(\epsilon)$ poloidal asymmetries in TFTR is discussed in Chapter 8.

Next, we determine if the dependences of the momentum confinement time on $T_i(0)$, $\bar{Z}(Z_{eff})$ and B predicted by the gyroviscous theory are consistent with the data. It does not suffice to merely plot the experimental τ_ϕ^{ex} against each of these variables, because there may be a correlation among the value of two or more of the variables appearing in Eq.(3.21). To account for the possibility of such correlations, we will divide the experimental τ_ϕ^{ex} by Eq.(3.21), but with the variable whose dependence is to be checked suppressed, and plot the resulting ratio (or its inverse) against the suppressed variable. If the dependence upon the suppressed variable predicted by Eq.(3.21) is consistent with the data, then the resulting plot should consist of points all falling on the 45° line. For example, the ratio

$$T_i^{gv}(0) = \frac{eBR_o^2\bar{Z}}{\tau_\phi^{ex}} \frac{n_{eth}(0) h_{nvT}}{n_e(0) h_{n_{th}T}\bar{\Theta}} \quad (6.1)$$

should plot as a straight line against $T_i(0)$. Similarly the quantities:

$$\bar{Z}^{gv} = \frac{\tau_\phi^{ex} T_i(0) n_e(0) h_{n_{th}T}\bar{\Theta}}{eBR_o^2} \frac{1}{n_{eth}(0)h_{nvT}} \quad (6.2)$$

and

$$B^{gv} = \frac{\tau_\phi^{ex} T_i(0) n_e(0) h_{n_{th}T}\bar{\Theta}}{eR_o^2\bar{Z}} \frac{1}{n_{eth}(0)h_{nvT}} \quad (6.3)$$

should plot as straight 45° lines against \bar{Z} and B , respectively.

The quantities $T_i^{gv}(0)$ and \bar{Z}^{gv} are plotted against $T_i(0)$ and \bar{Z} , respectively in Figs. 6.3 and 6.4 for all the shots in Exp.44. The quantity B^{gv} is plotted against B in Fig. 6.5 for the more limited set of data points in the B scan. The parametric dependence predicted by Eq.(3.21) is consistent with the data for $T_i(0)$ and not inconsistent with the data for $\bar{Z}(Z_{eff})$, as shown in Figs. 6.3 and 6.4, respectively. The parametric dependence on B predicted by Eq.(3.21) is not so evident in Fig. 6.5.

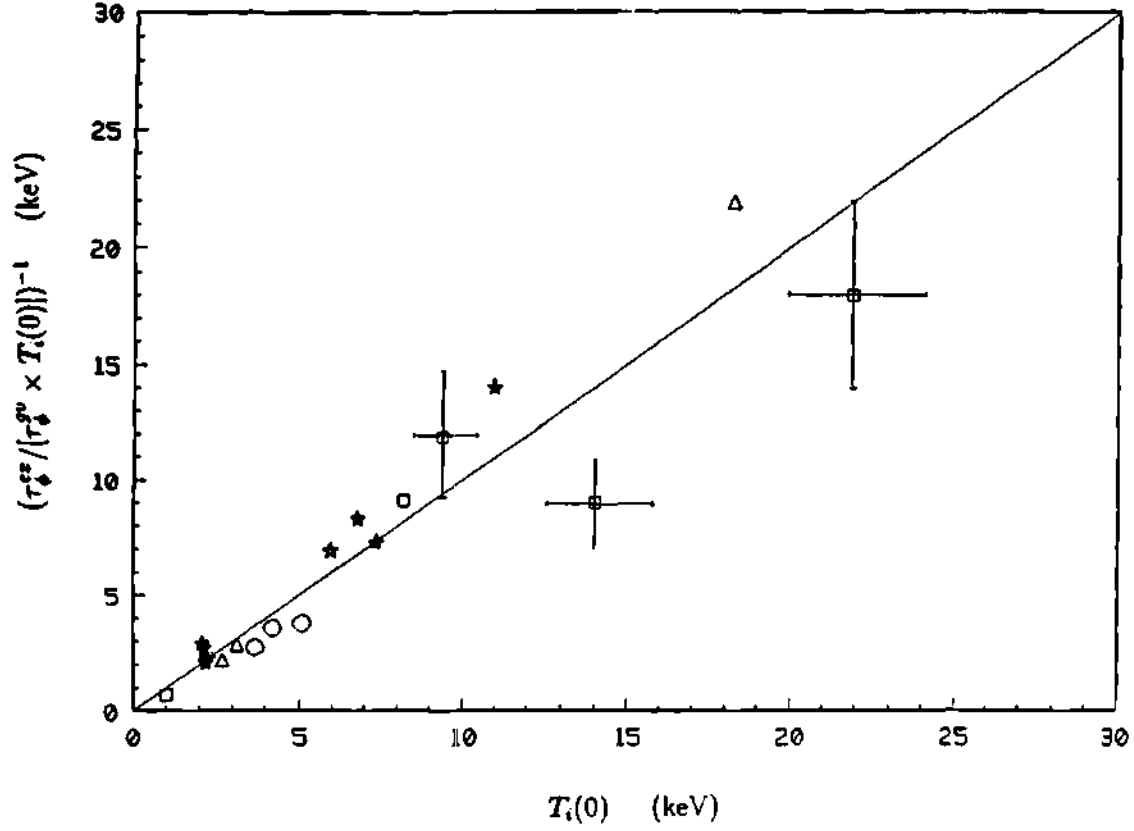


Figure 6.3: Scaling of the experimental momentum confinement, τ_{ϕ}^{ex} , with the central ion temperature, $T_i(0)$. (\square : co-injection shots at $I_p = 1.1$ MA; \circ : co-injection shots at $I_p = 1.7-1.8$ MA; \triangle : counter-injection shots at $I_p = 1.1$ MA; \star : counter-injection shots at $I_p = 1.7-1.8$ MA).

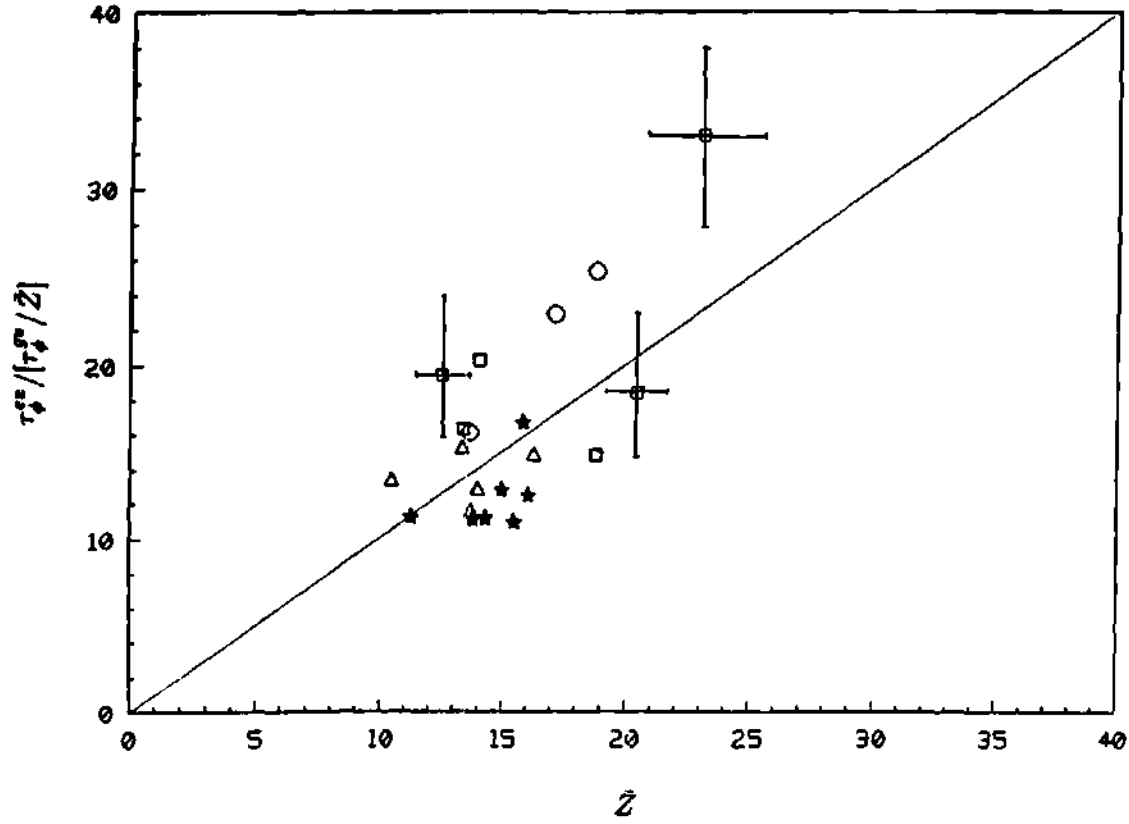


Figure 6.4: Scaling of the experimental momentum confinement, τ_{ϕ}^{ex} , with the parameter \bar{Z} . (\square : co-injection shots at $I_p = 1.1-1.7$ MA; \circ : co-injection shots at $I_p = 1.7-1.8$ MA; \triangle : counter-injection shots at $I_p = 1.1-1.7$ MA; \star : counter-injection shots at $I_p = 1.7-1.8$ MA).

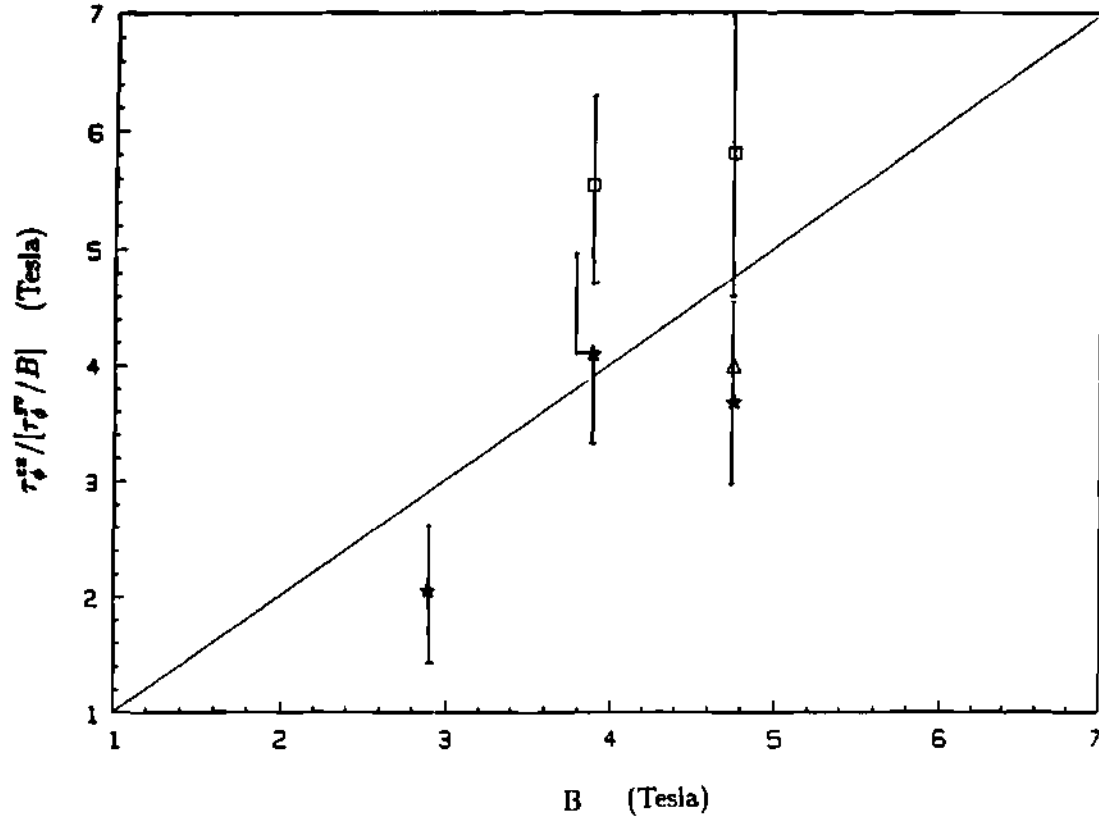


Figure 6.5: Scaling of the experimental momentum confinement, τ_ϕ^{ex} , with the magnetic field, B . (\square : co-injection shots at $I_p = 1-1.1$ MA; \circ : co-injection shots at $I_p = 1.7-1.8$ MA; \triangle : counter-injection shots at $I_p = 1-1.1$ MA; \star : counter-injection shots at $I_p = 1.7-1.8$ MA).

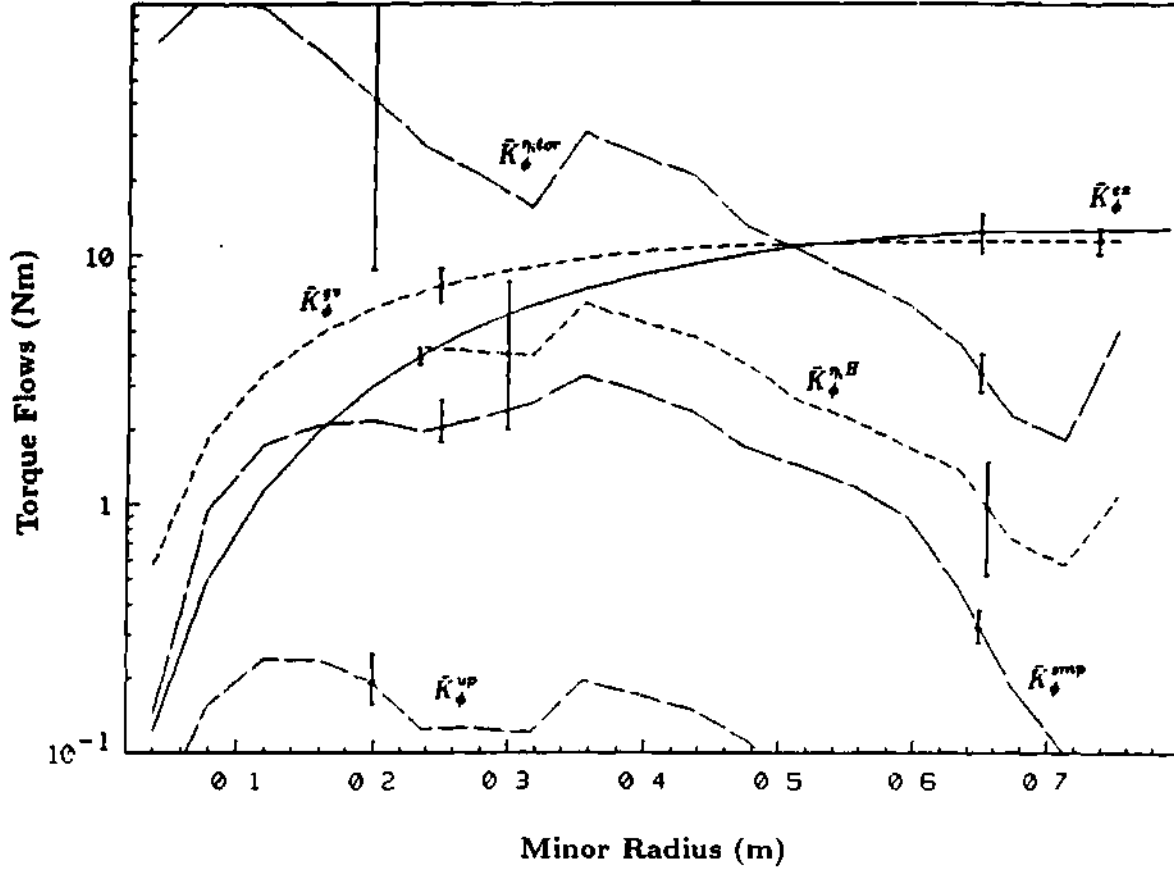


Figure 6.6: Comparison of experimental torque flow, K_{ϕ}^{ex} , with the theoretical predictions of the gyroviscous theory (gv), of the stochastic magnetic perturbation theory (smp), of the untrapped particle modes theory (up) and of the ion temperature gradient driven modes theory (η_i) for Shot 37309.

The torque flow, K_{ϕ}^{gv} , consistent with the above gyroviscous theory predictions, given by Eq.(3.20), is compared with the same quantity constructed from the experimental data in Fig. 6.6. The comparisons were similar for all shots examined. There is a significant overprediction in the center, but reasonable agreement in the outer regions. The same constant $\tilde{\Theta} = 1.5$ was used in this prediction, as in the previous predictions, and the disagreement in shape could indicate a radial dependence of $\tilde{\Theta}$.

Case $\hat{Z} = Z_{eff}$, Eq.(3.24). - Figure 6.7 shows the comparison between experimental and theoretical central velocity, as predicted by Eq.(3.22) using the $\hat{Z} = Z_{eff}$ model. A value of $\tilde{\Theta} = 0.4$ was used in this case to obtain a good fit of $v_{\phi}^{gv}(0)$ to the data, which implies the assumptions $\tilde{\Omega}_{\phi js} \sim O(0.2\epsilon)$ or/and $\tilde{\Omega}_{\phi jc}\tilde{n}_{js} \sim O(0.2\epsilon)$. The $v_{\phi}^{gv}(0)$ formula reproduces the trend of variation of the experimental data.

The scatter in the comparison of τ_{ϕ}^{gv} , $T_i^{gv}(0)$, B_{gv} and \tilde{Z} , with the experimental data are larger with the $\hat{Z} = Z_{eff}$ model than with the $\hat{Z} = Z(Z-1)/(Z_{eff}-Z_{met}-1)$ model for summing over ion species. This suggests the dominance of impurities in determining the gyroviscous torque.

The neoclassical viscosities derived by Hsu and Sigmar^[73] and by Stacey and Neeley^[27] lead to momentum confinement times with the same parametric dependences and a similar dependence on poloidal asymmetries as for the gyroviscosity. Because the Hsu-Sigmar and Stacey-Neeley results are of a collisional origin and were derived for highly collisional ions, while gyroviscosity is of a non-collisional origin and may therefore be expected to be independent of collisionality, gyroviscosity would seem to be the more plausible explanation. However, the predictions of the Hsu-Sigmar and Stacey-Neeley formulas would reproduce the gyroviscous predictions shown in Figs. 6.1 - 6.5, subject to the same qualifications regarding $\tilde{\Theta}$.

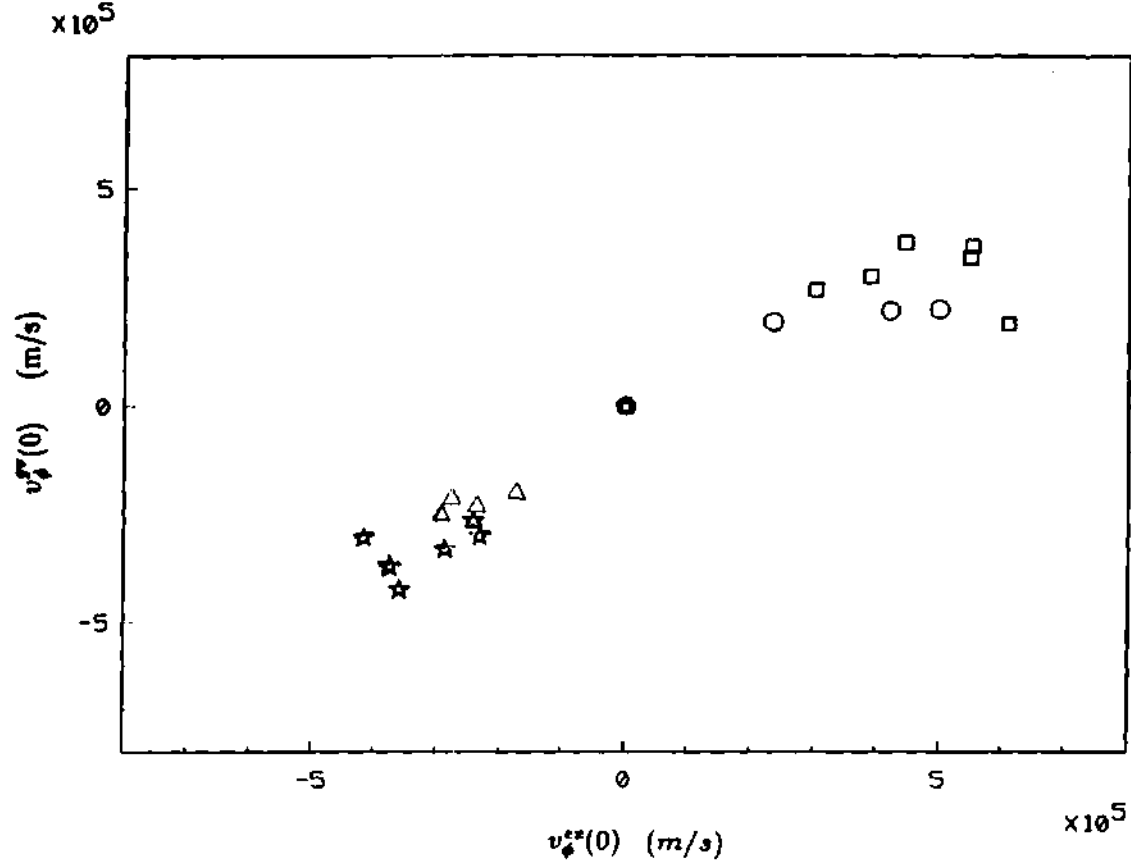


Figure 6.7: Comparison of the toroidal central velocity ($v_{\phi}^{gv}(0)$) predicted by the $\hat{Z} = Z_{eff}$ gyroviscous theory model with the experimental measurements ($v_{\phi}^{ex}(0)$). (\square : co-injection shots at $I_p = 1-1.1$ MA; \circ : co-injection shots at $I_p = 1.7-1.8$ MA; \triangle : counter-injection shots at $I_p = 1-1.1$ MA; \star : counter-injection shots at $I_p = 1.7-1.8$ MA).

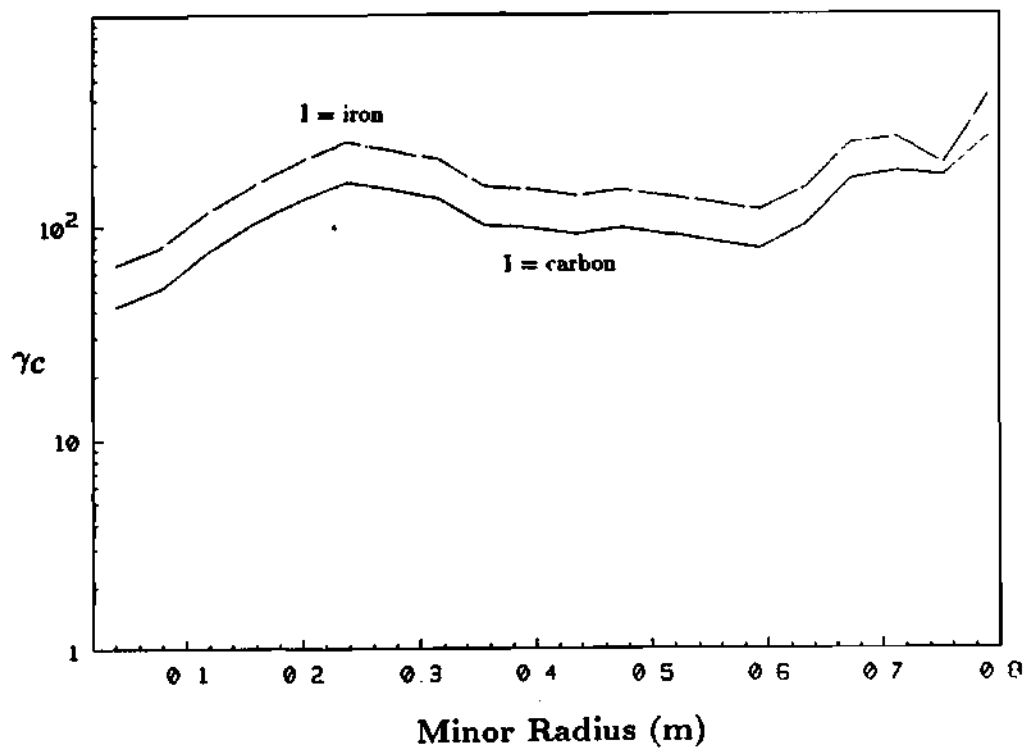


Figure 6.8: Evaluation of the parameter γ_c from Eq.(3.37) for Shot 37309, needed to match experimental data (Shot 37309) with $I = \text{carbon (C)}$ and $I = \text{iron (Fe)}$.

6.2 Ware's cold ions theory

In order to evaluate Ware's expression for the torque flow, Eq.(3.32), the cold ion density and temperature must be known. Since neither theoretical expressions nor measurements of these quantities are available, we proceeded by determining the magnitude of the ratio γ_c , in Eq.(3.37), that is required to fit that expression to the experimental data ($K_\phi^{cold}(r) = K_\phi^{ex}(r)$). This value of γ_c is shown in Fig. 6.8. The collision frequency ν_{cI} , Eq.(3.33), has been evaluated assuming carbon (C) and iron (Fe), alternatively, as impurity 'I'. In both cases, the required value of this ratio is well above any value that is plausible. Similar results were found for the other shots.

6.3 Anomalous torque flows

The torque flows, $K_\phi(r)$, predicted by the various anomalous theories described in Section 3.3 have been compared with the torque flow interpreted from the local momentum balance measurements and constructed according to Eq.(2.13), for each shot of the rotation experiment. A representative shot (37309) was chosen to illustrate the results, which were similar for all shots in Exp. 44.

There is a substantial disagreement in radial profile and in magnitude between each of the anomalous theoretical torque flows and the experimental torque flow, as can be seen in Fig. 6.6. The predicted torque flow due to untrapped particle modes, K^{up} , Eq.(3.55), severely underestimates (1-2 orders of magnitude) the experimental torque flow everywhere except very near the center of the plasma.

The predicted torque flow due to stochastic magnetic perturbations, K^{stp} , Eq.(3.45), is in reasonable agreement with experiment near the center of the discharge, but decreases with plasma radius for $r/a \geq 0.5$ and severely underpredicts (~ 2 orders of magnitude) the experimental torque flow near the plasma edge. $C_1 = 1$ and $\gamma = 2$ have been used to evaluate χ_ϕ^{stp} .

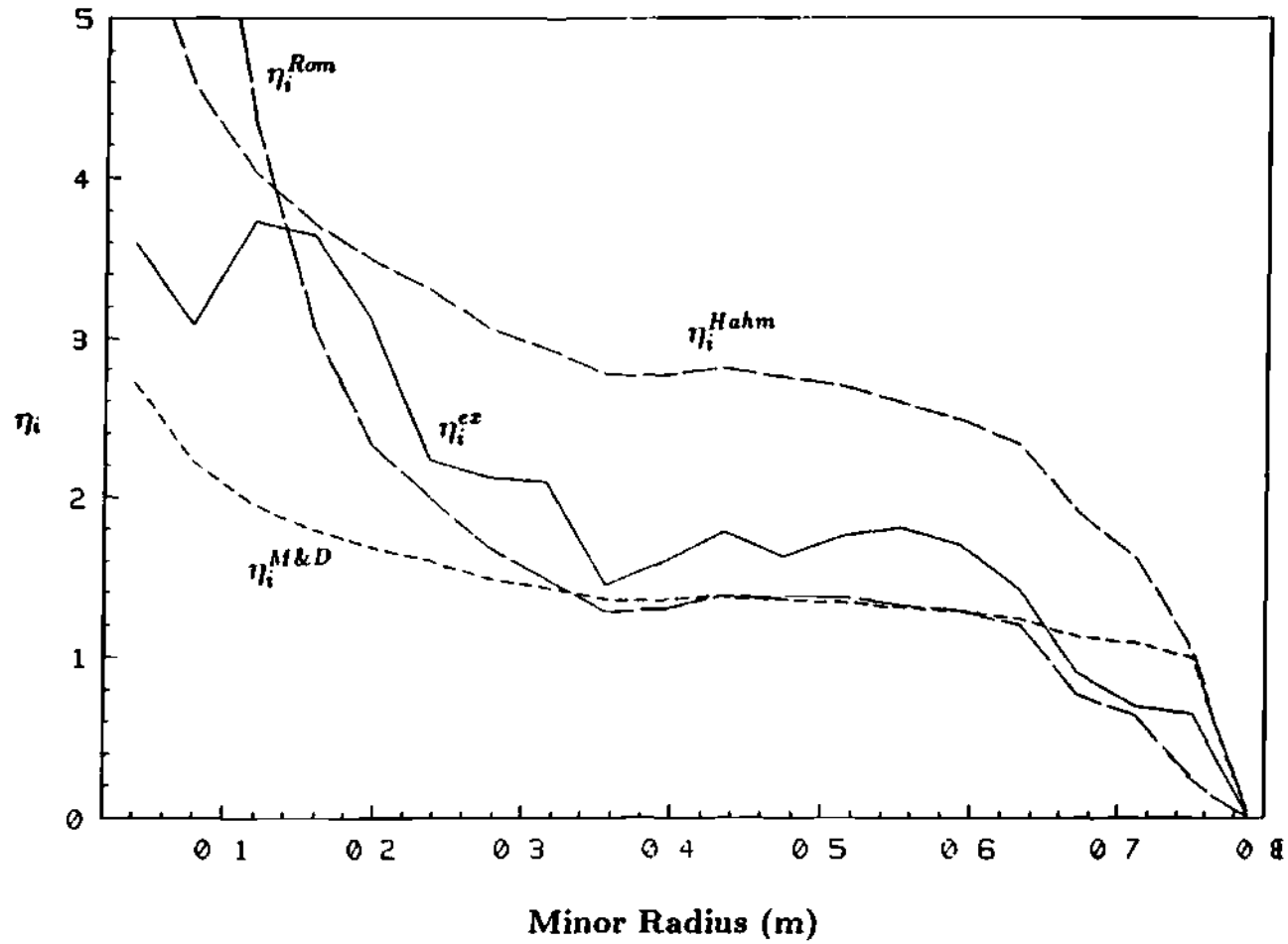


Figure 6.9: Comparison of the experimental η_i^{ex} with the theoretical η_i^{Rom} , η_i^{Hahm} and $\eta_i^{M\&D}$, for Shot 37313.

The ' $\eta_i H$ ' torque flow is computed using $\chi_\phi^{\eta_i} = \chi_i^{\eta_i H}$, Eq.(3.52) in Eq.(3.46), in conjunction with Romanelli's formula, Eq.(3.50), for η_i^{cr} . For $r \leq 0.1 - 0.2$ m, the experimental η_i is smaller than η_i^{Rom} and the ITG flux vanishes. For $r \geq 0.1 - 0.2$ m, up to the plasma edge, η_i^{ex} exceeds the theoretical critical value and the difference ($\eta_i^{ex} - \eta_i^{Rom}$) remains confined in the range 0-1.2. The ' $\eta_i H$ ' momentum flux is absent in the center of the plasma, becomes comparable in magnitude to the experimental flux for $0.3 \leq r \leq 0.5$, and then drops to a small fraction of the experimental flux towards the edge.

Figure 6.9 illustrates the radial profiles of η_i^{ex} and those of several theoretical expressions of η_i^{cr} . The error bars affecting the evaluation of η_i , and subsequently of $\chi_i^{\eta_i}$, are relatively large. They were estimated by performing a series of 100 transport analysis varying the input plasma parameters within their ranges of uncertainty by Monte Carlo sampling a Gaussian error distribution [16]. The error bars on the computed and measured η_i (and on the other figures) represent the standard deviation of the calculated η_i . The correlation between the experimental and the theoretical η_i has also been discussed in Ref. [16].

Among the other expressions for the diffusion coefficient discussed in Section 3.3.2, $\chi_i^{\eta_i tor}$, Eq.(3.49), predicts the smallest diffusion coefficient. The torque flow evaluated assuming $\chi_\phi^{\eta_i} = \chi_i^{\eta_i tor}$ in Eq.(3.46) is indicated by $K_\phi^{\eta_i tor}$ in Fig. 6.6; it overestimates the experimental flux by an order of magnitude in the center and underestimates it by a factor of $\sim 2-4$ for $r > 0.6$ m.

While the different momentum diffusivities based on the ITG theory fail to reproduce the experimental data, $\eta_i^{ex} \sim \eta_i^{cr}$ over most of the plasma region, both for Romanelli's η_i^{cr} , Eq.(3.50) [38], and for Hahm's η_i^{cr} , Eq.(3.51) [39] (having assumed $b_s = 0.1$), as shown in Fig. 6.9. These results would support the hypothesis that ITG transport is regulated by marginal stability. However, more recent experiments have provided firm evidence that ion transport is not regulated by marginal stability [15]. Also the appropriateness of the transport coefficients $\chi_\phi^{\eta_i tor}$, Eq.(3.49), and

$\chi_i^{\eta_i H}$, Eq.(3.52), which were derived for η_i well above threshold, are questionable for the experiments analyzed in this paper.

6.4 Anomalous momentum diffusivities

Starting from the torque flux, K_ϕ^{ex} of Eq.(2.13), interpreted from the local momentum balance measurements, it is possible to construct an experimental momentum diffusivity, but in order to do so it is necessary to make an assumption about the mathematical form for of K_ϕ^{ex} . The most common assumption is that it has the form:

$$\chi_\phi^{ex}(r) = \frac{K_\phi^{ex}(r)}{(2\pi)^2 R_o r m_D \frac{\partial}{\partial r} v_\phi} \quad (6.4)$$

The experimental χ_ϕ^{ex} and the anomalous χ_ϕ , constructed by using the measured plasma parameters to evaluate Eqs. (3.45), (3.49), (3.52) and (3.55) are compared in Fig. 6.10. The differences between experimental and predicted values are similar to the differences among the K_ϕ 's discussed in Section 6.3.

It is of interest, however, to examine how the parametric dependences predicted by the various theories compare with the experimental data. A regression analysis of χ_ϕ^{ex} in the range $0.25 < \frac{r}{a} < 0.7$ produced the following parametric dependence [16]:

$$\chi_\phi^{ex} \propto C B^{0.16} I_p^{-0.59} P_b^{0.23} \left(\frac{r}{a}\right)^{1.22} \quad (6.5)$$

where $C = 1$ and 1.15 for co- and counter-injection, respectively.

A similar regression analysis, using as data points the values of χ_ϕ predicted by the different anomalous theories and as variables $(B, I_p, P_b, r/a)$ produced a correlation able to fit the experimental data no better than 40%. This large range of scatter of the data around the fitting curve leads to the conclusion that this set of parameters cannot properly represent the parametric dependence of the theoretical χ_ϕ 's.

Since the magnitude of the χ_ϕ^{theo} is comparable to the χ_ϕ^{ex} only over a small range of the minor radius, we checked if χ_ϕ^{ex} correlates with the following factors, representing

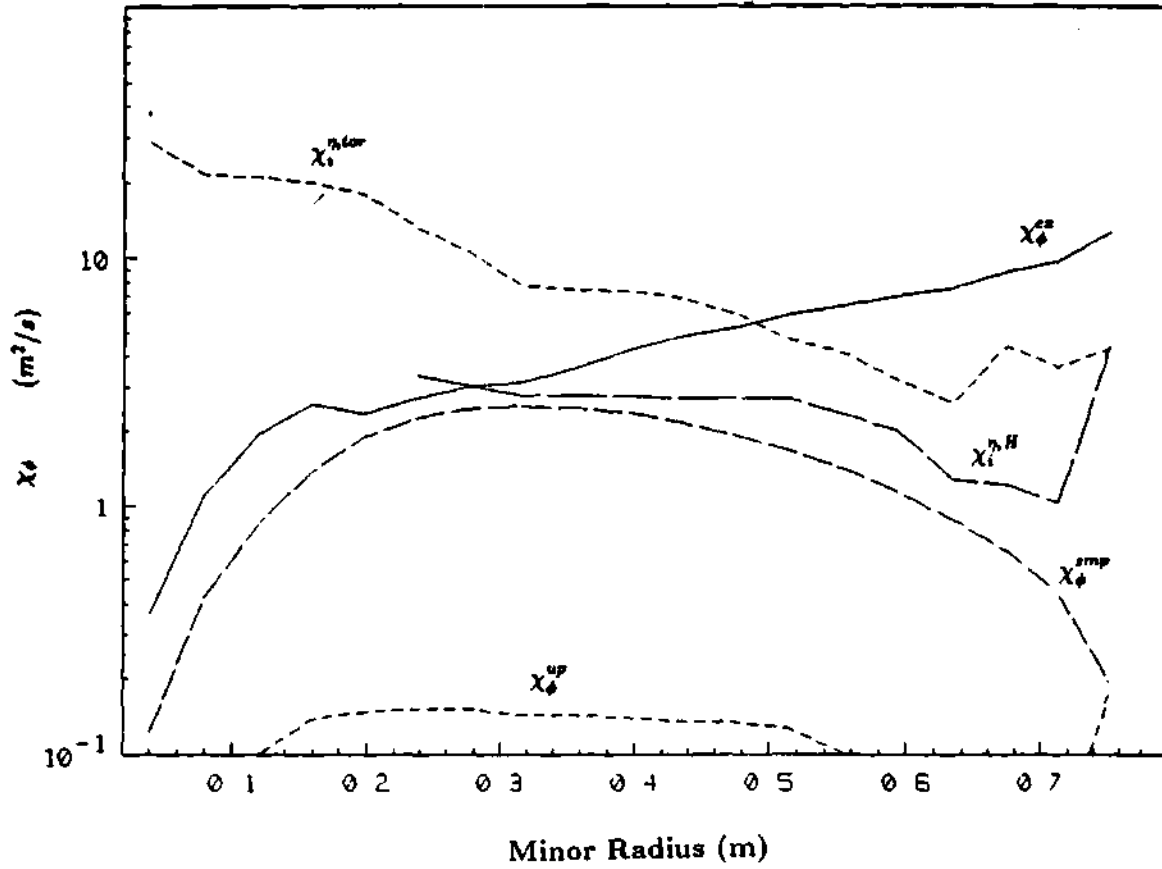


Figure 6.10: Comparison of momentum diffusivities, χ_ϕ , for Shot 37513 (counter-injection of 12.7 MW at $I_p = 1$ MA and $B_t = 2.9$ tesla). Legend: ex = experimental; smp = from Eq.(3.45); ηH = from Eq.(3.52); η_{tor} = from Eq.(3.49); up = from Eq.(3.55).

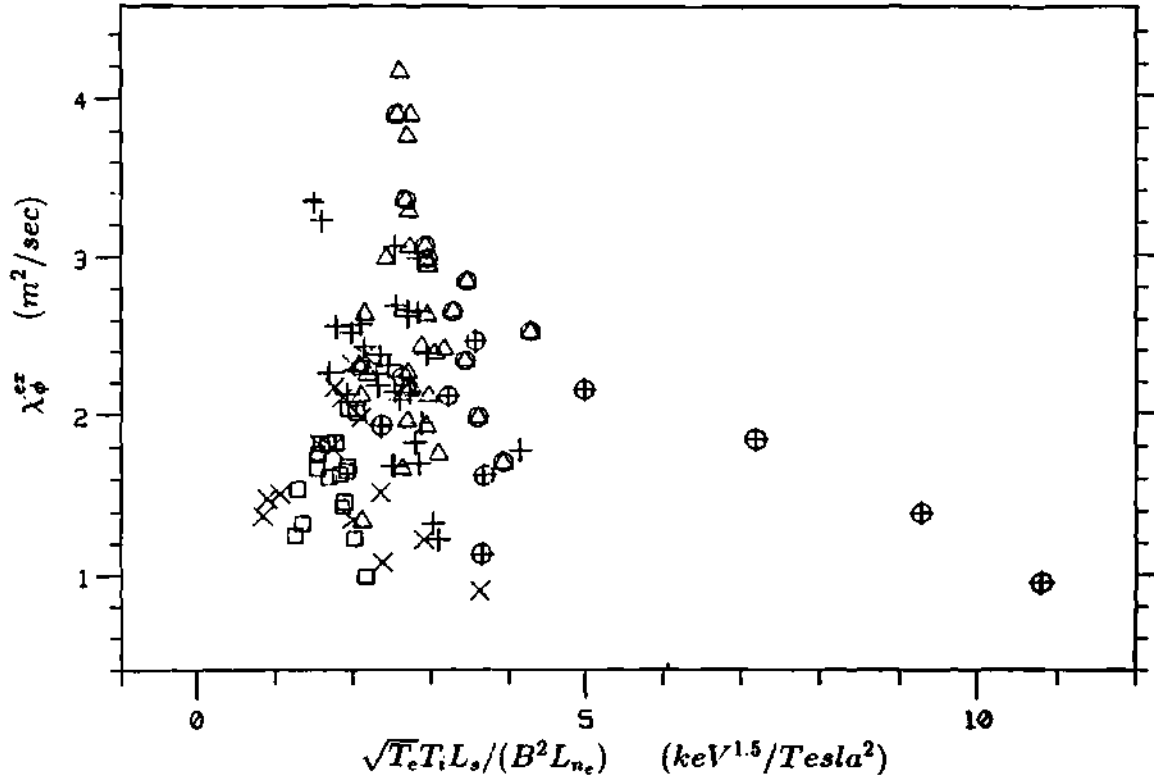


Figure 6.11: Scaling of χ_{ϕ}^{ex} with the parameter $\sqrt{T_e T_i} L_s / (B^2 L_{ne})$ in the range $r=0.2-0.4$ cm. (+ : co-injection shots at $I_p = 1-1.1$ MA; x: co-injection shots at $I_p = 1.7-1.8$ MA; Δ : counter-injection shots at $I_p = 1-1.1$ MA; \square : counter-injection shots at $I_p = 1.7-1.8$ MA; O: $B < 4$ Tesla).

the χ_ϕ 's given by Eqs. (3.45), (3.49), (3.52) and (3.55), in the range $r = 0.2 - 0.4, m$:

$$\frac{\epsilon^2 T_e^{1.5}}{qRB^2}, \quad \frac{\sqrt{T_e} T_i L_s}{RB^2 L_n}, \quad \sqrt{\eta_i - \eta_i^{cr}} \frac{T_e^{1.5} L_s}{RB^2 L_n}, \quad \frac{T_e^{2.5}}{L_n B^2 T_i} \quad (6.6)$$

The comparison with the second of the four factors is shown in Fig. 6.11. Similar results were found for the other three correlation factors. We have been unable to identify any meaningful correlation between measured χ_ϕ values and the factors listed above.

Chapter 7

VARIATION ON THE FLUX SURFACE OF n_j AND $\Omega_{\phi j}$: THEORIES AND PREVIOUS EXPERIMENTS

7.1 Introduction

Ion densities and toroidal rotation frequencies can manifest observable poloidal variations on a given flux surface. Due to the role played by the magnitude of these poloidal variations in determining the magnitude of the gyroviscous torque flux, Eq.(3.16), of Hsu's and Sigmar's torque flux, Eq.(3.41) and of the torque flux due to the rotational viscosity, Eq.(3.44), this Chapter is dedicated to a review of experimental evidence and theoretical predictions of such poloidal asymmetries.

Poloidal asymmetries of impurity ion radiation have been observed at the edge and in the plasma bulk of different tokamaks [84],[85]–[89]. Several plausible explanations have been explored experimentally and theoretically to understand why the usual rapid parallel transport fails in maintaining the symmetry [90]–[26].

Asymmetries of particle sources and sinks, and interruption of transport along the field lines (which prevents the rapid reestablishment of uniform pressure on the flux surface following a perturbation in the density) are among the plausible explanations for plasma asymmetries at the edge.

MARFE phenomena [95], characterized by increased radiation and density and decreased temperature in a relatively poloidally-localized small volume at the inner edge of the plasma, have been observed on a large number of machines and attributed to a local thermal instability. Since their presence is limited to the plasma edge and does not affect the confinement properties of the bulk plasma, they will not be considered here.

Within the plasma, a residual effect of the edge processes could affect the impurities at higher ionization state, coupled through collisional ionization and radial transport to the lower ionization states. The ∇B drift was also hypothesized to be the cause of up-down asymmetry in Alcator A [85].

Several theoretical analysis have concluded that a large collision frequency between main ions and impurities (which results in a large friction force), inertial forces in strongly rotating plasmas, poloidal asymmetric particle sources and NBI momentum input can produce $O(\epsilon)$ variation of density and electrostatic potential on the flux surface.

Rotation velocity profiles in JET [17] and TFTR (see Section 5) were found to be in-out asymmetric. Simple considerations of momentum balance predict that $v_\theta \sim \beta v_{\phi j}$ originates a $\tilde{\Omega}_{\phi j} \sim \epsilon$, suggesting that this could be the origin of such experimental observations. Therefore, we review recent measurements and theoretical work related to $v_{\theta j}$ at the end of this Chapter.

7.2 Theoretical estimates of \tilde{n}_j

7.2.1 \tilde{n}_j due to friction forces

Chang and Hazeltine [90] clarified the role of the friction force in driving up-down asymmetries of ion densities, while studying the neoclassical transport problem for a non-rotating plasma, with main ion species and high Z impurity species in the collisional regime.

The parallel component of the momentum balance equation (Eq.(2.2)), where inertia, source and viscous terms have been neglected,

$$\frac{1}{n_j} \frac{\partial n_j}{\partial \theta} + \frac{e_j}{T_j} \frac{\partial \Phi}{\partial \theta} = R_{||j} \frac{r}{b_\theta p_j} \quad (7.1)$$

relates the poloidal variation of density and electrostatic potential to the friction term, which is the driving force of the asymmetries, in this case.

For the main ions, indicating $x(r, \theta) = x_0(r) + x_1(r, \theta)$, ($\langle x_1/h \rangle = 0$) :

$$\frac{r}{b_\theta p_j} R_{||i1} = \frac{m_i r \nu_{ii}}{b_\theta T_i} (v_{i1} - v_{I1})_{||} \sim \epsilon \frac{\nu_{ii} \delta_{\theta i}}{\omega_{tri}} \cos \theta \quad b_\theta \equiv \frac{B_\theta}{B} \quad (7.2)$$

where $\omega_{tri} = v_{thi}/(qR)$; $\delta_{\theta i} = \rho_{\theta i}/L_{pi}$. It follows that the ordering $\delta_{\theta i} \sim \omega_{tri}/\nu_{ii}$ leads to $\tilde{n}_{si} \sim \Phi_0 \tilde{\Phi} e/T_e \sim \epsilon$.

The magnitude of \tilde{n}_{Is} , not discussed by Chang and Hazeltine, but easily derivable for $j=I$ in Eq.(7.2), is:

$$\tilde{n}_{Is} = \epsilon \frac{\nu_{ii} Z_I^2}{\omega_{tri}} \delta_{\theta i} \quad (7.3)$$

It follows that the ordering $\nu_{ii} Z_I^2 \delta_{\theta i} / \omega_{tri} \sim 1$ leads to $\tilde{n}_{Is} \sim \epsilon$, in this case. This expression for the up-down poloidal asymmetry of the impurity density coincides with the first term of η_{qf} , Eq.(7.4), the expression used to fit the experimental measurements on PDX some years later.

S.W. Wong [88] reformulated the neoclassical problem of impurity transport, in which atomic physics and radial anomalous terms are included, to derive an expression for the asymmetry parameter η_{qf} , defined by: $n_I(r, \theta) = n_I(r)(1 + \eta_{qf} \sin \theta)$. The impurity transport was described by the particle continuity and momentum balance equations, Eqs. (2.1) and (2.2), with the inertia, the viscosity and the momentum source term neglected. Expressions for v_θ and $\partial \Phi / \partial \theta$ were borrowed from a previous solution of the neoclassical transport problem in non rotating plasmas [59].

An equation for $\partial n_I / \partial \theta$ was written by deriving the parallel and perpendicular impurity flows from the momentum equation and substituting them into the continuity equation, and used to obtain:

$$\eta_{qf} = \frac{2\sqrt{2}m_i R Z_I^2 \nu_{ii}}{e B_\phi} \left[\frac{1}{L_n} + (1 - \xi - \frac{1}{Z_I}) \frac{1}{L_T} \right] - \frac{A \epsilon \rho_{\theta i}}{L_T (1 + T_i/T_e)} \quad (7.4)$$

where ξ and A are parameters dependent on the ion collisional regime (and proportional to the thermal contribution to the friction force and to the poloidal variation of the potential on the flux surface, respectively).

Since $Z_I \nu_{ii} = \nu_{Ii}$, the first term in Eq.(7.4) is of the form: $q^2 R Z_I \nu_{Ii} / (\omega_{ci} L_{pi})$, equal to $d_{\nabla B} Z_I / L_{pi}$, with $d_{\nabla B}$ given by:

$$d_{\nabla B} = v_{\nabla B} \tau_{Rq} = \left[\frac{1.5 T_I(r)}{e B R Z_I} \right] \left[\frac{m_I q^2 R^2 \nu_{Ii}}{T_I(r)} \right] = \frac{1.5 q^2 R \nu_{Ii}}{\Omega_{ci}} \quad (7.5)$$

The experimentally observed asymmetry parameter in the PDX experiment described in Section 7.3.3 was in agreement with η_{qf} estimates when the main ions, that were in the transition region between the plateau and the banana regime, were assumed to be collisionless.

Hsu and Sigmar [26] have studied the particle and momentum transport in a strongly rotating ($v_{thj} \sim v_{\phi j}$), impure plasma (two ion species), in P-S regime and neglecting temperature variations. They adopt the Larmor radius expansion of the kinetic equations ($f_j = f_j^{(0)} + f_j^{(1)} + O(\delta_{\theta j}^2)$ with $f_j^{(1)} \sim \delta_{\theta j} f_j^{(0)}$), in conjunction with a moment approach. Their transport problem is described by the following set of equations:

- O(1) continuity equation (in the absence of O(1) sources, that is a realistic assumption for actual plasmas):

$$\nabla \cdot (n_j^{(0)} \vec{v}_j^{(0)}) = 0 \quad (7.6)$$

- $O(\delta_{\theta}^{-1})$ momentum equation:

$$\nabla \Phi^{-1} = \vec{v}_j^{(0)} \times \vec{B} \quad (7.7)$$

- O(1) momentum equation:

$$m_j \vec{v}_j^{(0)} \cdot \nabla \vec{v}_j^{(0)} + \nabla \ln(n_j^{(0)} T_j^{(0)}) = -e_j \nabla \Phi^{(0)} + e_j \vec{v}_j^{(1)} \times \vec{B} + (\vec{R}_j) \quad (7.8)$$

The friction term is included in the O(1) equation for impurities when

$$\Delta \equiv \delta_{\theta i} Z^2 \nu_{ii} \sqrt{2} / \omega_{ti} \sim 1.$$

In the case of $\Delta \sim \delta_{\theta i}$, the friction term is included in the higher order equation.

- odd part of the $O(\delta_\theta)$ parallel momentum equation:

$$n_j^{(0)} T_j \vec{B} \cdot \nabla \frac{n_{j-}^{(1)}}{n_j^{(0)}} + \vec{B} \cdot \nabla \Pi_{||j-}^{(1)} - 1.5 \Pi_{||j-}^{(1)} \hat{b} \cdot \nabla B - e_j n_j^{(0)} \vec{B} \cdot \nabla \Phi_-^{(1)} + B R_{||j+}^{(1)} \quad (7.9)$$

($x_j = x_{j+} + x_{j-}$, respectively up-down symmetric and up-down asymmetric parts).

- $O(1)$ and $O(\delta_\theta)$ viscosity equations (See Ref. [26]) , essentially the Braginskii tensor with corrections of the parallel viscosity due to the presence of the impurity.

From the solution of the first two equations, and from the $O(1)$ parallel projection of the $[m_j(\vec{v}_j \vec{v}_j - v^2/3 \vec{I})]$ moment equation, one derives that $\Omega_{\phi j}^{(0)}$ is a flux surface constant.

$n_j^{(0)}$ is found by solving the parallel projection of Eq.(7.2.1). In the case of $\Delta \sim \delta_{\theta i}$:

$$n_j^{(0)} = N_j(r) \exp\left(\frac{0.5 m_j v_{\phi j}^{(0)2} - e_j \Phi^{(0)}}{T_j}\right) \quad (7.10)$$

is an in-out asymmetric function, with asymmetries of magnitude $\tilde{n}_{jc} \sim \epsilon v_{\phi j}^2 / v_{thj}^2$ driven by the centrifugal force.

The FSA of Eq.(7.9), for $j=i, I$, constitute a system of equations in the poloidal variations, the solution of which gives: $v_{\theta i} \sim O(\delta_{\theta i}) \ll v_{\theta I}$. Eq.(7.9) can then be solved for the impurity species, to derive the up-down density asymmetry, driven by the parallel i-I friction, the magnitude of which is found to be $n_{I-}^{(1)} \sim \epsilon \Delta$. This result coincide with those of Chang et al. [90], Burrell et al. [93], Stacey et al. [94] and is proportional to Terry's result [85].

In the case of $\Delta \sim 1$, the $n_{I+}^{(0)}$ is strongly coupled with $n_{I-}^{(0)} \sim \epsilon$.

The transport fluxes were calculated for the strong up-down density variation case and found to be induced by parallel friction.

This “strong ordering non linear theory ($\Delta \sim 1$)” was employed in the comparison with the TEXT measurements [96]. The theoretical expectation for the impurity densities asymmetries, that is:

$$\tilde{n}_{I_s} = \frac{2\epsilon\mu Z_f^2}{1 + \mu^2 Z_f^4} \quad \mu = \frac{aD\Delta}{Z_f^2(\frac{\alpha T_e}{T_e + T_i} + \frac{T_i}{T_i})} \left[\frac{\partial}{\partial r} \ln(p_i) - \frac{T_f}{T_i Z_f} \ln(p_f) \right] \quad (7.11)$$

was found in agreement with the measurements, as shown in Fig. 7.1.

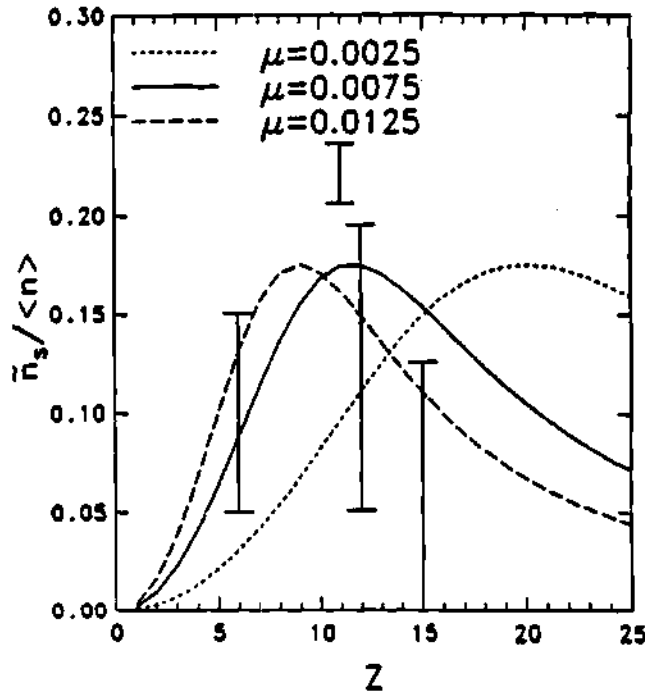


Figure 7.1: Theoretical predictions of \tilde{n}_{f_s} for carbon, aluminum, titanium and iron (lines). Experimental data points are shown as error bars. [96]

7.2.2 \tilde{n}_{fi} due to perpendicular NBI

In the case of perpendicular NBI, the perpendicular energy of the fast ions (‘fi’) is higher than the parallel energy and the majority of the fast ions can be trapped in

the magnetic well on the outboard side of the torus, creating a poloidal modulation of n_{fi} on the flux surface.

Chang and Harvey [92] calculated the magnitude of $\tilde{n}_{fi}(\theta)$ using the fluid equation approach for the background species and a kinetic approach for the fast ion species and found values close to 0.5 in the case of perpendicular injection.

From the quasi-neutrality condition and the parallel component of the momentum equation for the different particle species, one derives that the contribution of \tilde{n}_{fi} to the poloidal variation of the electrostatic potential is:

$$\frac{e\Phi_0\tilde{\Phi}}{T_e} = \tilde{n}_{fi} \frac{n_{fi}}{n_e} \cos\theta \left[\frac{T_i}{T_e} + Z_{eff} - \frac{n_{fi}}{n_e} \right]^{-1} \quad (7.12)$$

For quasi perpendicular injection in PDX, the contribution of the fast ions to the normalized electrostatic potential variation was estimated to be of order ϵ [92].

7.2.3 \tilde{n}_j due to asymmetric particle sources

The effect of poloidal asymmetries in the sources of impurities on the poloidal distribution of the impurity density was discussed in Ref. [91]. The continuity and momentum balance equations, for a neoclassical two ion species plasma, were used to derive expressions for \tilde{n}_{Is} and \tilde{n}_{Ic} in term of \tilde{S}_{Is} and \tilde{S}_{Ic} . It was shown that for a $\tilde{S}_I \sim O(\epsilon)$ to have a substantial effect on the density poloidal asymmetry, the source strength had to be $S_I \sim n_I \times 10^3 (s)^{-1}$, for parameters representative of present tokamak plasmas. Making realistic assumptions for the limiter sputtering rate, recycling factors, mean free path, etc., it was concluded that impurity source strengths of this order are plausible in the plasma edge region.

7.2.4 \tilde{n}_j due to inertia forces

Burrell et al. [93] pointed out the role of the inertia term in Eq.(2.2) in driving density asymmetries that strongly affect radial particle transport.

The parallel projection of Eq.(2.2), with the viscous and source term neglected, was solved for the density variation on the flux surface, assuming:

- large aspect ratio limit,
 - $m_I/m_i \gg 1$ so that $v_{thI} \sim v_\phi \ll v_{thi}$;
 - $n_I Z_I^2/n_i \ll 1$ so that $\nabla\Phi$ and v_ϕ are not affected by the presence of impurities;
 - v_θ , Φ_1 and the thermal portion of the frictional force are as derived in Ref. [59];
- to obtain:

$$\tilde{n}_{Is} \sim \frac{m_i q^2 R Z_I^2 \nu_{ii}}{e B_\phi L_n} = \epsilon \frac{\nu_{ii} Z_I^2}{\omega_{tri}} \delta_{\theta i} \quad (7.13)$$

$$\tilde{n}_{Ic} \sim \epsilon \frac{m_I v_\parallel^2}{T_I} \quad (7.14)$$

where: $n_I(r, \theta) = n_{I0}(r)(\tilde{n}_{Ic}(r) \cos\theta + \tilde{n}_{Is}(r) \sin\theta)$.

The magnitude of the up-down asymmetry confirms the result of Refs [90] and [85]. The magnitude of the in-out asymmetry, due to the centrifugal force, is of $O(\epsilon)$ when the ions have a toroidal velocity comparable to their sonic speed. The magnitude of the up-down asymmetry is $O(\epsilon)$ when $\nu_{ii} Z_I^2 \delta_{\theta i} / \omega_{tri} \sim 1$.

7.2.5 \tilde{n}_j due to momentum input, inertia and friction

Stacey and Sigmar [97],[94] presented a self-consistent derivation of the poloidal variation of density and potential, while solving the problem of radial transport and particle flow in the flux surface. The description of the transport problem consisted of the continuity and momentum equation, Eqs. (2.1) and (2.2), the charge neutrality condition for a two ion species plasma ($\sum_j e_j n_j = 0$) and the ambipolarity assumption ($\sum_j e_j \Gamma_j = 0$), solved omitting ∇T effects, in the large aspect ratio approximation.

The toroidal viscous term $\langle R \hat{\phi} \nabla \cdot \vec{\Pi}_j \rangle$ was represented by a phenomenological term of the form: $-m_j n_j \nu_{dj} v_{\phi j} R$, in Ref. [97]. The parallel viscous term $\langle \vec{B} \cdot \nabla \cdot \vec{\Pi}_j \rangle$ was written as sum of the usual neoclassical parallel viscosity term (Eq.(3.3)) and the parallel projection of this phenomenological viscous term. The momentum transfer coefficient, ν_{dj} , was inferred from experimental data.

The variation of density and potential on the flux surface was calculated from the parallel projection of the momentum equation. This was done self-consistently,

in conjunction with the evaluation of the poloidal velocity, by solution of the flux surface average (FSA) parallel component of the momentum balance equation, and with the evaluation of $\partial\Phi/\partial r$, from the sum of the FSA toroidal component of the momentum balance equation over species and using the ambipolarity assumption.

Densities and potential were assumed of the form given by Eq.(3.15) , with the simplifying assumption of \tilde{n} and $\tilde{\Phi}$ independent of r . The electron momentum equation was used to relate $\tilde{\Phi}$ with \tilde{n}_j , and a set of coupled equations for the coefficients $\tilde{n}_{s,j}$ and $\tilde{n}_{c,j}$ (with $j=i,I$) was obtained by taking the $\sin\theta$ and $\cos\theta$ projections of the parallel component of the momentum equation for main ions and impurities.

The poloidal variations were calculated for the titanium impurity in ISX-B ($\alpha = 0.05$ and $Z_{Ti} = 22$) and for the tungsten impurity in PLT ($\alpha = 0.1$ and $Z_W = 74$). Both the up-down and in-out asymmetries were found to be $O(\epsilon)$. It was found that the NBI momentum input was the main driver for the high Z impurity density asymmetry.

Subsequently, Stacey and Neeley [27] have developed a consistently ordered hierarchy of fluid equations from kinetic theory, which they solved for \tilde{n}_j , and \tilde{n}_{jc} . They found, for the collisional ordering $\nu_{jk}/\omega_{trj} \sim \delta_j^{-1}$, that $\tilde{n}_{js} \sim \tilde{n}_{jc} \sim \epsilon$.

7.3 Experimental measurements of \tilde{n}_j

7.3.1 \tilde{n}_I in ALCATOR A

Up-down asymmetries of highly collisional impurity ions (O, N), near the plasma edge of OH discharges of Alcator A, were reported in Ref. [85].

The measured quantity was the volume VUV emission rate of a particular impurity ion (for example OV (630 Å)) along chords of the plasma cross section. This quantity is proportional to the density of the ion along the line of sight, since the excitation rate should be poloidally symmetric. The asymmetry was found to become visible for $\bar{n}_e > 5 \times 10^{19} m^{-3}$, to increase with density and to reverse when the direction of the magnetic field was changed. This last observation eliminated the possibility

that the effect was instrumental, due to gas puffing or to uncentered plasma, and the asymmetry was attributed to the ∇B drift.

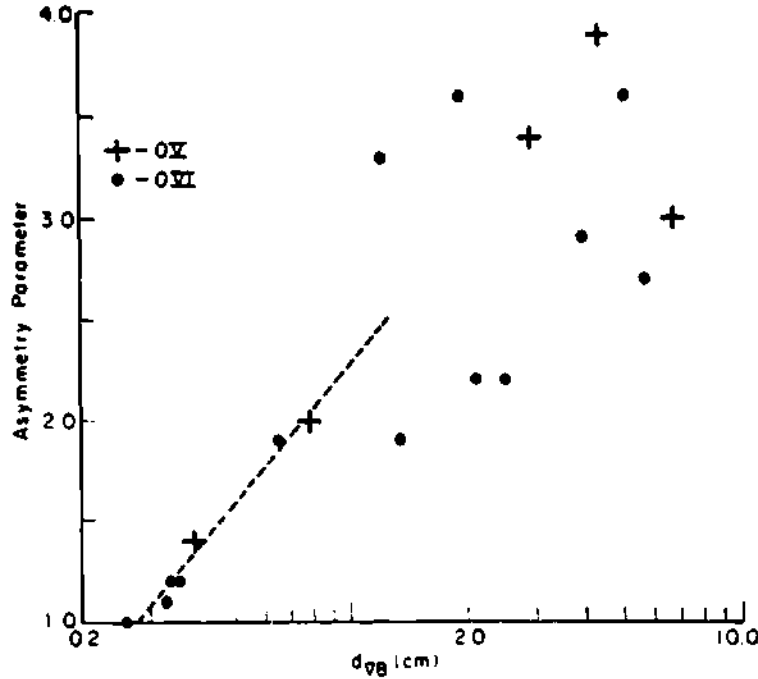


Figure 7.2: Variation of the Asymmetry Parameter with $d_{\nabla B}$, Eq.(7.5), in Alcator A [85]

The ratio between the larger and the smaller peak in the brightness profiles (see Fig. 7.3) was found to scale linearly with the distance which an impurity ion drifts radially during a poloidal excursion of one radian (see Fig. 7.2), defined by Eq.(7.5). For a density of $\bar{n}_e = 3.6 \times 10^{20} \text{ m}^{-3}$, $d_{\nabla B}$ for CV is 4.0 cm. For the range of plasma parameters given in Table 4.1, the asymmetry parameter (a.p.) varied in the range 1-4 and, correspondingly, $d_{\nabla B} = 0.2 - 7 \text{ cm}$. Assuming constant temperature on the flux surface and that the brightness is proportional to the density, these values of the asymmetry parameters should correspond to $\bar{n}_I \sim (a.p. - 1)/(a.p. + 1) = 0 - 0.5$. The following explanation was given: the OV ions located in the region where the ∇B drift is inward will penetrate to the higher-T region and be ionized, causing the

observed asymmetry in OVI emission.

It was then concluded that this was the first experimental evidence that the ∇B drift affects transport and that it had to be included explicitly as a major impurity transport process in tokamaks. Further theoretical works showed that friction effects produce asymmetries with the same scaling, as discussed in Section 7.2.1.

In a later paper ^[86], observations of enhanced impurity line radiation emission near the limiter in Alcator A were attributed not to the ∇B drift but rather to the effect of local recycling.

7.3.2 \tilde{n}_I in PLT

Radial profiles of spectral line intensities from different H, He, C and O ionization states were measured in PLT OH plasmas with an optical system from simultaneous spatial and spectral scanning ^[87]. The common feature of several scans was the strong top-bottom asymmetry of impurity densities, which could change during the discharge and even reverse direction.

The ∇B drift of ions could not explain the asymmetries, which rather were found to be correlated with the gas feeding program, the relative position of the limiter, the T_i near the edge and the developing of disruptive instabilities. In general, the lines of higher states of ionization were more symmetric than those of lower states. All of these observations suggested the influence of the plasma-wall interaction and localized sources of main and impurity ions on the observed phenomena.

7.3.3 \tilde{n}_I in PDX

Results of the investigation of the causes of poloidal asymmetries in impurity density observed in the ohmically heated PDX plasma were reported in Ref. [88]. Chordal profiles of line emission from C and O ions, in the range 2000-3000 Å, measured with the Fast-Rotating Mirror diagnostic, were found to be up-down asymmetric. The direction of the asymmetries of the C and O ions were found to be opposite to the

vertical ion drift and more pronounced for the lower ionization states (see Fig. 7.3), in agreement with the observations on Alcator A.

The hypothesis that asymmetries of the higher ionization state in the main plasma can be due to coupling with lower ionization states from recycling of local impurity sources was ruled out by simultaneous measurements of an extremely asymmetric emission profile from CIII, mostly concentrated at the edge, and a symmetric emission profile from CV, present in the plasma bulk.

The hypothesis that impurity poloidal asymmetries were due to charge exchange recombination with an asymmetric neutral hydrogen background was also ruled out by the observation that asymmetry in the radial profiles of H_β , CIII and CV emission could change sign independently.

Results of a 2D transport simulation of carbon impurities, performed assuming reasonable values of a neutral source at the wall, of convective velocities and diffusion coefficients, showed that the parallel transport in PDX is too rapid to sustain poloidal asymmetries caused by asymmetric neutral wall sources or asymmetric diffusion coefficients.

The neoclassical expression for the asymmetry parameter η_{qf} , defined by: $n_I(r, \theta) = n_I(r)(1 + \eta_{qf} \sin \theta)$ and given in Eq.(7.4), was in agreement with the experimentally observed asymmetry parameter (see Fig. 7.4). The η_{qf}^{ex} data for CV (at an unspecified radial location) spanned the range 0-0.4, that is of $O(a/R)$. The corresponding range of variation of the plasma parameters was not specified.

In a series of NBI discharges on PDX, electron density horizontal-midplane profiles showed an in/out asymmetry as expected because of centrifugal forces [89]. The surprising result was that the in-out asymmetry increased with \bar{n}_e , despite $v_\phi \propto 1/\bar{n}_e$, $T_i \propto 1/\bar{n}_e$ and the other experimental conditions kept constant. According to momentum balance, the centrifugal force drives [72]:

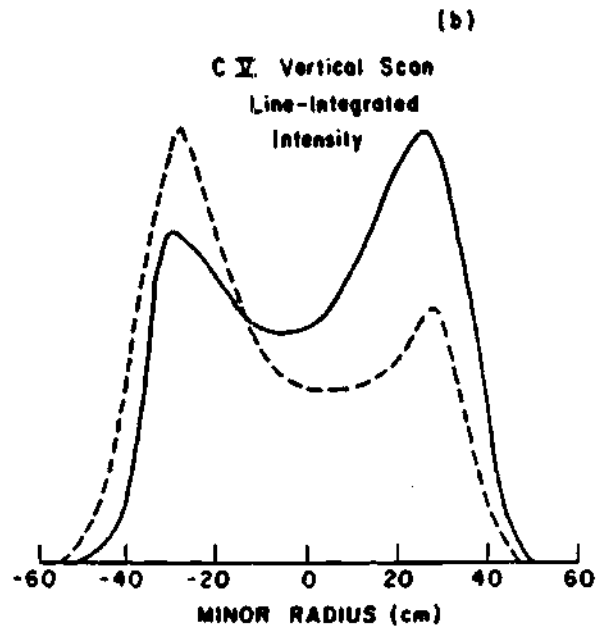
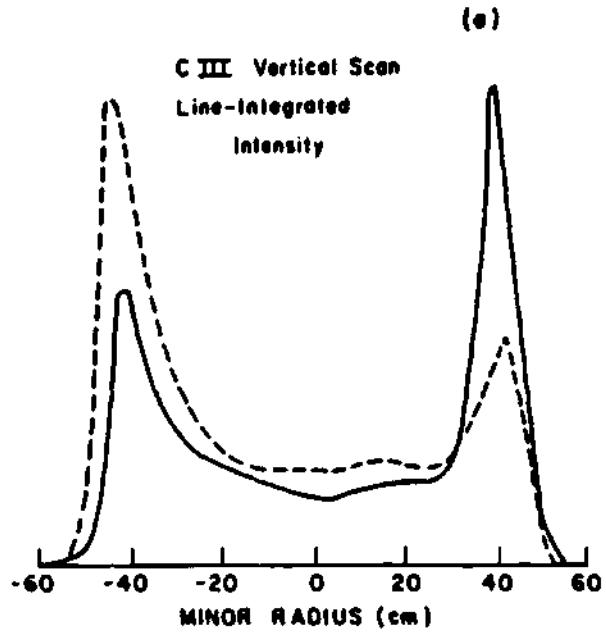


Figure 7.3: Density asymmetry in PDX.^[88] The dashed(solid) curve corresponds to a vertical ion drift directed upward(downward).

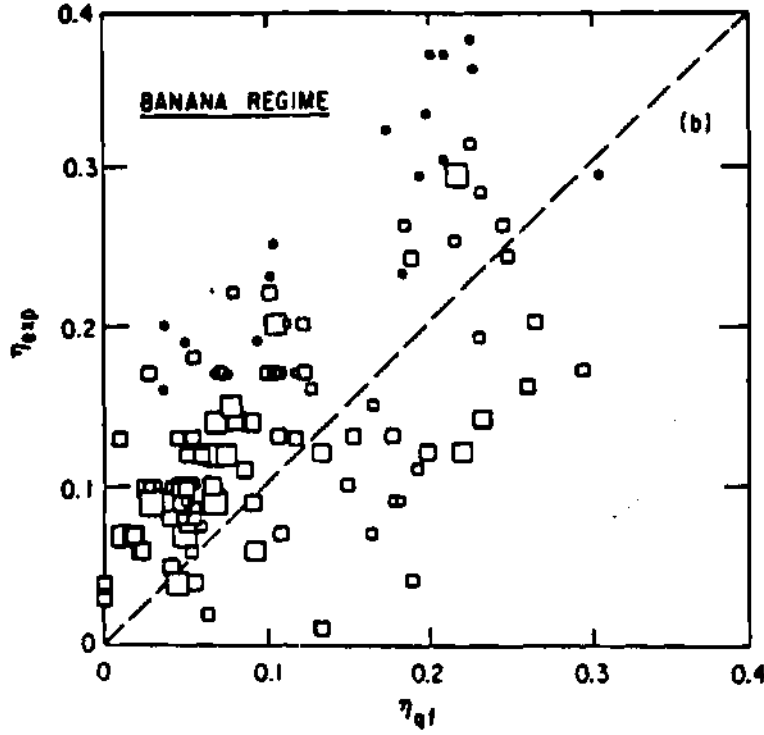


Figure 7.4: Experimentally observed value of η_{qf} for CV plotted versus its theoretical prediction from Eq.(7.4) [88]

$\tilde{n}_{ec} = m_i v_\phi^2 \epsilon / (T_i + T_e)$, and \tilde{n}_e should vary as $1/\tilde{n}_e$ for $T_i \ll T_e$, or as $1/\tilde{n}_e^2$ for $T_e \ll T_i$, which was in disagreement with experiments.

7.3.4 \tilde{n}_I in ASDEX

Large poloidal asymmetries in the distribution of impurity ions over the flux surface were observed during NBI, L- and H-regime, ELM-free discharges in ASDEX [89].

ELMs (Edge Localized Modes), a type of MHD instability (helical $m=3,4$, $n=1$) observed in H-regime only, increases the transport in the plasma periphery and prevents impurity accumulation. (They appear as periodic and irregular events causing spikes in the H_α and x-ray emissions from the edge, decrease of β_θ and they are interpreted as fast H-L-H transitions) [98].

When ELMs are absent, a high-confinement regime (H^*) is reached, and impurity

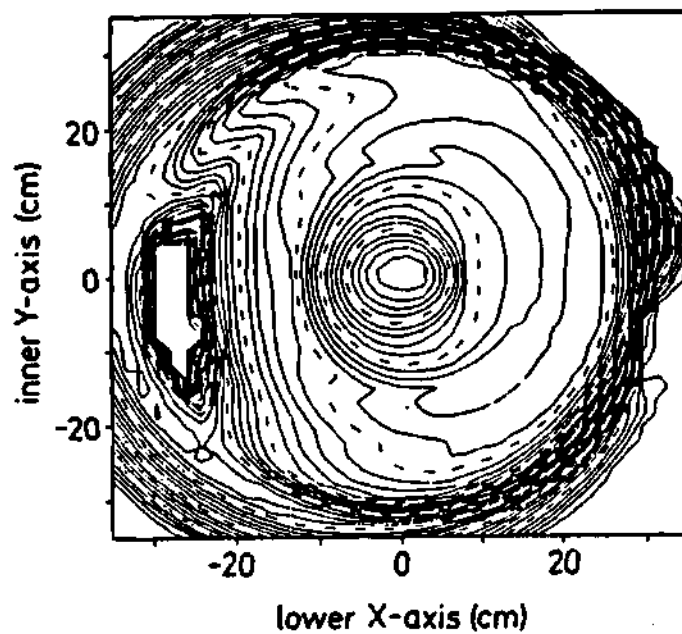


Figure 7.5: USX-ray image of NBI, H-mode type plasma (just before an ELM disruption) [84]

accumulation takes place. Emissivity of impurity ions (mainly Fe) over the entire cross section was measured by USX-ray (Ultra-Soft-X-ray) cameras at different times during a OH \rightarrow NBI discharge. The x-ray image of the plasma shows concentric, nearly circular surfaces of constant emission during the OH and the L-mode phases. Immediately after L-H transition, asymmetries, due to a redistribution of impurity ions, appear. The visible up-down asymmetry is in the direction of the ∇B drift, opposite to the direction observed in Alcator A and PDX (see Fig. 7.5). The in-out asymmetry is attributed to the increased centrifugal force acting on the metal ions, since the momentum confinement is seen to improve, along with the particle and energy confinement, from the L to the H mode. No comments on the correspondent density asymmetries were published. Values of v_ϕ during the L-phase were not reported; during the H^* phase, $v_\phi \sim 2 \cdot 10^5 \text{ m/s}$, and $\tau_\phi \sim 150 \text{ ms} \sim \tau_E$.

7.3.5 \bar{n}_I in TEXT

Recently [96], carbon, aluminum, titanium and iron were injected into TEXT via laser ablation or pellet injection. Poloidal up/down asymmetries of these impurity densities were observed using a horizontal x-ray imaging array. Figure 7.6 shows the value of \bar{n}_{Is} , for aluminum, at three different radii. Typical TEXT parameters are: $B=2.5 \text{ T}$, $I_p=300 \text{ kA}$, $\bar{n}_e = 3 \cdot 10^{20} \text{ cm}^{-3}$, $T_e(0) = 1 \text{ keV}$, $a=26 \text{ cm}$ and $R=100 \text{ cm}$.

While it was not possible to reverse the toroidal B-field, these measurements were repeated after reversing the plasma current, but no clear current direction dependence was found.

Fluctuations of Φ , n_e and T_e also exhibit an asymmetrical nature in their spatial as well as spectral resolution. In particular, the up-down asymmetry in the turbulent fluctuation has been observed to change sign when the plasma current is reversed [33].

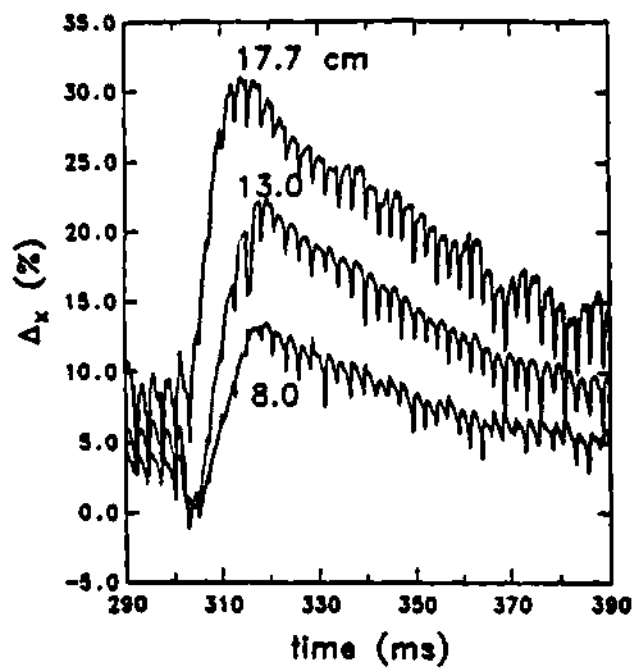


Figure 7.6: $\bar{n}_{I,}$ for aluminum at three different radii [96]

7.4 Theoretical estimates of $\tilde{\Omega}_{\phi j}$

The toroidal rotation frequency can be written as: [70]

$$\Omega_{\phi j} = \frac{v_{\theta j}}{R} \frac{B_\phi}{B_\theta} - \frac{1}{e_j n_j} p_j' - \Phi' \quad (7.15)$$

The magnitude of $\tilde{\Omega}_{\phi j}$ is therefore a function of the poloidal variations of the RHS terms in Eq.(7.15). The magnitude of $\tilde{\Omega}_{\phi j} \sim \epsilon$ was discussed in Refs. [70] and [99].

Ref. [70] discusses poloidal variations of $\Omega_{\phi j}$ which result from poloidal variations of the electrostatic potential. The toroidal rotation frequency can in fact be written as: [70]

$$\Omega_{\phi j} = \frac{v_{\theta j}}{R} \frac{B_\phi}{B_\theta} - \left(\frac{1}{e_j n_j} p_j' - \Phi' \right) \quad (7.16)$$

where the ' indicates $\partial/(B_\theta R \partial r)$. Ref. [70] points out that if the last term is poloidally asymmetric and large enough, it could drive relevant $\tilde{\Omega}_{\phi j}$. Several References ([90], [92], [100], [101]) are cited in support of the possibility that $\partial\Phi'/\partial\theta \sim \epsilon\Phi'$ and that this would lead to $\tilde{\Omega}_{\phi j} \sim \epsilon$.

Ref. [70] also reviews previous theoretical-computational work which led to relatively large values of $v_{\theta I}$ (case with collisional impurities and ions in plateau regime). Since $v_{\theta j} = K_\phi B_\theta / n_j$ for values of $v_{\theta j} \sim \beta v_{\phi j}$ one expects $\tilde{\Omega}_{\phi jc} \sim \epsilon$. If the conditions $v_{\theta j} \sim \beta v_{\phi j}$ and \tilde{n}_{sj} are both verified, Eq.(7.15) predicts $\tilde{\Omega}_{\phi j} \sim \epsilon$.

Ref. [99] also discusses the arguments presented in Ref. [70] in support of $\tilde{\Omega}_{\phi j} \sim \epsilon$ and it points out the following facts.

- Possible mechanisms causing $\tilde{\Phi}' \sim \epsilon$ studied in Refs. [92], [101], namely perpendicular injection and RF heating, are not necessarily associated with plasma rotation. In any case they would not lead to any substantial up-down asymmetry of the rotation velocity and they would drive $\tilde{\Phi}'$ mainly $\sim \tilde{\Phi}'_c \cos\theta$. If $\tilde{\Phi}'_c \sim \epsilon$, it follows that:

$$\tilde{\Omega}_{\phi jc} \sim \epsilon \frac{\rho_{\theta j}}{a} \frac{v_{thj}}{v_{\phi j}} \quad \tilde{\Omega}_{\phi js} \ll \epsilon \quad (7.17)$$

(For the data in Table 4.1, $(\rho_{\theta i}/a)(v_{thi}/v_{\phi i}) = 0.1 - 0.3$, assuming $q=2$). For an impurity species, this same factor would be a factor Z_I smaller.

- Only trace impurities can be sufficiently collisional to give rise to a large friction force able to drive $\tilde{n}_{js} \sim \epsilon$. But in this case, because of the low density of these impurities, $\tilde{\Phi}'_s \ll \epsilon$.
- The \tilde{p}_j term alone would give rise to poloidal variation of $\Omega_{\phi j}$ of the following order:

$$\tilde{\Omega}_{\phi js} \ll \tilde{\Omega}_{\phi jc} \sim \frac{\rho_{\theta j}}{r} \frac{v_{\phi j}}{v_{thj}} \epsilon \ll \epsilon \quad (7.18)$$

(Eq.(7.18) is derived from Eq.(13) in Ref. [99]. Eq.(7.18) is based on the assumption that \tilde{n}_{cj} is driven by centrifugal force and that \tilde{n}_{js} can be $\sim \epsilon$ only for trace impurities).

In summary, theory supports the possibility of $\tilde{\Omega}_{\phi jc} \sim \epsilon$ in case of $v_{\theta j} \sim \beta v_{\phi j}$, and of $\tilde{\Omega}_{\phi js} \sim \epsilon$ when both conditions $v_{\theta j} \sim \beta v_{\phi j}$ and $\tilde{n}_{js} \sim \epsilon$ are verified. In case of $\tilde{n}_j \sim \epsilon$, the Φ' and p'_j alone (E.(7.15), would generate $\tilde{\Omega}_{\phi j} < \epsilon$.

7.5 Experimental measurements of $\tilde{\Omega}_{\phi j}$

Measurements of v_{ϕ} radial profiles are usually done in the horizontal midplane and cover the $R > R_0$ plasma region, including often a few data points for $(R_0 - 10/20 \text{ cm}) < R < R_0$. The data for $R < R_0$ are usually neglected because the error bars increase as R decreases. This limited information on the velocity profile makes it difficult to comment on the $\Omega_{\phi}(\theta)$ dependence.

Ref. [17] reported the observation that the peak rotation (toroidal velocity of carbon) appeared shifted by 10-15 cm with respect to the T_e profile in JET [17] but the origin of the shift was not discussed. On the contrary, as result of analysis of rotation measurements on DIII, Ω_{ϕ} was found to be a flux surface function , within

the experimental errors (which, from the figure in Ref. [5] appears to be of the order of 10 %). Toroidal rotation of helium was measured in this case.

7.6 Poloidal velocity

7.6.1 Theoretical estimates of the poloidal velocity

In the framework of the neoclassical theory, the theoretical evaluation of the poloidal velocity has been attempted in a variety of ways.

For OH heated plasmas, v_θ has been estimated [102] from an expression by Hirshman [61],

$$v_{\theta i} = -\frac{1}{eB} \frac{\mu_{2i}}{\mu_{1i}} \frac{\partial T_i}{\partial r} \quad (7.19)$$

where μ_{1i} and μ_{2i} are the ion parallel viscosity coefficients associated to the flow and the heat flux respectively. The value of μ_{2i}/μ_{1i} was estimated to be -1.7, 0.5 and 1.69 in the banana ($\nu_j^* < 1$), the plateau ($1 < \nu_j^* < \epsilon^{-1.5}$) and the Pfirsch-Shlüter ($\epsilon^{-1.5} < \nu_j^*$) regimes, respectively [63]. This expression is valid when $\langle q_{\parallel} B \rangle$ can be neglected with respect to $\langle q_{\theta} B \rangle$ and therefore $q_{\theta j}/p_j$ becomes $\sim 5/(2e_j B) \partial T_j / \partial r$.

Refs. [63] and [64] prescribe that $v_{\theta j}$, along with $q_{\theta j}$, can be calculated from the system of simplified FSA parallel momentum and heat flux equations. The simplification consists in neglecting the momentum input term and the viscous forces, other than the parallel viscosity, in Eq.(2.2) and the electric field, viscosity and source terms in Eq.(A.1) to obtain:

$$\begin{aligned} \langle \vec{B} \cdot \nabla \cdot \vec{\Pi}_j \rangle &= \langle \vec{B} \cdot \vec{R}_j \rangle \\ \langle \vec{B} \cdot \nabla \cdot \vec{\Theta}_j \rangle &= \langle \vec{B} \cdot \vec{F}_j \rangle \end{aligned} \quad (7.20)$$

Substituting the viscous-flows and friction-flows relations, Eqs. (B.1), one obtains:

$$\zeta_{1j} v_{\theta j} - \zeta_{2j} \frac{2 q_{\theta j}}{5 p_j} = \frac{\tau_{jj}}{m_j n_j} \sum_k [l_{00}^{jk} (v_{\theta k} + V_{0k} \frac{\beta}{B}) + l_{01}^{jk} (-\frac{2 q_{\theta k}}{5 p_k} + V_{1k} \frac{\beta}{B})] \quad (7.21)$$

$$\zeta_{2j}v_{\theta j} - \zeta_{3j}\frac{2}{5}\frac{q_{\theta j}}{p_j} = \frac{\tau_{jj}}{m_j n_j} \sum_k [l_{10}^{jk}(v_{\theta k} + V_{0k}\frac{\beta}{B}) + l_{11}^{jk}(-\frac{2}{5}\frac{q_{\theta k}}{p_k} + V_{1k}\frac{\beta}{B})] \quad (7.22)$$

with $\zeta_{3j} = g[39/(4\sqrt{2}) - 25 \ln(1 + \sqrt{2})/4]$, $\zeta_{(1,2)j}$ given by Eq.(3.9) and

$$V_{0k} = \frac{1}{\beta}(\frac{1}{e_k n_k} \frac{\partial p_k}{\partial r} + \frac{\partial \Phi}{\partial r}) \quad V_{1k} = \frac{1}{e_k \beta} \frac{\partial T_k}{\partial r} \quad (7.23)$$

In NBI discharges, the momentum input term and the toroidal viscosity, in Eq.(2.2) can have magnitudes comparable to the magnitude of the leading terms in the equations and should not be neglected.

In the transport problem of Ref. [94], the heat flux was neglected and the FSA parallel momentum balance equation was solved including momentum input, inertial and parallel viscosity terms and a phenomenological representation of the perpendicular viscosity, along with an equation for the electric field, to calculate v_θ . For the ISX-B deuterium plasma, with a titanium impurity ($Z_{met} = 0.05$) and for the PLT deuterium plasma, with a tungsten impurity ($Z_{met} = 0.1$) it was found that $v_{\theta I} \sim \beta v_{\phi I}$ and that $|v_{\theta i}| \ll |v_{\theta I}|$, since $v_{\theta i} \sim -v_{\theta I} \mu_I / \mu_i$.

A neoclassical model for the poloidal velocity driving/damping forces has been recently given by Shaing and Crume [103]. They use the FSA poloidal momentum balance equation for a one-fluid plasma

$$\langle \vec{B}_\theta \nabla \cdot \vec{\Pi} \rangle = \langle \vec{B}_\theta \vec{B} \times e \vec{\Gamma}_{orb} \rangle \quad (7.24)$$

including the ion flux, $\vec{\Gamma}_{orb}$, associated with ion-orbit loss, and a form of the parallel viscosity valid in collisional regime and up to values of $v_\theta \sim v_{th} B_\theta / B$. Their formulas show that the combined action of the radial current and the parallel viscosity leads to a bifurcation of the solution v_θ .

A.B. Hassam has recently pointed out [104] that a poloidal asymmetry of the radial velocity is naturally coupled to the poloidal velocity through the inertia term.

Using continuity, toroidal and parallel momentum one-fluid equations, and neglecting sources and toroidal viscous forces, he derived the equation that links v_θ and \tilde{v}_r :

$$\frac{\epsilon}{q}(1+2q^2)\frac{\partial \langle v_\theta h \rangle}{\partial t} + \gamma_{MP} \langle v_\theta h \rangle + \langle v_\theta h \rangle \frac{q}{nr} \frac{\partial}{\partial r}(nr \langle 2 \cos\theta v_r \rangle) = 0 \quad (7.25)$$

where $\gamma_{MP} \langle v_\theta h \rangle = \langle \vec{B}/B_0 \nabla \cdot \vec{\Pi} \rangle$. If the viscosity damping is small enough, that is if $\gamma_{MP} \ll \langle 2 \cos\theta v_r \rangle / (\epsilon L_n)$, a relatively large in-out asymmetry of v_r (the neoclassical v_r is too small to produce such an effect, but the actual v_r can) drives the poloidal velocity.

7.6.2 Experimental measurements of v_θ

Measurements of the poloidal velocity have always been of fundamental importance in the investigation of viscosity, the radial electric field and transport in general. The recent finding^[105] that changes in v_θ at the plasma edge accompanies the L-H mode transition has motivated several experimental investigations of the edge v_θ , as well as theoretical speculations. While measurements of v_θ at the plasma center have not been too successful in the past, v_θ profiles have recently been measured successfully near the separatrix of several tokamaks and in the central plasma region of TFTR. A brief description of these measurements follows.

Ref. [3] reported the first measurements of $v_{\theta I}$ during NBI in PDX. In order to impart poloidal momentum to the plasma, the vertical coordinate of the magnetic axis was varied as much as 10 cm in either direction. It was found that the poloidal rotation velocities in the plasma outer region were lower than the limit of sensitivity of the FARM diagnostic ($\|v_\theta\| < 3 \times 10^3$ m/s), while the emission from ions close to the center was too weak to perform the measurements. During the OH phase, no poloidal rotation was observed and the central toroidal rotation was found to be $\sim 10^3 - 10^4$ m/s and in the direction opposite to the current.

Measurements of $v_{\theta I}$ in TFTR discharges, during NBI, were recently reported in

Ref. [106]. Poloidal rotation of 1.2×10^4 m/s in the ion diamagnetic drift direction was measured at $r/a \sim 0.25$ during nearly balance injection of 11 MW, using the vertical x-ray crystal spectrometer (FeXXV, K_α line). The toroidal velocity reached 5×10^4 m/s in the counter direction. It was reported that the magnitude of $v_{\theta Fe}$ was consistent with the neoclassical predictions according to Ref. [107]. (If we use the expression $v_{\theta Fe} = -k/(eB) dT_i/dr = 4.3 \times 10^3$ m/s, with k in the range $[-1.7, 0.5]$, according to Ref. [107] because $(\nu/\omega_{tr})_{Fe, r=0.2} \sim \epsilon^{3/2}$, we obtain $v_{\theta Fe}$ in the range $[-1.5 \times 10^4$ to $4.3 \times 10^3]$ m/s. This indicates that the measured value of v_θ is not inconsistent with Hirshman's neoclassical estimate.

There are no measurements of $v_{\theta I}$ in unbalanced NBI shots with higher value of v_ϕ ($> 10^5$ m/s) because the vertical spectrometer picks up 7% of the toroidal speed and the accuracy of the evaluation of $v_{\theta I}$ becomes critical.

The magnitude of v_θ was also measured in the edge and scrape-off layer of DIII-D in NBI and OH plasmas, in L and H modes, with a CHERS diagnostic (He II, 4686 Å) [105]. Changes of $v_{\theta I}$ at the edge from 10^4 to 3×10^4 m/s, accompanied by changes of v_ϕ from 3×10^4 to 5×10^4 m/s were reported for NBI discharges. The main ion collisionality parameter was $\nu_i^* = 1 - 10$ at the edge of these discharges; since $\nu_I^* \sim \nu_i^* Z_I^2$, the impurities were in the highly collisional regime. The $v_{\theta I}$ was in the ion diamagnetic drift direction. The observed values of $v_{\theta I}$ were reported to be at least one order of magnitude larger than calculated from the version of the neoclassical theory as formulated, for example, in Ref. [64], but they were in agreement with the ion-orbit-loss model of Shaing and Crume [103].

The poloidal velocity was measured at the plasma periphery of JFT-2M in the spatial range $[a - 3$ cm, $a + 1.5$ cm] with a CHERS diagnostic (CVI, 5292 Å) [108]. Data were reported for 0.7 MW of co-injected NB power with a L-H transition occurring after 25 ms of NBI. The main ions collisionality parameter, ν_i^* changed from 44 to 22 at the transition from L to H mode. The $v_{\theta I}$ was observed to be in the electron dia-

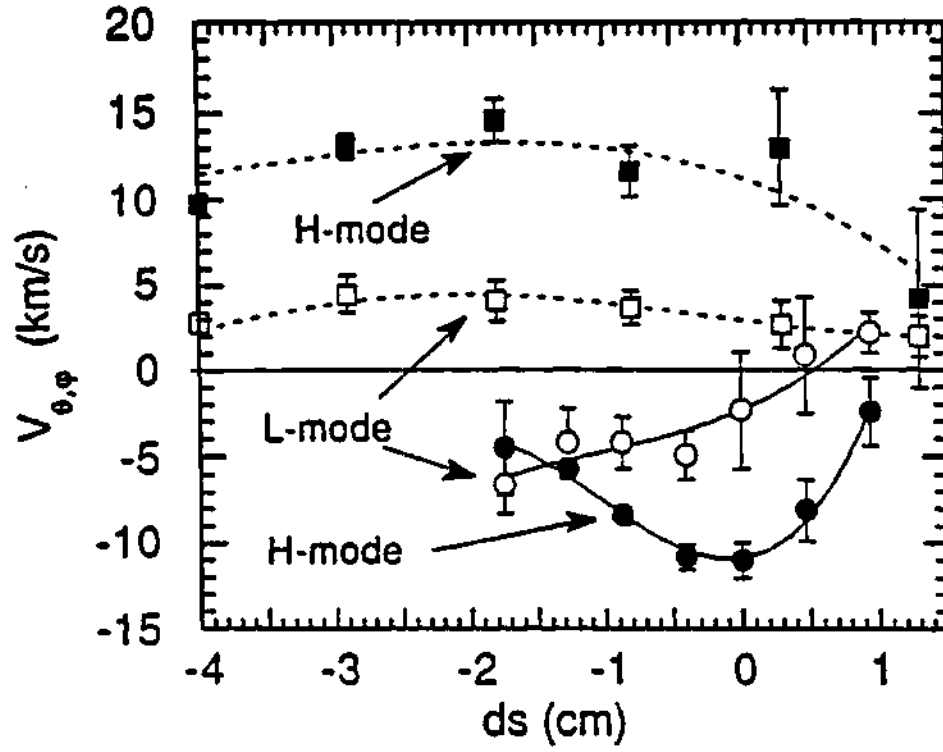


Figure 7.7: Radial profiles of poloidal (circles) and toroidal (squares) rotation velocities, as a function of the distance from the separatrix, for L-mode and H mode in JFT-2M. d_s is negative inside the separatrix. [108]

magnetic drift direction and to increase in magnitude at the L-H transition regardless of the direction of I_p and injection; the change was fairly localized near the separatrix. Figure 7.7 shows the v_ϕ and v_θ profiles before and after the L-H transition; they are of the same magnitude and they both increase in the H mode. The change of v_θ at the L-H transition was found to agree with the prediction of Shaing and Crume's model [103] by including the additional effect of fast ion losses.

Spectrometric measurements (CIII, 4647.4 Å) of v_θ from the plasma edge of ASDEX [109] were also taken during the OH phase and the NB co-injection of 2.7 MW of a plasma discharge. The OH phase did not show any measurable v_θ ; during the NB H-mode, v_θ rose up to $1.6 \pm 0.3 \times 10^3$ m/s (presumably in the ion diamagnetic drift direction, but non specified) while v_ϕ was about 4×10^4 m/s. No comments were made in Ref.[109] regarding comparison of the data with theories.

Summary of v_θ measurements - The picture resulting from the available poloidal velocity measurements is far from complete. From TFTR there is some experimental evidence that $v_{\theta I}$ can be comparable to v_ϕ in the plasma center in case of balance injection and $v_\phi \sim 5 \times 10^4$ m/s. The plasma was found to rotate poloidally in the ion diamagnetic drift direction, as prescribed by Eq.(7.19) for impurities in the plateau and collisional regimes, but its magnitude is a factor of 3 smaller than the prediction by Eq.(7.19).

Measurements at the edge of several machines have revealed that $v_{\theta I} \sim v_\phi$ for a range of values of v_ϕ that does not exceed 5×10^4 m/s. The neoclassical predictions underestimate the edge velocities by one order of magnitude, and in this region the Shaing and Crume predictions are found to be in agreement with the experimental values.

It is impossible at this point to extrapolate the experimental results for the higher regimes of toroidal velocity pertaining to NBI discharges since the mechanisms that control the magnitude of v_θ are not well understood.

7.7 Summary

Up-down density asymmetry of collisional impurities were observed in OH plasmas, namely in Alcator A, PLT, PDX and ASDEX, and in the NBI ASDEX rotating plasma. An in-out asymmetry of Fe ions and n_e were observed, respectively, in ASDEX and PDX in rotating plasmas. There is no experimental observation of up-down asymmetries of main ions or n_e .

Neoclassical theory predicts variations of the ion densities on the flux surface under certain conditions. The parallel friction drives an up-down asymmetry of the impurities of order $\tilde{n}_{Is} \sim \epsilon \Delta$, where Δ is a parameter proportional to the ion collision frequency and it is $\sim O(1)$ for highly collisional ion species ($\nu_j^* \sim (\epsilon^{-1.5} \delta_{\theta j})^{-1}$). The up-down asymmetry of the main ions is predicted to be much smaller, i.e. $\tilde{n}_i \sim \tilde{n}_I n_I / (n_i Z_I)$.

The centrifugal force drives an in-out asymmetry of the density, $\tilde{n}_{jc} \sim \epsilon (v_{\phi j} / v_{thj})^2$, that is of $O(\epsilon)$ for sonic ions. The main ions have a smaller in-out poloidal variation, compared to the impurities, since $v_{thi}^2 \sim Z_I v_{thI}^2$. The centrifugal force also drives an up-down asymmetry $\tilde{n}_{Is} \sim \epsilon \Delta$ for collisional impurities.

Momentum input can drive $\tilde{n}_I \sim \epsilon$ for high Z impurities. The theory also predicts that localized impurity sources at the wall may drive large and localized \tilde{n}_I .

There is some degree of agreement between the experimental observations of poloidal variations of impurity density and the neoclassical theory. While the up-down asymmetry of n_I in Alcator A and PDX agreed qualitatively with the neoclassical predictions of \tilde{n}_{Is} driven by the friction force, the in-out asymmetry of the electron density in rotating PDX plasma, attributed to the centrifugal force, did not scale as predicted. The in-out and up-down asymmetries of the Fe impurities, observed on ASDEX, during NBI, were not studied qualitatively.

There is some experimental evidence of in-out asymmetry of $\Omega_{\phi j}$ from JET; up-down asymmetries of $\Omega_{\phi j}$ have never been measured.

Theory predicts:

$$\tilde{\Omega}_{\phi j} \simeq -(2\epsilon \cos\theta + \tilde{n}_j) \frac{v_{\theta j}}{v_{\phi j} \beta} - \frac{p'_{j1}}{e_j n_j \Omega_{\phi j}} + \frac{\Phi'_1}{\Omega_{\phi j}} \quad (7.26)$$

Equation 7.26 shows that poloidal variations of order $v_{\phi j} \beta$ would lead to in-out asymmetry of the rotation frequency of order $2\epsilon + \tilde{n}_{jc}$ and to up-down asymmetries of order \tilde{n}_{js} . The order of magnitude of the pressure gradient term is $\tilde{n}_j(\rho_{\theta j}/a)(v_{\phi j}/v_{thj}) < \tilde{n}_j$. Asymmetries of the electrostatic potential alone would cause $\tilde{\Omega}_{\phi j} \sim \tilde{\Phi}$.

There is experimental evidence of $v_{\theta I} \sim v_{\phi}$ at the edge of several tokamaks, that is explained by the presence of a strong particle flux due to first orbit losses [103]. There is experimental evidence of $v_{\theta Fe} \sim \beta v_{\phi}$ in the center of balance NBI discharges in TFTR. As discussed, these values of $v_{\theta j}$ should result in an observable (order of ϵ or larger) in-out asymmetry of $\Omega_{\phi j}$.

In summary, there is experimental and theoretical evidence that $O(\epsilon)$ poloidal asymmetries in the impurity density and rotation can occur in tokamaks under certain conditions. In Chapter 8 we will examine further if the conditions, which have been identified as drivers for the discussed poloidal asymmetries, are present in Exp.44.

Chapter 8

POLOIDAL VARIATIONS OF DENSITY AND ROTATION FREQUENCY IN TFTR Exp. 44

8.1 Introduction

This Chapter is dedicated to the study of poloidal variations of ion densities and toroidal rotation in the TFTR Exp.44 plasma.

In Section 8.2 we discuss measurements that can be interpreted in terms of poloidal variations of density and rotation velocity. Measurements of the $n_e^2 Z_{eff}$ vertical profile and of the $\Omega_{\phi I}$ horizontal radial profile are available. Direct measurements of ion radial profiles are not available for Exp.44.

In the following Sections, the poloidal variations of density and rotation frequency are evaluated from theoretical expressions. Only neoclassical mechanisms for producing density and rotation frequency asymmetries are treated in the calculations, although the effects of anomalous mechanisms are discussed.

It is assumed that the temperatures are flux surface functions. The mechanisms producing temperature equilibration over the flux surface are, in fact, stronger than those involved in producing density equilibration. Moreover, the evaluation of $\tilde{T}_j(r, \theta)$ would require the solution of the energy equations, which would further complicate the already complex formulation and introduce further unknown quantities.

For simplicity, \tilde{n}_j and $\tilde{\Omega}_{\phi j}$ are first calculated by neglecting the contribution of the conductive heat flux in the viscous and friction forces. The additional contribution of the heat flux is subsequently discussed. The continuity equation and the radial momentum balance equation are employed to determine the forms of the poloidal and toroidal velocities. The form of $\tilde{\Omega}_{\phi j}$, in terms of \tilde{n}_j and other quantities, is then

derived. The poloidal projection of the momentum equation is the balance equation that relates $\tilde{n}_{j,s}$ and $\tilde{n}_{j,c}$ to the driving (inertia, viscous, etc.) forces. The FSA poloidal or parallel momentum balance equation (and the FSA parallel heat flux equation, in the case $\tilde{q}_j \neq 0$) must also be solved to evaluate $v_{\theta j}$, upon which $\tilde{n}_{j(c,s)}$ depend.

The magnitudes of the various terms are estimated making use of the plasma parameter measurements for TFTR Exp.44, when available, or of plausible estimates, when necessary; terms that are estimated not to affect the balance equations are neglected at the outset, with the purpose of simplifying the derivation. The toroidal and radial velocities are not calculated selfconsistently; instead the measured values are used.

While perpendicular neoclassical transport is generally believed to underestimate the actual transport in tokamaks, the parallel transport seems to be dominated by neoclassical mechanisms. In fact, neoclassical parallel transport can account fairly well for resistivity, bootstrap current and damping of poloidal velocity [110]. In the derivation that follows, the viscosity is assumed to be neoclassical. Viscous forces arise only in the poloidal projection of the momentum equation, where the parallel viscosity is the dominant mechanism.

At the end of the Chapter, we present a discussion of the \tilde{n}_j , $\tilde{\Omega}_{\phi j}$ and $\tilde{\Phi}$ results and of how they compare to the previous estimates, that were reviewed in Chapter 7.

8.2 Measurements of \tilde{n}_j and $\tilde{\Omega}_{\phi j}$ in TFTR Exp.44

8.2.1 Measurements of $n_e^2 Z_{eff}(R)$

Measurements of the vertical profile of $n_e^2 Z_{eff}$ were carried out for the shots of Exp.44 [111]. The x-ray emission intensity measured by the XIS diagnostic has been measured for a series of co- and counter-injection shots, both for the OH and NB phase. Fig. 8.1 shows the measured intensity as a function of the tangency radius of the viewing sightline normalized to the minor radius, for shot 37309 (co-injection of ~ 10 MW of beam power at $I_p = 1.1$ MA) and after 500 ms of NB injection. The solid line is a

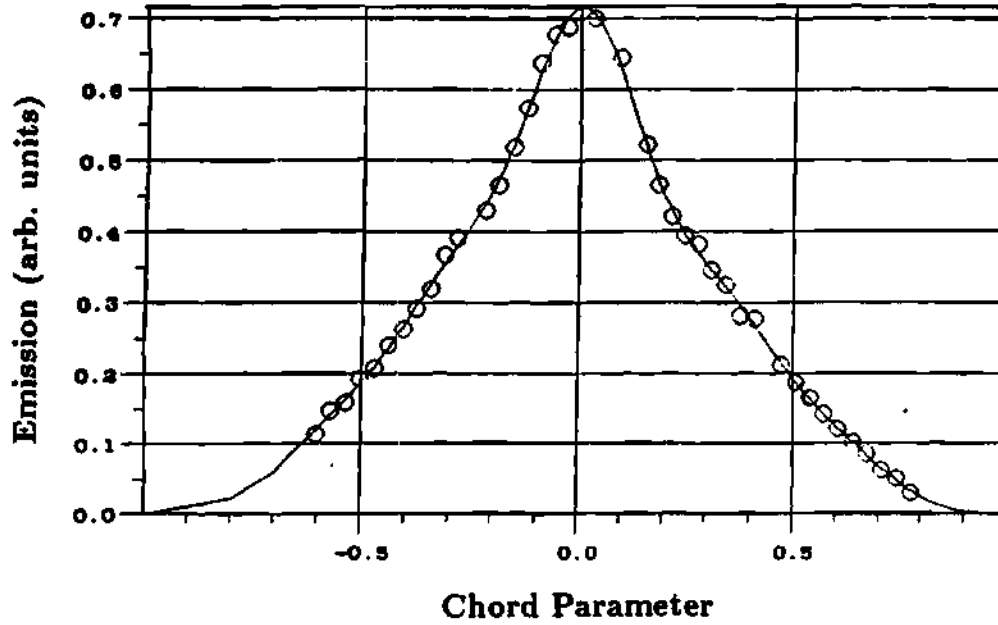


Figure 8.1: X-ray emission integrated along the sightlines of the XIS diagnostics (arbitrary units) as function of the tangency radius of the sightline normalized to minor radius (Shot 37309, after 500 ms of NBI injection).

smooth fit to the data. This figure and all the other plots of the x-ray emission show profiles symmetric with respect to the midplane, indicating the absence of poloidal asymmetries of $n_e^2 Z_{eff}$ within the error bar affecting the measurements themselves. The error bar affecting the measurement of each of the 40 detectors is $\sim 10\%$. The uncertainty in the overall up-down asymmetry is therefore reduced by a factor of $1/\sqrt{40}$ [56].

The symmetry of the XIS emission profiles does not rule out compensating asymmetries in the main ion and impurity densities, but implies that a relation among them must be satisfied. In fact, if compensating ion and impurity asymmetries of relevant magnitude are present they would have to satisfy:

$$\frac{|\tilde{n}_i n_{i0}(1 + Z_{eff}) + \tilde{n}_I n_{I0} Z_I (Z_I + Z_{eff}) + \tilde{n}_M n_{M0} Z_M (Z_M + Z_{eff})|}{(n_e Z_{eff})} \ll 10\% \quad (8.1)$$

where $n_j = n_{j0}(1 + \tilde{n}_j)$.

In case of $Z_{eff} = 3$, $Z_{met} = 0.5$, $Z_I = 6$ and $Z_M = 26$, this relation among the ion densities becomes:

$$|\tilde{n}_i + \tilde{n}_I + 0.2\tilde{n}_M| \ll 0.1 \quad (8.2)$$

In case of $\tilde{n}_I \sim \tilde{n}_M \sim \pm\epsilon$ at $r=a/2$, this relation would result in the requirement $|\tilde{n}_i| \sim \epsilon$, in order for \tilde{n}_i to compensate $O(\epsilon)$ values of \tilde{n}_I and \tilde{n}_M .

8.2.2 Measurements of $\Omega_{\phi I}(R)$

Figure 5.3 shows the toroidal velocity radial profile as measured by CHERS for one shot of Exp.44. The in-out asymmetry of $\Omega_{\phi I}(R)$, visible in the plasma center, of $O(\epsilon)$ or larger, was characteristic of most of the measured velocity radial profiles of the Exp.44 shots. The $T_I(R)$ profiles (same Figure), measured by the same diagnostic, appear symmetric. The symmetry of the $T_I(R)$ profile, which is expected theoretically, seems to rule out the possibility of an error in the evaluation of the plasma center location; it suggests that the in-out asymmetry of the toroidal rotation is real, or that the errors in the T_I and $v_{\phi I}$ data propagate in different ways.

The PPPL diagnosticians do not have confidence ^[56] in the ability of CHERS to diagnose in-out asymmetries in $T_I(R)$ and $\Omega_{\phi I}(R)$, since the measured signal attenuates exponentially with the distance from the plasma edge, due to beam attenuation. This causes the signal-noise ratio to decrease and the accuracy of the data to deteriorate. The study of propagation error in the CHERS analysis is still underway.

Nevertheless, even if the origin of the asymmetry in the $\Omega_{\phi I}$ profile is still unknown, we point out that, as discussed in Section 8.5.1, an in-out asymmetry of $O(\epsilon)$ would be consistent with poloidal velocities $v_{\theta I} \sim \beta v_{\phi I}$. Figure 5.3 shows a negative $\tilde{\Omega}_{\phi Ic}$ for both co- and counter- injection which, according to Eq.(8.32), $\tilde{\Omega}_{\phi Ic} = -v_{\theta I}/(v_{\phi I}\beta) \cos\theta$, would be consistent with $v_{\theta I}$ in the electron/ion diamagnetic drift direction in the case of co/counter toroidal rotation of the plasma.

8.3 Continuity equation and form of the poloidal flow

By subtracting the FSA of the continuity equation, Eq. 2.1, from Eq. 2.1 one obtains:

$$B_\theta \frac{\partial}{\partial \theta} \left(\frac{n_j v_{\theta j}}{B_\theta} \right) = r S_j - \frac{1}{R} \frac{\partial}{\partial r} (n_j v_{rj} r R) - \langle r S_j - \frac{1}{R} \frac{\partial}{\partial r} (n_j v_{rj} r R) \rangle (\equiv C_j) \quad (8.3)$$

The LHS term of the equation is $\sim (\epsilon n_j v_{\theta j})$, while the RHS is :

$$C_j \sim r S_{j0} \tilde{S}_j - n_j v_{rj} \epsilon \cos \theta - \frac{\partial}{\partial r} [r (\tilde{n}_j v_{rj} + n_j \tilde{v}_{rj})] \quad (8.4)$$

The RHS of Eq.(8.3) is usually negligible with respect to the LHS and the equation is commonly solved to obtain:

$$\frac{n_j v_{\theta j}}{B_\theta} \equiv K_j [= \text{const}(\theta)] \quad (8.5)$$

When the RHS of Eq.(8.3) cannot be neglected because large poloidal asymmetries of localized sources ^[91] or a large radial particle flux are present, the proper form of the poloidal velocity becomes:

$$v_{\theta j} = \frac{B_\theta}{n_j} (K_j + \int_0^\theta \frac{C_j}{B_\theta} d\theta) \quad (8.6)$$

TFTR plasma parameters - In the TFTR Exp.44 plasma, the radial electron velocity inferred from experimental measurements increases from zero at the center to a few m/s at the edge, and it is several orders of magnitude smaller than the calculated and measured (not in these but in similar discharges) ion poloidal velocity, $v_\theta \sim 10^{3-4} \text{ m/s}$. Therefore the radial flux terms of Eq.(8.3) are negligible with respect to the LHS of the same equation.

The main (deuterium) ion source is the sum of the NBI source, which dominates the center of the discharge, and of the recycling source, localized near the edge. The total main ion source, S_i , as calculated by SNAP and normalized to the main ion density, is plotted in Fig. 8.2 for the shots of Exp.44. The magnitude of $(r S_i)$ is a few orders of magnitude smaller than the LHS of Eq.(8.3). Since $\langle r S_j \rangle = \langle$

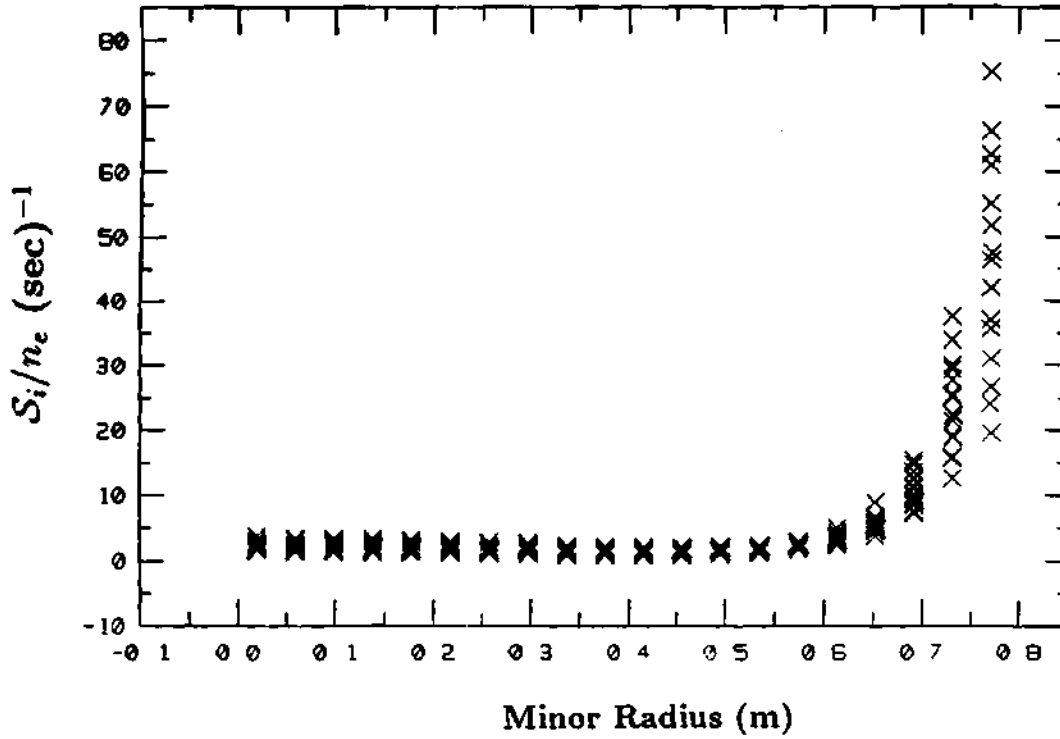


Figure 8.2: Radial profile of the main ion source, S_i , divided by n_i , for the shots of Exp.44

$\frac{\partial}{\partial r}(n_i v_{ri} r R)/R >$, we can conclude that the RHS of Eq.(8.3) is negligible over most of the plasma region for main ions. In the region $(a - r) = 5 - 10$ cm, near the edge, the source term becomes larger but the RHS is still two orders of magnitude smaller than the LHS of Eq.(8.3).

The impurity source is localized at the plasma edge. As is typical in most TFTR discharges, the oxygen and metal impurities play little role in the particle balance, and the main impurity is the carbon that originates from physical sputtering of the graphite limiter. Typically, the area of the inner bumper limiter wetted by the plasma is $\sim 6 \text{ m}^2$ [112]. The mean free path for atomic carbon at the plasma edge characterized by $n_e = 5 \times 10^{18} \text{ m}^{-3}$, $T_e = 100 \text{ eV}$, $v_o = 10^4 \text{ m/s}$ (neutral carbon velocity), $\langle \sigma v \rangle_{C^0} = 1.1 \times 10^{-13} \text{ m}^3/\text{s}$ (calculated using Eq.(7) in Ref. [113]) is:

$$\lambda_{C^0} = v_o / (n_e \langle \sigma v \rangle_{C^0}) = 2 \text{ cm}.$$

Carbon fluxes from the limiter of order $\Gamma_C \sim 10^{21} \text{ 1/s}$ have been measured in TFTR L-mode plasmas [112]. This flux would correspond to a source strength of $S_{C+1} = \Gamma_C / (0.02 \times 6) \simeq 10^{22} (\text{sm}^3)^{-1}$, localized within a few cms at the edge and strongly poloidally asymmetric. With this value of particle source, the RHS of Eq.(8.3) becomes comparable to the magnitude of the term $(n_j v_{\theta j})$ and cannot be neglected for the carbon impurity.

A calculation of the distribution of different ionization states of C, in a typical TFTR Exp44 shot showed that the carbon is completely ionized (C^{+6}) over most of the plasma region and that the lower ionization states (mainly C^{+5} and C^{+4}) are localized over the region $r/a = 0.9 - 1$.

We conclude that Eq.(8.5) is a valid representation of the form of the poloidal flow over most of the plasma region, i.e. for $r/a \sim 0 - 0.9$. Thus, we use Eq.(8.5) in the subsequent calculations, but keep in mind that source effects could alter the results that we obtain in the outer region $r/a \geq 0.9$. A study of poloidal variations of plasma parameters at the edge would also require a careful modelling of the plasma edge transport (and the accurate measurement of plasma edge conditions), which is beyond the scope of this work.

8.4 Radial momentum balance equation and form of the toroidal flow

The radial projection of the momentum balance equation, Eq.(2.2), for the particle species j, is:

$$g_{rj} + \frac{\partial p_j}{\partial r} + e_j n_j \frac{\partial \Phi}{\partial r} + e_j n_j (v_{\phi j} B_{\theta} - v_{\theta j} B_{\phi}) - \mathcal{M}_{rj} - R_{rj} + \Pi_{rj} + m_j v_{rj} S_j = 0 \quad (8.7)$$

where:

$$g_{yj} \equiv \hat{y} \cdot [m_j n_j (\tilde{v}_j \cdot \nabla) \tilde{v}_j], \quad \Pi_{yj} \equiv \hat{y} \cdot \nabla \cdot \tilde{\Pi}_j \quad (8.8)$$

This equation can be used to write the toroidal velocity as:

$$v_{\phi j} = \frac{v_{\theta j}}{\beta} - \frac{1}{e_j n_j B_\theta} (g_{rj} + \frac{\partial p_j}{\partial r} + e_j n_j \frac{\partial \Phi}{\partial r} + \Pi_{rj}) \quad (8.9)$$

where the radial friction, momentum input and particle source terms can be neglected because they are several orders of magnitude smaller than the other terms in the equation, for TFTR Exp.44. The inertia term can be written as:

$$g_{rj} = -m_j n_j \left(\frac{v_{\theta j}^2}{r} + \frac{v_{\phi j}^2}{R} \cos\theta - \frac{1}{2} \frac{\partial v_{rj}^2}{\partial r} + \frac{v_{\theta j}}{r} \frac{\partial v_{rj}}{\partial \theta} \right) \quad (8.10)$$

and the viscous force, Π_{rj} , is given in Appendix C.

We rewrite the toroidal velocity as:

$$v_{\phi j} = \frac{v_{\theta j}}{\beta} - \frac{1}{B_\theta} \left(\frac{1}{e_j n_j} \frac{\partial p_j}{\partial r} + \frac{\partial \Phi}{\partial r} \right) + R \Omega_{\phi j} U_j \quad (8.11)$$

where:

$$U_j = U_{jc} \cos\theta + U_{js} \sin\theta \simeq \frac{m_j}{e_j} \frac{\Omega_{\phi j}}{B_\theta} \cos\theta - \frac{1}{3e_j n_j v_{\phi j} B_\theta} \frac{\partial}{\partial r} (p_{\parallel j} - p_{\perp j})_s \sin\theta \quad (8.12)$$

In the case where the poloidal heat flux ($q_{\theta j}$) contribution to the parallel viscous force is neglected:

$$\begin{aligned} U_j &= U_{jc} \cos\theta + U_{js} \sin\theta \simeq \\ &\frac{\eta_{0j}}{e_j n_j r v_{\phi j} B_\theta R} \left\{ v_{\theta j} \left[\left(\frac{r}{L_{\eta_{0j}}} + \frac{r}{L_{v_{\theta j}}} \right) \sin\theta + \frac{2}{3} \frac{v_{\theta j}}{\epsilon} \left(1 + \frac{r}{L_{\theta j}} + \frac{r}{L_{\eta_{0j}}} + \frac{r}{L_{v_{\theta j}}} \right) \right] \right. \\ &\left. + \frac{\beta A_j R}{\epsilon} \left(\frac{r}{L_{\eta_{0j}}} + \frac{r}{L_{A_j/r}} - \frac{r}{L_q} \right) \right\} + \frac{m_j}{e_j} \frac{\Omega_{\phi j}}{B_\theta} \cos\theta \end{aligned} \quad (8.13)$$

One has defined $L_x \equiv -x(dx/dr)^{-1}$.

TFTR plasma parameters - The expression for $v_{\phi j}$ is usually further simplified by neglecting the inertia and the viscosity, Π_{rj} , terms. In fact, the g_{rj} term contributes to the FSA of the toroidal velocity with a term proportional to $m_j n_j v_{\theta j}^2 / r \ll (\partial p_j / \partial r)$ and to the poloidally varying component of $\Omega_{\phi j}$ with a $\cos\theta$ term whose magnitude, relative to $\Omega_{\phi j}$, is $m_j \Omega_{\phi j} / (e_j B_\theta)$, $\sim 10^{-3}$ for the TFTR Exp.44 plasma (see Fig. 8.3).

The radial viscous forces, Π_{rj} (see Appendix C), contribute to the FSA with terms like

$$\frac{\eta_{4j}}{e_j n_j B_\theta} \frac{\beta}{\epsilon} \frac{\partial \Omega_{\phi j}}{\partial r} \ll \frac{1}{e_j n_j B_\theta} \frac{\partial p_j}{\partial r} \quad (8.14)$$

and smaller, and to the poloidally varying component with terms like

$$\frac{1}{3e_j n_j B_\theta} \frac{\partial}{\partial r} (p_{\parallel j} - p_{\perp j})_s \sin\theta \quad \text{and} \quad \frac{3\eta_{4j}\beta}{e_j n_j B_\theta} \frac{\partial \Omega_{\phi j}}{\partial r} \cos\theta \quad (8.15)$$

whose amplitudes, relative to $\Omega_{\phi j}$, in the $q_\theta = 0$ case, of the order of:

$$\frac{\eta_{0j}}{e_j n_j r B_\phi R} \frac{v_{\theta j}}{\beta v_{\phi j}} \quad \text{and} \quad 3 \frac{m_j T_j}{e_j^2 r R B_\phi^2} \quad (8.16)$$

The factor $\eta_{0j} v_{\theta j} / (e_j n_j r v_{\phi j} \beta B_\theta R)$ has been plotted in Fig. 8.3 for main ions and carbon and $v_{\theta j} / (\beta v_{\phi j}) = 1$. For the light impurities, this parallel viscous force can give rise to $\tilde{\Omega}_{\phi j} \sim 10^{-2}$. The term from the gyroviscous tensor is very small, as shown in Fig. 8.3. These poloidal variations are $< \epsilon$, but since, at this point, the magnitude of the contributions to $\tilde{\Omega}_{\phi j}$ from the other terms in the expression of $v_{\phi j}$, Eq.(8.9), are not known, we retain the g_{rj} and Π_{rj} contributions.

8.5 Form of $\tilde{\Omega}_{\phi j}(r, \theta)$ and $\Xi_j(r)$

8.5.1 Poloidal variations of $\Omega_{\phi j}$

An expression for the toroidal velocity in term of other plasma parameters has previously been derived (Eq.(8.11)):

$$\frac{v_{\phi j}}{R} \equiv \Omega_{\phi j} \equiv \Omega_{\phi j 0}(r) [1 + \tilde{\Omega}_{\phi j}(r, \theta)] = \frac{v_{\theta j}}{\beta R} - \frac{1}{B_{\theta} R} \left(\frac{1}{e_j n_j} \frac{\partial p_j}{\partial r} + \frac{\partial \Phi}{\partial r} \right) + \Omega_{\phi j} U_j \quad (8.17)$$

This equation can be used to express $\tilde{\Omega}_{\phi j}$ in terms of \tilde{n}_j and other parameters.

The contributions of the poloidal velocity, the pressure and the potential terms to $\tilde{\Omega}_{\phi j}$ can be written, respectively as:

$$\tilde{\Omega}_{\phi j(v_{\theta})} = -\frac{v_{\theta j 0}}{v_{\phi j 0}} \frac{1}{\beta} (\tilde{n}_j + 2\epsilon \cos\theta) \quad (8.18)$$

$$\tilde{\Omega}_{\phi j(p)} = \frac{T_j}{e_j} \frac{\tilde{n}_{j(c,s)}}{v_{\phi j 0}} \frac{1}{B_{\theta 0} L_{\tilde{n}_{j(c,s)}}} \equiv \mathcal{V}_j^* \tilde{n}_{j(c,s)} \frac{a}{L_{\tilde{n}_{j(c,s)}}} \equiv \mathcal{V}_{j(c,s)} \tilde{n}_{j(c,s)} \quad (8.19)$$

and

$$\tilde{\Omega}_{\phi j(\Phi)} = -\frac{1}{v_{\phi j 0} B_{\theta 0}} \frac{\partial \Phi_1}{\partial r} \quad (8.20)$$

where one has written $\Phi(r, \theta) = \Phi_0(r) + \Phi_1(r, \theta)$ (the subscripts '0' and '1' do not refer to the order of magnitude of the functions but, respectively, to the FSA part and to the remaining part of the Φ function).

The parallel momentum equation for electrons,

$$\frac{1}{en_e} \frac{\partial p_e}{\partial \theta} = \frac{\partial \Phi}{\partial \theta}, \quad (8.21)$$

can be rewritten as:

$$\frac{\partial}{\partial \theta} \left[\frac{T_e}{e} \ln(1 + \tilde{n}_e) \right] = \frac{\partial \Phi_1}{\partial \theta} \quad (8.22)$$

and it can be used to derive:

$$\Phi_1(r, \theta) = \frac{T_e}{e} [\ln(1 + \tilde{n}_e) + O(<\tilde{n}_e^2>)] \simeq \frac{T_e}{e} \tilde{n}_e \quad (8.23)$$

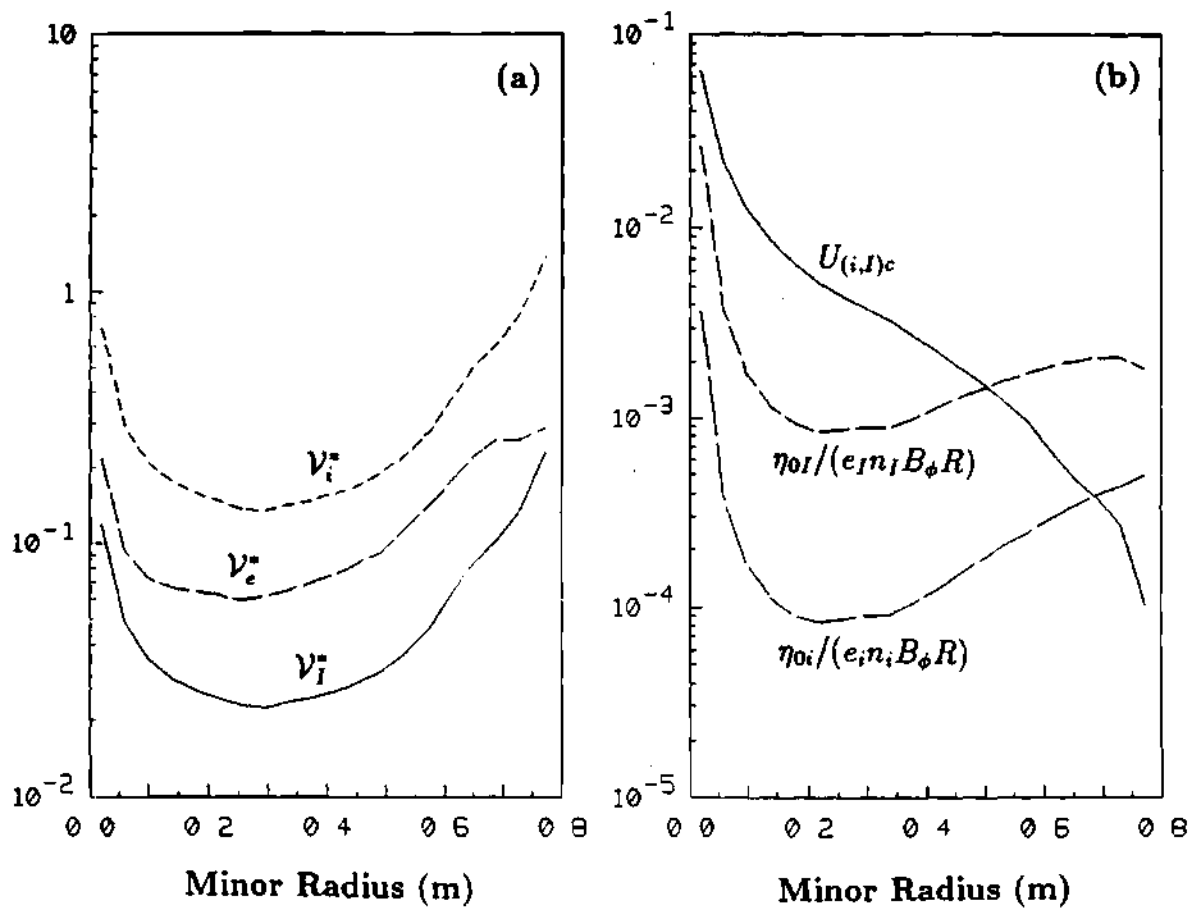


Figure 8.3: Magnitude of terms entering the expression of $\Omega_{\phi j}$ versus minor radius (shot 37309-123): (a) ν_j^* , with $j=e, i, I$, as defined in Eqs. (8.19) and (8.28); (b) U_{jc} as defined by Eq.(8.12); $\eta_{0j}/(e_j n_j B_\phi R)$, proportional to U_j , Eq.(8.13) ($j=i, I$).

and therefore

$$\frac{\partial \Phi_1}{\partial r} = -\frac{T_e \tilde{n}_e}{e} \left(\frac{1}{L_{T_e}} + \frac{1}{L_{\tilde{n}_e}} \right) \quad (8.24)$$

This formulation incorporates the measured value of the electron temperature gradient in the determination of $\partial \Phi_1 / \partial r$.

Alternatively one can also rewrite [114]:

$$\Phi_1(r, \theta) = \Phi_0(r) \tilde{\Phi}(r, \theta) \quad \text{and} \quad \frac{\partial \Phi_1}{\partial r} = \frac{\partial \Phi_0}{\partial r} \tilde{\Phi} + \frac{\partial \tilde{\Phi}}{\partial r} \Phi_0 \quad (8.25)$$

which, upon using Eq.(8.23), becomes:

$$\frac{\partial \Phi_1}{\partial r} = \frac{T_e}{e \Phi_0} \left[\frac{\partial \Phi_0}{\partial r} - \frac{\Phi_0}{L_{\tilde{\Phi}}} \right] \tilde{n}_e \quad (8.26)$$

This formulation provides an *alternative* form for the evaluation of $\partial \Phi_1 / \partial r$ which incorporates the constraint

$$\frac{\partial \Phi_0}{\partial r} = B_\phi v_{\theta j} - B_\theta v_{\phi j}, \quad (8.27)$$

the measured value of $v_{\phi j}$ and a constraint on the quantity $(T_e / e \Phi_0)$ which can be related to experiment. Experimental measurements of the plasma potential on ISX-B [115] have reported values of $\Phi_0 \sim T_e / e$. We note that the two forms, Eqs. (8.24) and (8.26) are formally equivalent, but have different explicit dependences on measured quantities. Both forms suffer from the need to evaluate $L_{\tilde{x}}$ quantities approximately.

The contribution of the potential to $\tilde{\Omega}_{\phi j}$, Eq.(8.20), can be formally written as $\tilde{\Omega}_{\phi j(\Phi)} = \mathcal{V}_{e(c,s)} \tilde{n}_{e(c,s)}$ and specifically as

$$\tilde{\Omega}_{\phi j(\Phi)} = \frac{1}{B_\theta} \frac{T_e}{e} \frac{\tilde{n}_{e(c,s)}}{v_{\phi j}} \left(\frac{1}{L_{T_e}} + \frac{1}{L_{\tilde{n}_{e(c,s)}}} \right) \equiv \mathcal{V}_e^* \left(\frac{a}{L_{T_e}} + \frac{a}{L_{\tilde{n}_{e(c,s)}}} \right) \tilde{n}_{e(c,s)}, \quad (8.28)$$

when Eq.(8.24) is used to evaluate $\partial \Phi_1 / \partial r$, or as

$$\tilde{\Omega}_{\phi j(\Phi)} = \left(1 - \frac{v_{\theta j}}{\beta v_{\phi j}} - \frac{\Phi_0}{B_\theta L_{\tilde{\Phi}} v_{\phi j}} \right) \frac{T_e}{e \Phi_0} \tilde{n}_e, \quad (8.29)$$

when Eq.(8.26) is used instead.

The \mathcal{V}_j^* and \mathcal{V}_e^* functions have been plotted in Fig. 8.3 for a TFTR shot.

Equations (8.28) and (8.29) provide similar results when $[1 - v_{\theta j}/(\beta v_{\phi j}) - \Phi_0/(B_\theta L_{\tilde{\Phi}} v_{\phi j})] \sim \mathcal{V}_e^*$ [114]. The formulation of Eq.(8.24) allows the use of measured T_e gradients, while the formulation of Eq.(8.26) allows the use of experimental Φ_0 and v_ϕ . Since the Φ_0 data are non-existent for the TFTR experiments, we will base our calculations on Eq.(8.24) and discuss how the results would be affected if we had used Eq.(8.26) [114]. To this end, we note that the value $\mathcal{V}_e^* \sim 0.1$, in the plasma center (Fig. 8.3), implies that the term $T_e/(e\Phi_0)[1 - v_{\theta j}/(\beta v_{\phi j}) - \Phi_0/(B_\theta L_{\tilde{\Phi}} v_\phi)] \sim 0.1$, if the formulations of Eqs. (8.24) and (8.26) are consistent with each other. Our subsequent calculations with the $q=0$ model will give $v_{\theta I}/\beta v_{\phi I} \ll 1$ as a result, thus implying $(T_e/e\Phi_0) \sim 0.1$, which is rather smaller than expected on the basis of the ISX-B results [115].

The contribution of inertia and viscosity terms, the magnitude of which has been discussed earlier, are:

$$\tilde{\Omega}_{\phi j(g_r)} + \tilde{\Omega}_{\phi j(\Pi_r^e)} \equiv U_{jc} \cos\theta + U_{js} \sin\theta \quad (8.30)$$

Summing all the terms that contribute to the poloidally varying part of $\Omega_{\phi j}$, one obtains:

$$\tilde{\Omega}_{\phi j}(r, \theta) = \tilde{\Omega}_{\phi jc}(r) \cos\theta + \tilde{\Omega}_{\phi js}(r) \sin\theta \quad (8.31)$$

with:

$$\tilde{\Omega}_{\phi jc}(r) = -\frac{v_{\theta j}}{v_{\phi j}\beta}(2\epsilon + \tilde{n}_{jc}) + \mathcal{V}_{jc}\tilde{n}_{jc} + \mathcal{V}_{ec}\tilde{n}_{ec} + U_{jc} \quad (8.32)$$

$$\tilde{\Omega}_{\phi js}(r) = -\frac{v_{\theta j}}{v_{\phi j}} \frac{\tilde{n}_{js}}{\beta} + \mathcal{V}_{js}\tilde{n}_{js} + \mathcal{V}_{es}\tilde{n}_{es} + U_{js} \quad (8.33)$$

The magnitude of the $\tilde{\Omega}_{\phi j}$ is determined by the magnitudes of \tilde{n}_j and $v_{\theta j}$, which one must now proceed to evaluate. Indications concerning the importance of the different terms in Eqs. (8.32) and (8.33) are given by Fig. 8.3.

8.5.2 Relation to gyroviscous torque

Relation between $\tilde{\Theta}$ and Ξ_j [114]

The gyroviscous torque of Eq.(3.13) can be written

$$\langle R\hat{\phi}\nabla\cdot\Pi_j^{3,4} \rangle = -\frac{R_0}{r}\frac{\partial}{\partial r}(\eta_{4j0}v_{\phi j0}\Xi_j) \quad (8.34)$$

where

$$\Xi_j \equiv \frac{\tilde{\Omega}_{\phi js}(4\epsilon + \tilde{n}_{jc}) - \tilde{n}_{js}\tilde{\Omega}_{\phi jc}}{2} \quad (8.35)$$

The gyroviscous model that was used to analyze the experimental data in Chapter 6 was based on Eq.(3.16), which leads for an expression for the total torque summed over (ion) species

$$\sum_j \langle R\hat{\phi}\nabla\cdot\Pi_j^{3,4} \rangle = -\sum_j \frac{\tilde{\Theta}_j}{2} \frac{r}{R_0} \frac{\partial}{\partial r}(\eta_{4j0}v_{\phi j0}) \quad (8.36)$$

which, upon defining

$$G_j \equiv -\frac{r}{\eta_{4j0}v_{\phi j}} \frac{\partial(\eta_{4j}v_{\phi j})}{\partial r} \quad (8.37)$$

and assuming $v_{\phi j}$ independent of ion species, can be written

$$\begin{aligned} \sum_j \langle R\hat{\phi}\nabla\cdot\Pi_j^{3,4} \rangle &= -\sum_j \frac{\tilde{\Theta}_j G_j}{2} \frac{v_{\phi}}{R} \frac{m_j n_j T_j}{e B Z_j} \\ &= -\frac{m_D n_e v_{\phi} T_I}{2e B R} \sum_j \frac{n_{j0}}{n_e} \tilde{\Theta}_j G_j \equiv -\frac{m_D n_e v_{\phi} T_I}{2e B R} \left(\frac{\Theta G}{Z}\right)_{eff} \end{aligned} \quad (8.38)$$

when $n_j \simeq m_D Z_j$ is used.

Two models for estimating the quantity $(\Theta G/Z)_{eff}$ were discussed in Section 3.2.2. It was shown in Chapter 6 that $(\tilde{\Theta} = 1.5, G = 1, Z = \tilde{Z})$ and $(\tilde{\Theta} = 0.4, G = 1, Z = Z_{eff})$ models could both reproduce the experimental data on $v_{\phi}(0)$ and τ_{ϕ} . Both of these models correspond to $(\Theta G/Z)_{eff} \sim O(0.1)$. Thus, in order to check the reasonableness of the values of $(\Theta G/Z)_{eff}$ chosen to fit the experimental data in Chapter 6, we will estimate

$$\left(\frac{\Theta G}{Z}\right)_{eff} \equiv G_i \tilde{\Theta}_i \frac{n_i}{n_e} + G_I \tilde{\Theta}_I \frac{n_I}{n_e} \quad (8.39)$$

where the expression for the individual species asymmetry function is given by

$$\tilde{\Theta}_j \equiv \frac{2}{\epsilon^2} \Xi_j \quad (8.40)$$

Note that the contribution to $(\Theta G/Z)_{eff}$ from the metallic impurities is not being treated explicitly. Charge neutrality and the definition of Z_{eff} lead to

$$\frac{n_i}{n_e} = \frac{Z_I - Z_{eff}}{Z_I - 1} \quad \frac{n_I}{n_e} = \frac{Z_{eff} - 1}{Z_I(Z_I - 1)} \quad (8.41)$$

Different formulations of the gyroviscous torque flow [114]

The experimental torque flow is constructed from

$$K_{\phi}^{ex}(r) = (2\pi)^2 R \int_0^r < R \mathcal{M}_{\phi} > r' dr' \quad (8.42)$$

where \mathcal{M}_{ϕ} is the toroidal component of the NBI momentum input rate. The corresponding theoretical quantity is obtained by replacing $< R \mathcal{M}_{\phi} >$ with

$\sum_j < R \hat{\phi} \cdot \nabla \cdot \vec{\Pi}_j >$ when acceleration and convective terms can be neglected. For the gyroviscous torque

$$< R \hat{\phi} \cdot \nabla \cdot \vec{\Pi}_j > = -\frac{R_0}{r} \frac{\partial}{\partial r} (\eta_{4j} v_{\phi j} \Xi_j) \quad (8.43)$$

which leads to

$$\begin{aligned} K_{\phi}^{GV}(r) &= -(2\pi R)^2 \sum_j \int_0^r \frac{\partial}{\partial r'} (\eta_{4j} v_{\phi j} \Xi_j) dr' \\ &= -(2\pi R)^2 \sum_j \int_0^r \eta_{4j} v_{\phi j} \frac{\Xi_j}{(r')^2} \left(\frac{r'}{\eta_{4j} v_{\phi j} \Xi_j} \frac{\partial (\eta_{4j} v_{\phi j} \Xi_j)}{\partial r'} \right) r' dr' \\ &= (2\pi R)^2 \sum_j \int_0^r \eta_{4j} v_{\phi j} \frac{\Xi_j}{(r')^2} G_j r' dr' \end{aligned} \quad (8.44)$$

where

$$G_j \equiv -\frac{r'}{\eta_{4j} v_{\phi j} \Xi_j} \frac{\partial (\eta_{4j} v_{\phi j} \Xi_j)}{\partial r'} = -\frac{r'}{\eta_{4j} v_{\phi j}} \frac{\partial (\eta_{4j} v_{\phi j})}{\partial r'} - \frac{r'}{\Xi_j} \frac{\partial \Xi_j}{\partial r'} \equiv G_{\eta v_j} + G_{\Xi_j} \quad (8.45)$$

The original formulation of the gyroviscous torque flow was based upon making the separation of variables, or weak-radial-dependence of poloidal asymmetries, assumption in the evaluation of the radial profile factor G_j , which is equivalent to setting the G_{Ξ_j} term to zero in Eq.(8.45). This leads to

$$\begin{aligned} K_{\phi}^{gv*} &= (2\pi R)^2 \sum_j \int_0^r \eta_{4j} v_{\phi j} \frac{\Xi_j}{(r')^2} G_{\eta v_j} r' dr' \\ &= (2\pi)^2 \sum_j \int_0^r \eta_{4j} v_{\phi j} \frac{\tilde{\Theta}_j}{2} G_{\eta v_j} r' dr' \end{aligned} \quad (8.46)$$

Making the further approximation that an effective value of Ξ_j/ϵ^2 can be defined and removed from the integral leads to Eq.(3.20) and to

$$K_\phi^{gv} = (2\pi)^2 \sum_j \frac{\Xi_j}{\epsilon^2} \int_0^r \eta_{4j} v_{\phi j} G_{\eta v_j} r' dr' = (2\pi)^2 \sum_j \frac{\tilde{\Theta}_j}{2} \int_0^r \eta_{4j} v_{\phi j} G_{\eta v_j} r' dr' \quad (8.47)$$

which is the expression plotted in Fig. 6.6.

The above formulation of the gyroviscous theory treats the torque as the fundamental quantity and performs a volume integral of the gyroviscous torque to compare with a volume integral of the input torque - the experimental torque flow [114]. The essential approximation is separation of variables, or $G_{\Xi_j} = 0$. Since the one presented in this thesis is the first calculation of the poloidal asymmetries, $\tilde{\Theta}$ and Ξ_j , the previous evaluation of the gyroviscous torque flow used effective $\tilde{\Theta}_j$ motivated by physical considerations. We are able, for the first time, to evaluate these poloidal asymmetry factors.

A *third* formulation of the gyroviscous torque flow, which avoids the separation of variables approximations, follows from simple integration of Eq.(8.44)

$$\hat{K}_\phi^{gv}(r) = -(2\pi R)^2 \sum_j (\eta_{4j} v_{\phi j} \Xi_j)|_r \quad (8.48)$$

One has made use of $\Xi_j(0) = 0$, which can be argued from physical considerations.

We note that [114] \hat{K}_ϕ^{gv} is mathematically equivalent to K_ϕ^{gv*} when $G_{\eta v_j}$ is replaced by $(G_{\eta v_j} + G_{\Xi_j})$ in Eq.(8.46).

8.6 Poloidal momentum balance equation

8.6.1 General case

The steady state poloidal projection of the momentum equation, for ion species j , is:

$$g_{\theta j} + \frac{\partial}{\partial l_\theta} p_j + e_j n_j \frac{\partial \Phi}{\partial l_\theta} + e_j n_j v_{rj} B_\phi - \mathcal{M}_{\theta j} - R_{\theta j} + \Pi_{\theta j} + m_j v_{\theta j} \mathcal{S}_j = 0 \quad (8.49)$$

where the inertia term can be written:

$$\begin{aligned} g_{\theta j} &= m_j n_j \left[-\frac{v_{\phi j}^2}{R} \frac{\partial R}{\partial l_\theta} + \frac{1}{2} \frac{\partial v_{\theta j}^2}{\partial l_\theta} + \frac{v_{rj}}{r} \frac{\partial (rv_{\theta j})}{\partial r} \right] = \\ &= m_j n_j \left[v_{\phi j}^2 \frac{\sin \theta}{R} + v_{\theta j}^2 \left(\frac{\sin \theta}{R} - \frac{\vartheta_j}{r} \right) \right] + \frac{v_{rj}}{r} \frac{\partial (rv_{\theta j})}{\partial r} \end{aligned} \quad (8.50)$$

The flux surface average of (Eq.(8.49))/($n_j h$) is:

$$\begin{aligned} m_j R_0 \langle \Omega_{\phi j}^2 \sin \theta \rangle + \frac{m_j}{r} \langle \frac{v_{rj}}{h} \frac{\partial (rv_{\theta j})}{\partial r} \rangle + \langle \frac{e_j v_{rj} B_\phi}{h} \rangle \\ - \langle \frac{R_{\theta j}}{h n_j} \rangle + \langle \frac{\Pi_{\theta j}}{h n_j} \rangle - \langle \frac{\mathcal{M}_{\theta j}}{h n_j} \rangle + \langle \frac{m_j v_{\theta j} \mathcal{S}_j}{h n_j} \rangle = 0 \end{aligned} \quad (8.51)$$

Subtracting Eq. 8.51 from (Eq. 8.49)/(n_j), one obtains an equation that describes the poloidal variations of the density, as result of the equilibrium between the pressure, electric field, centrifugal and viscous forces:

$$\frac{1}{n_j} \frac{\partial n_j}{\partial \theta} + Z_j \frac{T_e}{T_j} \frac{1}{n_e} \frac{\partial n_e}{\partial \theta} + \frac{m_j (v_{\phi j}^2 + v_{\theta j}^2)}{T_j} \epsilon \sin \theta + \frac{r}{T_j} \left(\frac{\Pi_{\theta j}}{n_j} - \langle \frac{\Pi_{\theta j}}{h n_j} \rangle \right) + \mathcal{H}_j = 0 \quad (8.52)$$

with

$$\begin{aligned} \mathcal{H}_j &\simeq -m_j \frac{v_{\theta j}^2}{T_j} \vartheta_j + \frac{r}{T_j} \left[e_j v_{rj} B_\phi \bar{v}_{rj} - \frac{\mathcal{M}_{\theta j}}{n_j} - \left(\frac{R_{\theta j}}{n_j} - \langle \frac{R_{\theta j}}{h n_j} \rangle \right) \right] \\ &+ \frac{m_j}{T_j} \left[v_{\theta j} \frac{\partial (rv_{rj})}{\partial r} - \langle \frac{v_{\theta j}}{h} \frac{\partial (rv_{rj})}{\partial r} \rangle \right] + \frac{r}{T_j} \left(\frac{\Pi_{\theta j}}{n_j} - \langle \frac{\Pi_{\theta j}}{h n_j} \rangle \right)_{\text{residual terms}} \end{aligned} \quad (8.53)$$

Let's rewrite Eq.(8.52) as:

$$\frac{1}{n_j} \frac{\partial n_j}{\partial \theta} + Z_j \frac{T_e}{T_j} \frac{1}{n_e} \frac{\partial n_e}{\partial \theta} + \mathcal{D}_j = 0 \quad (8.54)$$

For a two ion species plasma (i=main ions; I=light impurity) the system of Eqs. (8.54)_{j=i,I} can be solved in terms of \tilde{n}_j . The presence of the metal impurities, which would affect the other ions through the potential and collision terms, can be neglected since we are considering discharges with $Z_{met} \equiv Z_M^2 n_M / n_e = 0.1 - 0.6$ (M=metal impurity). The poloidal variation of the impurity density, in the case of $m_I = m_i Z_I$, $v_{\phi i} \sim v_{\phi I}$ and $T_i \sim T_I$ is described by:

$$\frac{1}{n_I} \frac{\partial n_I}{\partial \theta} = [-\mathcal{D}_I (1 + Z_i^2 \frac{n_i T_e}{n_e T_I}) + \mathcal{D}_i Z_i Z_I \frac{n_i T_e}{n_e T_I}] (1 + \frac{T_e}{T_I} Z_{eff})^{-1} \quad (8.55)$$

For the main ions:

$$\frac{1}{n_i} \frac{\partial n_i}{\partial \theta} = -[\mathcal{D}_i + Z_i Z_I \frac{n_I T_e}{n_e T_i} (\frac{1}{n_I} \frac{\partial n_I}{\partial \theta})] (1 + Z_i \frac{n_i T_e}{n_e T_i})^{-1} \quad (8.56)$$

8.6.2 Case $\tilde{q}_j = 0$

For simplicity, we first evaluate \tilde{n}_j by neglecting the contribution of the heat flux to the viscous and friction forces. Eq. 8.52 becomes:

$$\begin{aligned} \frac{1}{n_j} \frac{\partial n_j}{\partial \theta} + Z_j \frac{T_e}{T_j} \frac{1}{n_e} \frac{\partial n_e}{\partial \theta} + \left(\frac{m_j(v_{\phi j}^2 + v_{\theta j}^2)}{T_j} - \frac{13}{2} \frac{\beta R}{\omega_{cj}} \frac{\partial \Omega_{\phi j}}{\partial r} \right) \epsilon \sin \theta \\ + \frac{\eta_{0j} v_{\theta j}}{r p_j} \left(\epsilon \cos \theta - \frac{2}{3} \frac{\partial \vartheta_j}{\partial \theta} \right) - \frac{\eta_{0j} \beta}{\epsilon p_j} \frac{\partial A_j}{\partial \theta} + \mathcal{H}_j = 0 \end{aligned} \quad (8.57)$$

where the following expressions have been used (see also Appendix C):

$$\frac{\Pi_{\theta j}^0}{n_j} - \left\langle \frac{\Pi_{\theta j}^0}{h n_j} \right\rangle = \frac{\eta_{0j} v_{\theta j}}{n_j r^2} \left[\epsilon \cos \theta - \frac{2}{3} \frac{\partial \vartheta_j}{\partial \theta} + O(\epsilon^2) \right] - \frac{\eta_{0j} \beta}{\epsilon r n_j} \left(\frac{\partial A_j}{\partial \theta} + O(\epsilon^2) \right) \quad (8.58)$$

$$\begin{aligned} \frac{\Pi_{\theta j}^{3,4}}{n_j} - \left\langle \frac{\Pi_{\theta j}^{3,4}}{h n_j} \right\rangle \simeq \frac{T_j}{\omega_{cj}} \left[- (13 \sin \theta - 3 \frac{\vartheta_j}{\epsilon}) \frac{\beta}{2} \frac{\partial \Omega_{\phi j}}{\partial r} + \frac{v_{\theta j}}{2 r R} (-\mathcal{P}_{2j} \sin \theta \right. \\ \left. + \mathcal{P}_{3j} \frac{\vartheta_j}{\epsilon}) + \frac{\beta}{\epsilon} \frac{\mathcal{P}_{1j}}{2} \frac{A_j}{r} - \frac{\beta}{\epsilon} \frac{\partial A_j}{\partial r} \right] \end{aligned} \quad (8.59)$$

The terms that have been gathered under the \mathcal{H}_j term, have a magnitude that, for a TFTR-like plasma, is much smaller than the magnitude of the centrifugal force and viscosity terms in Eq.(8.52). Let us define a series of parameters representative of the order of magnitude of the terms in Eq.(8.52), which parameters are functions of experimental quantities:

$$\Upsilon_{g\theta j} = m_j \frac{v_{\phi j}^2}{T_j} \epsilon = 2 \epsilon \left(\frac{v_{\phi j}}{v_{thj}} \right)^2 \quad (8.60)$$

$$\Upsilon_{R\theta j} = m_j r v_{\theta j}^* \epsilon \nu_{jk} / T_j \quad (v_{\theta}^* \equiv \beta v_{\phi I}) \quad (8.61)$$

$$\Upsilon_{M\theta j} = r \beta \mathcal{M}_{\phi j} / p_j \quad (8.62)$$

$$\Upsilon_{\Pi_{\theta j}^0} = \frac{\eta_{0j} v_{\theta j}^*}{p_j R} \quad (8.63)$$

$$\Upsilon_{\Pi_{\theta j}^{3,4}} = - \frac{13}{2} \frac{\beta}{\omega_{cj}} \frac{\partial v_{\phi j}}{\partial r} \epsilon \quad (8.64)$$

$$\Upsilon_{J_{rj}} = e_j r v_{rj}^* \epsilon B_{\phi} / T_j \quad (v_{rj}^* \equiv \Gamma_e^{exp} / n_j Z_j) \quad (8.65)$$

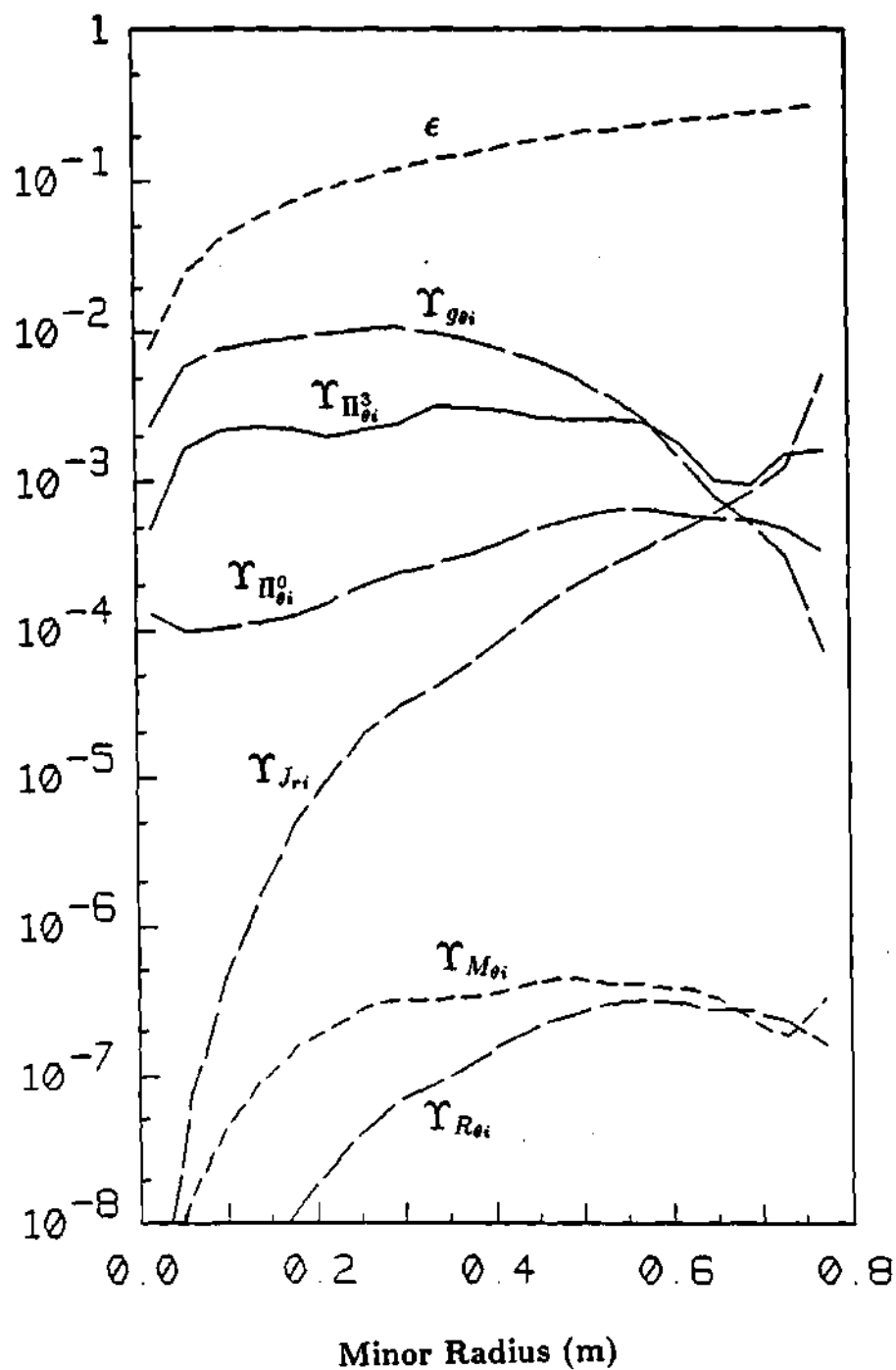


Figure 8.4: Radial profiles of the poloidal momentum balance equation terms, Υ_i , defined in Eqs. (8.60)-(8.65)), calculated for the deuterium main ions (Shot 37309-23).

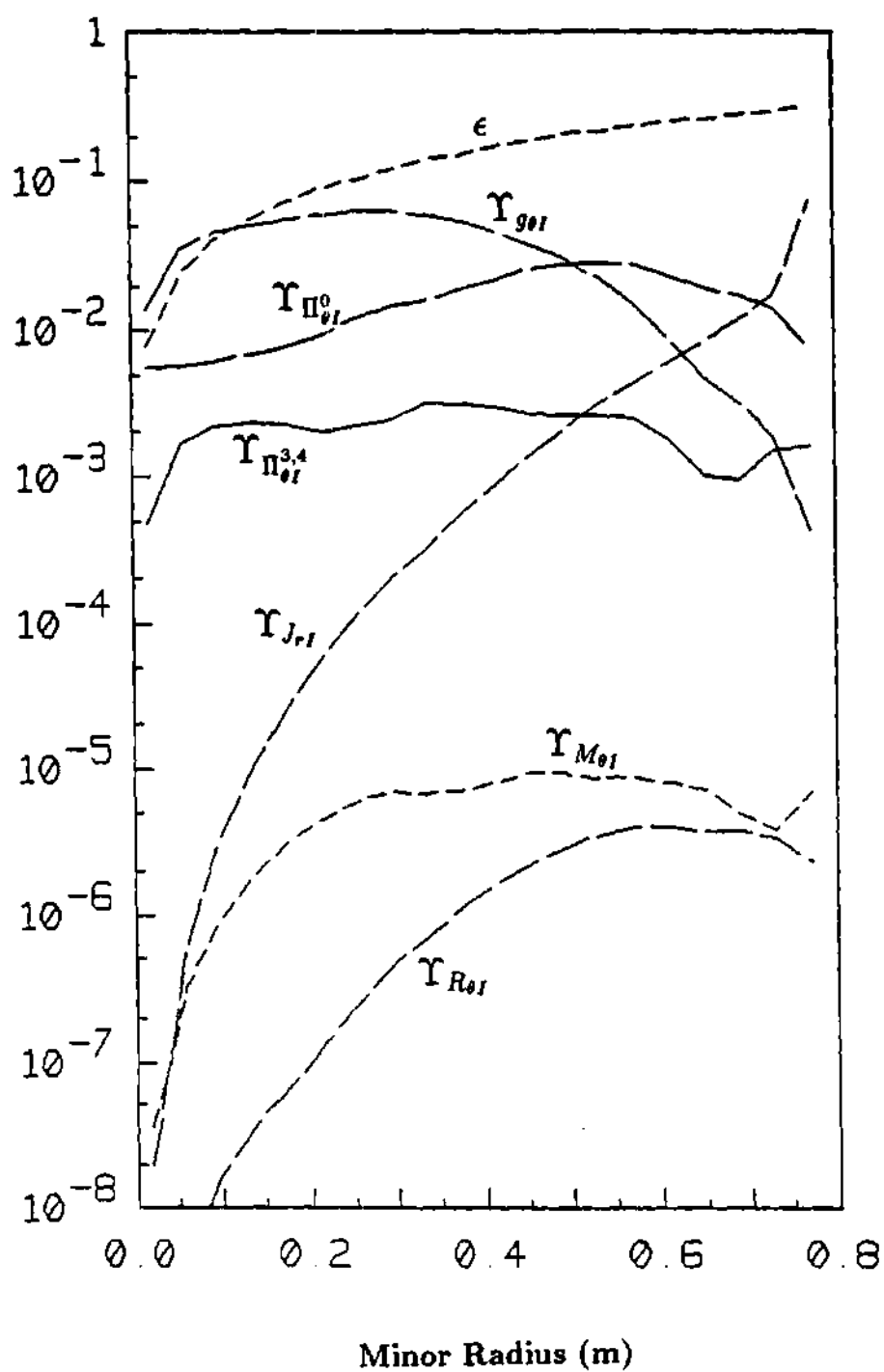


Figure 8.5: Radial profiles of the poloidal momentum balance equation terms, Υ_I , calculated for carbon impurities (Shot 37309-123)

It has been assumed that $\bar{n}_j \sim O(\epsilon)$ or smaller, and that $v_{\theta j} \sim O(v_{\phi j}\beta)$ or smaller. The Υ 's have been evaluated for a typical TFTR shot and their magnitudes are shown in Figs. 8.4 and 8.5 for deuterium main ions and carbon impurities.

$\Upsilon_{g\theta j}$ represents the order of magnitude of the inertia term; it is $< \epsilon$ because the main ions and the light impurities are subsonic. The ratio $v_{\phi j}/v_{th j}$, $j=i,I$, has been plotted in Fig. 8.6 for Shot 37309.

$\Upsilon_{R\theta j}$ represents the order of magnitude of the friction term. Differently from the cases of collisional plasmas, reviewed in Section 7.2, where $\bar{n}_{I\theta}$ was found to be driven by the friction force, this term is very small for this set of TFTR shots because of the low ion collisionality. The radial profiles of the collision frequencies, ν_j^* and ν_{jk} have been plotted in Fig. 8.6.

$\Upsilon_{\Pi_{\theta j}^0}$ represents terms from the parallel viscosity tensor. In case of $v_{\theta j}/(v_{\phi j}\beta) \sim 1$ ($\bar{q}_j = 0$ case) this term is $O(0.1 \epsilon)$ for the impurities and can drive the $\bar{n}_{I\theta} \sim 0.1\epsilon$.

$\Upsilon_{\Pi_{\theta j}^{3,4}}$ is of the order of the inertia term for the main ions but can be neglected in the case of impurities. $\Upsilon_{M_{\theta j}}$ represents the magnitude of the momentum input and can be neglected. $\Upsilon_{J_{rj}}$ represents the magnitude of the radial particle flux term and is negligible over most of the plasma region.

Since we can conclude that the \mathcal{H}_j 's terms are much smaller than the remaining terms in Eq.(8.52), for ions and carbon in a TFTR-like plasma, a proper way to evaluate the poloidal variations of density and velocity is the following.

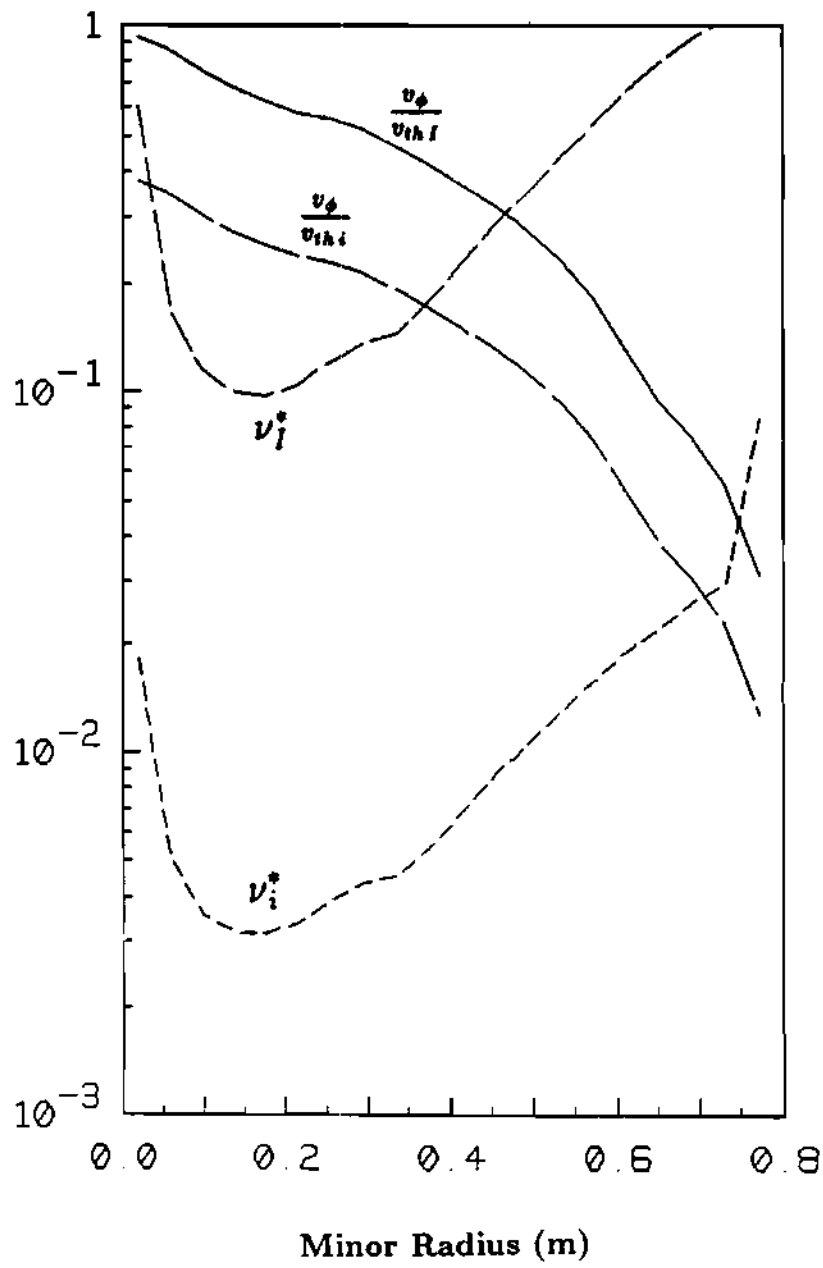


Figure 8.6: Radial profiles of $v_{\phi j}/v_{thj}$ and ν_j^* , $j=i,I$ (i = deuterium, I =carbon; Shot 37309-123).

8.7 Could anomalous forces affect \tilde{n}_j , $\tilde{\Omega}_{\phi j}$, $v_{\theta j}$?

8.7.1 Introduction

The fluid equations used so far in this Chapter describe neoclassical transport.

There are several disagreements between experimental results and neoclassical predictions of ion transport [116]: (1) density profile perturbation experiments, that allow simultaneously measurement of particle diffusion coefficient, D_i , and pinch velocity, v_j^{pinch} , give values of D_i and v_i^{pinch} that are 1-2 orders of magnitude larger than the neoclassical values; (2) ion thermal diffusivities are 1-2 orders of magnitude larger than the neoclassical estimate; (3) toroidal momentum transport is also a few orders of magnitude larger than predicted by neoclassical perpendicular viscosity. The hypothesis that gyroviscosity could account for the observed transport of toroidal momentum [24] is one of the points of investigation of this thesis and we reserve comment on the comparison between neoclassical momentum transport theory and experimental measurements to the end of the thesis.

Since there are also indications (discussed below) that anomalous mechanisms can account for some of the mentioned disagreements, we need to discuss if and how anomalous forces could arise in the momentum balance equation and heat flux equation, affecting therefore the magnitude of \tilde{n}_j , $\tilde{\Omega}_{\phi j}$ and $v_{\theta j}$.

The transport equations, used to investigate fluctuation-induced fluxes include a number of additional terms rising from the time-averaging of the fluctuating plasma parameters. In the presence of electrostatic and magnetic fluctuations driven transport, the poloidal momentum balance equation becomes: [117],[118]

$$\frac{\partial \bar{p}_j}{\partial t_\theta} + \bar{\Pi}_{\theta j} - e_j \bar{n}_j \bar{E}_\theta - e_j \langle \tilde{n}_j \tilde{E}_\theta \rangle + \langle \tilde{J}_{\parallel j} \tilde{B}_r \rangle + e_j B_\phi \bar{\Gamma}_j = 0 \quad (8.66)$$

where \bar{x} and \tilde{x} indicate the time-averaged and fluctuating component of the plasma parameter x in Eq.(8.66). The friction and momentum input terms do not appear because the collision frequency was assumed to be smaller than the fluctuation fre-

quency.

In case of fluctuation driven radial particle fluxes, the first three terms of Eq.(8.66) can be neglected with respect to the remaining terms and the radial particle flux is given by [116]:

$$\bar{\Gamma}_j = \langle \tilde{n}_j \tilde{E}_\theta \rangle / B_\phi - \langle \tilde{J}_{\parallel j} \tilde{b}_r \rangle / e_j \quad (8.67)$$

As reviewed in Section 7.6, the FSA heat flux poloidal or parallel balance equation must be used in conjunction with the FSA poloidal or parallel momentum balance equation if $v_{\theta j}$ has to be evaluated.

In the presence of electrostatic/magnetic driven transport, the terms $e_j q_{rj}^{\tilde{E}} B_\phi / T_j$ and $e_j q_{rj}^{\tilde{B}} B_\phi / T_j$, where

$$q_{rj}^{\tilde{E}} \equiv \frac{5}{2} n_j \langle \tilde{T}_j \tilde{E}_\theta \rangle / B_\phi \quad \text{and} \quad q_{rj}^{\tilde{B}} = g_j \langle \tilde{b}_r / B \rangle \nabla T_j \quad (8.68)$$

should be added to the LHS of Eq.(A.7) [117],[116].

8.7.2 Fluctuation measurements and inferred fluctuation-driven radial flux

Fluctuation of plasma parameters have been measured in several tokamaks, for a variety of plasma conditions, but a satisfactory theoretical model which explains the origin of the fluctuations has not yet been identified.

In the edge plasma region, \tilde{n}_j and \tilde{E}_θ are commonly measured with biased or fluctuating Langmuir probes [119]. The probe measures electron density fluctuations. At low frequencies ($1 \text{ kHz} - 1 \text{ MHz} \ll \omega_{pi} < \omega_{pe}$) it is commonly assumed that there are ion density fluctuations of the same frequency and amplitude. The Heavy Ion Beam Probe (HIBP) [120] allows simultaneous measurements of \tilde{n}_e and \tilde{E}_θ in the plasma bulk. Various laser and microwave scattering techniques [121] can be employed to measure the density fluctuations; the data can then be used to evaluate $\Gamma_e^{\tilde{E}} \equiv \langle \tilde{n}_e \tilde{E}_\theta \rangle / (e B_\phi)$, but some assumption about the electric field fluctuation is required in this case.

In order to evaluate the magnetic field term, $\Gamma_j^{\tilde{E}} \equiv - \langle \tilde{J}_{\parallel j} \tilde{b}_r \rangle / e_j$ one should measure both parallel current and magnetic field fluctuations, but this is not done. Instead, only the B_r fluctuations are measured with magnetic probes at the edge and a model [116] is employed to estimate $\tilde{J}_{\parallel j}$.

Most of the available edge fluctuation measurements pertain to OH plasmas; the probe survival becomes in fact critical at the high edge temperature associated with additional heating. The employment of the HIBP diagnostic to measure density and electric field fluctuations is recent and only a few sets of measurements are available (TEXT [122] and ISX-B NBI plasma [123]).

The magnitude of \tilde{n}_j / n_j and $\tilde{E}_\theta / E_\theta$ are in the range 10-60 % (depending on plasma parameters) at the edge and decrease toward the center, reducing to a few percent for $r/a < 0.5$; \tilde{B}_r / B is found to be smaller than 10^{-4} at the edge.

The analysis of the correlation between \tilde{n}_j and \tilde{E}_θ allows the evaluation of the magnitude of $\Gamma_j^{\tilde{E}}$ and the comparison with the estimated radial particle flux. Figure 8.7 [116] shows the comparison between the radial profile of ion particle flux from measurements of particle sources (H_α emission), designated as Γ_j , and the quantity $\Gamma_j^{\tilde{E}}$ in the TEXT OH plasma. In this case, the particle flux and the electrostatic fluctuation driven flux ($\Gamma_j^{\tilde{E}}$) have similar magnitude and radial dependence. Toward the plasma center, both Γ_j and the fluctuation amplitude decrease considerably with respect to the edge. In general the exact parameters required to determine the fluctuation driven fluxes are not available and one must interpret the limited data using analytical models.

Very recently, $\Gamma^{\tilde{E}}$ was calculated [122] for the interior OH TEXT plasma using \tilde{n}_j and Φ as measured by HIBP. The \tilde{E}_θ was estimated assuming that Dissipative Trapped Electron (DTE) modes were the cause of the observed turbulence. The magnitude of $\Gamma^{\tilde{E}}$ was found to explain the observed particle flux, but the magnitude of the wave-length number inferred from the experiment did not agree with the hypothesis

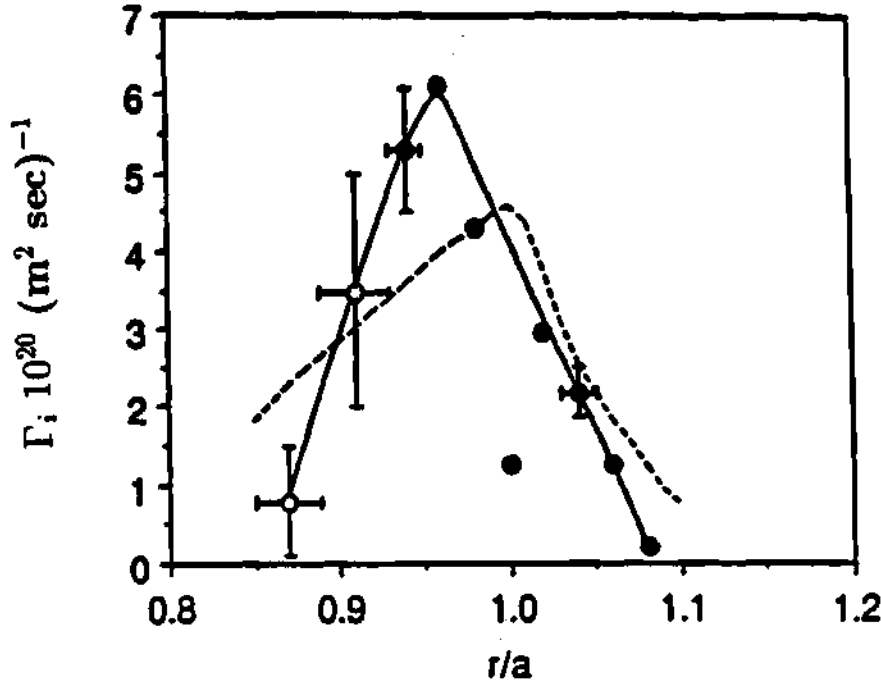


Figure 8.7: Comparison between the particle flux, Γ_i , inferred from H_α measurements (dotted line) and $\Gamma_i^{\hat{E}}$ calculated from Langmuir probes data (solid lines, solid points) and from HIBP data (open points). [116]

of DTE driven transport.

Experimental results from ISX-B show that NBI increases the fluctuation amplitude and therefore $\Gamma_e^{\hat{E}}$. The $\Gamma_e^{\hat{E}}$ was evaluated for both NBI and OH plasmas in ISX-B [123] in the region $r/a = [0.6 - 1]$, using density and electric field fluctuation measurements from the HIBP. The magnitude of $\Gamma_e^{\hat{E}}$ term was found to be one order of magnitude larger for NBI (0.8 MW) than for OH discharges. The particle confinement times, inferred by assuming $\Gamma_i = \Gamma_i^{\hat{E}}$, were larger than expected in the OH plasma (60 ± 30 ms), and in reasonable agreement with the values of τ_p (~ 3 ms) characteristic of the NBI case.

Therefore, nothing conclusive can be said about the magnitude of $\Gamma_j^{\hat{E}}$ with respect to Γ_j in the plasma center.

There are no comparisons of fluctuation driven radial fluxes in TFTR, neither in OH nor in NBI plasmas. There are indeed measurements of density fluctuations at $r/a \sim 0.3$ from microwave scattering [124] in OH, NBI L-mode and H-mode plasmas. The k_θ (wave-length number) spectra is very similar for all three regimes as long as machine parameters are kept constant. Also the magnitude of \tilde{n}/n is essentially the same in all three cases and less than 1 % at this particular radial location.

Experimental evidence suggests that fluctuation characteristics (amplitude, parameter dependence, frequency, wave length, etc.) have similar parametric dependence in all toroidal fusion devices [116], and this suggests that the electrostatic fluctuation term, in Eq.(8.66) could be also an important term for the TFTR plasma.

The $\Gamma_j^{\tilde{B}}$ term is commonly estimated to be $\ll \Gamma_j^{\tilde{E}}$ [116] near the plasma edge of OH plasmas.

Experiments on the Doublet III tokamak [125] and JET [126] have shown that the level of \tilde{B}_r (5-50 kHz) measured outside the limiter is strongly correlated with confinement degradation in high β_θ NBI discharges and it increases with β_θ and from H to L mode. Ref. [125] comments that the measured fluctuation amplitudes indicate island structure of size sufficient to enhance transport.

Existing probe measurements [127] also show that \tilde{B}_r/B increases toward the interior.

\tilde{T}_{ions} is not measured and therefore $q_{rj}^{\tilde{E}}$ can be estimated only in conjunction with a model for ion temperature fluctuations. At the edge $\tilde{T}_e/T_e < 0.1$ and the computed $q_{re}^{\tilde{E}}$ has been found of the order of magnitude of q_{re} at the edge of several OH plasmas [116]. In the plasma interior, the investigation of correlations between measured fluctuations and q_{rj} must resort to theoretical models to evaluate $q_{rj}^{\tilde{E}}$; these results are not always in agreement with the estimate of q_{rj} from energy balance calculations [116].

8.7.3 Conclusion

A consistent treatment of coexisting neoclassical and anomalous transport mechanisms in plasmas requires a different and more radical kind of approach [128] than the simple addition of anomalous terms to neoclassical equations. Nevertheless we think that the investigation of the effect of the

$$\Gamma_j^{(\sim)} \equiv \Gamma_j^{\tilde{E}} + \Gamma_j^{\tilde{B}} \quad (8.69)$$

$$q_{rj}^{(\sim)} \equiv q_{rj}^{\tilde{E}} + q_{rj}^{\tilde{B}} \quad (8.70)$$

terms on the results is instructive and we include them in the FSA poloidal momentum equation, Eq.(8.51), and FSA heat flux balance equation, Eq.(A.7), respectively.

The anomalous term $\Gamma_j^{(\sim)}$ is not likely to affect the magnitude of \tilde{n}_j directly through the balance equation, Eq.(8.57). In fact, if $\Gamma_j^{(\sim)}$ and Γ_j are of the same order of magnitude (and this is the case at the edge), the anomalous force would be a negligible term in Eq.(8.57). In order to directly (i.e. through Eq.(8.57)) influence the magnitude of \tilde{n}_j , $\Gamma_j^{(\sim)}$ would have to manifest amplitude of poloidal variation several orders of magnitude larger than Γ_j , and this is really impossible given the magnitude of the fluctuations in the plasma center.

In conclusion, the force is going to affect only the FSA poloidal momentum balance equation, and therefore the magnitude of \tilde{n}_j and $\Omega_{\phi j}$ indirectly, through the magnitude of $\Pi_{\theta j}$.

8.8 Radial velocities

The computation of the \tilde{n}_j , $\tilde{\Omega}_j$ and $v_{\theta j}$ radial profiles requires $v_{rj}(r)$ as input. The radial electron flux can be evaluated from experimental data, as outlined in Section 2.2. The radial flux of each ion species could also be calculated if an accurate radial profile distribution of the different ion species were available. Since the impurity density profile was not measured in TFTR Exp.44, the radial ion fluxes have not been determined in this work. Nevertheless, the possible range of variability of v_{rj} is defined by the ambipolarity condition:

$$n_e v_{re} = n_i v_{ri} Z_i + n_I v_{rI} Z_I \quad (8.71)$$

and by the following observations.

The analysis of the plasma parameters of Exp.44 has been restricted to the steady state phase of the discharge. In some of the shots, neutral beam injection lasted one second, at constant power and direction. During the last 600 ms, at least, the plasma parameter measurements, including the Z_{eff} measurement, appeared stationary. As discussed in Section 8.3, the impurity source is limited to a few cms near the plasma edge. According to the continuity equation, a steady state density and the absence of sources/sinks imply a vanishing radial particle flux.

We can estimate an upper limit for the impurity flux magnitude related to possible variations of the impurity density which can occur during the steady state phase of the discharge and which are not clearly observable. The error affecting the total impurity particles ΔN_I , where $N_I = \int_{V_p} n_I dV_p$ (V_p = plasma volume), can be written in terms of Z_{eff} , N_e and their error bars, as:

$$\Delta N_I = \Delta N_e \frac{Z_{eff} - 1}{Z_I(Z_I - 1)} + \Delta Z_{eff} \frac{N_e}{Z_I(Z_I - 1)} \quad (8.72)$$

The impurity flux associated with such a variation of N_I is: $(2\pi)^2 r R \Gamma_I = -\Delta N_I / \Delta t$, where Δt is the time length of the steady state phase of the discharge.

The ratio between the impurity and electron radial current is:

$$\frac{Z_I \Gamma_I}{\Gamma_e} = \frac{Z_I \Gamma_I \tau_e}{N_e} = \frac{\tau_e}{\Delta t} \left(\frac{\Delta N_e}{N_e} \frac{Z_{eff} - 1}{Z_I - 1} + \frac{\Delta Z_{eff}}{Z_I - 1} \right) \quad (8.73)$$

The particle confinement time, τ_e , was in the range [0.2-0.4] s over most of the plasma region and it was $\simeq 0.3$ s at $r/a=0.9$. With $Z_{eff} = 3$, $\Delta N_e/N_e = 0.1$ and $\Delta Z_{eff}/Z_{eff} = 0.2$ [48], values typical of Exp.44, we obtain:

$$Z_I \frac{\Gamma_I(a)}{\Gamma_e(a)} < 0.1 \quad (8.74)$$

This implies that the impurity radial flux is a small fraction of the electron radial flux and that Eq.(8.71) reduces to $\Gamma_e \sim \Gamma_i$.

We also recognize that the observed particle flux is likely to have an anomalous component. As justified in Section 8.7, we include the anomalous term $\Gamma_j^{(\sim)}$ in the FSA poloidal momentum equation, Eq.(8.51):

$$m_j v_{\phi j o} \Omega_{\phi j} + Z_j \frac{\Gamma_j B_{\phi o}}{n_{j o}} - Z_j \frac{\Gamma_j^{(\sim)} B_{\phi o}}{n_{j o}} + \left\langle \frac{\Pi_{\theta j}}{h n_j} \right\rangle \simeq 0 \quad (8.75)$$

We can define:

$$\gamma'_j \equiv Z_j \Gamma_j / \Gamma_e \quad \text{and} \quad \gamma''_j \equiv \Gamma_j^{(\sim)} / \Gamma_j \quad (8.76)$$

and rewrite:

$$Z_j (\Gamma_j - \Gamma_j^{(\sim)}) = \gamma'_j \Gamma_e (1 - \gamma''_j) \equiv \gamma_j \Gamma_e \quad (8.77)$$

In the following numerical evaluation of \tilde{n}_j and $\tilde{\Omega}_{\phi j}$, we consider values of γ'_j and γ''_j such that:

$|\gamma'_j| \leq 0.1$, according to Eq.(8.74) and related discussion;

$\gamma'_i + \gamma'_I = 1$, by ambipolarity, and

γ''_j is a parameter assumed to vary in the range [0 - 1]. The limiting values $\gamma''_j = 0$ and $\gamma''_j = 1$ corresponds respectively to the cases where the anomalous force, Eq.(8.69), is negligible with respect to the particle flux, or it is its main driving term. With

these values of γ_j' and γ_j'' the ranges of variability of the γ_j factors are: $\gamma_i = [0, 1]$ and $\gamma_I = [0, 0.1]$. In the case $q=0$, we are also going to discuss which values of γ_I are consistent with the magnitudes of poloidal velocities that have been observed in different machines.

8.9 Poloidal variations of n_j and $\Omega_{\phi j}$ (case $\vec{q}_j = 0$)

8.9.1 Poloidal variations of n_I

In the case of $\eta_{0i} v_{\theta i} Z_I T_e / (n_e T_i) < \eta_{0I} v_{\theta I} / n_I$ and $Z_i = 1$, which is the case for Exp.44, the \mathcal{D}_i term can be neglected and Eq.(8.55) becomes independent of \tilde{n}_i and $v_{\theta i}$. One derives:

$$\begin{aligned}
 \frac{1}{n_I} \frac{\partial n_I}{\partial \theta} &= -\tilde{n}_{Ic} \sin \theta + \tilde{n}_{Is} \cos \theta = \\
 &- \left\{ m_I v_{\phi I}^2 - \frac{13}{2} \frac{\beta}{\omega_{cI}} \frac{\partial v_{\phi}}{\partial r} [T_I - (Z_I - 1) \frac{n_i}{n_e} T_e] \right\} (T_I + T_e Z_{eff})^{-1} \epsilon \sin \theta \\
 &+ \left\{ -\frac{\eta_{0I} v_{\theta I}}{r p_I} \frac{2}{3} \tilde{n}_{Is} \sin \theta - \frac{\eta_{0I} v_{\theta I}}{r p_I} \left(\epsilon + \frac{2}{3} \tilde{n}_{Ic} \right) \cos \theta \right. \\
 &+ \frac{\eta_{0I}}{\epsilon p_I} \beta a_{Is} \tilde{n}_{Ic} \cos \theta + \frac{\eta_{0I}}{\epsilon p_I} \beta \Omega_{\phi I} U_{Ic} \cos \theta \left. \right\} \frac{T_I + T_e n_i / n_e}{T_I + T_e Z_{eff}} \equiv \\
 &- E_I \sin \theta - C_I \tilde{n}_{Is} \sin \theta - C_I \left(\frac{3}{2} \epsilon + \tilde{n}_{Ic} \right) \cos \theta + D_I \tilde{n}_{Ic} \cos \theta + F_I \cos \theta
 \end{aligned} \tag{8.78}$$

The terms from $\Pi_{\theta I}$ that have been neglected in Eq.(8.78) are at least a factor of ϵ smaller than the terms that have been included. $\tilde{n}_e \sim \tilde{n}_I Z_I n_I / n_e$ has been assumed, anticipating $\tilde{n}_i \ll \tilde{n}_I$.

It is worth commenting that E_I represents the centrifugal force and a contribution from the gyroviscous tensor; C_I , D_I and F_I are contributions from the parallel viscous tensor.

The following definitions have also been used:

$$A_j \equiv A_{js} \sin \theta + A_{jc} \cos \theta \tag{8.79}$$

$$\begin{aligned}
 &\equiv a_{js} \tilde{n}_{jc} \sin \theta + a_{jc} \tilde{n}_{js} \cos \theta + \Omega_{\phi j} U_{jc} \sin \theta - \Omega_{\phi j} U_{js} \cos \theta \\
 &\tag{8.80}
 \end{aligned}$$

with

$$\begin{aligned}
 a_{jc} &= - \left[\frac{T_j}{e Z_j L_{\tilde{n}_{js}}} + \frac{T_e}{e} \frac{Z_I n_I}{n_e} \left(\frac{1}{L_{T_e}} + \frac{1}{L_{\tilde{n}_{Is}}} \right) \right] \frac{1}{B_{\theta} R} \\
 a_{js} &= \left[\frac{T_j}{e Z_j L_{\tilde{n}_{jc}}} + \frac{T_e}{e} \frac{Z_I n_I}{n_e} \left(\frac{1}{L_{T_e}} + \frac{1}{L_{\tilde{n}_{Ic}}} \right) \right] \frac{1}{B_{\theta} R}
 \end{aligned} \tag{8.81}$$

Equation (8.78) can be solved in terms of the poloidal variations of the density:

$$\tilde{n}_{Ic} = E_I + C_I \tilde{n}_{Is} \quad (8.82)$$

and

$$\tilde{n}_{Is} = \frac{D_I E_I - C_I(\frac{3}{2}\epsilon + E_I) + F_I}{1 + C_I(C_I - D_I)} \quad (8.83)$$

The \tilde{n}_I 's are functions of $v_{\theta I}$, which can be determined by solving the FSA poloidal momentum balance equation, Eq.(8.51).

8.9.2 Impurities poloidal flow

One can write: $\langle \Omega_{\phi j}^2 \sin\theta \rangle \simeq (\Omega_{\phi jo} \Omega_{\phi js})$ and

$$\Omega_{\phi Is} \simeq -(\frac{v_{\theta I}}{\beta R} + a_{Ic})\tilde{n}_{Is} + \Omega_{\phi I} U_{Is} \quad (8.84)$$

Substituting this expression for $\Omega_{\phi Is}$ in Eq.(8.51) and noting that the friction term and the terms from the gyroviscous tensor can be neglected, we obtain a polynomial in $v_{\theta I}$ (third degree) that can be solved with a numerical method:

$$\begin{aligned} & - m_I \tilde{n}_{Is} v_{\phi I} (a_{Ic} + \frac{v_{\theta I}}{\beta R}) + m_I v_{\phi I}^2 \frac{U_{Is}}{R} + \frac{e}{n_I} \gamma_I \Gamma_e B_\phi \\ & + \frac{\eta_{0I} v_{\theta I}}{n_I R^2} [-\frac{3}{2} + \frac{\tilde{n}_{Is}}{\epsilon} - \frac{\tilde{n}_{Ic}}{2\epsilon} + \frac{1}{3\epsilon^2} (\tilde{n}_{Ic}^2 + \tilde{n}_{Is}^2)] \\ & + \frac{\eta_{0I} \beta}{n_I r} [A_{Is} (\frac{3}{2} - \frac{\tilde{n}_{Is}}{\epsilon} - \frac{\tilde{n}_{Ic}}{2\epsilon}) + A_{Ic} (\frac{\tilde{n}_{Is}}{2\epsilon} - \frac{\tilde{n}_{Ic}}{\epsilon})] = 0 \end{aligned} \quad (8.85)$$

The L_x s, with $x = \tilde{n}, v_\theta, \tilde{\Omega}$, etc., are evaluated with successive iterations.

8.9.3 Density poloidal variations and poloidal flow of main ions

\tilde{n}_i can be determined from Eq.(8.56), which can be rewritten as:

$$\begin{aligned} \frac{1}{n_i} \frac{\partial n_i}{\partial \theta} &= -\tilde{n}_{ic} \sin\theta + \tilde{n}_{is} \cos\theta = \\ & - (m_i v_{\phi i}^2 - \frac{13}{2} \frac{\beta}{\omega_{ci}} \frac{\partial v_\phi}{\partial r} T_i - T_e Z_I \frac{n_I}{n_e} \frac{\tilde{n}_{Ic}}{\epsilon}) (T_i + T_e \frac{n_i}{n_e})^{-1} \epsilon \sin\theta \end{aligned} \quad (8.86)$$

$$\begin{aligned}
& - \left(\frac{\eta_{0i} v_{\theta i}}{r n_i} \epsilon + T_e Z_I \frac{n_I}{n_e} \tilde{n}_{Is} \right) (T_i + T_e \frac{n_i}{n_e})^{-1} \cos \theta \\
& - \frac{\eta_{0i} v_{\theta i}}{r n_i} \frac{2}{3} (\tilde{n}_{ic} \cos \theta + \tilde{n}_{is} \sin \theta) (T_i + T_e \frac{n_i}{n_e})^{-1} \\
& + \frac{\eta_{0i}}{\epsilon n_i} \beta (-a_{ic} \tilde{n}_{ic} \cos \theta + a_{is} \tilde{n}_{is} \sin \theta) (T_i + T_e \frac{n_i}{n_e})^{-1} \\
& + \frac{\eta_{0i}}{\epsilon n_i} \beta \Omega_{\phi i} (U_{ic} \cos \theta + U_{is} \sin \theta) (T_i + T_e \frac{n_i}{n_e})^{-1} \equiv \\
& - E_i \sin \theta - C_i \cos \theta - G_i (\tilde{n}_{ic} \cos \theta + \tilde{n}_{is} \sin \theta) \\
& + D_{ci} \tilde{n}_{ic} \cos \theta + D_{si} \tilde{n}_{is} \sin \theta + F_{ci} \cos \theta + F_{si} \sin \theta
\end{aligned}$$

Eq.(8.86) can be solved in terms of the poloidal variations of the main ions density:

$$\tilde{n}_{ic} = E_i + (G_i - D_{si}) \tilde{n}_{is} + F_{si} \quad (8.87)$$

and

$$\tilde{n}_{is} = \frac{E_i (D_{ci} - G_i) - C_i + F_{ci}}{1 + (G_i - D_{ci})(G_i - D_{si})} \quad (8.88)$$

The poloidal velocity, of which the $\tilde{n}_{(c,s)i}$ are functions, can be determined by solving the FSA poloidal momentum balance equation for the main ions:

$$\begin{aligned}
& - m_i \tilde{n}_{is} v_{\phi i} (a_{ic} + \frac{v_{\theta i}}{\beta R}) + m_i v_{\phi i}^2 \frac{U_{is}}{R} + \frac{e}{n_i} \gamma_i \Gamma_I B_\phi \\
& + \frac{\eta_{0i} v_{\theta i}}{n_i R^2} \left[-\frac{3}{2} + \frac{\tilde{n}_{is}}{\epsilon} - \frac{\tilde{n}_{ic}}{2\epsilon} + \frac{1}{3\epsilon^2} (\tilde{n}_{ic}^2 + \tilde{n}_{is}^2) \right] \\
& + \frac{\eta_{0i} \beta}{n_i r} \left[A_{is} \left(\frac{3}{2} - \frac{\tilde{n}_{is}}{\epsilon} - \frac{\tilde{n}_{ic}}{2\epsilon} \right) + A_{ic} \left(\frac{\tilde{n}_{is}}{2\epsilon} - \frac{\tilde{n}_{ic}}{\epsilon} \right) \right] \\
& + \frac{\beta}{4 \omega_{ci}} \left(-13 \frac{\partial \Omega_{\phi is}}{\partial r} + 3 \frac{\tilde{n}_{ic}}{\epsilon} \frac{\partial \Omega_{\phi is}}{\partial r} - 3 \frac{\tilde{n}_{is}}{\epsilon} \frac{\partial \Omega_{\phi ic}}{\partial r} \right) = 0
\end{aligned} \quad (8.89)$$

8.9.4 Discussion of the results

The results of the calculations outlined in the previous Sections of this Chapter are illustrated for one shot, 37309-123, from Exp. 44. Although the results vary slightly within the set of discharges, these results are quite representative of the whole experiment.

For the impurities, Eq.(8.85) has one solution, $v_{\theta I}$, approximately given by:

$$v_{\theta I} \simeq A_I R \frac{\beta}{\epsilon} + \frac{2}{3} \frac{e \gamma_I \Gamma_e}{\eta_{\theta I}} B_\phi R^2 \quad (8.90)$$

and plotted in Fig. 8.8, for $\gamma_I = 0.0$ and 0.1 . The poloidal velocity is driven by the pressure radial gradient and by the radial flux, when present. In the case of $\gamma_I = 0.1$, the first and third terms of Eq.(8.85) are the driving terms for $v_{\theta I}$ in the central and edge region, respectively. A similar result is obtained when $T_e/(e\Phi_0)$ varying from ~ 1 at the center to ~ 0.1 at the edge is used in Eq.(8.29). (See Ref. [114] for all the comments, in this Section, about the relation between values of $v_{\theta j}$ and $T_e/(e\Phi_0)$) A constant $T_e/(e\Phi_0) \sim 1$ would predict a poloidal velocity at the edge of $O(\beta v_\phi)$ and therefore a smaller \tilde{n}_I . In fact, as shown in Fig. 8.8, the magnitude of $v_{\theta I}$ remains $\sim (0.1\beta v_\phi)$ at $r=0.2$ m, independently from Γ_I ; it ranges from 0 to $\sim (\beta v_\phi)$ for $\gamma_I = 0 \rightarrow 0.1$, at $r=0.7$ m; it is one order of magnitude smaller than βv_ϕ over most of the plasma region.

These estimates of $v_{\theta I}$ are 1-2 orders of magnitude smaller than measurements of $v_{\theta I}$ on TFTR and discharges in other machines (see Section 7.6). Also, these small values of $v_{\theta I}$ imply (Section 8.5.1) a value of the parameter $T_e/(e\Phi_0) \sim 0.1$. This disagreement may be due to the fact that the heat flux, here neglected, plays an important role in determining the magnitude of $v_{\theta j}$, or to anomalous effects.

In order to investigate the effect of a larger poloidal velocity on the magnitude of \tilde{n}_j and $\Omega_{\phi j}$, we introduce, as input to the calculation, a value of $v_{\theta I}$ obtained from a "trial" poloidal velocity profile, $v_{\theta*}$, shown in Fig. 8.8, and based on the experimental observation of $v_{\theta I}(r/a \sim 0.25) = 1.2 \cdot 10^4$ m/s in TFTR and $v_{\theta I} \sim v_{\phi i} \sim O(10^4)$ at the

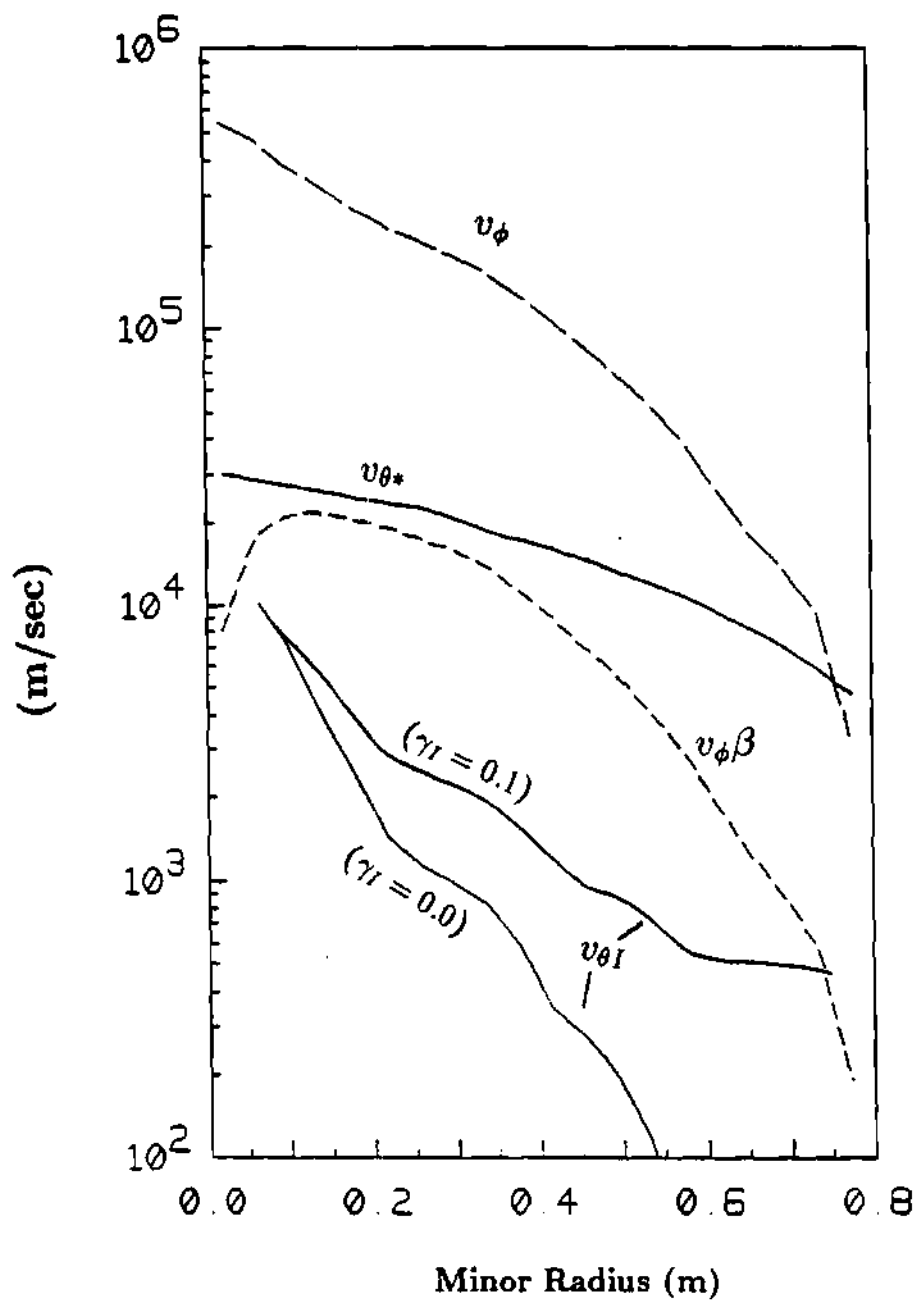


Figure 8.8: Radial profiles of $v_{\theta I}(r)$ computed for $\gamma_I = 0.0$ and 0.1 ($q=0$ case). The $v_{\theta*}$ is a "trial" function. The $v_{\phi}(r)$ and $\beta v_{\phi}(r)$ profiles are also shown for comparison (Shot 37309-123).

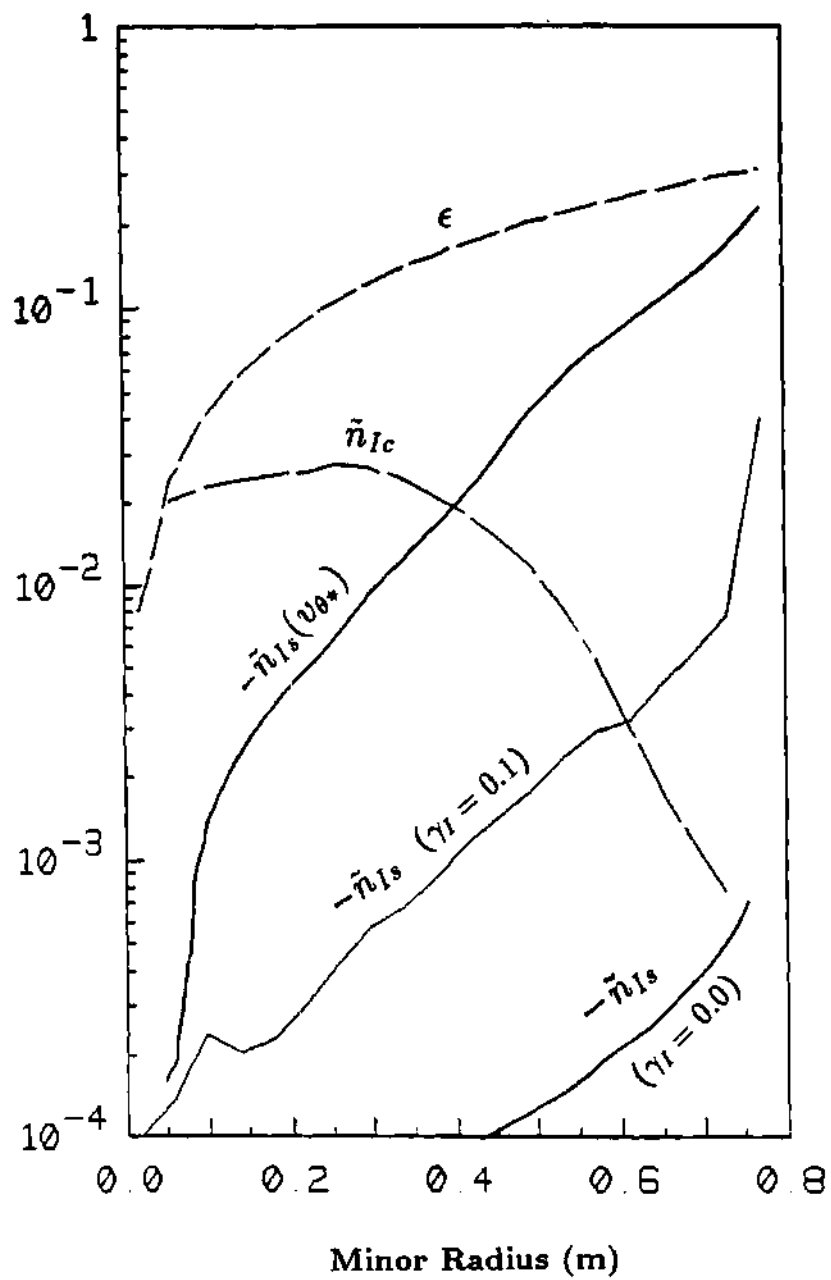


Figure 8.9: Radial profiles of \tilde{n}_{Ic} and \tilde{n}_{Is} , (a) evaluated for $\gamma_I = 0.0$ and 0.1 , and (b) assuming $v_{\theta I} = v_{\theta*}$. The parameter ϵ is also shown for comparison (Shot 37309-123).

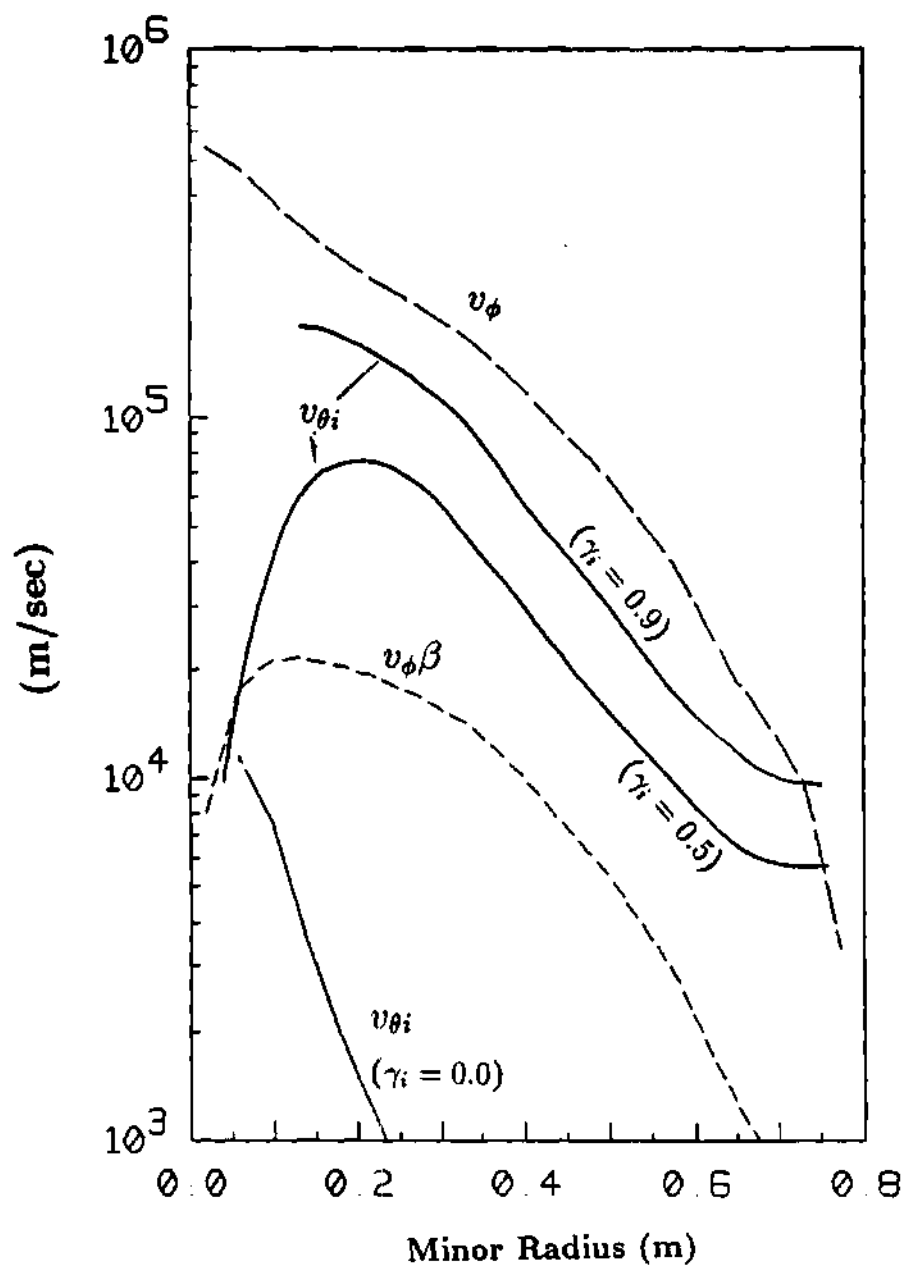


Figure 8.10: Radial profiles of $v_{\theta i}(r)$ evaluated for $\gamma_i = 0.0, 0.5, 0.9$, and $\gamma_I = 0.1$ ($q=0$ case). The $v_{\phi}(r)$, and $\beta v_{\phi}(r)$ profiles are also shown for comparison (Shot 37309-123).

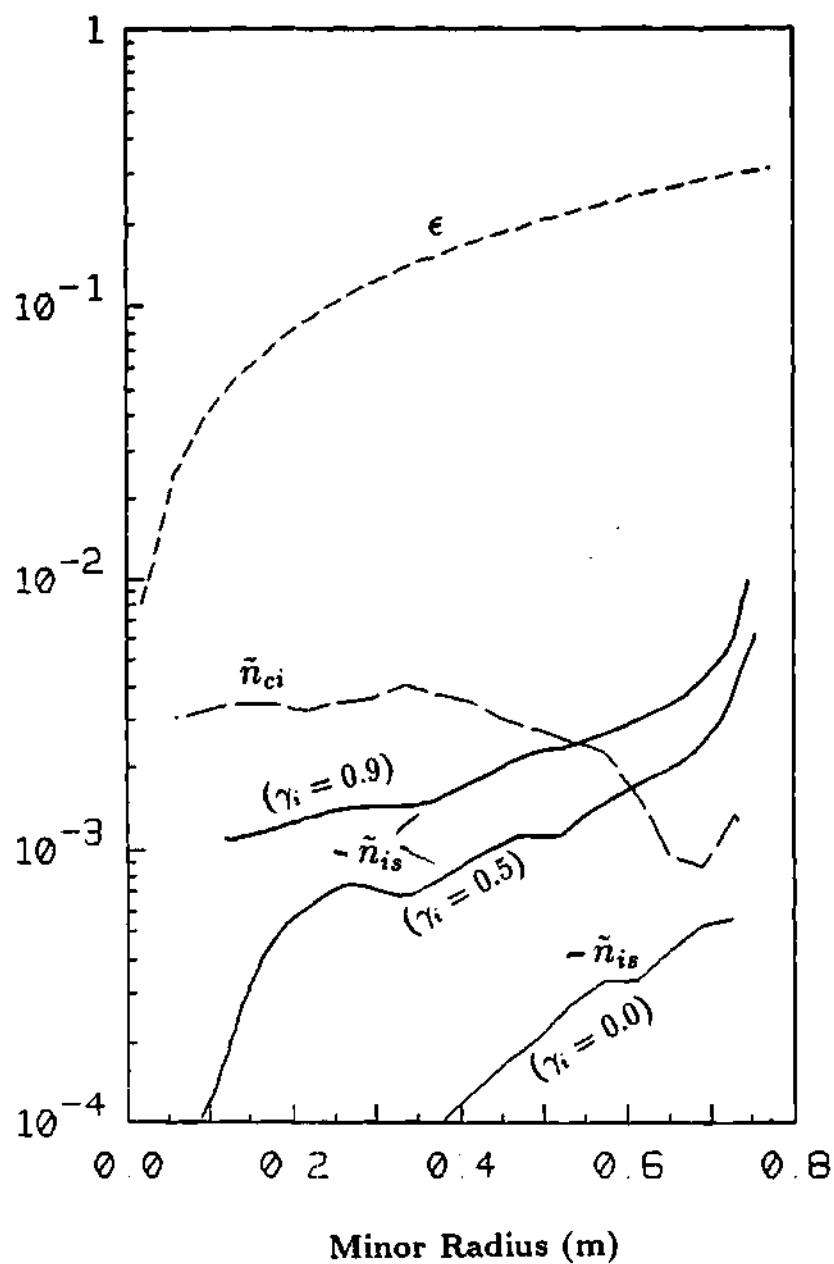


Figure 8.11: Radial profiles of \tilde{n}_{ci} and \tilde{n}_{is} evaluated for $\gamma_i = 0.0, 0.5, 0.9$, and $\gamma_I = 0.1$. The parameter ϵ is also shown for comparison (Shot 37309-123).

edge of several other machines. We note that this constructed $v_{\theta*}$ is much flatter than other calculated or inferred (from Φ_0 and v_ϕ measurements) ^[114] velocity profiles and that this may overemphasize v_θ -driven effects in the outer part of the plasma. We further note that a value $\gamma_I \sim O(-1)$ would yield calculated $v_{\theta I}$ that are consistent with the $v_{\theta*}$ profile. Such a large value of γ_I would literally imply large impurity fluxes that are inconsistent with the measured steady-state Z_{eff} . However, $\gamma_I \sim O(1)$ can also be interpreted as representing other, anomalous forces which enter the poloidal momentum balance equation.

We also used the formalism of Eq.(8.29) in Section 8.5.1 and adjusted $T_e/(e\Phi_0)$ to bring the calculated $v_{\theta I}$ into line with the experimental $v_{\theta*}$. Values of $T_e/(e\Phi_0) \sim 1$ at the center and ~ 0.1 towards the edge yield calculated $v_{\theta I}$ that are consistent with the $v_{\theta*}$ profile. These values of $T_e/(e\Phi_0)$ seem plausible based on the ISX-B measurements and associated calculations ^[115].

The correspondent poloidal asymmetries of the impurity density have been plotted in Fig. 8.9. The in-out asymmetry is essentially driven by the centrifugal force, that is:

$$\tilde{n}_{Ic} \simeq \epsilon m_I (v_{\phi I} + v_{\theta I})^2 (T_I + T_e \frac{T_i}{n_e})^{-1}$$

while the up-down asymmetry, in this case analyzed, is given by:

$$\tilde{n}_{Is} \simeq -\frac{r}{n_I} \frac{\Pi_{\theta Ic}}{T_I + T_e n_i/n_e} = -\frac{\eta_{\theta I}}{n_I R} (v_{\theta I} - R \frac{\beta}{\epsilon} a_{Is} \tilde{n}_{Ic}) (T_I + T_e Z_{eff})^{-1} \quad (8.91)$$

As already discussed earlier, $\tilde{n}_{Ic} < \epsilon$ because the carbon impurity ions are subsonic.

\tilde{n}_{Is} is driven by the parallel viscous force, is negative over all the plasma region, and essentially proportional to the in-out asymmetry of the toroidal rotation frequency, whose magnitude depends on $v_{\theta I}$ and $a_{Is} \tilde{n}_{Ic}$. Its magnitude varies from $\sim 10^{-4}$ to 10^{-3} for $\gamma_I = 0 \rightarrow 0.1$ in the plasma bulk. The $\tilde{n}_{Is}(v_{\theta*})$ profile, shown in Fig. 8.9, has been calculated using $v_{\theta I} = v_{\theta*}$; its magnitude is $\sim 0.1\epsilon$ and $\sim \epsilon$ at $r/a=0.5$ and $r/a=1$ respectively.

The radial profile of $v_{\theta i}$ is shown in Fig. 8.10 for three different values of Γ_i ($\gamma_i =$

0.0, 0.5, 0.9; $\gamma_I = 0.1$). The main ions poloidal velocity is positive and approximately given by:

$$v_{\theta i} \simeq A_{i\theta} R \frac{\beta}{\epsilon} + \frac{2}{3} \frac{e \gamma_i \Gamma_e}{\eta_{0i}} B_\phi R^2 \quad (8.92)$$

The first term is important only in the central region and for small Γ_i ; otherwise the main ions poloidal velocity is essentially driven by the radial flux term and, for $\gamma_i > 0.1$, it is larger than βv_ϕ .

The in-out asymmetry of the main ion density is coupled to the in-out impurity density asymmetry through the potential gradient, and it is approximately given by:

$$\tilde{n}_{ic} \simeq E_i = -\epsilon [m_i (v_{\phi i} + v_{\theta i})^2 - \frac{13}{2} \frac{\beta}{\omega_{ci}} \frac{\partial v_\phi}{\partial r} T_i - T_e Z_I \frac{n_I}{n_e} \frac{\tilde{n}_{Ic}}{\epsilon}] (T_i + T_e \frac{n_i}{n_e})^{-1} \quad (8.93)$$

The electric field and centrifugal forces are of the same order of magnitude and have opposite effects: the electric field tends to drive a negative in-out main ion density asymmetry in order to re-establish $\partial n_e / \partial \theta = 0$. The radial profile of \tilde{n}_{Ic} , whose magnitude is independent of the ions radial flux levels, is shown in Fig. 8.9.

The combined effects of viscous and electrostatic forces determine the magnitude of \tilde{n}_{is} :

$$\tilde{n}_{is} \simeq -C_i = -\left(\frac{r \Pi_{\theta ic}}{n_i} + T_e Z_I \frac{n_I}{n_e} \tilde{n}_{Is} \right) (T_i + T_e \frac{n_i}{n_e})^{-1} \quad (8.94)$$

$$= -\left(\frac{\eta_{0i} v_{\theta i}}{r n_i} \epsilon + T_e Z_I \frac{n_I}{n_e} \tilde{n}_{Is} \right) (T_i + T_e \frac{n_i}{n_e})^{-1} \quad (8.95)$$

Radial profiles of \tilde{n}_{is} are shown in Fig. 8.11 for different values of the ion radial flux term ($\gamma_i = 0.0, 0.5, 0.9$; $\gamma_I = 0.1$). \tilde{n}_{is} varies from 0.001ϵ to 0.01ϵ , increasing with the increasing of the main ions radial flux term. The magnitude of \tilde{n}_{is} , calculated using $\gamma = 0.9$, $v_{\theta I} = v_{\theta*}$ is $\sim 0.01\epsilon$ over most of the plasma region.

The relatively small values of \tilde{n}_{js} predicted by these calculations are consistent with the observation of up-down symmetric $Z_{eff} n_e^2$ radial profile to within 10% measurement accuracy.

The $\tilde{\Omega}_{\phi jc}$ profile is essentially $\sim v_{\theta j} \epsilon / (\beta v_{\phi j})$. Due to the relatively large $v_{\theta j}$, the in-out asymmetries, $\tilde{\Omega}_{\phi jc}$, are $O(\epsilon)$ and larger; the same result is obtained when $T_e / (e\Phi_0)$ varying from ~ 1 at the center to ~ 0.1 at the edge is used in Eq.(8.29). Both up-down asymmetries, $\tilde{\Omega}_{\phi i}$, and $\tilde{\Omega}_{\phi I}$, are $\ll \epsilon$ in the case $\gamma_i = \gamma_I = 0.1$. When the calculation is performed using the measured $v_{\theta*}$ for $v_{\theta I}$, the relatively large \tilde{n}_{I*} give rise to a $\tilde{\Omega}_{\phi I*}(r > a/2)$ of $O(\epsilon)$ and larger.

$\Xi_i(\gamma_i = 0.1)$ and $\Xi_I(\gamma_I = 0.1)$ are positive and two orders of magnitude smaller than ϵ^2 over most of the plasma region. Ξ_i increases with γ_i because of the increase of \tilde{n}_i and $\tilde{\Omega}_{\phi i}$ with γ_i . $\Xi_i(\gamma_i = 0.9)$ is one order of magnitude smaller than ϵ^2 over most of the plasma region. The magnitude of Ξ_j becomes comparable and even larger than ϵ^2 at the plasma edge because of large values of $\tilde{\Omega}_{\phi j}$ in this region. When the calculation is performed using the measured $v_{\theta*}$ for $v_{\theta I}$, Ξ_I is $O(0.1 - 1)\epsilon^2$ in the plasma interior and becomes $O(10\epsilon^2)$ toward the plasma edge; the large edge value is due to the flat $v_{\theta*}$ profile and is probably unrealistic.

The $(\Theta G/Z)_{eff}$ parameter, Eq.(8.39), has been evaluated for the case $\gamma_i = 0.9$, $\gamma_I = 0.1$ and for the case $\gamma_i = 0.9$ and $v_{\theta I} = v_{\theta*}$. The results of the calculations are shown in Fig. 8.12. In the first case, the find $(\Theta G/Z)_{eff} \sim 0.1$ in the plasma center and $(\Theta G/Z)_{eff}$ increasing up to ~ 10 at the plasma edge. In the second case, the function $(\Theta G/Z)_{eff}$ increases from $\sim 10^{-2}$ in the center up to ~ 10 at the edge.

In Chapter 6 it was found that using a radially-averaged value of $(\Theta G/Z)_{eff} \sim 0.1$ led to predictions of momentum confinement times and central rotation velocities that agreed reasonably well with experiment. These calculations of the poloidal asymmetries support $(\Theta G/Z)_{eff}$ of $O(0.1)$ but suggest a radial dependence. The main ion asymmetries contribute significantly to the value of $(\Theta G/Z)_{eff}$, which is different than previously thought [20].

The magnitude of the gyroviscous torque flows \hat{K}_ϕ and K_ϕ^{gv*} , given in Eqs. (8.48)

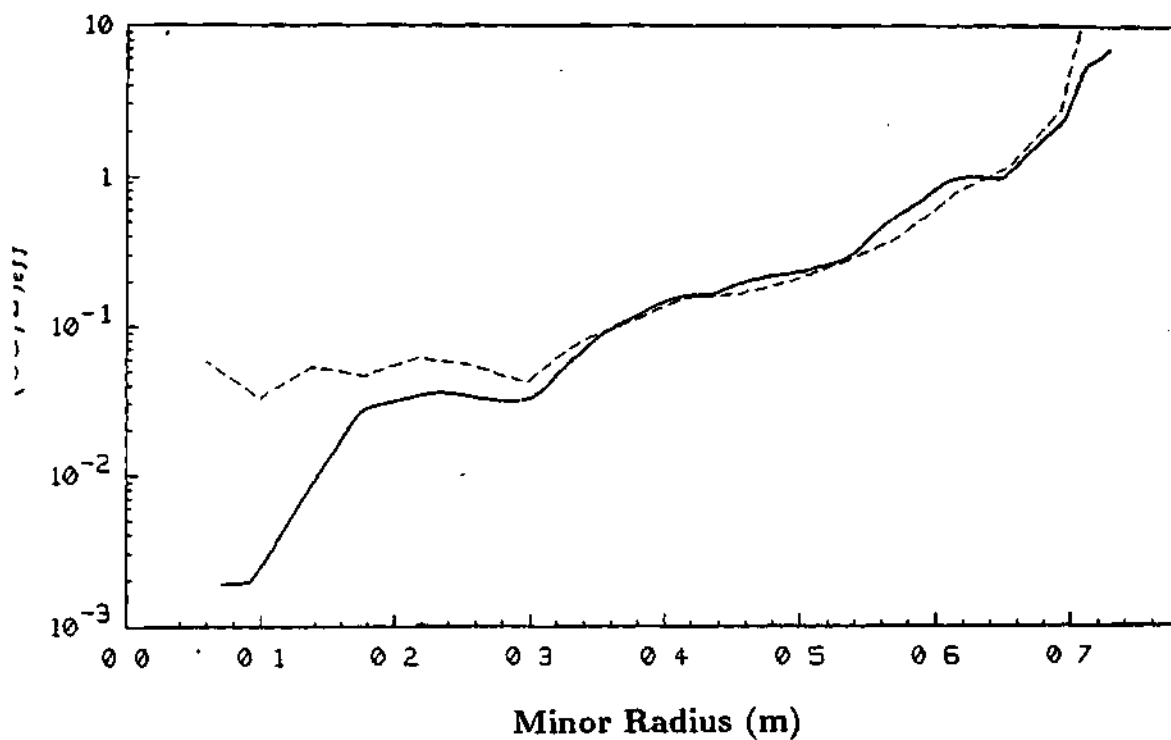


Figure 8.12: Radial profiles of $(\Theta G/Z)_{eff}$ evaluated for the case $\gamma_i = 0.9$, $\gamma_I = 0.1$, (---) and for the case $\gamma_i = 0.9$ and $v_{\theta I} = v_{\theta*}$ (—)

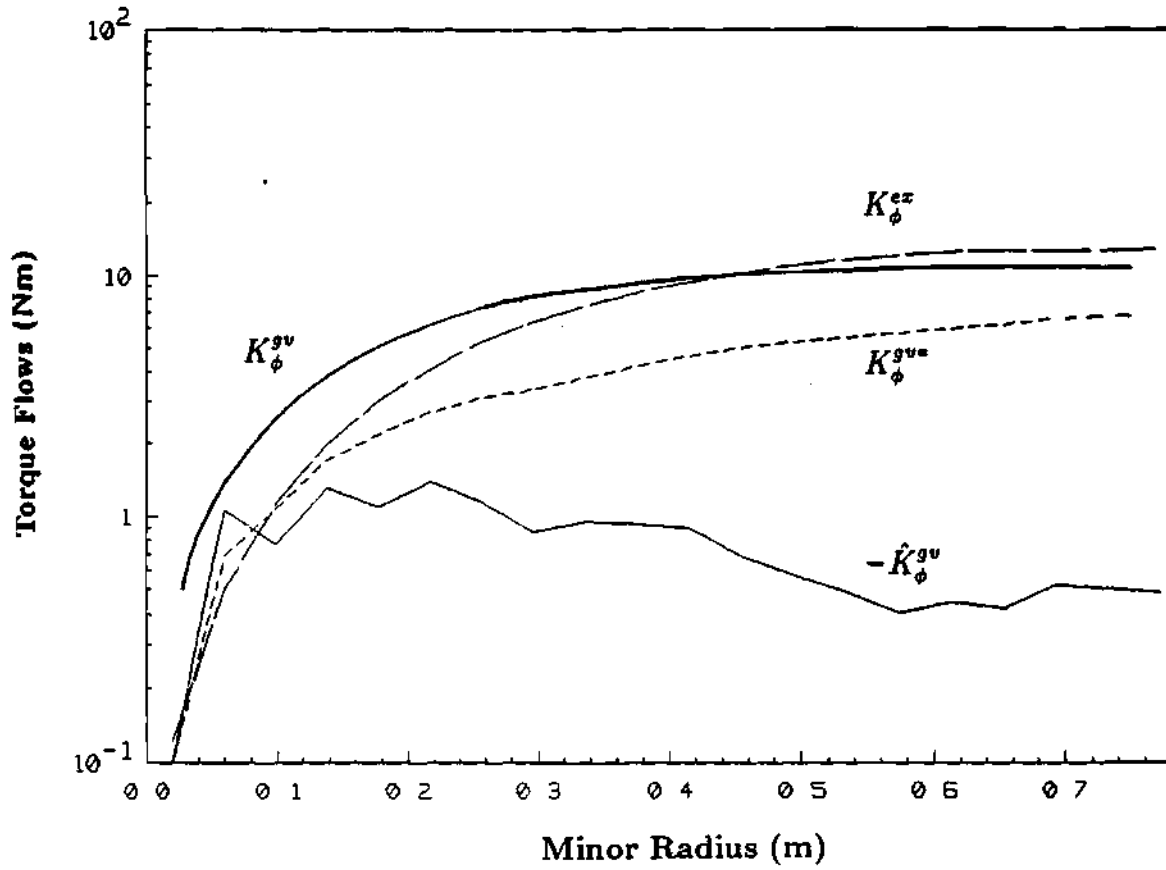


Figure 8.13: Radial profiles of K_{ϕ}^{gv} (case $\tilde{\Theta} = 1.5$ and $\bar{Z} = Z_{eff}$), \hat{K}_{ϕ}^{gv} and K_{ϕ}^{gv*} (case $\gamma_i = 0.9$, $\gamma_I = 0.1$). The experimental K_{ϕ}^{ex} profile is also shown for comparison.

and (8.46) are illustrated in Fig. 8.13 for the case $\gamma_i = 0.9$ and $\gamma_I = 0.1$. Figure 8.13 also shows the experimental torque flow, K_ϕ^{ex} , and the K_ϕ^{gv} profile result (evaluated for $\tilde{\Theta} = 1.5$ and $\tilde{Z} = Z_{eff}$) already illustrated in Chapter 6. The K_ϕ^{gv*} profile was evaluated taking into account the radial dependence of $(\Theta G/Z)_{eff}$ evaluated from experimental η_{Aj} and $v_{\phi j}$ profiles and calculated poloidal variations. This procedure leads to a profile of K_ϕ^{gv*} similar to the K_ϕ^{ex} and K_ϕ^{gv} profiles, the last carried out assuming $\tilde{\Theta}$ as a constant independent of r (see Fig. 8.13). The magnitude of K_ϕ^{gv*} is a factor of two smaller than K_ϕ^{ex} over most of the plasma bulk. Thus, using poloidal asymmetry factors $\tilde{\Theta}_j$, or Ξ_j , evaluated from first-principle calculations of the \tilde{n}_j and $\tilde{\Omega}_{\phi j}$, Eq.(8.46) for K_ϕ^{gv*} predicts the experimental torque flow to within a factor of two over most of the plasma.

Both K_ϕ^{gv} and K_ϕ^{gv*} have similar magnitude and radial dependence (close to the magnitude and the profile of K_ϕ^{ex}). We deduce that the difference in the formulation of K_ϕ^{gv} (i.e. $\tilde{\Theta} = const(r)$ and $G_{\Xi_j} = 0$) and K_ϕ^{gv*} (i.e. $\tilde{\Theta}(r)$ and $G_{\Xi_j} = 0$) did not generate a considerable difference in the results.

How do we interpret the different predictions of K_ϕ^{gv} , K_ϕ^{gv*} and \hat{K}_ϕ^{gv} ?

The \hat{K}_ϕ^{gv} , which was evaluated from Eq.(8.48) using calculated Ξ_j and G_{Ξ_j} profiles, is negative and its magnitude is one order of magnitude smaller than K_ϕ^{ex} . The difference between \hat{K}_ϕ^{gv} and K_ϕ^{gv*} is entirely in the different treatment of G_{Ξ_j} , which is neglected in K_ϕ^{gv*} . We can calculate G_{Ξ_j} by solving for Ξ_j at different radial locations and evaluating the radially gradient numerically. Figure 8.14 shows the radial profiles of G_{Ξ_i} and $G_{\eta v_i}$ for the case $\gamma_I = 0.1$ and $\gamma_i = 0.9$; they have similar magnitude and radial profiles but opposite signs. Indeed the G_{Ξ_i} function is not negligible with respect to $G_{\eta v_i}$; actually $|G_{\Xi_i}|$ is larger than $G_{\eta v_i}$ and this explains why \hat{K}_ϕ^{gv} is negative.

The $\gamma_i = 0.9$ and $v_{\theta I} = v_{\theta*}$ case was also studied and the different torque flows

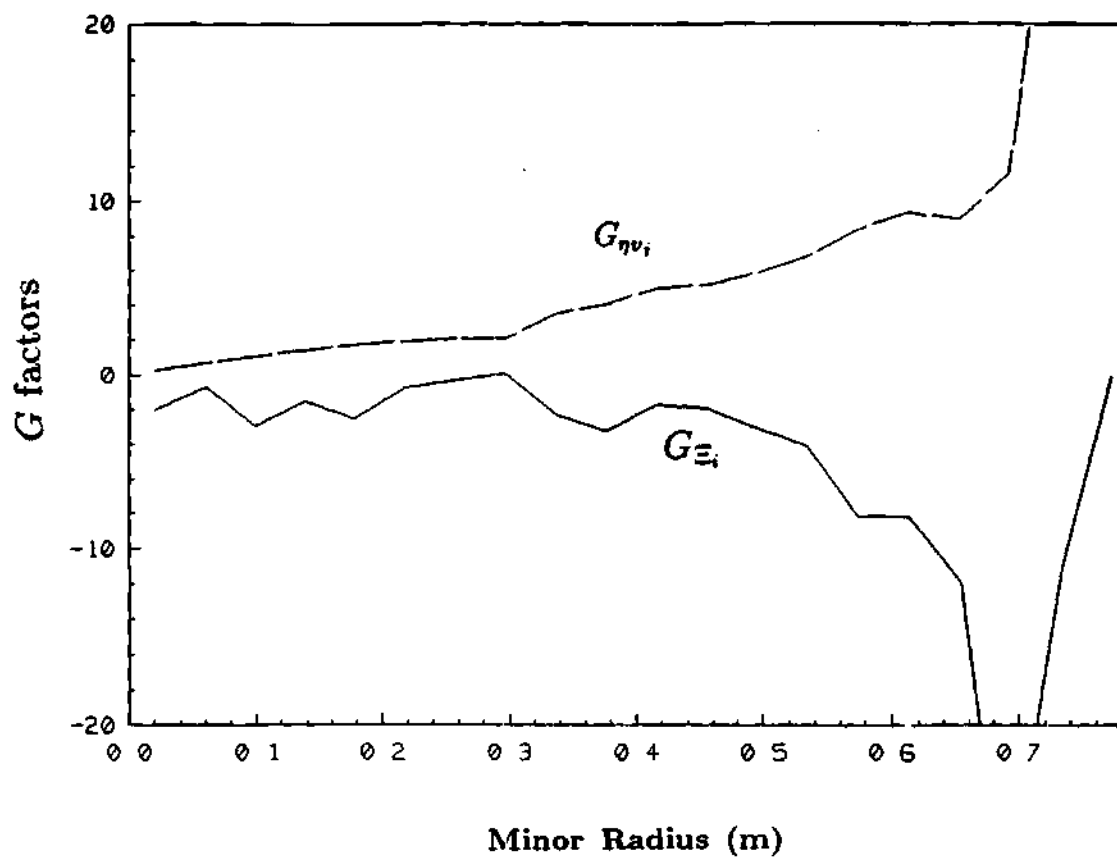


Figure 8.14: Radial profiles of $G_{\eta v_i}$ and G_{Ξ_i} , Eq.(8.45), for the case $\gamma_I = 0.1$ and $\gamma_i = 0.9$.

were found to be similar to the results of the $\gamma_i = 0.9$ and $\gamma_I = 0.1$ case. The fundamental difference consisted in the fact that, in this second ($v_{\theta I} = v_{\theta*}$) case, the impurities were contributing the largest part to the total torque flows, while in the previous case the main ions contribution was dominant.

In spite of the good agreement of K_ϕ^{gv} and K_ϕ^{gv*} with the experimental torque flow, one must conclude that the approximation (the separation-of-variables, $G_{\Xi_j} = 0$), on which these two formulas are based, is not supported by our calculations of the radial dependence of the poloidal asymmetry factor Ξ_j .

The \hat{K}_ϕ^{gv} radial profile, computed removing this approximation, underpredicts the experimental torque flow by at least one order of magnitude and represents an inward flow.

In this Section we have calculated $\tilde{n}_{j(c,s)}$, $\tilde{\Omega}_{\phi j(c,s)}$, $v_{\theta j}$, and then estimated $(\Theta G/Z)_{eff}$, K_ϕ^{gv*} and \hat{K}_ϕ^{gv} , using a model for the parallel viscosity which neglects the heat flux contribution, and allowing anomalous effects to enter the poloidal momentum balance equation via the use of measured radial particle fluxes and the $\Gamma_j^{(\sim)}$ term.

With the assumption $|\Gamma_j^{(\sim)}| \leq |\Gamma_j|$, one obtains $v_{\theta I}$ smaller than the values of impurity poloidal velocities experimentally observed, and rather larger values of $v_{\theta i}$. The total torque flow is essentially given by the main ions torque flow. When possible anomalous forces are neglected ($\Gamma_j^{(\sim)} = 0$), the theoretical torque flows reach their largest value. K_ϕ^{gv*} appears as a good representation of the experimental torque; \hat{K}_ϕ^{gv} , instead, is negative and at least one order of magnitude smaller than the experimental torque flow.

Assuming for $v_{\theta I}$ a trial radial profile based on different experimental measurements of v_θ , one obtains values of $\tilde{n}_{I,s}$ and $\tilde{\Omega}_{I,s}$ of $O(\epsilon)$ and larger, and therefore a torque flow dominated by the impurities. Also in this case K_ϕ^{gv*} represent the K_ϕ^{ex} reasonably well, and \hat{K}_ϕ^{gv} is still negative and one order of magnitude smaller than

the experimental torque flow.

Values of $\gamma_I \sim 1$ are consistent with $v_{\theta I} = v_{\theta*}$. Such values of γ_I correspond to $|\Gamma_I^{(\sim)}| \sim |\Gamma_e^{(\sim)}|$ that appears rather unphysical. In fact, to the extent that quasineutrality is maintained [34], $\tilde{n}_e \simeq \sum_j Z_j \tilde{n}_j$, the flow due to electrostatic perturbations is ambipolar. The magnetic fluctuation terms, $\Gamma_j^{\tilde{B}}$, due to local normal modes, have also been shown to be ambipolar [118]. But we cannot exclude that γ_I , which has been defined here to represent anomalous flux terms, could also originate from other forces that we neglect.

8.10 Evaluation of \tilde{n}_j , $\tilde{\Omega}_{\phi j}$ and $K_{\phi}(r)$ (case $\tilde{q}_j \neq 0$)

8.10.1 Poloidal momentum balance equation

Starting from the general form of the parallel viscous tensor: [64] $\tilde{\Pi}_j^0 = (p_{\parallel} - p_{\perp})_j (\hat{b}\hat{b} - \tilde{I}/3)$, the poloidal viscous force can be written:

$$\Pi_{\theta j}^0 = \frac{1}{B_{\theta}} (p_{\parallel} - p_{\perp})_j (\tilde{b}_{\theta} \nabla) B - \frac{1}{B_{\theta}} \frac{1}{3} (\tilde{B}_{\theta} \nabla) (p_{\parallel} - p_{\perp})_j \quad (8.96)$$

With

$$(p_{\parallel} - p_{\perp})_j = (p_{\parallel} - p_{\perp})_{js} \sin \theta \quad (8.97)$$

as suggested by Eq.(3.8), one obtains:

$$\Pi_{\theta j}^0 = \frac{1}{r} (p_{\parallel} - p_{\perp})_{js} \epsilon \sin^2 \theta - \frac{1}{3} \frac{1}{r} (p_{\parallel} - p_{\perp})_{js} \cos \theta \quad (8.98)$$

(Equation (3.8) was derived assuming $\tilde{n}_j, \tilde{\Omega}_{\phi} = 0$, but we note that in the following calculations we do not need to specify the parametric dependence of the anisotropic pressure term).

Therefore:

$$\frac{\Pi_{\theta j}}{n_j} - \left\langle \frac{\Pi_{\theta j}}{h n_j} \right\rangle \simeq -\frac{1}{3} \frac{(p_{\parallel} - p_{\perp})_{js}}{n_j r} \cos \theta \quad (8.99)$$

The poloidal variation of the impurity density is described by:

$$\begin{aligned} \frac{1}{n_I} \frac{\partial n_I}{\partial \theta} &= -\tilde{n}_{Ic} \sin \theta + \tilde{n}_{Is} \cos \theta \\ &\simeq -[m_I (v_{\phi I}^2 + v_{\theta I}^2) \epsilon \sin \theta - \frac{1}{3} \frac{(p_{\parallel} - p_{\perp})_{Is}}{n_I} \cos \theta] (T_I + T_e Z_{eff})^{-1} \end{aligned} \quad (8.100)$$

from where one can easily derive the expressions for \tilde{n}_{Ic} and \tilde{n}_{Is} .

The poloidal variation of the main ion density is given by:

$$\begin{aligned} \frac{1}{n_i} \frac{\partial n_i}{\partial \theta} &= -\tilde{n}_{ic} \sin \theta + \tilde{n}_{is} \cos \theta = -[m_i (v_{\phi i}^2 + v_{\theta i}^2) \epsilon \sin \theta \\ &- \frac{1}{3} \frac{(p_{\parallel} - p_{\perp})_{is}}{n_i} \cos \theta + Z_i Z_I \frac{n_I}{n_e} T_e \frac{1}{n_I} \frac{\partial n_I}{\partial \theta}] (T_i + T_e \frac{n_i}{n_e})^{-1} \end{aligned} \quad (8.101)$$

The magnitude of $(p_{\parallel} - p_{\perp})_{js}$ is determined by the FSA poloidal momentum balance equation. By substituting:

$$\langle \frac{\Pi_{\theta j}}{hn_j} \rangle \simeq \frac{2}{3} \frac{(p_{\parallel} - p_{\perp})_{js}}{n_j R} \quad (8.102)$$

in Eq.(8.51) one derives:

$$(p_{\parallel} - p_{\perp})_{js} \simeq -\frac{3}{2} e\gamma_I \Gamma_e B_{\phi} R \quad (8.103)$$

where we have made use of the evaluation of the magnitude of the terms of Eq.(8.51) carried out in Section 8.6.2 and of the assumptions that $\gamma_j \geq 0.1$, $v_{\theta j} < v_{\phi j}$. Therefore the up-down poloidal variations of the ion densities are:

$$\tilde{n}_{Is} = \frac{r}{n_I} \frac{\Pi_{\theta Ic}}{T_I + T_e Z_{eff}} \simeq -\frac{e\gamma_I \Gamma_e B_{\phi} R}{2n_I(T_I + T_e Z_{eff})} \quad (8.104)$$

and

$$\tilde{n}_{is} \simeq -\frac{r\Pi_{\theta ic}/n_i + n_I \tilde{n}_{Is} T_e Z_I/n_e}{T_i + T_e n_i/n_e} = -\frac{e\gamma_i \Gamma_e B_{\phi} R/(2n_i) + n_I \tilde{n}_{Is} T_e Z_I/n_e}{T_i + T_e n_i/n_e} \quad (8.105)$$

It is clear that the magnitude of the poloidal variations of n_j are not affected by the magnitude of \vec{q}_j , in these shots were the friction term in Eq.(8.51) is smaller than the radial flux term. The parametric study of the dependence of \tilde{n}_j on γ_j , carried out in Section 8.6.2, is still valid in the case of $\vec{q}_j \neq 0$.

8.10.2 Finite-heat-flux viscosity model

The evaluation of $\bar{\Omega}_{\phi j}$, and therefore of Ξ_j , requires the evaluation of $v_{\theta j}$. In the previous section we have employed a zero-heat-flux viscosity model. In the case $\bar{q}_j \neq 0$, the poloidal velocity cannot be evaluated by simply solving the FSA poloidal momentum balance equation, since this last involves another unknown function, $q_{\theta j}$, the heat conductive flux. We indeed need to solve a system of four equations - the FSA poloidal projections of the momentum and heat flux equations, Eqs. (8.51) and (A.7), for main ions and light impurity - in the four unknown $v_{\theta i}$, $v_{\theta I}$, $q_{\theta i}$ and $q_{\theta I}$. With the inclusion of the anomalous terms $\Gamma_j^{(\sim)}$ and $q_{rj}^{(\sim)}$ discussed in Section 8.7 the system becomes:

$$\begin{aligned} \langle \bar{B}_\theta \nabla \cdot \bar{\vec{\Omega}}_j \rangle - \langle B_\theta F_{\theta j} \rangle &\simeq \frac{e_j}{T_j} \langle B_\theta B_\phi (q_{rj} - q_{rj}^{(\sim)}) \rangle \\ \langle \bar{B}_\theta \nabla \cdot \bar{\vec{\Pi}}_j \rangle - \langle B_\theta R_{\theta j} \rangle &= \langle B_\theta B_\phi e_j (\Gamma_j - \Gamma_j^{(\sim)}) \rangle \\ &- m_j B_{\theta 0} R_0 \langle n_j \Omega_{\phi j}^2 \sin \theta \rangle \end{aligned} \quad (8.108)$$

The heat conductive radial flux for species j , q_{rj} , is not known at this point and we do not attempt to model the complete energy transport problem to obtain an estimate of it. The total $q_{rions}^{ex} \equiv \sum_j q_{rj}$ is computed from energy balance calculations by SNAP. Typical values of q_{rions}^{ex} are $4 \cdot 10^4$ and $6 \cdot 10^4$ W/m² at $r = 0.2$ and 0.6 cm respectively, for a 10 MW NBI discharge. Formally we indicate $q_{rj} \equiv \gamma'_{qj} q_{rions}^{ex}$.

In addition, as discussed in Section 8.7, the $q_{rj}^{(\sim)}$ term, which represents the effects of anomalous forces that appear in the ion or impurity heat flux equation, could be of the same order of magnitude of the q_{rj} term and we want to study how the results would depend on the presence of this anomalous term. Therefore, as was done for the radial particle flux, it is convenient to define

$$q_{rj}^{(\sim)} \equiv \gamma_{qj} q_{rj}; \quad (q_{rj} - q_{rj}^{(\sim)}) \equiv \gamma'_{qj} (1 - \gamma_{qj}) q_{rions}^{ex} \equiv \gamma_{qj} q_{rions}^{ex} \quad (8.109)$$

The $v_{\theta j}$'s are therefore the solution of a system of equations depending on four unknown parameters, γ_i , γ_I , γ_{qi} and γ_{qI} (actually only three since $\gamma_I \sim 0$), whose reasonable range of variation, suggested by experimental measurements, is $[0 - 1]$.

We have evaluated $v_{\theta j}$ (and $q_{\theta j}$) and found that for values of γ_i and γ_{qi} varying in the range $[0 - 1]$ the ranges of variation of $|v_{\theta i}|$ and $|v_{\theta I}|$ are very large. With γ_i or $\gamma_{qi} \sim 1$, for example, we obtain $v_{\theta i}$ larger than v_ϕ while $v_{\theta i} \rightarrow 0$ when $\gamma_i, \gamma_{qi} \rightarrow 0$.

Since at this moment we are unable to evaluate the γ parameters, or justify a given set of values for them, the present $q \neq 0$ model cannot predict the poloidal velocities with any degree of accuracy. The magnitude of the poloidal variations and of the torque flow depend considerably on the magnitude of the poloidal velocity. We find that the range of variation of the torque flow - corresponding to the ample range of variation of the poloidal velocities - is too ample to allow the establishment of meaningful boundary on the magnitude of the calculated neoclassical torque flow.

Therefore we leave to future investigation the problem of evaluating poloidal velocities and torque flow in the presence of a heat flux.

8.10.3 Discussion of K_{ϕ}^{gv*} and \hat{K}_{ϕ}^{gv} [114]

From Eqs. (8.44)-(8.48), it follows that the two formulations of the total (ion + impurity) gyroviscous torque flows may be written

$$K_{\phi}^{gv*} \equiv K_{\phi i}^{gv*} + K_{\phi I}^{gv*} \equiv K_{\phi i}^{GV}(G_{\eta vi}) + K_{\phi I}^{GV}(G_{\eta vI}) \quad (8.110)$$

and

$$\hat{K}_{\phi}^{gv} = \hat{K}_{\phi i}^{gv} + \hat{K}_{\phi I}^{gv} \equiv [K_{\phi i}^{GV}(G_{\eta vi}) + K_{\phi i}^{GV}(G_{\Xi i})] + [K_{\phi I}^{GV}(G_{\eta vI}) + K_{\phi I}^{GV}(G_{\Xi I})] \quad (8.111)$$

where $K_{\phi j}^{GV}(G_{xj})$ is the quantity defined by Eq.(8.44), with G_{xj} defined by Eq.(8.45). The gyroviscous formulation K_{ϕ}^{gv*} , which assumes $G_{\Xi j} = 0$ ($j=i,I$), agrees rather well with experiment for all the cases considered. However, when we calculate $\Xi_j(\tau)$, we find $G_{\Xi j} \neq 0$. In fact $K_{\phi j}^{GV}(G_{\eta vj}) \simeq -K_{\phi j}^{GV}(G_{\Xi j})$ for many of the cases that we considered, resulting in a near cancellation for each species and an order of magnitude underprediction of the experimental data by \hat{K}_{ϕ}^{gv} .

The qualitative result $G_{\Xi j} < 0$ is probably independent of the calculation model for poloidal asymmetries, implying in general off-setting values of $K_{\phi j}^{GV}(G_{\eta vj})$ and $K_{\phi j}^{GV}(G_{\Xi j})$. However, the degree of cancelation between $K_{\phi j}^{GV}(G_{\eta vj})$ and $K_{\phi j}^{GV}(G_{\Xi j})$ is clearly dependent on the calculation model for Ξ_j , as was illustrated by our calculations with different values of γ_j . Use of spatially dependent γ factors to represent a spatial dependence of the anomalous forces in our model, for example, would clearly alter the $\Xi_j(\tau)$ profile.

8.11 Comparison of results with previous work and discussion of uncertainties

8.11.1 Comparison of results with previous works

The general feature of the results presented in the previous Sections is that the poloidal asymmetries of the ion densities are much smaller than ϵ over most of the plasma. The same is true for the up-down asymmetry of $\Omega_{\phi j}$. The in-out asymmetry of $\Omega_{\phi j}$ can be of order ϵ or larger, when $v_{\theta j} \sim \beta v_{\phi j}$ or larger. The neoclassical (gyroviscous) torque flow evaluated making use of the \tilde{n}_j and $\tilde{\Omega}_{\phi j}$ computed radial profiles is smaller by a factor of two than K_{ϕ}^{ez} when the formulation K_{ϕ}^{gv*} (based on the separation of variables) is used, and at least one order of magnitude smaller than the experimental torque flow when the formulation \hat{K}_{ϕ}^{gv} is used.

Two new results came out of our calculations: 1) the main ions, as well as the impurity ions, can contribute significantly to the gyroviscous torque flow; and 2) density asymmetries $\tilde{n}_i \ll \epsilon$ can drive gyroviscous torque flows of the magnitude of the experimental values, in the K_{ϕ}^{gv*} formulation. Poloidal density asymmetries $\tilde{n}_i \sim \epsilon$ would still be required to drive gyroviscous torque flows of this magnitude in the \hat{K}_{ϕ} formulation.

Let us briefly review how these results compare with previous evaluations of poloidal asymmetries and related momentum fluxes.

Density poloidal asymmetries - Several theoretical analyses and experimental investigations, reviewed in Chapter 7, pointed out that density poloidal asymmetries of $O(\epsilon)$ and larger could be observed (and have been) in specific plasma regimes.

Refs. [93], [26] predicted that centrifugal force can drive in-out density poloidal asymmetry, and that $\tilde{n}_{jc} \sim \epsilon$ for sonic 'j' ion species. We arrive at the same conclusion, but $\tilde{n}_{jc} < \epsilon$ in TFTR Exp.44 because, as shown in Fig. 8.6, both main ions and carbon are subsonic.

Refs. [3], [90], [93], [26] and [97] in Chapter 7, concluded that up-down ion density

asymmetries could be observed in the case of collisional ions. In fact, when the condition $\delta\theta_i \nu_{ii} Z_I^2 / \omega_{ti} \sim 1$ is satisfied, the friction term in Eq.(8.49) becomes the driving force of $\tilde{n}_{sj} \sim \epsilon$. This condition is not satisfied in the TFTR Exp.44, where the friction force, in Eq.(8.49), is negligible with respect to the parallel viscous force. In the case of TFTR Exp.44 plasmas, it is the viscous force term which drives $\tilde{n}_{sj} \sim -(p_{\parallel} - p_{\perp})_{js} / p_j$.

The magnitude of this parallel viscous force can be evaluated from the FSA momentum balance equation and, in our problem, it is proportional to the radial particle flux term, Eq.(8.77). The magnitude of this radial flux term, which is the difference between the particle radial flux and the electrostatic-fluctuations driving force, is not known, essentially because the second term has not been evaluated in TFTR. Based on the experimental observation that the impurity plasma inventory appears to remain constant during the last phase of NBI, we have argued that the impurity radial flux must be a small fraction of the radial electron flux and established a limit for it: $\Gamma_I Z_I < 0.1 \Gamma_e$. No such constraints can be placed on the main ion flux. Therefore we treated $(\Gamma_{ri} - \Gamma_i^{(\sim)})$ as parameter which can vary from zero to a value equal to the measured electron flux and studied the sensitivity of the results to it.

The \tilde{n}_{js} are indirectly driven by the radial flux terms. The case with $\gamma_i \sim 1$ establishes the upper limit to the magnitude of the driving friction force and therefore to the magnitude of \tilde{n}_{sj} . For both ion species and independently of the value of \tilde{q}_j and $v_{\theta j}$, \tilde{n}_{js} was found to be $\ll \epsilon$.

Ref. [91] pointed out that asymmetric particle sources can drive \tilde{n}_j . In Section 8.3, we argued that this can also be the case for the Exp.44 plasma, but that this effect is limited to a few centimeters near the plasma edge. The evaluation of \tilde{n}_j driven by source terms has not been carried out in the present work.

In Ref. [94] it was found that momentum input can drive $\tilde{n}_{Is} \sim \epsilon$. The parallel projection of the momentum equation was used to evaluate \tilde{n}_j . In case of \tilde{n}_j mainly driven by momentum input, one would obtain: $\frac{1}{n_j} \frac{\partial n_j}{\partial \theta} \propto \tilde{M}_{\phi j} \propto Z_j^2 \tilde{n}_j$. In particular,

in the presence of sonic impurities (high Z impurities) the in-out density asymmetry, driven by centrifugal force, scales as Z_j and one obtains: $\tilde{n}_{js} \propto \tilde{M}_{\phi jc} \propto Z_j^2 \tilde{n}_{jc} \propto Z_j^3$. The calculations of \tilde{n}_{js} , in Ref. [94] were performed for Tungsten ($Z_W = 74$) and Titanium ($Z_{Ti} = 22$) and an input power in the range $[-2.4 - 2.4]$ MW. Even taking into account the fact that in TFTR the input power can be higher, the momentum input would not drive any significative up-down asymmetry of the Carbon impurity density ($Z_C = 6$) in TFTR.

Electrostatic potential asymmetry - As shown in Eq.(8.49), $e_j \partial \Phi / (r \partial \theta)$ is a potential driving force for \tilde{n}_j . In addition $\tilde{\Phi}$ appears in the $\tilde{\Omega}_{\phi j}$ expression (Eq.(8.29)) and, if large enough, can determine its magnitude.

In Ref. [92], $\tilde{\Phi}$ was evaluated in case of perpendicular NBI and found to be of $O(\epsilon)$. This was the effect of a relatively large in-out density poloidal variation of the fast ions, a large fraction of which were trapped in the outer region of the tokamak by the “magnetic mirror force”.

The presence of the fast ions is not accounted for in our calculation of poloidal variations. Nevertheless we can here discuss the effect of their presence upon $\tilde{\Phi}_c$ and therefore \tilde{n}_{jc} .

The contribution of an asymmetric fast ion density, \tilde{n}_{fi} , to $\tilde{\Phi}_c$ is given by:

$$\tilde{\Phi}_{c(fi)} \frac{e\Phi_o}{T_i} = \tilde{n}_{fi} \frac{n_{fi}}{n_e} \left(\frac{T_i}{T_e} + Z_{eff} - \frac{n_{fi}}{n_e} \right)^{-1} \quad (8.112)$$

Using the following values, characteristic of Exp.44: $n_{fi}/n_e = 0.25$, $T_i/T_e = 2.5$ and $Z_{eff} = 3$, one obtains:

$$\tilde{\Phi}_{c(fi)} \frac{e\Phi_o}{T_i} \simeq 0.05 \tilde{n}_{fi} \quad (8.113)$$

Chang and Harvey [92] evaluated $\tilde{n}_{fi} = 0.5 - 0.6$ for quasi-perpendicular injection in DIII and PDX, and $\tilde{n}_{fi} = 0.1$ for tangential injection in ISX-B. Using these values to estimate a possible range of variation of \tilde{n}_{fi} in TFTR (whose NBI has a perpendicular component), one estimates:

$0.005 < \bar{\Phi}_{\alpha(fi)} e\Phi_o/T_i < 0.025$. In TFTR $\epsilon = 0.3$ r/a. Therefore $\bar{\Phi}_{\alpha(fi)} \ll \epsilon$ when we make use of the ordering $e\Phi_o/T_e \sim 1$.

Chang and Hazeltine [90] pointed out that $\tilde{n}_j Z_j n_j / n_e \sim \epsilon$ would lead to $\bar{\Phi} \sim \epsilon$. This is consistent with our expression of $\bar{\Phi}$, Eq.(8.23). But in the shots analyzed in this work $\tilde{n}_j \ll \epsilon$ and therefore $\bar{\Phi} \ll \epsilon$.

Rotation frequency poloidal asymmetry - To our knowledge, estimates of $\tilde{\Omega}_{\phi j}$ have not been published before. There are observations of in-out asymmetry of $\Omega_{\phi j}$ from JET and TFTR, but it is the opinion of the TFTR experimentalists that these asymmetries could be attributed to systematic error bars of the CHERS diagnostics itself. Nevertheless, the form of $v_{\phi j}$, Eq.(8.9), that originates from simple considerations of momentum and particle conservation, predicts $\tilde{\Omega}_{\phi jc} \sim \epsilon$ whenever $v_{\theta j} \sim \beta v_{\phi j}$. Since there is experimental evidence of poloidal velocity of this magnitude in TFTR (in balance NBI, and of larger magnitude at the edge of other tokamaks) one should expect to observe in-out poloidal asymmetries of $\Omega_{\phi j}$.

Ref. [70] pointed out that: (1) $\bar{\Phi} \sim \epsilon$ would lead to $\tilde{\Omega}_{\phi j} \sim \epsilon$; and, (2) $v_{\theta j} \sim \beta v_{\phi j}$ generates $\tilde{\Omega}_{\phi jc} \sim \epsilon$ and, when associated with $\tilde{n}_{js} \sim \epsilon$, it would also cause $\tilde{\Omega}_{\phi js} \sim \epsilon$. For the TFTR EXp.44 plasma $\bar{\Phi} \ll \epsilon$ and therefore the potential asymmetries cannot drive considerable $\tilde{\Omega}_{\phi j}$. In addition, as discussed above, also $\tilde{n}_{js} \ll \epsilon$ and therefore $\tilde{\Omega}_{\phi js} \ll \epsilon$. But there is experimental evidence that $v_{\theta I} \sim \beta v_{\phi I}$ and, using values of the poloidal velocities of this magnitude, we evaluate $\tilde{\Omega}_{\phi jc} \sim \epsilon$.

Poloidal velocities - $v_{\theta i}$ and $v_{\theta I}$ were evaluated in Ref. [94] for collisional impurities and main ions in the plateau regime (ISX-B, PLT), by solving the FSA parallel momentum balance equation and neglecting the heat flux. It was found that $v_{\theta I} \sim O(\beta v_{\phi}) > v_{\theta i}$, driven by momentum input and, to a lesser extent, by pressure gradients. This is consistent with the fact that $\eta_{0i} > \eta_{0I}$ (Eq.(3.3)) and that $v_{\theta i} \eta_{0i} \simeq v_{\theta I} \eta_{0I}$. Analogously, for the case $\bar{q}_j = 0$, we solve the poloidal FSA poloidal balance equation and find $v_{\theta i} \sim O(\beta v_{\phi}) > v_{\theta I}$, consistent with $\eta_{0i} < \eta_{0I}$ and with the

fact that both ions and impurities are in the banana regime.

The FSA parallel momentum balance equation, used to evaluate $v_{\theta j}$, contains the unknown toroidal projection of the perpendicular viscous force; this force was represented by an anomalous drag force in Ref.[94] and the dependence of the $v_{\theta j}$ results on magnitude of this term was then studied.

We include an unknown anomalous force in the FSA poloidal momentum balance equation (via the γ_j) and we also have to study the dependence of the $v_{\theta j}$ results on the magnitude of this parameter. In our model, the poloidal velocities are driven by the radial particle flux and are larger when the mentioned anomalous force is absent.

For the case $\tilde{q}_j \neq 0$, $v_{\theta j}$ is usually evaluated by solving the system of equations Eq.(7.20). These balance equations neglect momentum and power input, and toroidal viscous force and heat viscous terms that are important in NBI plasma. These equations are therefore used for OH plasmas; nevertheless these equations have been unable to explain the large $v_{\theta I} \sim v_{\phi I}$ observed in OH (as NBI as well) plasmas.

We used the FSA poloidal momentum and heat flux balance system of equations to evaluate $v_{\theta j}$ (and $q_{\theta j}$). Our equations include anomalous terms. We found that neglecting the presence of these anomalous terms while using experimental values of the radial conductive heat flux would lead to values of v_{θ} too large to be consistent with experimental observations. The inclusion of these anomalous terms in the momentum and heat balance equations can give values of $v_{\theta j}$ that are closer to the experimental observations.

8.11.2 How believable are our estimate of \tilde{n}_j , $\tilde{\Omega}_{\phi j}$ and Ξ_j for TFTR Exp.44 ?

The main uncertainties in our calculations of \tilde{n}_j and $\tilde{\Omega}_{\phi j}$ (and therefore of the gyroviscous momentum flux) are: (1) the radial profile and magnitude of the poloidal velocities of main ions and impurities; (2) the radial profile and magnitude of the anomalous terms that have been formally included in the momentum balance equa-

tion; (3) the possible presence of anomalous forces that have not been included in our equations; and, (4) the form of the forces, taken into account in the balance equations, for which the neoclassical formulas have been used. Let us discuss these uncertainties in detail.

Poloidal velocity - We have calculated $v_{\theta I}$ and $v_{\theta i}$ from first principles and neglecting the heat flux; we found that $v_{\theta I} \ll \beta v_{\phi I}$ and that $v_{\theta i}$ could be comparable with $\beta v_{\phi I}$. There are no measurements of $v_{\theta i}$ and very few measurements of $v_{\theta I}$ in any tokamaks (none in Exp.44). In order to estimate an upper bound on \tilde{n}_j and $\tilde{\Omega}_{\phi j}$, we also used a trial $v_{\theta*}$ profile, for $v_{\theta I}$, based on a few experimental measurements of the poloidal velocity on different machines. These experimental observations (see Section 7.6) were associated with plasma conditions different from the TFTR Exp.44 ones and we have no certain reason to believe that the actual $v_{\theta I}$, in Exp.44, is close to the trial $v_{\theta*}$. But how much different could it be? Our concern is: could $v_{\theta I}(r)$ be more than a factor of order unity larger than the trial $v_{\theta*}(r)$? If the actual poloidal velocities are smaller than the one we assumed, we have in fact overestimated $\tilde{\Omega}_{\phi j}$ and our calculations must be regarded as conservative estimate of the toroidal rotation poloidal asymmetries and therefore of the neoclassical momentum flux. The possibility that $v_{\theta I}(r)$ were one or more orders of magnitude larger than the trial profile appear very unlikely: in fact one would be able to observe a $v_{\theta} \sim O(v_{\phi})$ and, as a consequence of this, $\tilde{\Omega}_{\phi jc} \sim 1$ and $E_r \sim O(v_{\phi} B_{\phi})$. This is in disagreement with experimental observations.

It is in fact likely that the actual poloidal velocities have radial profiles and direction different from the ones assumed in the trial $v_{\theta*}$ profile, in which case the radial profile of $\tilde{\Omega}_{\phi j}$ (and therefore Ξ_j) would have different radial behaviour, but our estimate should provide an upper boundary to their magnitude.

Particle fluxes and driving anomalous forces. The magnitude of the particle fluxes and of the $\Gamma_j^{(\sim)}$ force determine the magnitude of the parallel viscous force, $(p_{\parallel} - p_{\perp})_j$, of \tilde{n}_{js} and $\tilde{\Omega}_{\phi js}$. We discussed that, since the Exp.44 plasma parameters were

steady state $\sim 600\text{ ms}$ at the end of the discharge, the radial ion fluxes magnitudes must have been within certain ranges, namely $Z_I \Gamma_I < 0.1 \Gamma_e$ and $\Gamma_i > 0.9 \Gamma_e$. These conditions represent a small uncertainty for the values of Γ_j .

The possible presence of anomalous forces, $\Gamma_j^{(\sim)}$, was discussed and values of $\Gamma_j^{(\sim)}/\Gamma_e = [0 - 1]$, constant of r , were assumed in the calculation of the poloidal variations. There is no experimental evidence or reason to believe that the anomalous force has such a radial profile. But our real concern is: could $\Gamma_j^{(\sim)}$ be larger (one order of magnitude or more) than our assumption? Since we are interest in mechanisms able to drive up-down asymmetries of density and velocity of order ϵ , we note that $\Gamma_j^{(\sim)}/\Gamma_e$ should be of order $10^2 - 10^3$ in order to drive $\tilde{n}_{js} \sim \epsilon$. The evaluation of $\Gamma_j^{(\sim)}$ from fluctuation measurements, with or without employing a theoretical assumption for the turbulent-mechanism, have produced estimates of $\Gamma_j^{(\sim)} \leq \Gamma_e$. Even if the evaluations of this anomalous term are affected by large error bars, we can exclude the possibility that the measurements are off by a factor of $10^2 - 10^3$.

Other anomalous forces. Other forces of anomalous origin could affect the momentum balance equations but as far as we know they have not yet been identified.

Neoclassical forces modified by turbulence. The friction force is so small for the collisionless TFTR Exp.44 plasma that, even if its magnitude is affected by non-neoclassical transport mechanisms, it is very unlikely that \tilde{R}_j could increase by several (7-8) orders of magnitude and become a force large enough to affect \tilde{n}_j .

The parallel viscosity, whose actual value is considered to be close to the neoclassical prediction, could also been affected by anomalous mechanisms. The relation

$$\langle \tilde{B}_\theta \nabla \cdot \tilde{\Pi}_j^0 \rangle \propto \tilde{B}_\theta \nabla \cdot \tilde{\Pi}_j^0 \propto (p_{\parallel} - p_{\perp})_{js} \quad (8.114)$$

is an intrinsic property of the parallel viscosity tensor. In fact we did not make use of any expression for $(p_{\parallel} - p_{\perp})_{js}$ in determining $\tilde{n}_{js} \propto (p_{\parallel} - p_{\perp})_{js}$, and our results are valid for any parallel viscosity satisfying Eq.(8.114).

In conclusion we believe that our calculations of \tilde{n}_j , $\tilde{\Omega}_{\phi j}$, and hence the neoclassical

torque flux, represent an estimate of the upper limit for the magnitude that these quantities can assume in the TFTR Exp.44 plasma.

Chapter 9

SUMMARY, CONCLUSIONS AND FUTURE WORK

9.1 Summary and conclusions

A well-diagnosed rotation experiment has been carried out in TFTR with the purpose to obtaining measurements of the radial profiles of v_ϕ and T_i for a variety of plasma and machine parameter conditions. These measurements, carried out with the recently installed CHERS diagnostic, allowed, in particular, the computation of the radial profiles of the torque flux and momentum diffusivities, quantities that previously were only known at the edge or unknown, respectively.

The data were analyzed with the 1D transport code SNAP. The discharges in this experiment showed characteristics intermediate between L-mode shots and Super-shots. Rotation velocities, up to $5.5 \cdot 10^5$ m/s, were found to be higher in low current, co-injection shots and in low B discharges. Experimental momentum confinement times, in the range 24-50 ms, were found to decrease weakly with input torque per particle, to increase with plasma current and to be independent of B.

The momentum confinement properties (τ_ϕ , $v_\phi(0)$, K_ϕ and χ_ϕ), inferred from experimental data, were compared with the predictions of several neoclassical and anomalous theories.

The gyroviscous theory, with the assumption of impurity poloidal asymmetries \tilde{n}_I , $\tilde{\Omega}_{\phi I} \sim \epsilon$ and of negligible main ion poloidal asymmetries, was shown to predict the magnitude and the parametric dependence of τ_ϕ , $v_\phi(0)$ and K_ϕ^{gv} . Other theories, namely Hsu-Sigmar's theory and the rotational viscosity theory, based on neoclassical mechanisms of momentum transport different from the gyroviscous one, would

reproduce the gyroviscous results when the same assumptions are made about the poloidal asymmetries [114].

Ware's cold ions theory underestimated the observed viscosity. In fact, the momentum flux caused by the presence of a plausible amount of cold ions was found to be negligible with respect to the actual magnitude of the momentum flux.

Each of the anomalous theories considered (ITG, untrapped particles and stochastic magnetic perturbation modes) predicted torque flows which show magnitudes, radial profiles and parametric dependences on plasma parameters different from those of the experimental torque flow. While the agreement between η_i^{ex} and η_i^{theo} , found in this experiment, would support the presence of ITG modes, perturbation studies in later (1989) discharges have revealed behaviours of the ion and electron temperature profiles that are in disagreement with the predicted behaviour of η_i modes at marginal stability.

Since the gyroviscous formalism was successful in predicting τ_ϕ , $v_\phi(0)$ and K_ϕ , when an effective poloidal asymmetry factor of $\bar{\Theta} = 1.5$ was used (based on the assumption of $O(\epsilon)$ impurity density asymmetries and $\ll O(\epsilon)$ main ion density asymmetries), a detailed calculation of \tilde{n}_j and $\tilde{\Omega}_{\phi j}$ was performed. Poloidal density asymmetries smaller than ϵ were calculated for both ions and impurities; but the same calculation (case $q_j = 0$) also yielded impurity poloidal velocities much less than suggested by the limited experimental data. Using the calculated poloidal density asymmetries to evaluate the original formulation of the gyroviscous torque flow resulted in torque flows in good agreement with experimental values. However, our calculations of the radial dependence of the poloidal density asymmetries do not support the separation-of-variables approximation used in the original formulation of the gyroviscous flow. When we evaluate an *alternative* formulation of the gyroviscous torque, which removes this approximation, we predict values that are at least one order of magnitude smaller than the experimental torque flows.

9.2 Suggestions for future work

Theoretical calculations indicate that neoclassical forces and the effect of anomalous radial particle fluxes give rise to a momentum flux which is at least one order of magnitude smaller than the momentum flux experimentally inferred. These results leave open the question of what mechanisms - probably anomalous - can be responsible for the observed agreement of $v_{\phi}^{ex}(0)$ and τ_{ϕ}^{ex} with $v_{\phi}^{gv}(0)$ and τ_{ϕ}^{gv} . The disagreement of the anomalous theories does not exclude the anomalous nature of momentum transport. In fact, while theory has failed to identify the driving forces of the plasma parameter fluctuation, the evaluation of particle and heat flux directly from the fluctuation measurements has given results comparable to the experimental measurements [129]. A next step in the comparison of experiments and theory would in fact be the computation of the momentum flux directly from the measured fluctuation spectra and amplitude.

The poloidal velocity, which was not the main issue in this Thesis, offers many opportunities for both experimental investigation and theoretical speculation. Measurements of the poloidal velocity in the bulk plasma should be possible with the same CHERS diagnostics that have been successfully measuring the edge v_{θ} profiles. The theoretical investigation of v_{θ} in unbalanced NBI plasmas requires the use of transport equations which, in addition to retaining the neoclassical transport description, should include anomalous driving terms.

Appendix A

Heat flow balance equation

Taking the velocity moment $m_j v_j^2 \vec{v}_j$ of the kinetic equation one obtains the heat flow balance equation: [53]

$$\frac{\partial \vec{Q}_j}{\partial t} + \nabla \cdot \vec{\vec{\Lambda}}_j - \frac{1}{2} \frac{e_j}{m_j} (m_j n_j v_j^2 + 3p_j) \vec{E} - (m_j n_j \vec{v}_j \vec{v}_j + \vec{\vec{\Pi}}_j + p_j \vec{\vec{I}}) \cdot \vec{E} \quad (\text{A.1})$$

$$- \frac{e_j}{m_j} \vec{Q}_j \times \vec{B} = \frac{T_j}{m_j} \left(\frac{5}{2} \vec{R}_j - \vec{F}_j + \vec{W}_j \right) \quad (\text{A.2})$$

where:

$$\vec{Q}_j = \frac{1}{2} m_j n_j v_j^2 \vec{v}_j + \frac{5}{2} p_j \vec{v}_j + \vec{v}_j \vec{\vec{\Pi}}_j + \vec{q}_j \quad (\text{A.3})$$

is the total energy flow, \vec{q}_j is the conductive heat flux, $\vec{\vec{\Lambda}}_j$ is the energy flux tensor, \vec{F}_j is the heat friction force and \vec{W}_j is the source term.

Combining Eq.(2.2) with Eq.(A.1) one obtains the following balance equation:

$$\frac{\partial}{\partial t} (\vec{Q}_j - \frac{5}{2} p_j \vec{v}_j) + \frac{5}{2} n_j \vec{v}_j \frac{\partial T_j}{\partial t} + \nabla \cdot \vec{\vec{\Lambda}}_j - \frac{5}{2} \frac{T_j}{m_j} \nabla \cdot (m_j n_j \vec{v}_j \vec{v}_j + \vec{\vec{\Pi}}_j) \quad (\text{A.4})$$

$$+ p_j \vec{\vec{I}}) - \frac{e_j}{m_j} (\vec{Q}_j - \frac{5}{2} p_j \vec{v}_j) \times \vec{B} - \frac{e_j}{m_j} \vec{E} [m_j n_j \vec{v}_j \vec{v}_j + \vec{\vec{\Pi}}_j + p_j \vec{\vec{I}} - \frac{1}{3} m_j n_j v_j^2 \vec{\vec{I}}] = \frac{T_j}{m_j} (\vec{W}_j - \vec{F}_j - \frac{5}{2} \vec{S}_j) \quad (\text{A.5})$$

The following definition is commonly encountered:

$$\nabla \cdot \vec{\vec{\Theta}}_j = - \frac{m_j}{T_j} [\nabla \cdot \vec{\vec{\Lambda}}_j - \frac{5}{2} \frac{T_j}{m_j} \nabla \cdot (m_j n_j \vec{v}_j \vec{v}_j + \vec{\vec{\Pi}}_j + p_j \vec{\vec{I}})] \quad (\text{A.6})$$

In steady state, Eq.(A.4) can be written:

$$\nabla \cdot \vec{\vec{\Theta}}_j + \frac{e_j}{T_j} (\vec{q}_j + \vec{v}_j \vec{\vec{\Pi}}_j) \times \vec{B} + \frac{e_j}{T_j} \vec{E} \cdot [\vec{\vec{\Sigma}}_j] = \vec{F}_j - \vec{W}_j + \frac{5}{2} \vec{S}_j \quad (\text{A.7})$$

Appendix B

Friction force

The expressions for the friction and heat friction forces, \vec{R}_j and \vec{F}_j respectively, have been shown to be linearly related to the fluid velocity, \vec{v}_j , and the conductive heat flux, \vec{q}_j [63], [64]:

$$\vec{R}_j = \sum_k [l_{00}^{jk} \vec{v}_k + l_{01}^{jk} (-\frac{2}{5} \frac{\vec{q}_k}{p_k})] \quad (\text{B.1})$$

$$\vec{F}_j = \sum_k [l_{10}^{jk} \vec{v}_k + l_{11}^{jk} (-\frac{2}{5} \frac{\vec{q}_k}{p_k})] \quad (\text{B.2})$$

where the friction coefficients, l_{nm}^{jk} , can be written:

$$l_{nm}^{jk} = (\sum_i \frac{m_j n_j}{\tau_{ji}} M_{ji}^{nm}) \delta_{jk} + \frac{m_j n_j}{\tau_{jk}} N_{jk}^{nm} \quad (\text{B.3})$$

$$M_{jk}^{nm} = M_{jk}^{mn} \quad (\text{B.4})$$

$$N_{jk}^{nm} = \frac{T_j v_{thj}}{T_k v_{thk}} N_{kj}^{mn} \quad (\text{B.5})$$

$$x_{jk} = \frac{v_{thk}}{v_{thj}} \quad (\text{B.6})$$

$$M_{jk}^{00} = -(1 + \frac{m_j}{m_k})(1 + x_{jk}^2)^{-3/2} = -N_{jk}^{00} \quad (\text{B.7})$$

$$M_{jk}^{01} = M_{jk}^{10} = -\frac{3}{2}(1 + \frac{m_j}{m_k})(1 + x_{jk}^2)^{-5/2} = -N_{jk}^{10} \quad (\text{B.8})$$

$$M_{jk}^{11} = -(\frac{13}{4} + 4x_{jk}^2 + \frac{15}{2}x_{jk}^4)(1 + x_{jk}^2)^{-5/2} \quad (\text{B.9})$$

$$N_{jk}^{11} = \frac{27}{4}x_{jk}^2 \frac{T_j}{T_k} (1 + x_{jk}^2)^{-5/2} \quad (\text{B.10})$$

Appendix C

Neoclassical viscous forces

For the case $\vec{q}_j = 0$, we are going to use Braginskii's neoclassical tensor, rewritten for flux-surface coordinate [23]. The toroidal, poloidal and radial projection of the viscous forces have been rewritten in order to show their parametric dependence more explicitly.

- The poloidal component of the parallel viscous force is:

$$\begin{aligned} \hat{\theta} \cdot \nabla \cdot \vec{\Pi}_j^0 &\equiv \Pi_{\theta j}^0 = \\ &\frac{\eta_{0j} v_{\theta j}}{r^2} \left\{ \epsilon \cos \theta - \frac{2}{3} \frac{\partial \vartheta_j}{\partial \theta} + \epsilon (\varrho_{0j} + \frac{\vartheta_j}{3}) \sin \theta - (\epsilon \sin \theta)^2 + \right. \\ &\left. \frac{2}{3} \vartheta_j (\vartheta_j - \varrho_{0j}) \right\} + \eta_{0j} \frac{\beta A_j}{\epsilon r} \left(4 \epsilon \sin \theta - \varrho_{0j} - \frac{1}{A_j} \frac{\partial A_j}{\partial \theta} \right) \end{aligned} \quad (C.1)$$

with

$$\begin{aligned} A_j &\equiv \frac{1}{B_\theta R} \frac{\partial}{\partial \theta} \left(\frac{1}{e_j n_j} \frac{\partial p_j}{\partial r} + \frac{\partial \Phi}{\partial r} \right) - \Omega_{\phi j 0} \frac{\partial U_j}{\partial \theta} \\ &= \frac{1}{B_\theta R} \left[\frac{T_j}{e_j} \frac{\partial \vartheta_j}{\partial r} + \frac{1}{e} \frac{\partial}{\partial r} (T_e \vartheta_e) \right] + \Omega_{\phi j 0} U_{jc} \sin \theta - \Omega_{\phi j 0} U_{js} \cos \theta \end{aligned} \quad (C.2)$$

$$\varrho_{0j} \equiv \frac{1}{\eta_{0j}} \frac{\partial \eta_{0j}}{\partial \theta} \quad \vartheta_j \equiv \frac{1}{n_j} \frac{\partial n_j}{\partial \theta} \quad (C.3)$$

For a i-I plasma, with both ions species in banana regime, $\varrho_{0j} \sim (\tilde{n}_j + \tilde{n}_I)$.

The FSA of Eq.(C.1)/($h n_j$) is:

$$\begin{aligned}
\langle \frac{\Pi_{\theta j}^0}{h n_j} \rangle &= \frac{\eta_{0j} v_{\theta j}}{n_j R^2} \left[-\frac{3}{2} + \frac{\tilde{n}_{js}}{2\epsilon} + \frac{\tilde{n}_{Is}}{2\epsilon} + \frac{\tilde{n}_{Ic}}{2\epsilon} - \frac{\tilde{n}_{jc}}{\epsilon} \right. \\
&\quad + \frac{1}{3\epsilon^2} (\tilde{n}_{Ic} \tilde{n}_{jc} + \tilde{n}_{Is} \tilde{n}_{js} + \tilde{n}_{jc} \tilde{n}_{Is} - \tilde{n}_{js} \tilde{n}_{Ic}) \Big] \\
&\quad + \frac{\eta_{0j} \beta}{2 n_j r} \left[A_{js} \left(3 - \frac{\tilde{n}_{Is} + \tilde{n}_{js} + \tilde{n}_{jc}}{\epsilon} \right) - A_{jc} \frac{\tilde{n}_{Ic} + \tilde{n}_{jc} - \tilde{n}_{js}}{\epsilon} \right]
\end{aligned} \tag{C.4}$$

- The poloidal component of the gyroviscous force is:

$$\begin{aligned}
\hat{\theta} \cdot \nabla \cdot \vec{\Pi}_j^{3,4} &\equiv \Pi_{\theta j}^{3,4} = \\
&\frac{\eta_{4j}}{2} \left[-\beta (13 \sin \theta - 3 \frac{\vartheta_j}{\epsilon}) \frac{\partial \Omega_{\phi j}}{\partial r} + \mathcal{P}_{1j} \frac{\beta A_j}{\epsilon r} - 2 \frac{\beta}{\epsilon} \frac{\partial A_j}{\partial r} + \right. \\
&\left. \frac{v_{\theta j}}{r R} (-\mathcal{P}_{2j} \sin \theta + \mathcal{P}_{3j} \frac{\vartheta_j}{\epsilon}) \right]
\end{aligned} \tag{C.5}$$

with

$$\mathcal{P}_{1j} \equiv 2 + \frac{r}{L_q} - \frac{r}{L_{p_j}} + 3\epsilon \cos \theta \quad (L_x^{-1} \equiv -\frac{1}{x} \frac{\partial x}{\partial r}) \tag{C.6}$$

$$\mathcal{P}_{2j} \equiv 4 + 6 \frac{r}{L_q} - 3 \frac{r}{L_{p_j}} + 2 \frac{r}{L_{v_{\theta j}}} + 16\epsilon \cos \theta \quad q = \epsilon_0 / \beta \tag{C.7}$$

$$\mathcal{P}_{3j} \equiv 5 + 3 \frac{r}{L_q} - 2 \frac{r}{L_{p_j}} + 2 \frac{r}{L_{\vartheta_j}} + \frac{r}{L_{v_{\theta j}}} + 7\epsilon \cos \theta \tag{C.8}$$

The FSA of Eq.(C.5)/($h n_j$) is:

$$\langle \frac{\Pi_{\theta j}^{3,4}}{h n_j} \rangle \sim \frac{\beta T_j}{4 \omega_{cj}} \left(-13 \frac{\partial \Omega_{\phi js}}{\partial r} + 3 \frac{\tilde{n}_{jc}}{\epsilon} \frac{\partial \Omega_{\phi js}}{\partial r} - 3 \frac{\tilde{n}_{js}}{\epsilon} \frac{\partial \Omega_{\phi jc}}{\partial r} \right) \tag{C.9}$$

- The toroidal component of the parallel viscous force is:

$$\begin{aligned}
\hat{\phi} \cdot \nabla \cdot \vec{\Pi}_j^0 &\equiv \Pi_{\phi j}^0 = \\
&\frac{\beta \eta_0}{r^2} \left\{ v_{\theta j} \left[-3\epsilon \cos \theta + 2 \frac{\partial \vartheta_j}{\partial \theta} + \epsilon (\vartheta_j - 3 \varrho_{0j}) \sin \theta + 2 \vartheta_j (\varrho_{0j} - \vartheta_j) \right] + \right. \\
&\left. 3 A_j \beta R (\varrho_{0j} - 3\epsilon \sin \theta + \frac{1}{A_j} \frac{\partial A_j}{\partial \theta}) \right\}
\end{aligned} \tag{C.10}$$

- The toroidal component of the gyroviscous force is:

$$\begin{aligned} \hat{\phi} \cdot \nabla \cdot \vec{\Pi}_j^{3,4} &\equiv \Pi_{\phi j}^{3,4} = \\ &\frac{\eta_{4j}}{rR} [\mathcal{E}_j \frac{v_\theta}{\beta} (2 \sin \theta - \frac{\vartheta_j}{\epsilon}) + v_{\phi j} \mathcal{F}_j (4 \sin \theta - \frac{\vartheta_j}{\epsilon}) - \frac{1}{\epsilon} A_j R \mathcal{E}_j] \end{aligned} \quad (\text{C.11})$$

with

$$\mathcal{E}_j \equiv -\frac{r}{\eta_{4j} R^3} \frac{\partial \eta_{4j} R^3}{\partial r}, \quad \mathcal{F}_j \equiv -\frac{rR}{v_{\phi j}} \frac{\partial \Omega_{\phi j}}{\partial r} \quad (\text{C.12})$$

- The radial component of the parallel viscous force is:

$$\begin{aligned} \hat{r} \cdot \nabla \cdot \vec{\Pi}_j^0 &\equiv \Pi_{rj}^0 = \\ &\frac{\eta_{0j}}{r} \left\{ \frac{v_{\theta j}}{r} \left[-(\epsilon \sin \theta - \frac{2}{3} \vartheta_j) \frac{r}{L_{\eta_{0j}}} - r^2 \frac{2}{3} \frac{\partial}{\partial r} \left(\frac{\vartheta_j}{r} \right) \right. \right. \\ &\quad \left. \left. + \epsilon^2 \sin 2\theta - 2\epsilon \vartheta_j \cos \theta \right] + \frac{\partial v_{\theta j}}{\partial r} (\epsilon \sin \theta - \frac{2}{3} \vartheta_j) \right. \\ &\quad \left. - \frac{\beta A_j}{\epsilon} \left(4\epsilon \cos \theta - \frac{r}{L_{\eta_{0j}}} - \frac{r}{L_{A_j/r}} + \frac{r}{L_q} \right) \right\} \end{aligned} \quad (\text{C.13})$$

For $\tilde{q}_j \neq 0$, one derives from Eq.(3.6):

$$\Pi_{rj}^0 = -\frac{1}{3} \frac{\partial}{\partial r} (p_{\parallel j} - p_{\perp j})_s \sin \theta - \frac{(p_{\parallel j} - p_{\perp j})_s}{r} (\beta^2 + \epsilon \cos \theta) \sin \theta \quad (\text{C.14})$$

- The radial component of the gyroviscosity is:

$$\begin{aligned} \hat{r} \cdot \nabla \cdot \vec{\Pi}_j^{3,4} &\equiv \Pi_{rj}^{3,4} = \\ &\frac{\eta_{4j}}{2} \left[\frac{v_{\theta j}}{r^2} (-2\epsilon \cos \theta + 2 \frac{\partial \vartheta_j}{\partial \theta} - 2\epsilon \vartheta_j \sin \theta + 1 - \frac{r}{L_{\eta_{4j}}}) - \right. \\ &\quad \frac{1}{r} \frac{\partial v_{\theta j}}{\partial r} (\epsilon \cos \theta + 1 - \frac{r}{L_{\eta_{4j}}}) - \frac{\partial^2 v_{\theta j}}{\partial r^2} + \\ &\quad \frac{A_j \beta}{r \epsilon} (\vartheta_j - 3\epsilon \sin \theta + \frac{\partial A_j}{\partial \theta}) + \\ &\quad \left. \frac{\partial \Omega_{\phi j}}{\partial r} \frac{\beta}{\epsilon} (6\epsilon \cos \theta - 2 - \frac{r}{L_{\eta_{4j}}}) + \beta R \frac{\partial^2 \Omega_{\phi j}}{\partial r^2} \right] \end{aligned} \quad (\text{C.15})$$

- The terms from the perpendicular viscosity tensor can be neglected because

$$\eta_{2j} \ll \eta_{4j}, \eta_{0j}.$$

Bibliography

- [1] S. Suckewer et al., Phys. Rev. Lett. **43**, 207 (1979).
- [2] S. Suckewer et al., Nucl. Fusion **21**, 1301 (1981).
- [3] K. Brau et al., Nucl. Fusion **23**, 1643 (1983).
- [4] R.C. Isler et al., Nucl. Fusion **26**, 391 (1986) ; R.C. Isler and L.E. Murray, Appl. Phys. Lett. **42**, 355 (1983).
- [5] K.H. Burrell et al., Nucl. Fusion **28**, 3 (1988).
- [6] R.J. Groebner et al., Nucl. Fusion **26**, 543 (1986).
- [7] H. St. John et al., "Analysis of toroidal rotation data for the DIII-D tokamak", General Atomics Report GA-A19563 (January 1989).
- [8] A. Kallenback et al., "Momentum confinement studies on ASDEX", *Proc. 16th Europ. Conf. Cont. Fusion and Plasma Phys.*, Venice, 1989.
- [9] D.E. Roberts et al., "Momentum confinement of ASDEX plasmas during co and counter neutral beam injection", *Proc. 15th Europ. Conf. Cont. Fusion and Plasma Phys.*, Dubrovnik, 1988.
- [10] A. Kallenback et al., Nucl. Fusion **30**, 645 (1990).
- [11] M. Bitter et al., Plasma Phys. and Cont. Fusion **29**, 1234 (1987).
- [12] M. Murakami et al., Plasma Phys. and Cont. Fusion **28**, 17 (1986).

- [13] S.D. Scott et al., "Analysis of rotation speed radial profiles on TFTR", *Proc. 15th Europ. Conf. Cont. Fusion and Plasma Phys.*, Dubrovick, 1988.
- [14] S.D. Scott et al., "Current drive and confinement of angular momentum in TFTR", *Proc. 12th Int. Conf. Plasma Phys. and Cont. Nucl. Fusion*, Nice, 1988 (IAEA-CN-50/E-III-5).
- [15] S.D. Scott et al., *Phys. Fluids B* **2**, 1304 (1990).
- [16] S.D. Scott et al., *Phys. Rev. Lett.* **64**, 531 (1990).
- [17] D. Stork et al., "Momentum transport and scaling effects observed in neutral beam heated rotating plasmas in JET", *Proc. 14th Europ. Conf. Cont. Fusion and Plasma Phys.*, Madrid, 1987.
- [18] N.C. Hawkes et al., "Profiles of toroidal plasmas rotation", *Proc. 15th Europ. Conf. Cont. Fusion and Plasma Phys.*, Dubrovick, 1988.
- [19] H.P.L. de Esch et al., "Toroidal Plasma Rotation in JET", Joint European Torus Report JET-P(90)14 (June 1990).
- [20] W.M. Stacey, *Nucl. Fusion* **31**, 31 (1991).
- [21] J.A. Snipes et al., "Plasma stored energy and momentum losses during large MHD activity in JET", Joint European Torus Report JET-P(89)64 (September 1989).
- [22] N. Asakura et al., *Bull. Am. Phys. Soc.* **34**, 2049 (1989).
- [23] W.M. Stacey and D.J. Sigmar, *Phys. Fluids* **28**, 2800 (1985).
- [24] W.M. Stacey et al., *Nucl. Fusion* **26**, 293 (1986).
- [25] A.A. Ware, *Phys. Rev. Lett.* **64**, 2655 (1990).
- [26] C.T. Hsu and D. Sigmar, *Plasma Phys. and Cont. Fusion* **32**, 499 (1990).

- [27] W.M. Stacey and G.W. Neeley, "Neoclassical theory of momentum transport by marginally collisional ions in strongly-rotating tokamak plasmas with unbalanced neutral beam injection", Georgia Tech Report GTFR 96 (1990)
- [28] D.Kh. Morozov and O.P. Pogutse, "Relaxation of plasma toroidal rotation in tokamaks and anomalous viscosity", *Proc. 11th Int. Conf. Plasma Phys. and Cont. Nucl. Fusion*, Kyoto, 1986.
- [29] B.B. Kadomtsev and O.P. Pogutse, "Electron heat conductivity of the plasma across a 'braided' magnetic field", *Proc. 7th Int. Conf. Plasma Phys. and Cont. Nucl. Fusion*, Innsbruck, 1978.
- [30] D.K. Morozov and O.P. Pogutse, *Sov. J. Plasma Phys.* **12**(6), 381 (1986).
- [31] D.Kh. Morozov et al., *Sov. J. Plasma Phys.* **14**, 147 (1988).
- [32] M.V. Osipenko et al., "Damping of toroidal rotation by anomalous ion viscosity", *Proc. 12th Int. Conf. Plasma Phys. and Cont. Nucl. Fusion*, Nice, 1988 (IAEA-CN-50/D-4-4).
- [33] D.L. Brower, *Phys. Rev. Lett.* **59**, 48 (1987).
- [34] N. Mattor and P.H. Diamond, *Phys. Fluids* **31**, 1180 (1988).
- [35] G.S. Lee and P.H. Diamond, *Phys. Fluids* **29**, 3291 (1986).
- [36] H. Biglari et al., "Advances in the theory of ion-temperature-gradient-driven turbulence", *Proc. 12th Int. Conf. Plasma Phys. and Cont. Nucl. Fusion*, Nice, 1988 (IAEA, Vienna, 1989; Vol 2, p. 261).
- [37] R. Dominguez and R.E. Waltz, *Nucl. Fusion* **29**, 885 (1989).
- [38] F. Romanelli, *Phys. Fluids* **B5**, 1018 (1989).

- [39] T. Hahm and W. Tang, *Phys. Fluids* **B1**, 1185 (1989).
- [40] N. Mattor and P.H. Diamond, *Phys. Fluids* **B1**, 1980 (1989).
- [41] R.B. Howell, *Rev. Sci. Instrum.* **59**, 1521 (1988).
- [42] D.V. Orlinskij and G. Magyar, *Nucl. Fusion* **28**, 611 (1988).
- [43] M. Bitter et al., "High resolution x-ray spectroscopy". Student Seminar Notes. (November 1987) Princeton Plasma Physics Laboratory.
- [44] H. Park, Princeton Plasma Physics Laboratory Report PPPL-2592 (1989).
- [45] G. Taylor et al., *Rev. Sci. Instrum.* **55**, 1739 (1984).
- [46] M. Bitter et al., *Rev. Sci. Instrum.* **59**, 1852 (1988).
- [47] A.T. Ramsey and S.L. Turner, "HAIFA: Modular, Fiber-Optic Coupled, Spectroscopic Diagnostic for Plasmas", Princeton Plasma Physics Laboratory Report PPPL-2407.
- [48] K.W. Hill, *private communication* (PPPL, 1988).
- [49] R.V. Budney et al., "Deuterium recycling, confinement, and limiter flux in TFTR", Princeton Plasma Physics Laboratory Report PPPL-2705 (July 1990).
- [50] H.W. Hendel et al., *Rev. Sci. Instrum.* **59**, 1682 (1988).
- [51] K.W. Hill et al., *Rev. Sci. Instrum.* **56**, 83 (1985).
- [52] R.J. Goldston, "Topics in confinement analysis of tokamaks with auxiliary heating", *Proc. of Course and Workshop on "Basic physical processes of toroidal fusion plasmas"*, Varenna, 1985 (Monotypia Franchi, Italy, 1985), p. 165.
- [53] W.M. Stacey, *Fusion Plasma Analysis* (Wiley-Interscience Publ., 1981), p. 78.

- [54] R.H. Radeztsky et al., *Proc. 15th Europ. Conf. Contr. Fusion and Plasma Phys.*, Dubrovick, 1988 (EPS 1988) Vol.1, p.79.
- [55] D.F. Duchs, "3/2 or 5/2 for convective thermal transport?", Joint European Torus Report JET-R(89)13 (July 1989).
- [56] S.D. Scott, *private communication* (PPPL, December 1990).
- [57] J. Schivell, *Rev. Sci. Instrum.* **56**, 972 (1985).
- [58] S.I. Braginskii, in *Review of Plasma Physics*, edited by M.A. Leontovich (Consultant Bureau, New York, 1965) Vol.1, p. 205.
- [59] F.L. Hinton and R.D. Hazeltine, *Rev. Mod. Phys.* **48**, 239 (1976).
- [60] P.C. Liewer, *Nucl. Fusion* **25**, 543 (1985).
- [61] S.P. Hirshman, *Phys. Fluids* **21**, 224 (1978).
- [62] K.C. Shaing and J.D. Callen, *Phys. Fluids* **26**, 1526 (1983); K.C. Shaing and S.P. Hirshman, *Phys. Fluids* **B1**, 705 (1989).
- [63] S.P. Hirshman and D.J. Sigmar, *Nucl. Fusion* **21**, 1152 (1981).
- [64] Y.B. Kim, "Moment Approach to Neoclassical Flows, Currents and Transport in Auxiliart Heated Tokamaks", University of Wisconsin Report UWPR 88-2 (February 1988).
- [65] M.N. Rosenbluth et al., "Neoclassical effects on plasma equilibria and rotation", in *Plasma Phys. and Cont. Nucl. Fusion Res.*, 1971 (IAEA, Vienna, 1971) Vol.1, p.495.
- [66] K.T. Tsang and E.A. Frieman, *Phys. Fluids***19**, 747 (1976).
- [67] J.T. Hogan, *Phys. Fluids* **27**, 2308 (1984).

- [68] F.L. Hinton and S.K. Wong, *Phys. Fluids* **28**, 3082 (1985).
- [69] S.K. Wong, *Phys. Fluids* **30**, 818 (1987).
- [70] W.M. Stacey, *Plasma Phys. Cont. Fusion* **31**, 1451 (1989).
- [71] G. Pautasso and W.M. Stacey, "A review of momentum confinement in tokamak plasmas", Georgia Tech Report GTFR 95 (January 1991).
- [72] A.A. Ware, "The rapid inward diffusion of cold ions in tokamaks and their effect on ion transport", The University of Texas Report IFSR-405 (October 1989).
- [73] C.T. Hsu and D.J. Sigmar, "Transport theory of impure tokamak plasma with strong rotation in the Pfirsch-Schluter regime", M.I.T. Plasma Fusion Center Report PFC/JA-88-14 (April 1988).
- [74] D.W. Ross et al., "IPSG Panel Report: Thermal and particle transport in tokamaks. Theoretical models for ignition studies. Version 2.2" (6/1987) ; also Horton's private communication to D.J.Sigmar and C.T.Hsu, *Proc. 12th Int. Conf. Plasma Phys. and Cont. Nucl. Fusion*, Nice, 1988 (IAEA-CN-50/D-2-3-3).
- [75] S.D. Scott et al., *Nucl. Fusion* **25**, 359 (1985).
- [76] S.D. Scott et al., "Measurements of toroidal rotation on TFTR", *Proc. 14th Europ. Conf. Cont. Fusion and Plasma Phys.*, Madrid, 1987.
- [77] S.D. Scott "Projection of rotation velocity for ITER", ITER Meeting on Energy Confinement, Garching, 1988.
- [78] N.A. Uckan, "Tokamak confinement projections and performance goals", Oak Ridge National Laboratory Report ORNL/TM-10854 (1988).
- [79] M. Redi et al., *Nucl. Fusion* **27**, 2001 (1987).
- [80] R.J. Goldston et al., *Bull. Am. Phys. Soc.* **34**, 1964 (1989).

- [81] R. Dominguez and R.E. Waltz, Nucl. Fusion **27**, 65 (1987).
- [82] R.J. Hawryluk, *Physics of plasma close Thermonuclear Conditions*, B. Coppi et al. editors, Vol. 1, p. 19, Brussels, 1980
- [83] R. Goldston, Plasma Phys. Cont. Nucl. Fusion **26**, 87 (1984).
- [84] P. Smeulders, Nucl. Fusion **26**, 267 (1986); ASDEX- and NI- teams, "Poloidal Asymmetric impurity radiation in Asdex in the presence of neutral injection", *Proc. 12th Europ. Conf. Cont. Fusion and Plasma Phys.*, Budapest, 1985.
- [85] J.L. Terry et al., Phys. Rev. Lett. **39**, 1615 (1977).
- [86] S.L. Allen et al., Nucl. Fusion **21**, 251 (1981).
- [87] S. Suckewer et al., "Rapid scanning of spatial distribution of spectral line intensities in PLT tokamak", Princeton Plasma Physics Laboratory Report PPPL-1430 (March 1978).
- [88] K. Brau et al., Nucl. Fusion **23**, 1657 (1983).
- [89] B. Grek and D. Johnson, Bull. Amer. Phys. Soc **27**, 1048 (1982) [6P19]; R.J. Goldston, *Workshop on parallel confinement in Tokamaks and transverse confinement in Tandem Mirrors*, Massachusetts Institute of Technology (September 28, 1983).
- [90] C.S. Chang and R.D. Hazeltine, Nucl. Fusion **20**, 1397 (1980).
- [91] W.M. Stacey, Nucl. Fusion, **27**, 1213 (1987).
- [92] C.S. Chang and R.W. Harvey, Nucl. Fusion **23**, 935 (1983).
- [93] K.H. Burrell et al., Phys. Rev. Lett. **47**, 511 (1981).
- [94] W.M. Stacey et al., Nucl. Fusion **25**, 463 (1985).
- [95] B. Lipshultz et al., Nucl. Fusion **24**, 977 (1984).

- [96] D.J. Sigmar et al., "Nonlinear collisional impurity transport including bifurcations, and coupling to rippling mode", M.I.T. Plasma Fusion Center Report PFC/JA-90-28 (August 1990); K.W. Wenzel, Bull. Am. Phys. Soc. **34**, 2153 (1989).
- [97] W.M. Stacey and D.J. Sigmar, Phys. Fluids **27**, 2076 (1984).
- [98] S. von Goeler et al., "MHD activity during ELMs", Max Plank Institute Report IPP III/143 (January 1989).
- [99] J.W. Connor et al., Plasma Phys. Cont. Fusion **31**, 1469 (1989).
- [100] R.D. Hazeltine and A.A. Ware, Phys. Fluids, **19**, 1163 (1976).
- [101] J.Y. Hsu, Phys. Rev. Lett. **53**, 564 (1984).
- [102] G.A. Hallock et al., Phys. Rev. Lett. **56**, 1248 (1986).
- [103] K.C. Shaing and E.C. Crume, Phys. Rev. Lett. **63**, 2369 (1989).
- [104] A.B. Hassam et al., Phys. Rev. Lett. **66**, 309 (1991).
- [105] R.J. Groebner et al., Phys. Rev. Lett. **64**, 3015 (1990).
- [106] H. Hsuan et al., Bull. Am. Phys. Soc **35**, 2084 (1990); also: H. Hsuan *private communication* .
- [107] R.D. Hazeltine, Phys. Fluids **17**, 961 (1974).
- [108] K. Ida and S. Hidekuma, Phys. Rev. Lett. **65**, 1364 (1990).
- [109] J.V. Hofmann et al., "Measurement of poloidal rotation on ASDEX", Max-Plank-Institute Report IPP 111/164 (September 1990).
- [110] J.D. Callen, "Transport Models; Anomalous Transport", *School on Plasma Turbulence and Transport*, Madison, Wisconsin (19-23 August 1991).
- [111] Y. Nagayama, *private communication* (PPPL, March 1991).

- [112] C.S. Pitcher et al., "Power and Particle Balance During NBI in TFTR", Princeton Plasma Physics Laboratory Report PPPL-2757 (May 1991).
- [113] K.L. Bell et al., J. Phys. Chem. Ref. Data **12**, 891 (1983).
- [114] W.M. Stacey, *private communication* (GIT, 1991).
- [115] J. Mathew et al., "Investigation of the Electric Field Structure in ISX-B Plasmas", Oak Ridge National Laboratory Report ORNL/TM-9386 (April 1986).
- [116] A.J. Wootton et al., Phys. Fluids **B2 12**, 2879 (1990).
- [117] D.W. Ross et al., "On Standard Forms for Transport Equations and Fluxes - Part II", The University of Texas Report FRCR 357 (March 1990).
- [118] R.E. Waltz, Phys. Fluids **25**, 1269 (1982).
- [119] A. Demetraidis et al., AIAA Jour. **4**, 451 (1966).
- [120] P. Schoch et al., Rev. Sci. Instrum. **9**, 1646 (1988).
- [121] C.P. Ritz et al., Nucl. Fusion **27**, 1125 (1987).
- [122] R.V. Bravenec et al., Bull. Am. Phys. Soc. **35**, 2026 (1990).
- [123] G.A. Hallock et al., Phys. Rev. Lett. **59**, 1301 (1987).
- [124] N.L. Bretz et al., "Density Fluctuation Measurements from Microwave Scattering on TFTR", *Proc. 17th EPS Conf. Cont. Fusion and Plasma Heat.*, Amsterdam, June 25-29 1990.
- [125] N. Ohyaib et al., Phys. Rev. Lett. **58**, 120 (1987).
- [126] M. Malacarne and P.A. Duperrex, Nucl. Fusion **27**, 2113 (1987).
- [127] D.E. Graessle et al., Phys. Rev. Lett. **62**, 535 (1989).

[128] J.D. Callen et al., Bull. Am. Phys. Soc. **34**, 2043 (1989).

[129] A.J. Wootton, "Edge Turbulence", The University of Texas Report FRCR 371 (1990).